UNIVERSITEIT VAN PRETORIA
UNIVERSITY OF PRETORIA
YUNIBESITHI YA PRETORIA

Modelling and characterization of a modified 3-DoF pneumatic Gough-Stewart platform

by

Hendrik Jacobus Theron

Submitted in partial fulfilment of the requirements for the degree

Master of Engineering (Mechanical Engineering)

in the

Department of Mechanical and Aeronautical Engineering
Faculty of Engineering, Built Environment and Information Technology
UNIVERSITY OF PRETORIA

July 2016

SUMMARY

Modelling and characterization of a modified 3-DoF pneumatic Gough-Stewart platform

by

Hendrik Jacobus Theron

Supervisor(s):	Prof N J Theron
Department:	Mechanical and Aeronautical Engineering
University:	University of Pretoria
Degree:	Master of Engineering (Mechanical Engineering)
Keywords:	Pneumatic, Stribeck, Gough-Stewart, Matlab®, Simulink®, MSC ADAMS®, ISO-6358, Co-simulation, Inverse Kinematics, Mass Flow, Deck Motion Simulator, Nonlinear

Stabilised line of sight optical payloads for maritime vessels require variable platform conditions during the development, test and evaluation phases. A ship deck motion simulator is one means of generating such conditions in a controlled laboratory environment. This dissertation describes the aspects of the modelling, identification and validation of a ship motion simulator, in the form of a pneumatically actuated 3-DOF modified Gough-Stewart manipulator, to generate a realistic simulation environment for controller design. The simulation environment is a Matlab® supervised MSC ADAMS®/Matlab® Simulink® co-simulation in which Simulink® houses the pneumatic model, the friction model, and the controller, and ADAMS® runs the dynamic model of the physical hardware. A similar simulator cannot be found in published literature forcing a development of the model from the ground up, using published information as a foundation. The simulator model is broken up at the subsystem level which comprises the valve mass flow model, the piston chamber and force model, the complete actuator model and finally the complete ship simulator model. Each of these is derived, identified, and validated. The requirements of the simulator as well as the simulation environment is derived from real-life measurements done on seafaring vessels. An inverse kinematic solution is presented as a set of lookup tables which are generated from the outputs of MSC ADAMS® by manipulating the simulator platform over the whole range of movements through Matlab®. The reverse of the process is then used to ensure that actuator extensions generate the correct platform attitude -

the attitude errors as shown to be infinitely small. Two valve mass flow models are proposed, a classical model and an ISO model, the first derived from thermodynamic principles and the second based on the ISO-6358 standard. The parameters of the two models are identified through experimental charging and discharging of a constant volume pressure chamber and sampling the temporal pressure and temperature outputs. The mass flow is calculated from the measured data through parameter estimation. Validation is done by comparing the temporal pressure outputs of the models with the actual measured pressure signals. The mean absolute error for the best fit ISO model is less than half of the Classic model at 0.4 MPa ($MAE < 2\ kPa$) and the temporal pressure relationships in the closed-loop and open-loop tests shows a 93% correlation against measured pressure signals. The combination of the derived actuator chamber model and the valve mass flow model produces a realistic actuator model. The force equation of each of the actuators makes provision for a nonlinear friction component. The actuator friction model is based on a simple stick-slip relation with an acceleration dependent Stribeck function and an exponential viscous friction component. This model is also identified with data from the actual hardware. The complete ship motion simulator model is validated through open-loop as well as closed-loop tests. The open-loop tests are performed with chirp or sinusoidal signal excitation from a stable elevated offset starting condition. The ratio of the measured and simulated extension amplitudes in the open-loop is larger than 0.95 while the ratio of the rise times (t_m/t_s) is approximately 0.85. The closed-loop validation tests are conducted with both heave and roll inputs and compared well with the real system. A 14% difference in the actuator position amplitude (between the simulated and measured systems), and a 20% slower extension rate at 0.05 Hz that increases at 1 Hz to match the measured rate are observed. The maximum large signal bandwidth is 0.617 Hz, and is only limited by the mass flow. A simplified plant model is derived and compared with the high performance model and is subsequently used for a state feedback controller design and evaluation. The final controller gains deliver a stable system with the same 0.617Hz bandwidth limitation and a controller that is insensitive to loop gain changes from 0.5 to 15.

OPSOMMING

Die modellering en karakterisering van ’n gemodifiseerde 3-GvV pneumatiese Gough-Stewart platform

deur

Hendrik Jacobus Theron

Studieleier(s):	Prof N J Theron
Departement:	Meganiese en Lugvaartkundige Ingieurswese
Universiteit:	Universiteit van Pretoria
Graad:	Magister in Ingenieurswese (Meganiese Ingenieurswese)
Sleutelwoorde:	Pneumaties, Stribeck, Gough-Stewart, Matlab®, Simulink®, MSC ADAMS®, ISO-6358, Inverse kinematika, Massavloei, Skeepsdeksimulator, Nie-linieêr

Optiese loonvragte vir maritieme vaartuie, waarvan die siglyn gestabiliseer word, benodig veranderlike platform toestande tydens ontwikkeling, toets en evaluasie. Een manier om veranderlike dektoestande in ’n laboratorium te emuleer, is deur ’n skeepsdeksimulator te gebruik. Hierdie verhandeling beskryf aspekte van die modelering, stelsel identifikasie en validasie van ’n drie grade van vryheid skeepsdeksimulator wat gebruik word om ’n realistiese simulasieomgewing te skep. Die simulator is in die vorm van ’n gemodifiseerde pneumatiese Gough-Stewart manipulator. ’n Gesamentlike MSC ADAMS®/Matlab® Simulink® simulasie, wat deur Matlab® bedryf word, vorm ’n simulasieomgewing waarin ADAMS® die dinamiese model van die fisiese hardeware huisves, en Simulink® die pneumatiese model, die wrywingsmodel en die beheerder hanteer. Daar kan geen soortgelyke simulator gevind word in gepubliseerde literatuur nie, wat tot gevolg het dat ’n model van eerste beginsels opgestel is deur die gepubliseerde inligting as fondasie te gebruik. Die simulasiemodel is opgebreek op substelselvlak wat die massavloei model van die klep, die silinderkamermodel, sowel as die kragmodel van die suier, die volledige aktuatormodel en ook, laastens, die volledige skeepsdeksimulatormodel insluit. Al hierdie modelle is afgelei, die parameters geïdentifiseer and gevalideer. Die behoeftestellings van die simulator, sowel as die simulasieomgewing, is afgelei uit werklike metings van soortgelyke seevarende vaartuie. Opsoektabelle, wat bereken is deur met Matlab® die simu-

latorplatform binne MSC ADAMS® deur sy volledige bewegingsberyk te manipuleer, stel die inverse kinematika voor. Infinietdesimale klein foute is verkry deur die proses in tru aan te wend en die platform oriëntasie tydens verskeie aktuatortposisies te toets. Daar is twee klep massavloeimodelle beskryf, 'n klassieke model wat van basiese termodinamiese geginsels afgelei is, en 'n ISO model wat gebaseer is op die ISO-6358 standaard. Beide hierdie modelle se parameters is deur eksperimentele stelselidentifikasieprosedures bepaal tydens opblaas- en afblaastoetse. Hiervoor is 'n konstante volume druktenk gebruik en beide die tydafhanklike interne druk en lugtemperature is gemeet. Die massavloei is bepaal deur parameterestimasietegnieke toe te pas op die voorgestelde modelle, en validering deur die tydafhanklike druk te vergelyk met die uitsette van die modelle. By 'n werksdruk van 0.4 MPa is die gemiddelde absolute fout van die ISO model minder as die helfte van die fout van die klassieke model ($MAE < 2\ kPa$), en die tydafhanklike drukverwantskap in beide die geslotelus-, sowel as die ooplustoetse toon 'n 93% korrelasie teen die gemete drukwaardes. Die kombinasie van die afgeleide silindermodel en die klep massavloeimodel lewer 'n geloofwaardige wrywingslose aktuatormodel, en deur die dinamiese kragvergelyking te gebruik, word dit aangevul deur 'n nie-linieêre wrywingskomponent. 'n Steek-glip wrywingsmodel met 'n versnellingsafhanklike Stribeckfunksie en 'n eksponetiële viskeuse wrywingskomponent stel die aktuatorwrywing voor. Die wrywingsmodel is ook geïdentifiseer deur werklike gemete data. Die valideringsoefening van die volledige skeepsdeksimulator is voltooi deur beide ooplustoetse, sowel as gelotelustoetse uit te voer. Die ooplustoetse is vanaf halfuitgestrekte aktuatorposisies gedoen deur sinusoïdale en tjirp opwekkingsseine te gebruik. Die amplitudeverhouding tussen die gemete posisies en die gesimuleerde posisies is groter as 95%, terwyl die stygtydverhouding (t_m/t_s) ongeveer 0.85 is. Vir geslotelusvaliderinstoetse is beide deining and rol stelpunte as insette gebruik en die simulasie resultate is met die werklike gemete waardes vergeleik. Die gemete amplitude van die aktuatorposisie is ongeveer 14% kleiner as die gesimuleerde amplitude, die gemete aktuatorspoed is ongeveer 20% stadiger by 0.06 Hz en terwyl dit ongeveer dieselfde is by 1 Hz. Die maksimum grootseinbandwydte is 0.617 Hz en word beperk deur die massvloeivermoë van die klep. 'n Vereenvoudigde stelselmodel is afgelei, 'n toestandsterugvoerbeheerder is ontwerp en die beheerder ge-evalueer met beide die hoë akkuraatheid model, sowel as die vereenvoudigde model. Die finale beheerder lewer 'n stabiele stelsel met dieselfde 0.617Hz bandwydte wat onsensitief is vir luswinsveranderinge vanaf 0.5 tot 15.

TABLE OF CONTENTS

Acronyms

List of symbols

CHAPTER 1 Introduction **19**

1.1 Problem Statement 19

1.1.1 Background 19

1.1.2 Research gap 20

1.2 Research Goals 21

1.3 Research Objectives 21

1.4 Contribution 23

1.5 Overview of study 23

CHAPTER 2 System Description and Literature Survey **25**

2.1 Ship Dynamics 25

2.2 Modular Stand Alone Tracker (MODSAT) 27

2.3 Ship Motion Simulator (SMS) 29

2.4 Combined MODSAT and SMS 32

2.5 Literature Survey 32

2.5.1 Geometry, Kinematics and Dynamics 33

2.5.2 Pneumatic Actuators 34

2.5.3 Control 39

CHAPTER 3 SMS Kinematics **41**

3.1 SMS Computer Aided Design (CAD) Model 41

3.2 SMS Kinematic Vector Diagram Model 44

3.2.1 Gough-Stewart Vector Kinematics 44

3.2.2 SMS Vector Kinematics 47
3.3 MSC ADAMS® Multi-body Dynamics 49
3.4 Integration between MSC ADAMS® and Matlab® 51
3.5 ADAMS® Kinematic Simulation 57

CHAPTER 4 Theoretical Pneumatic Models 60
4.1 Pneumatic System 60
4.1.1 Pneumatic Actuator Subsystem Matlab® Model 62
4.1.2 Valve 63
4.1.3 Actuator 73
4.1.4 Pneumatic Connections 79
4.1.5 Pneumatic Reservoir 81

CHAPTER 5 Mass Flow Characterisation 82
5.1 Theoretical Models 82
5.1.1 Classic Mass Flow Model 82
5.1.2 ISO Mass Flow Model 84
5.2 Valve Flow Measurements 86
5.2.1 Pneumatic Measurement setup 86
5.2.2 Temperature Measurement 87
5.2.3 Test Matrix 89
5.3 Valve Characteristics - Processing 90
5.3.1 Signal Processing 90
5.3.2 Discharge Coefficient 95
5.3.3 Sonic Conductance 101
5.4 Coefficient and Model Validity 107
5.4.1 Classic Model and ISO Model Temporal Pressure Comparison 109
5.4.2 Classic Model and ISO Model Mass Flow Comparison 115
5.4.3 ISO Model Coefficients 121

CHAPTER 6 Friction In Pneumatic Systems 124
6.1 Friction Identification Test Setup 125
6.2 Friction Identification Procedure 128
6.3 Friction Identification Data Sets 129

6.4 Friction Model 135
6.5 Festo Actuator Friction Model 138

CHAPTER 7 Simulation Model Validation 142
7.1 Festo Actuator Model Validation 142
7.1.1 Matlab® Simulink® Model Description 142
7.1.2 Matlab®/ADAMS® Actuator Model Description 146
7.2 Actuator Model Validation 147
7.3 SMS Model Validation 151
7.3.1 SMS Matlab® Simulink® Model 152
7.3.2 Real Time Work Shop (RTW) Controller 154
7.3.3 SMS Controller Hardware 157
7.3.4 Open-Loop Tests 160
7.3.5 Closed-loop Tests 167
7.3.6 Closed-loop Results 170

CHAPTER 8 SMS Controller 175
8.1 Simplified Plant Model 175
8.2 State Feedback Compensation 178

CHAPTER 9 Conclusion 184
9.1 Summary 184
9.1.1 Kinematics 185
9.1.2 Pneumatic Models and Mass Flow Characterisation 185
9.1.3 Friction Model and Friction Identification 186
9.1.4 SMS Model Validation 187
9.1.5 Simplified Plant Model and Control 189
9.2 Evaluation of Objectives 190
9.3 Future Work 193

REFERENCES 195

APPENDIX A Definitions 201

APPENDIX B Matlab® RTW Embedded Coder Integration With Code Composer Studio V5.5 204

B.1 Overview 204
B.1.1 Guide 205
B.1.2 Code Composer Studio (CCS) 207

APPENDIX C NIST Thermocouple Coefficients 210

APPENDIX D Simplified Model Parameters 211

APPENDIX E Simplified Model Controller Design Parameters 212

ACRONYMS

ADAMS Automated Dynamic Analysis of Mechanical Systems

ADC Analog to Digital Converter

APRBS Amplitude Modulated Pseudo-Random Binary Signal

CAD Computer Aided Design

CAN Controller Area Network

CCS Code Composer Studio

CoG Centre of Gravity

CSIR Council For Scientific And Industrial Research

DAC Digital to Analog Converter

DIN Deutsches Institut für Normung

DPSS Defence, Peace, Safety and Security

DSP Digital Signal Processor

EMF Electromotive Force

FOV Field Of View

GUI Graphical User Interface

IMU Inertial Measurement Unit

INS Inertial Navigation System

ISO International Organisation for Standardisation

JTAG Joint Test Action Group

LOS Line Of Sight

MAE Mean Absolute Error

MBD Multibody Dynamic

MISO Multi Input Single Output

MODSAT Modular Stand Alone Tracker

MSC MacNeal-Schwendler Corporation

NIST National Institute of Standards and Technology

OSS Optronics Sensor Systems

PC Personal Computer

PD Proportional Differential

PI Proportional Integral

PID Proportional Differential Integral

PSD Power Spectral Density

PWM Pulse Width Modulation

RTW Real Time Work Shop

RX Receive

SAT Stand Alone Tracker

SBD Specification Based Design

SCI Serial Communication Interface

SF State Feedback

SID System Identification

SMC Sliding Mode Controller

SMS Ship Motion Simulator

SNR Signal to Noise Ratio

STP Standard Temperature and Pressure

TI Texas Instruments

UAV Unmanned Aerial Vehicle

USB Universal Serial Bus

LIST OF SYMBOLS

A	Area $[m^2]$, Surface Environment
a	Acceleration $[m.s^{-2}]$
A_a	Surface area of the piston in chambers a
A_b	Surface area of the piston in chambers b
a_{DB}	Dead band large signal gain coefficient
A_i	The i^{th} piston area
A_k	The k^{th} piston area
A_L	Lower piston area $[m^2]$
α	Specific heat capacity ratio for air in a chamber
α_c	Ratio of the system natural frequency and the closed-loop natural frequency
α_f	Friction transient function
α_i	Specific heat capacity ratios for air entering a chamber
α_o	Specific heat capacity ratios for air leaving a chamber
A_r	Sectional area of the piston rod
a_{RMS}	RMS Acceleration value $[m.s^{-2}]$
A_U	Upper piston area $[m^2]$
A_v	Valve orifice area
A_{va}	Valve Orifice a Area
A_{vb}	Valve Orifice b Area
A_{ve}	Effective valve orifice area
b	Critical pressure ratio
b_{DB}	Dead band y-intercept
β	Viscous friction coefficient
b_f	Viscous friction component $[N.s.m^{-1}]$
C	Sonic Conductance $[m^3.(s.Pa)^{-1}]$

c	Spring constant $[N.m^{-1}]$
C_0	Open-loop forward gain $[m.s^{-1}.V^{-1}]$
C_1	Choked flow function coefficient
c_1	Spring constant $[N.m^{-1}]$
C_2	Subsonic flow function coefficient
c_2	Spring constant $[N.m^{-1}]$
C_d	Nozzle discharge coefficient
c_{DB}	Dead band change over coefficient
c_i	Thermocouple temperature coefficients
c_p	Specific heat capacity at a constant pressure
c_V	Specific heat capacity at a constant volume
d_B	Spool barrel diameter
δ	Stribeck exponent
ΔF_f	Exponential friction force offset $[N]$
E	Thermocouple Electromotive Force (EMF) $[mV]$
e	Specific energy, energy per unit mass of a gas $[J.kg^{-1}]$
ε_f	Stiction velocity limit $[m.s^{-1}]$
e_k	Specific kinetic energy $[J.kg^{-1}]$
e_p	Specific potential energy $[J.kg^{-1}]$
f_1	Chirp generator initial frequency $[Hz]$
f_2	Chirp generator final frequency $[Hz]$
F_a	Force on surface a
F_b	Force on surface b
F_C	Coulomb friction force $[N]$
F_{C1}	Coulomb friction force for accelerating movement $[N]$
F_{C2}	Coulomb friction force for decelerating movement $[N]$
f_{cycle}	Actuator test frequency $[Hz]$
F_f	Friction force
F_{fric}	Friction force
F_L	External load force
f_{max}	Maximum frequency required by SMS $[Hz]$
F_P	Pneumatic force $[N]$
F_r	Force on the piston due to the rod area

F_{Res}	Resultant force, Difference between the pneumatic force and the friction force $[N]$
F_S	Stiction force $[N]$
F_{UE}	Unmodelled friction force effects $[N]$
F_V	Viscous friction force $[N]$
g	Gravitational constant
γ_2	Kurtosis of the data set
γ_f	Exponential friction force constant $[s.m^{-1}]$
G_D	Differential gain
G_I	Integral gain
G_P	Proportional gain
$G(s)$	System transfer function
H	Enthalpy
h	Specific enthalpy
H_1	Enthalpy in state 1
H_2	Enthalpy in state 2
h_i	Specific enthalpy of the input gas
h_o	Specific enthalpy of the outlet gas
K_a	Acceleration gain
κ	Ratio of specific heat capacities
K_c	Loop stability gain
k_m	Model adjustment gain
K_p	Proportional gain
K_v	Velocity gain
L	Actuator stroke length
ℓ	Liter
l_S	Valve orifice segment length
m	Mass in general
m	Subsonic Index
m_1	Mass in state one
m_2	Mass in state two
$\dot{m}$	Air Mass flow rate
$\dot{m}_a$	Air Mass flow rate into chamber a
$\dot{m}_b$	Air Mass flow rate into chamber b

$\dot{m}_i$	Inflowing Air Mass flow rate
$\dot{m}_o$	Outflowing Air Mass flow rate
$\dot{m}_v$	Valve Air Mass flow rate
min	Minute
M_L	Mass of the load
M_p	Mass of the piston
M_T	Total mass
μ	Mean of a data set
μ_{F_S}	Mean of a actuator stiction force samples $[N]$
μ_{p1}	Mean of a actuator chamber 1 pressure estimation residuals $[Pa]$
μ_{p2}	Mean of a actuator chamber 2 pressure estimation residuals $[Pa]$
μ_v	Mean of a actuator velocity estimation residuals $[m.s^{-1}]$
μ_x	Mean of a actuator linear displacement estimation residuals $[m]$
v_1	Air velocity in state 1 $[m.s^{-1}]$
N	Number of orifice slots
v	Air velocity $[m.s^{-1}]$
v_2	Air velocity in state 2 $[m.s^{-1}]$
v_i	Air velocity of the input
v_o	Air velocity of the output
ω_c	Closed-loop natural frequency $[rad.s^{-1}]$
ω_s	Characteristic natural frequency $[rad.s^{-1}]$
p	Pressure $[Pa]$
p_1	Pole 1
p_1	Pressure in state 1 $[Pa]$
p_2	Pole 2
p_2	Pressure in state 2 $[Pa]$
p_3	Pole 3
p_A	Ambient Pressure $[Pa]$
p_a	Pressure in chamber a $[Pa]$
p_b	Pressure in chamber b $[Pa]$
$\bar{p}$	Average absolute pressure $[Pa]$
p_c	Pressure in charging chamber $[Pa]$
p_{c0}	Initial pressure in charging chamber $[Pa]$

p_{cr}	Critical Pressure ratio
$\dot{p}_c$	Rate of pressure change in the charging chamber $[Pa.s^{-1}]$
$\dot{p}_k$	Rate of pressure change in the k^{th} chamber $[Pa.s^{-1}]$
$\dot{p}_l$	Rate of pressure change in the lower chamber $[Pa.s^{-1}]$
$\dot{p}_u$	Rate of pressure change in the upper chamber $[Pa.s^{-1}]$
p_e	End pressure $[Pa]$
p_{est}	Estimated pressure $[Pa]$
p_L	Pressure in the lower chamber $[Pa]$
p_l	Pressure in the lower chamber $[Pa]$
$p_{L(Measured)}$	Measured pressure in the lower chamber $[Pa]$
p_m	Measured pressure $[Pa]$
p_R	Reservoir pressure $[Pa]$
p_s	Supply Pressure $[Pa]$
Ψ	Flow function
p_s	Start pressure $[Pa]$
p_t	Theortical pressure $[Pa]$
p_U	Pressure in the upper chamber $[Pa]$
p_u	Pressure in the upper chamber $[Pa]$
$p_{U(Measured)}$	Measured pressure in the upper chamber $[Pa]$
Q	Thermal Energy $[J]$
q	Volumetric flow rate $[\ell.min^{-1}]$
$\dot{Q}$	Thermal Energy Rate $[J.s^{-1}]$
R	Specific gas constant = R/M $[R_0 = 288\ J.kg^{-1}.K^{-1}]$
r_B	Radius of the valve barrel
ρ	Density
$\ddot{x}$	Piston acceleration
σ	Standard deviation
σ_1	Viscous friction coefficient for accelerating movement $[N.s.m^{-1}]$
σ_2	Viscous friction coefficient for decelerating movement $[N.s.m^{-1}]$
σ_{F_S}	Standard deviation of the stiction force samples $[N]$
σ_{p1}	Standard deviation of the actuator chamber 1 pressure estimation residuals $[Pa]$
σ_{p2}	Standard deviation of the actuator chamber 2 pressure estimation residuals $[Pa]$
σ_v	Standard deviation of the actuator velocity estimation residuals $[m.s^{-1}]$

σ_x	Standard deviation of the actuator linear displacement estimation residuals $[m]$
T	Temperature [K]
t	Time [s]
T_1	Temperature in state 1 [K]
T_a	Temperature in chamber a [K]
T_b	Temperature in chamber b [K]
T_{CJ}	Thermocouple cold junction temperature $[^\circ C]$
t_e	End time
θ_S	Circle segment included angle
T_i	Inflow gas temperature [K]
T_K	Thermocouple temperature $[^\circ C]$
T_o	Outflow gas temperature [K]
$T(s)$	Closed-loop transfer function
T_s	Sample time
t_s	Start time
t_{Target}	Time at which the end frequency of a chirp signal will be generated
u	Internal system specific energy
$U(s)$	Laplace transform of the u state in the model $[V]$
U_w	Winding voltage $[V]$
V	Volumetric environment, Volume $[m^3]$
v	Per unit volume, Velocity $[m.s^{-1}]$
v_1	Per unit volume in state 1
v_2	Per unit volume in state 2
V_a	Volume in chamber a $[m^3]$
V_b	Volume in chamber b $[m^3]$
V_c	Volume in a chamber $[m^3]$
V_{di}	Dead volume in an actuator chamber $[m^3]$
V_{dk}	Dead volume in actuator chamber k $[m^3]$
$\dot{V}$	Temporal change in volume
V_i	Function input voltage $[V]$
V_{imax}	Maximum input voltage $[V]$
V_L	Lower chamber volume $[m^3]$
v_{max}	Maximum velocity $[m.s^{-1}]$

V_o	Function output voltage $[V]$
V_{omax}	Maximum output voltage $[V]$
V_R	Reservoir volume $[m^3]$
V_S	Valve spool voltage $[V]$
v_S	Stribeck velocity $[m.s^{-1}]$
$V_{Sol(Measured)}$	Measured solenoid signal $[V]$
V_U	Upper chamber volume $[m^3]$
V_{vs}	Valve input voltage $[V]$
V_x	Linear displacement senor voltage $[V]$
$\dot{W}$	Rate of mechanical energy
$\dot{W}_{flow}$	Rate of air flow energy
w_O	Width of the valve orifice
W_S	Mechanical shaft energy $[J]$
w_S	Width of the valve spool sealing surface
$\dot{W}_S$	Rate of mechanical shaft energy
x	x coordinate, Piston displacement
$\bar{x}$	Mean value of x
$\dot{x}$	Piston rate
x_O	Open distance of the valve orifice
$X(s)$	Laplace transform of the x state in the model $[m]$
x_S	Displacement of the valve spool
x_{Smax}	MAximum displacement of the valve spool
z	z coordinate
z_1	z_1 coordinate, height
z_2	z_2 coordinate, height
ζ	Stribeck velocity modification constant $[s^2.m^{-1}]$
ζ_c	Closed-loop damping ratio
ζ_f	Damping ratio
z	height
z_i	Height of the inlet state
z_o	Height of the oulet state

CHAPTER 1

INTRODUCTION

1.1 PROBLEM STATEMENT

1.1.1 Background

A maritime vessel can be equipped with a suite of sensors to enable the crew to monitor the vessel's surrounding environment. In many cases this includes short and long range electro-optical sensor packs. Maritime vessels are not stationary platforms and platform motion has to be countered by means of active Line Of Sight (LOS) stabilisation, especially in the case of the long range equipment. This is typically integrated into the pointing or tracking system carrying the electro-optical payloads. The development of a stabilisation system usually has a preliminary phase during which the algorithms are tested and refined in a controlled laboratory environment that can be far removed from the coast and suitable ships. The effectiveness of the stabilisation also has to be assessed through actual mounting platform motion before the integration onto the maritime vessels.

It is, therefore, necessary to simulate the hull and deck motion of, in this case, large maritime vessels under various conditions and to excite the tracking system realistically. A pneumatic Ship Motion Simulator (SMS) was designed and built by the Optronics Sensor Systems (OSS) group in the Defence, Peace, Safety and Security (DPSS) unit of the Council For Scientific And Industrial Research (CSIR) to emulate the movement of the ship deck, resulting in a cheap, effective, but highly nonlinear system which is challenging to control.

The CSIR sponsored SMS system by DPSS was initially designed as an open-loop excitation system as part of a larger stabilisation project. The envisaged method of usage of the SMS was only a

post design analysis of sensor stabilisation with arbitrary motion generated by random band limited signals measured with a frame mounted Inertial Measurement Unit (IMU). As the stabilisation project progressed, the necessity for closed-loop, real world representative motion became more important, requiring closed-loop control and measured attitude tracking from the SMS.

With the initial choices made on the usage of the system, the changes to that envisaged usage and the design choices made on the physical structure of the pneumatic system, a series of challenges arose in the downstream processes. The most dominant challenge is the understanding of the behaviour of a pneumatically actuated emulation platform, to generate a model of this platform that is an acceptable representation of reality, and to devise a control system for the platform.

1.1.2 Research gap

As part of any large scale study, the *status quo* in terms of the topic and the background science need to be assessed. An analysis of the system requirements, a reflection of the applied constraints, and a literature survey was done (described in detail in § 2). From this one could conclude that, although there are numerous motion simulation systems in operation and under development - many having a similar structure to the SMS - none could be found that had the exact same modified Gough-Stewart layout and make use of a pneumatic actuation system. These two facts were given as constraints to the development of the control system, as the actual system has already been constructed. It became clear that a reliable dynamic model of the physical system as well as a reliable model of the pneumatic subsystem were needed to derive a system transfer function through a system identification process. This is necessary for a systematic controller design procedure and to prevent unfounded controller architectures and gain values to be tried without prior knowledge of the expected performance.

In many of the published cases, various solutions to the modelling and control architecture problems were presented, ranging from very complex, single domain models to very simplistic ”text book” models. The gaps identified, relating to this specific engineering problem, are the absence of a dynamic model for this type of modified Gough-Stewart platform, a simulation environment that can use this model to develop controllers, and a proven controller architecture with controller configuration parameters.

1.2 RESEARCH GOALS

The primary focus of the research done by the project sponsor, the CSIR, is the improvement of the imaging suites on moving platforms. In this domain the CSIR is actively working on techniques to improve the LOS stability of electro-optical systems as well as the enhancement of the captured imagery through computational post processing. This research revolves around the mechanical stabilisation and the test and evaluation of stabilisation systems.

The goal of this engineering research project is to find an optimal combination of models, processes, and controlling techniques to enable the control systems engineer to excite a stabilised sensor pack in a real world realistic fashion, and to ultimately achieve a controllable simulator. In order to achieve this, a firm understanding of the dynamics of the simulator system, a working knowledge of pneumatic actuated systems, and a reliable simulation infrastructure is needed. This knowledge of pneumatic systems and physical modelling, together with the use of engineering tools such as MacNeal-Schwendler Corporation (MSC) Automated Dynamic Analysis of Mechanical Systems (ADAMS)® will enhance the long term strategic capability to design other simulators.

1.3 RESEARCH OBJECTIVES

The engineering problem statement of designing a stable, representative SMS to excite stabilised optronic sensor packs was derived from the characteristics of the maritime vessels to be fitted with the optronic sensor packs and the design constrained by the availability of development time, and the estimated budget for the development. A controller to augment the simulator and to realise realistic sea faring deck motion forms, therefore, an important part of the development.

Various ways to meet the controller requirements can be followed. A brute force, gut feel controller could be designed and the gains ”tweaked” until the system complies to requirements, a process that will most probably end in damage to the equipment or ultimate failure in the design task. A more theoretically based approach to follow would include the development of models by first principle derivation or black box system excitation and identification, and then model based controller design - a more favoured approach.

The modelling and characterisation of systems as complex and nonlinear as the SMS system is clearly not a simple task. The generation of explicit mathematical relationships will take up a lot of time, and

the validation thereof, even longer. Any previously published literature, validated models, and high level simulation tools will ease this task and expedite the project. Merging the validated model with a high level simulation environment then forms part of an evaluation suite that can be used to test a range of controllers, from simple linear controllers to complex nonlinear controllers.

The following objectives based on the envisaged activities listed above are:

- To effectively search the scholarly domains for published literature and to get an understanding of the scope of the modelling and control challenge that accompanies pneumatic systems. To find, during this survey, suitable system descriptions, models, controller techniques, and guidance to assumptions and pitfalls to expedite the development of a controllable SMS.

- To generate a detailed simulation model of the SMS that can be used to develop controller architectures and test the controlled system in simulation before transferring the controller to the actual hardware. This comprises a set of secondary objectives, *i.e.*:

  - to derive a detailed mechanical model of the system, including rotational points, moving masses, moments of inertia, and movement restrictions,

  - to generate a Multibody Dynamic (MBD) model to be used in MSC ADAMS® to simulate the dynamics of the SMS and non-pneumatic parts of the actuators,

  - to derive and validate a pneumatic model for the actuators,

  - to derive and validate a friction model for the actuators, and

  - to integrate the models into Matlab® Simulink®, and generate a co-simulation between MSC ADAMS® and Simulink®.

- To validate the dynamic simulation of the complete system and

- To linearise the system model and design a first order controller to meet the requirements of the simulator.

1.4 CONTRIBUTION

The most important contribution made through the study is a validated SMS simulation environment, using derived models of the mechanical structure, the pneumatic system, and the friction behaviour of the actuators in an MSC ADAMS® /Matlab® Simulink® co-simulation. This environment enables the CSIR to develop and test new controllers for the SMS, and other systems, before applying them to actual sensitive hardware.

A new process for finding the inverse kinematic solution for a modified Gough-Stewart manipulator, in the form of lookup tables, was defined and verified.

Two valve models were defined, one derived from basic thermodynamic principles and one based on model described in the ISO-6358 standard. A comparison was done between the two models and the ISO model found to be the more accurate of the two.

A non-linear phenomenon was observed on the viscous friction behaviour of the actuator, and a new stick-slip friction model proposed. This new model was validated through experimentation.

1.5 OVERVIEW OF STUDY

The study presented in this document was done in six separate parts or phases along six basic engineering disciplines. It started with a system and requirements analysis and literature survey, then a geometric and kinematic modelling and dynamic simulation phase, a pneumatic system modelling phase, a friction modelling phase, a model integration and validation phase, and a controller design phase.

In the first phase described in Chapter 2 the supplied SMS system was documented in terms of construction, size, weight, actuation, and payload. The requirements of the client, DPSS, for the final simulator system was analysed and the system parameters extracted from deck motion measurements of actual maritime vessels. With these requirements in mind, a literature survey was conducted to assess the state of available information on the subject and to determine the scope of the problem. The separate tasks to be completed to realise an operational simulator were planned.

During the second part of the study, the geometric model was defined and a solution for solving the inverse kinematics sought. A process to find a kinematic solution was defined using MSC ADAMS®

as a solving tool and a full kinematic (and dynamic) Matlab®/ADAMS® co-simulation was built to be used as a full dynamic simulator in the subsequent phases. This is described in Chapter 3.

The next two parts of the study were closely linked through the equipment and test procedures used. The third part revolved around deriving a physics based theoretical model, called the classic model, for the pneumatic system using thermodynamic principles (Chapter 4) and finding the coefficients that will describe the SMS system accurately (Chapter 5). A series of experiments were done to identify the coefficients used in the model. From a mismatch between actual measured mass flow and theoretical mass flow, an updated valve model, the ISO model (based on ISO-6358), was defined and a comparison done between this model and the classic model. This updated model was subsequently used in the full dynamic co-simulation.

The objective of the fourth part of the study as described in Chapter 6 was to model the friction in the pneumatic actuators. A friction model was derived and once again a series of experiments was done to identify the coefficients used in this model. A simple stick-slip model with a unique exponential viscous friction component was derived.

All the parts of the SMS model were then integrated and the actual hardware fitted with a controller and software support system. A model validation, both in open-loop and in closed-loop was conducted. This is described in Chapter 7 with the supporting results.

Finally, the sixth and last part of the study (Chapter 8), which will pave the way for future controller studies, was a simplification of the actuator system based on published literature and the evaluation of a state feedback controller.

The document is then concluded in Chapter 9 with an overview of the work done in each section of the study, an evaluation of the objectives and a proposal to continuation of the research.

CHAPTER 2

SYSTEM DESCRIPTION AND LITERATURE SURVEY

2.1 SHIP DYNAMICS

The main platforms which the SMS should emulate are large maritime ships in the 3500 metric ton displacement range with an overall length of around 120 *m* and a beam of around 16 *m*. Maritime vessels of this size have low frequency dynamics and large moments of inertia. Conditions under which they are used vary dramatically from calm to stormy and the mode of sailing and direction to the swell influence the behaviour. Rather than trying to model the ship dynamic behaviour from scratch, motion data was captured for two typical situations off the coast of South Africa. One is from a journey off the coast of Arniston (27 March, 2006), close to Cape Agulhas, and the other set from a test in False Bay (20 February, 2008). The following requirements for the SMS dynamic behaviour was compiled from this data (Table 2.1):

Table 2.1: SMS Performance Requirements

Criteria	Requirement		Specification
Movement Range	The SMS should be able to emulate the ship deck attitude during simulated sea conditions from Sea State 0 to Sea State 2.5	Roll: ± 8 °	Roll: ± 6 °
		Pitch: ± 4 °	Pitch: ± 6 °
		Heave: No Requirement	Heave: No Requirement

Criteria	Requirement		Specification
Movement Rate	The SMS should be able to emulate the ship deck rates during simulated sea conditions from Sea State 0 to Sea State 2.5	Roll: 5.35 $°s^{-1}$	Roll: 6 $°s^{-1}$
		Pitch: 3.53 $°s^{-1}$	Pitch: 4 $°s^{-1}$
		Heave Rate: No Requirement	Heave Rate: No Requirement
Movement Acceleration	The SMS should be able to emulate the ship deck accelerations during simulated sea conditions from Sea State 0 to Sea State 2.5	Roll: 5.1 $°s^{-2}$	Roll: 6.2 $°s^{-2}$
		Pitch: 6.2 $°s^{-2}$	Pitch: 6.2 $°s^{-2}$
		Heave Acceleration: No Requirement	Heave Acceleration: No Requirement
Accuracy	The SMS should be able to accurately emulate the ship deck attitude in simulated sea conditions from Sea State 0 to Sea State 2.5	Angular Error < 0.5°	Angular Error < 0.5°
Load	The SMS should be able to emulate the ship deck attitude in simulated sea conditions from Sea State 0 to Sea State 2.5 with a load similar to that of the MODSAT	Load: 260 kg	Load:280 kg
Bandwidth	The SMS should have enough bandwidth to be able to emulate the ship deck attitude in simulated sea conditions from Sea State 0 to Sea State 2.5	Bandwidth: 0.5 Hz	Bandwidth: 1 Hz

2.2 MODSAT

The effectiveness of the surveillance and the quality of the information gathered from a deck mounted surveillance system is a direct result of the quality of the images and the stabilisation of the surveillance equipment. The development of maritime stabilised surveillance systems is done in laboratory conditions using test beds such the MODSAT developed by CSIR's OSS group and made available for this study. The system is shown in Figure 2.1, and a line drawing indicating the typical sizes of the system is shown in Figure 2.2.

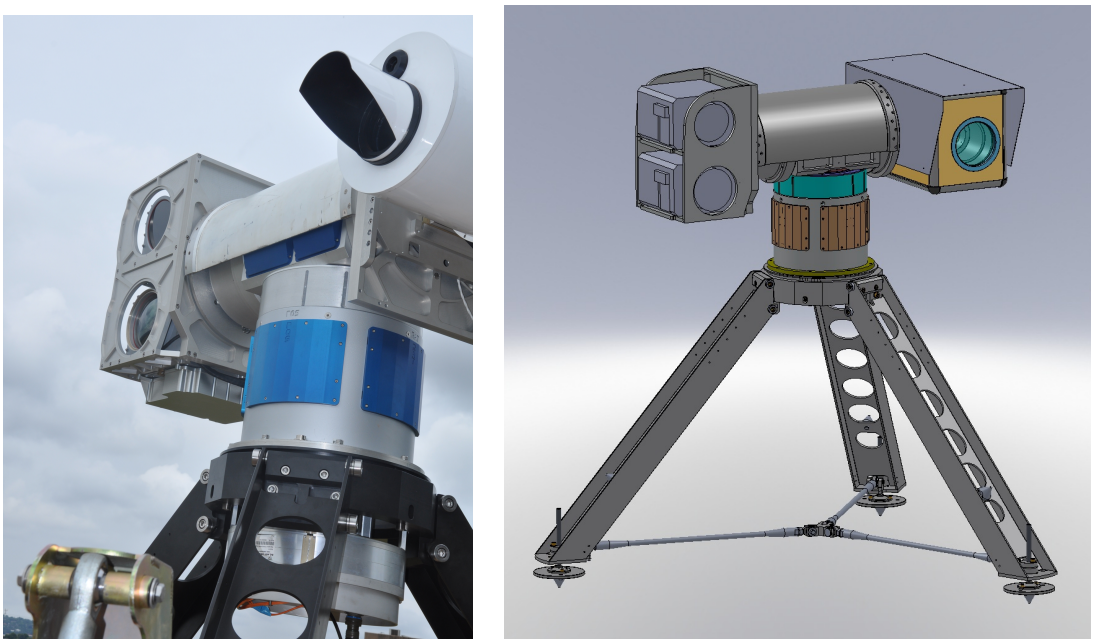

a) b)

Figure 2.1: The MODSAT Platform a) as Deployed During a Field Trial in Pretoria and b) as Presented by the SolidWorks® CAD Renderer

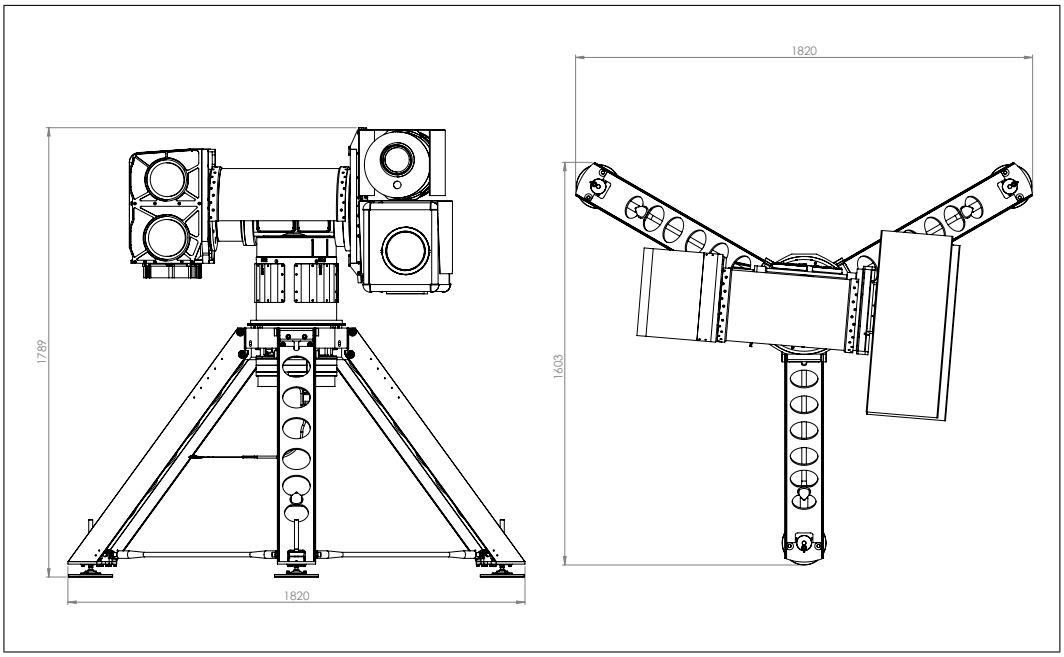

Figure 2.2: The MODSAT System Line Drawing Indicating the System Size [mm]

Figure 2.1a shows the tracker with a medium Field Of View (FOV) visible band camera in the top right hand corner of the image (left side of the tracker) and two thermal imaging systems on the left hand side of the image (right hand side of the tracker). In the foreground, the rod end of one of the SMS actuators can be seen. The blue covers in both the top assembly as well as the main body tube houses different parts of the control and drive system of the tracker. The CAD rendered image on the right hand side (Figure 2.1b) shows the portable, yet sturdy tripod system and the tracker fitted with the thermal imaging systems and a narrow FOV, long range zoom camera. The MODSAT weighs approximately 270 kg when mounted with two thermal imaging systems, the medium FOV camera and the long range narrow FOV camera mounted. This mass is dependent on the actual fitted payloads. The configuration of payloads on MODSAT can be changed to suit the test, as can be seen from the various images of the system. For the sake of modelling the system, the full compliment of sensors will be used to maximise the mass, *i.e.* the two thermal imaging cameras, the medium FOV camera and the narrow FOV camera. The MODSAT system is approximately 1.82 m wide and approximately 1.8 m high, depending on the foot extension and the balancing weights added.

2.3 SMS

The development of the surveillance system stabilisation techniques and image processing algorithms for the maritime environment needs to include a dynamic environment. That not only means that the scene changes, but also that the orientation of the the surveillance sensors changes. A large and heavy system such as MODSAT needs a very specific excitation platform to mimic the motion of the maritime vessels in question. Such a system was designed and built by the personnel of DPSS-OSS at the CSIR and was named the SMS. This system is shown in Figure 2.3. The SMS was the end

a) b)

Figure 2.3: The SMS as a) Deployed During a Field Trial in Pretoria and b) as Presented by the Rhino3D® CAD Renderer

result of a series of conceptual designs (the details which fall outside the scope of this document) which used various actuator and support configurations. The use of various actuating media, such as electrical current, hydraulic oil and compressed air were investigated. In the end it was decided to use compressed air as the actuating medium, minimising the amount of high cost items such as pneumatic actuators and designing the system to be as cost effective as possible while maintaining transportability and functionality. A mild steel frame was designed and constructed with the aim of lowering the Centre of Gravity (CoG) of the moving part of the system. This frame can be dismantled and broken down into six manageable size units for transportation plus the pneumatic system and the Panhard rods. The SMS system spans an area of 2.669 m by 2.312 m and is 0.89 m high in the resting position (Figure 2.4). It weighs approximately 160 kg.

The OSS SMS actuating system comprises three Festo DNC-100-400-PPV double acting pneumatic cylinders with cushioning, fitted with Festo MLO-POT-450-TLF analogue resistive linear displace-

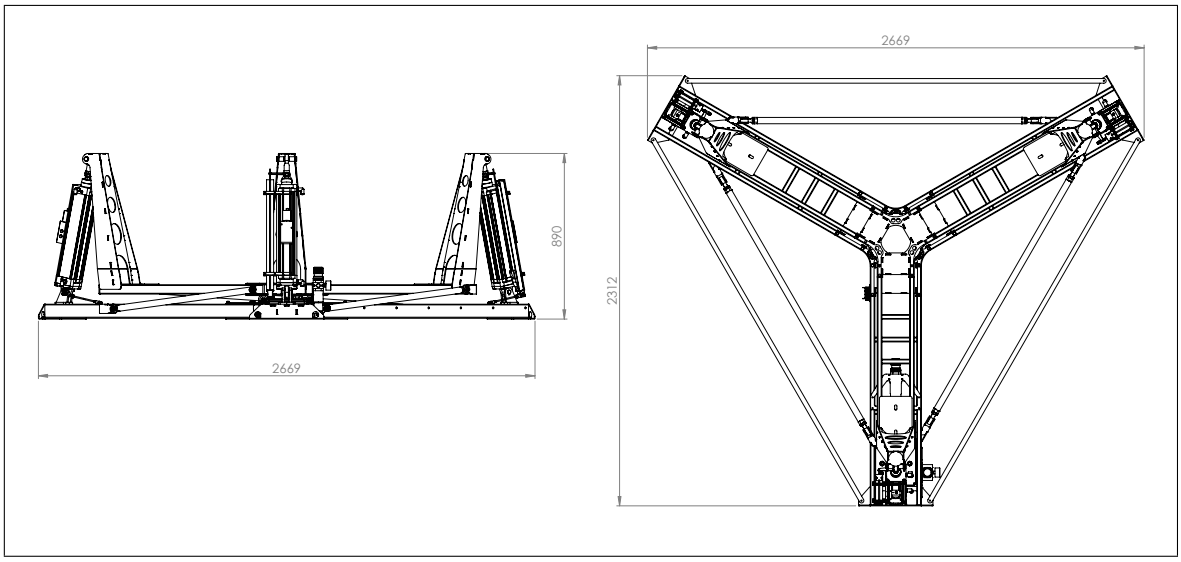

Figure 2.4: A Side and Top View of the SMS Indicating the Size of the System

ment encoders (potentiometers). These encoders are fitted to the cylinders and the sliders are connected via threaded rods to the piston rod end points, enabling relatively accurate measurement of the piston rod extension. Three Festo MPYE-5-3/8-010-B proportional directional control valves are used to control the flow of compressed air, each being actuated by a central Texas Instruments based system controller. The linear potentiometer output voltage is also fed back to the controller to close the control loops.

The actuator rod ends are terminated with Festo SGS-M20x1,5 rod eyes, and the bases of the cylinders with Festo SNCS-100 swivel flanges and Festo LBG-100 clevis feet. Compressed air is supplied at a maximum pressure of 0.6 MPa from any available air supply with adequate flow rate capability (maximum 6000 $\ell.min^{-1}$). The quality of the compressed air is not vitally important, but humidity content should be as low as practically possible and particles should be kept at a minimum. The air supply on SMS is filtered and the pressure regulated by means of a Festo LFR-3/8-D-0-MIDI filter/regulator. All the pneumatic components are connected via 10mm diameter blue Festo PUN-10x1,5-BL plastic tubing and Festo QSL-3/8-10 Quick Star connectors and manifolds. The SMS pneumatic system is shown diagrammatically in Figure 2.5.

The system comprises of (from the left hand side) a pneumatic pressure source, a pressure reservoir (both typically part of the compressor), a manual drain filter and a pressure gauge. The lubricator shown in the schematic is not used as per the recommendation of the Festo application notes when

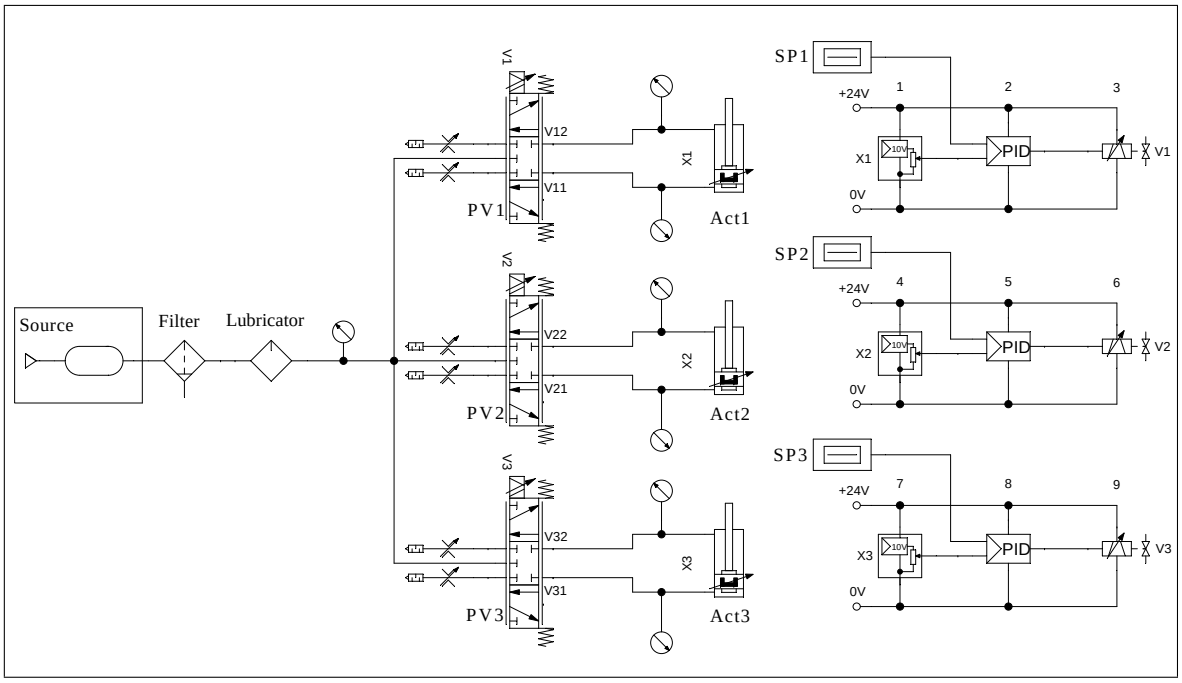

Figure 2.5: A Diagrammatic Representation of the SMS Pneumatic System as Defined in the Festo Didactic Fluidsim ® 4 Simulation Software

the proportional directional control valves are used. These valves have adequate lubrication for their lifetime and additional lubrication will deteriorate the bandwidth of the valves. The air is then distributed by pneumatic lines to three identical sections, each comprising a proportional directional control valve (PV1, PV2 and PV3) fitted with exhaust air flow control valves and silencers, and a double acting pneumatic cylinder (Act1, Act2 and Act3). In order to smooth out the air flow demand, reservoirs are added close to each of the actuators to act as a source of compressed air during high demand periods. The control of each of the pneumatic systems is done by a controller housed in the "PID" block, with a set point input (SP1, SP2 snd SP3) and displacement feedback (X1, X2 and X3) from the linear encoders. The output of the controllers are linked to the valves by means of variables V1, V2 and V3. In the final system, the controllers are all realised in the Digital Signal Processor (DSP) controller.

The dynamic behaviour of the pneumatic system can be simulated using Fluidsim® for simple load cases. The simulation results can be used as inputs to the characterisation process, as many hours of experience and lots of knowledge from one of the leading pneumatic suppliers (Festo) is embedded in the Festo simulation package. It can, unfortunately, not be used as an embedded process in the simulation of the complete system.

2.4 COMBINED MODSAT AND SMS

The combination of the MODSAT and the SMS described in the previous two sections results in a surveillance system with an emulated maritime vessel movement. The MODSAT and SMS are integrated by placing the tripod feet onto the end loading plates of the SMS. These feet are then bolted down to prevent them from slipping off the loading plates. The SMS base plate is secured to the ground by either bolting it to the floor or to large anchor plates fixed onto the ground by means of four 900mm long anchor pegs.

In this picture (Figure 2.6) the MODSAT and SMS systems are integrated and deployed outside the DPSS building in Pretoria to test the stabilisation of the MODSAT. From this picture it can be seen that the SMS is not used without any payload and the combined CoG of the two systems should be used when modeling the masses and inertias of the system. It would also be sensible to initially model the MODSAT as a rigid (no movement) structure, as the CoG will move as a function of the pan and tilt angles of the pointing system.

A point to note at this time is that surveillance systems are typically used at long distances, and any small translations on the camera side has a minimal effect on the rotational rates in the image plane. For this reason the heave of maritime vessels was not included in the design of SMS and is not an important entity in the control of the system. A similar argument can be made for the yaw angle, which is a parasitic effect of the Panhard rod constraints, of which the magnitude will change as a function of the vertical displacement of the top SMS frame.

2.5 LITERATURE SURVEY

The SMS system sponsored by the CSIR as described in § 2.3 is a pneumatically operated mechanical system system without any form of control. It was constructed out of a need for an unstable mounting platform with the initial intention to be operated only in an open-loop manner and without any predefined rates or angles. The main constraint for the design was the cost of the actuators and the usage of compressed air as a medium. This simulator hardware was also supplied completely constructed making it impossible to change the architecture. This posed a great challenge in terms of the geometric model and the inverse kinematic model. The choice of the air medium imposed a similar challenge to the design of the controller, which is best done with a known dynamic model of the system. A literature survey was done to assimilate the published information on the type of simulator,

Figure 2.6: The Stand Alone Tracker (SAT) on the SMS, Deployed Outside the DPSS Building in Pretoria and Secured to the Anchor Plates

other comparable or similar designs, the definition of the kinematic model, the dynamic behaviour of compressed air as a medium, controller designs and other possibly applicable constraints such as lubrication and air quality.

2.5.1 Geometry, Kinematics and Dynamics

The use of compressed air as a medium, mainly due to its cleanliness compared to hydraulics, is not new in simulators such as the SMS. This choice of medium has a remarkable influence on the geometry of simulators and mostly involves the use of linear pneumatic actuators together with some constrained nodes of movement. A very similar simulation requirement was solved by Smit [1] in the development of a 3-DOF motion simulation platform for the simulation of a maritime vessel landing deck. He presented three possible configurations, neither of which resembled the structure of the SMS, but some very valuable modelling insights and simplifications could be gained from his work. Smit developed one of the concepts and used simple geometric derivations to explicitly describe

the inverse kinematics of the simulator. The latter being made possible by the simplest choice of actuation.

Other contributions to the simulator design came from Chiew *et al.* [2] with a Gough-Stewart platform based driving simulator and Qu *et al.* [3] with the derivation of the inverse kinematics of variant of the Gough-Stewart platform replacing three of the actuators with fixed length rods, similar to the design philosophy of the SMS. In both these cases the Gough-Stewart platform was used as the basis of the design and in both cases the inverse kinematics was derived in explicit form. The Gough-Stewart platform is a well researched design based on the initial work done by Gough *et al.* [4] on a universal tyre test machine in 1962 and Stewart [5] on a variant of the 6-DOF parallel manipulator, mainly for flight simulation. The, now commonly phrased, hexapod has more similarity with the Gough design than that of Stewart, having six linear actuators connecting a movable platform to a static base through rotary joints. In the case of the normal hexapod, the inverse kinematics has a very simple explicit set of equations, whereas the forward kinematics has to be calculated using numerical solvers. The same explicit inverse kinematic solution is claimed by Qu *et al.* adding the fixed length arms into the equation solver. This method seems to have great potential for derivation of the SMS geometry and kinematics.

An approach to ease the design of complex systems in the Mechatronics domain is to migrate the model from a pure first principles derivation to a more abstract higher level model using simulation tools. This comes at the cost of getting familiar with the modelling and simulation software (in time) and the cost of the commercial software acquisition (in monetary value). Typical software packages that can be used for this purpose is Matlab®, Simulink®, Festo's Fluidsim and MSC ADAMS®. Based on publications by, amongst others, Brezina *et al.* [6] and Baran *et al.* [7], ADAMS® can be used as a development platform for dynamic modelling of a mechanical system such as SMS as well as for embedding controller designs and analyzing the implementations thereof with Matlab® Simulink® co-simulations. This method of development presents great promise in the definition of the inverse kinematics, the definition of the dynamic model, the system identification process as well as the testing of controller designs once the model is validated.

2.5.2 Pneumatic Actuators

Pneumatically operated systems, compared to their hydraulic counterparts, are preferred in environments where the actuation rates are slower, the positions or extensions of the actuators are controlled

by hard stops or buffers and where the impact of a compressible fluid is low on the controllability of the system. The cost of the actuators are typically much lower than that of electro-mechanical or hydraulic actuators. In the same light, the support and maintenance on pneumatic systems tends to be lower and the service air is available in most buildings.

With these reasons in mind, pneumatic actuators have been used fairly extensively in more precisely controlled systems and a fair amount of modelling, simulation and controller design has been done in this domain. The main topics addressed in the modeling of pneumatic circuits are the valve mass flow characteristics, the temporal air transport characteristics and the effects of changes in pressure and temperature in charging and discharging cycles of varying size volumes such as linear actuators

Pneumatic circuit theory is based in the thermodynamic behaviour of air under different pressures and flow rates. A physics based thermodynamic foundation as taught in most graduate engineering courses is a good starting point in understanding the issues at hand. Reference text books such as that by Crowe [8] is written in a more applied fashion and expands on many of the assumptions made to ease the modelling scope and effort. Other published works that can be used include texts on the design and analysis of pneumatic systems and circuits such as those by Anderson [9] and Beater [10]. The latter two of the text books have a very pragmatic way of approaching the modelling and control of pneumatic systems with a simplified entry from theoretical thermodynamic principles, making them ideal for engineering problem solving.

The problem statement of a pneumatic model and a control system for SMS can be broken down to generating the necessary models for the air flow or mass flow through the valve orifices, the rate of pressure change in the actuator volumes, the resultant actuator force that can be transferred to the load, the change of volume of actuator as a result of the movement of the load and and the effects of that pressure and volume change on the mass flow. In essence a set of differential equations that needs to be solved.

One of the most complete sources of pneumatic modelling found in the survey was that of Richer *et al.* [11]. In this publication Richer models the piston load dynamics, the cylinder chambers, the valves, the connecting lines and the friction. On closer inspection a series of assumptions and simplifications were made that would make the detailed models possibly incompatible with our system. These were primarily the use of the classic derivation for the mass flow through the valve and the valve orifices modelled as circular holes overlapping with straight edges.

Firstly, the initial investigation of the SMS pneumatic system revealed that the assumptions of single orifice valve flow models might not hold in a system with multiple orifices in the flow, most of which are not optimised for laminar flow. It is also very probable that contraction will occur between orifices and tubing. A further search for more realistic models resulted in the flow models described in the ISO-6358-1:2013(EN) [12] and ISO-6358-2:2013(EN) [13] standards, initially proposed by Purdue *et al.* [14] and generalised by Sanville [15]. These models effectively exchanges the discharge coefficient and effective area for a lumped sonic conductance entity, a variable critical pressure ratio and a modified flow function.

Secondly, the valve orifice geometry described in Richer's work differed from that of the Festo valves used in the SMS system. A simplified effective valve area model was proposed by Smit [1] and Šitum *et al.* [16] but still included an quadratic relationship between valve area and valve spool deflection that did not agree with the valve geometry.

Other very valuable sources of information include the valve flow models derived by Ben-Dov *et al.* [17] and that of Nouri *et al.* [18] that proposed a method of determining the effective valve area through a series of fixed volume measurement with the assumption of an ideal isentropic mass flow. The critical pressure ratio is also assumed to be constant; an assumption that needs to be verified. Also the model described in the paper by Van der Merwe *et al.* [19] that showed the relationship between the basic flow model through a restriction and the more general ISO-6358-1:2013(EN) description of the valve.

The theoretical models found in literature were numerous having varying amounts of assumption, simplification and accuracy. In most cases, the models were deemed too complex to determine the parameters accurately and too costly in terms of computation to consider for use in a large simulation. A well described model of the actual actuator used in SMS with identified and validated coefficients could not be found in literature. This forced the literature survey into the domain of experimental system identification.

The experimental configurations needed to accurately identify the parameters of the pneumatic system in many cases involved specialised equipment and sensors. Simple experiments with the inferring of entities such as flow rate from the measurement of pressure are used in many of the studies surveyed. The most representative flow measurements using the inference principle are done using isothermal discharge method described in ISO-6358-2:2013(E) [13]. This method relies on the change

of pressure in an isothermal chamber during a discharging cycle, using the choked flow region for the determination of the sonic conductance and the subsonic region for the critical pressure ratio and the flow function modifier. This method is described in great detail by Wang *et al.* [20] including the construction of the isothermal chamber, the assumptions and the calculation methods. This method involves both specialised equipment and is limited to on the discharging phase. A similar experiment is described by Kawashima *et al.* [21] for both the charging and discharging phases. Accuracy of the coefficients is, in both these cases, the major driving force behind the methods, delivering flow rates to within a 1 % error [22] and sonic conductance values to within 3 % uncertainty. As this level of accuracy is not of prime importance for a controller design process, the isothermal chamber can be exchanged for a normal pressure vessel with the accompanying assumptions regarding the heat transfer coefficient being close to 1 for a discharging process and 1.4 for a charging process. This method has successfully been used by Nouri *et al.* [23] and Van der Merwe *et al.* [19].

From this survey it can be seen that pneumatics models are in abundance, although the background and derivation of those models are in many cases unknown. It makes sense to understand the underlying thermodynamic principles and to redo some of the derivations to ensure that the assumptions are valid and that the models are not used outside of their designed conditions. A good example is the assumptions made to derive the valve flow model, being that of an adiabatic process (*i.e.* no heat exchange occurs), no contraction of flow and zero upstream velocity. The derivation is also done for a single orifice with well rounded edges, which has to be expanded to sharp edges and multiple orifices. A comparison and error analysis between these very theoretical (classical) models and the more realistic models such as the ISO-6358 model, and validating these models with experimental results would be time well spent.

2.5.2.1 Friction

From all the pneumatic systems modelling resources found in published literature the friction contribution to the nonlinear behaviour is noticeable. As described by Fleck *et al.* [24] pneumatic systems, especially miniature ones, are plagued by a discontinuous and highly nonlinear relationship between friction force and traversing velocity. This in combination with the compressibility of the operating medium, being compressed air, results in a lot of higher order modes in a control system. The drawback of pneumatic systems lie in the poor pneumatic force *vs.* friction force ratio. Similar statements are made by authors such as Nouri *et al.* [23], Ning *et al.* [25] and Richer *et al.* [26]. The friction

contribution is very often neglected due to the complexity of accurate friction models, and in many cases a static or semi-static model is derived and used in applications. These simplifications typically have adverse effects on the tracking performance of control systems.

Friction models in pneumatic systems presented in literature vary greatly in complexity and accuracy. These range from completely ignoring the fact of friction by assuming frictionless actuators [17], simple stick-slip friction models including static friction, Coulomb friction and velocity dependent viscous friction [1], [25], [27] to very complex friction models with static, pre-sliding, transient and sliding regimes and hysteresis [23], [28], [29]. These models have their origins in the friction model development of Dahl [30] describing the interference of surfaces as spring like interactions. This gave rise to a Coulomb friction model with lag being introduced in the friction force at velocity reversals. The inclusion of effects like the Stribeck effect and hysteresis has been most effectively added with the development of the LuGre model by Canudas de Wit *et al.* [31], a co-operation between the Lund Institute of Technology and the Polytechnic of Grenoble. The LuGre model was later improved by Swevers *et al.* to incorporate hysteresis [32], also known as the Leuven model. Improvements on the LuGre and Leuven models are ongoing. A model such as Dupont *et al.*'s elasto-plastic model [33] includes a function to minimize drift in the pre-sliding regime of the LuGre model, which includes an irreversible (plastic) component. Similarly, a computationally effective physically motivated general friction model such as the General Maxwell-Slip model is proposed by Lampaert *et al.* [34] to minimise stack overflow in the Leuven model.

The identification of the parameters in the friction models once again poses a challenge. Methods to exercise the systems to reveal their characteristics are well published, albeit complex in nature and resource intensive. Friction, as a parasitic force, can be derived from the common system dynamic equations if the forces can be measured with accuracy in the presence of uncertainty and noise. Using facilities to activate the friction modes in actuators and to effectively decouple the forces from each other is the preferred way to determine the friction model coefficients. In the absence of such facilities the actual instrumented actuators need to be used. A very applicable study was conducted by Belforte *et al.* [35] comparing the friction behaviour of cylinders of different diameters. The velocity steady state condition was the prime focus of the study, and less so the transients at zero velocity. A similar test series was conducted by Andrighetto *et al.* [36] comparing the friction behaviour in pneumatic actuators from several manufacturers. Static friction *vs.* velocity maps were generated through the inference of friction force from the load dynamic equation. Once again, the dynamically varying effects were ignored. A study that applied the Leeuven model and represented the hysteresis of the

pneumatic seals as well as the differences in the viscous friction coefficients for accelerating and decelerating movement was done by Nouri *et al.* [23]. Another noticeable contribution to the domain was made by the same author with experimental results pointing out the effects of supply pressure on the friction behaviour of the seals [37].

2.5.3 Control

Once the dynamic model of the system, consisting of the mechanical and geometric models, the influences of the payload, the dynamic characteristics of the pneumatic system and the influence of nonlinear effects such as friction and large scale mass flow is generated and validated, the model can be used for the development and testing of a control system. Controller design methodology is an extremely wide field of study, as is the choice of controller architecture and the type of controller.

Numerous text books have been published on the control of systems in the presence of friction as well as other nonlinear effects such as gear backlash, nonlinear gain and dead band behaviour. The most notable text referenced in the domain of controlling pneumatic systems with emphasis on control of machines is ”Control of Machines with Friction” by Brian Armstrong-Hélouvry [38]. The basic principles are covered in great detail and enables the reader to develop strategies for controller design. More generic text books such as [39] form the basis of the skill set of control engineering and is always a starting point for controller design. Other texts on nonlinear controller design methodology and structure are available and are too many to list.

In the light of the overwhelming amount of literature available, more focus was given to tried and tested control schemes of systems resembling the SMS system. That means others pneumatically actuated systems or subsystems with medium to low absolute accuracy and low bandwidth requirements. Once again the work done by Richer *et al.* [11] jumps to the foreground. In this study it was shown that a full order Sliding Mode Controller (SMC) provided excellent control and tracking of a pneumatic actuator. This came at the expense of a very complex control law and the use of numerical observers for the spool displacement and delayed variables. A reduced order controller gave slightly lower performance results but still required a vast amount of computational resources. This nonlinear controller was also adopted by Smit [1] in the control of an Unmanned Aerial Vehicle (UAV) landing platform simulator, and Laghrouche *et al.* [40] and Bigras [41] in general pneumatic control studies. A comparison between a SMC design based on the nonlinear model of the pneumatic plant *vs.* a design based on a linearized plant was conducted as presented by Bone *et al.* [42]. The tracking

performance of the nonlinear based controller was marginally better than that of the linearized model, and both were better than previously published controllers under the same conditions. Linearizing the plant does seem to add a bit of sensitivity on the working point and the load.

The use of fuzzy logic and neural networks have also been exploited, albeit to a lesser degree than other linear and nonlinear techniques. An example of an adaptive neural network control strategy is described in a paper delivered by Yu [43] outlining a Proportional Differential Integral (PID) controller that will ”self-tune” as the conditions change. A similar approach has been followed by Šitum *et al.* [44] to compensate for changing friction behaviour and air supply variations using a fuzzy logic modifier and a PID controller. In both cases the self-compensating behaviour of the controllers makes them more robust and involve less tuning during the life cycle of the systems.

The older and most often used methods of controlling pneumatic systems are still tuned PID controllers based on simplified and linearized plants. Proportional Integral (PI), Proportional Differential (PD) and PID controllers can be tuned to deliver good results on various system architectures, as long as a stable system can be realised to perform the identification process, as reported by Hamiti *et al.* [45]. Controllers can be synthesised by using auto-tuning methods such a the Chien-Hrones-Reswick method as described in this publication, or manually as described by Šitum *et al.* [16] and Beater [10]. Techniques to improve the response of the systems and to minimise limit cycles and the effect of stiction has been employed in many of the more traditional control schemes. Feedback from pressure sensors and acceleration feedback to stabilize the system has been employed by Wang *et al.* [46] with acceptable results. Traditional control techniques still have a role to play in pneumatic systems as it is well studied, well known and simple to implement. It does rely largely on knowledge of the behaviour of the plant model.

CHAPTER 3

SMS KINEMATICS

The SMS is a special form of a Gough-Stewart platform which can be defined as a subclass of parallel manipulators. Parallel manipulators, in contrast to serial manipulators that have a series of links joined by articulated joints in series (like a human arm), has multiple simple links all working in a parallel fashion, similar to two human arms lifting a load.

The first (known) example of such a manipulator was the tyre test machine constructed by Gough and Whitehall in 1954-1955 ([47], [4]). The publication that really sparked interest in research into parallel manipulators was the paper published by Stewart in 1965 [5], describing a flight simulator.

The definition of a Gough-Stewart platform can be formulated as a parallel manipulator consisting of two platforms connected by six prismatic joints acting in parallel. The one platform is fixed to the ground (base) and the other moving, with all the base platform joints in the base plane and moving the platform joints in the same moving platform plane.

Although the SMS is not strictly a Gough-Stewart platform, as some of the joints are not in the same plane, and three of the prismatic joints are replaced by Panhard rods, the same principles will hold for the kinematics and dynamics of the system.

3.1 SMS CAD MODEL

The SMS was designed by Mr. Mark Holloway (CSIR, DPSS-OSS) to be easily manufacturable, using the Solidworks® CAD package. Solid models of the pneumatic components were downloaded from the Festo web site, checked for dimensional conformance and used in the design process. The complete simulator, including fasteners, but excluding welding, was modelled to accurately determine

the mass and inertial properties of the structure. The complete SMS was designed to be manufactured from mild steel, either rectangular tubing or laser cut flat plate. A tongue and slot method was used to make the butt joints, primarily to reduce the amount of jigs needed during manufacture, and to ease the welding process. The CAD model is shown in Figure 3.1.

The detail for manufacturing was unnecessary for the purpose of kinematic and dynamic modelling of the simulator and therefore excluded as far as possible. All the parts were merged into a single solid shell, using the Rhino® 3D solid modelling package and exported as solid models to be imported into MSC ADAMS® for the kinematic and dynamic simulation. The base of the simulator is mechanically grounded, and has no other influence on the kinematics or dynamics of the system apart from defining the tie points of the Panhard rods and the actuators. It is therefore removed from the model. The complete SMS CAD model was simplified into solid shells with computed mass and inertia, to ensure correlation between Solidworks®, Rhino® and ADAMS®. The structure of the SMS has been assumed to be infinitely rigid and no deformation has been modelled or simulated. The solid shells transferred to ADAMS® is purely for esthetic purposes. The SAT is an extremely complex system

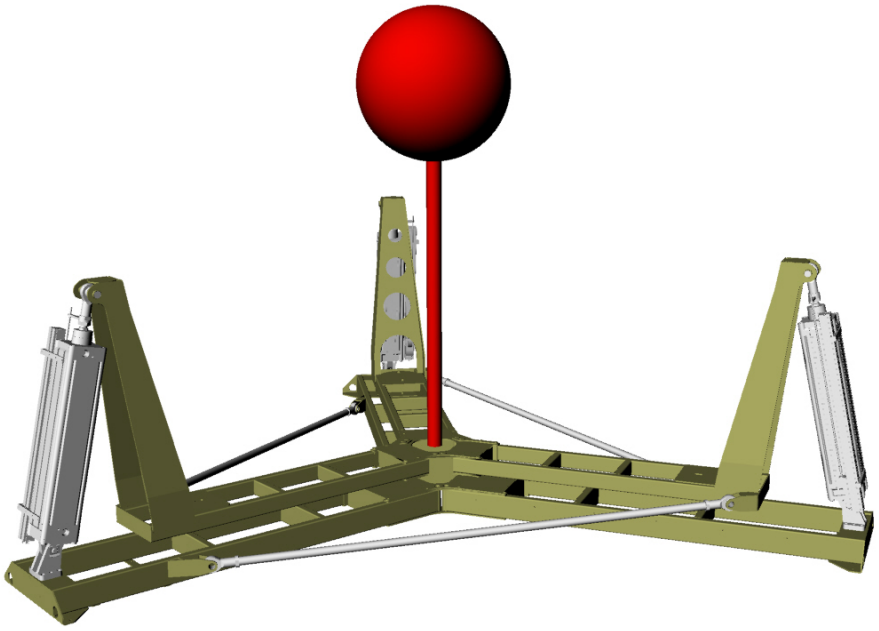

Figure 3.1: The Detailed CAD Model of the SMS with the Point Mass Substitute of the SAT (Red Sphere with Rod)

and has been modeled to the finest detail in Solidworks®. This model is superfluously complex for the primary objective of rigid body kinematic and dynamic modelling. The complete SAT system

has therefore been simplified to a rigid structure with a point mass and the moments of inertia calculated (courtesy of Mr. Holloway) using the functionality of Solidworks®. In Figure 3.1 the SAT is represented by the red sphere with the connecting rod to the mounting platform of SMS. Table 3.1 is a compilation of all the moving parts and their respective masses, centre of mass points (absolute coordinates) and moments of inertia as calculated in Rhino®3D and Solidworks®. The density of the aluminium parts are assumed to be 2740 $kg.m^{-3}$ and the steel parts to be 7801 $kg.m^{-3}$.

It should be noted that the the coordinate system used throughout this study is a Cartesian right handed system with the positive z-axis pointing downwards and the roll axis aligned with the positive x-axis. Rotation sequence is defined as 321 (or ZYX) with the input angles γ for Yaw (about the z-axis), β for Pitch (about the y′-axis) and α for Roll (about the x″-axis).

Table 3.1: Mass, Centre of Mass and Inertia Around the Centre of Mass of the SMS and SAT Systems

Component	Mass kg	CoG (x,y,z) m,m,m	I_{xx} $kg.m^2$	I_{yy} $kg.m^2$	I_{zz} $kg.m^2$
TopFrame	52.19322	(1.626E-003, -1.617E-003, -0.297561)	21.091744	21.091744	37.049942
Cylinder 1	10.0532	(1.308360, 1.690E-002, -0.446408)	0.363947	0.357131	0.050876
Cylinder 2	10.0532	(-0.651288, -1.126699, -0.445641)	0.359551	0.356058	0.050485
Cylinder 3	10.0532	(-0.668818, 1.124622, -0.446408)	0.355342	0.365757	0.050876
Piston 1	3.761557	(1.294688, 1.068E-002, -0.482190)	0.183415	0.183095	0.012805
Piston 2	3.76156	(-0.638091, -1.126575, -0.482190)	0.185953	0.180556	0.012805
Piston 3	3.76156	(-0.656596, 1.115891, -0.482190)	0.180397	0.186113	0.012805
Panhard 1	1.66732	(-0.645164, 3.402E-002, -0.1041)	0.463151	0.156245	0.614145
Panhard 2	1.66732	(0.352049, 0.541716, -0.1041)	0.002724	0.616673	0.614145
Panhard 3	1.66732	(0.293116, -0.575741, -0.1041)	0.463219	0.156177	0.614145
SAT	255.08	(0.0, 0.0, -1.3922)	57.58	78.58	42.28

3.2 SMS KINEMATIC VECTOR DIAGRAM MODEL

A complex model that contains physical dimensions, volume and stiffness constants does not add any value to the derivation of the kinematics of the SMS. As mentioned previously, the SMS is not strictly speaking a Gough-Stewart platform as all the joints of the moving platform are not in the same plane and neither are the joints on the stationary platform. A free body diagram of the simulator geometry has been generated to clarify the connections and to give insight into the possible mathematical definitions of the kinematics. This derivation is not seen as part of the problem statement, as the kinematics will be calculated by MSC ADAMS®, but is an ongoing effort to improve the mathematical model. The process of deriving a set of equations for the SMS geometry and kinematics has been based on existing derivations of firstly, the Gough-Stewart platform and secondly, the SMS.

3.2.1 Gough-Stewart Vector Kinematics

It can generally be stated that the inverse kinematics can be derived for a Gough-Stewart platform by using the principle of a rotated and translated platform [2], the orientation uniquely defined by the six leg lengths. The layout of a general Gough-Stewart platform is shown in Figure 3.2a. The system is referenced by a grounded right handed frame $\{B\}$ with axes x_B, y_B and z_B, and a moving right handed frame $\{P\}$ with axes x_P, y_P and z_P aligned with the platform. Points B_1 to B_6 are located on the base and are all stationary points. Points P_1 to P_6 are located on the moving platform and are connected to the base through legs l_1 to l_6. If we define a leg vector for the i^{th} leg l_i (Figure 3.2b), referenced in the B frame as ${}^B l_i = [l_{ix}, l_{iy}, l_{iz}]^T$ and a translation of ${}^B d$ and a rotation (defined by the input angles α,β and γ) is applied to the moving platform, the leg vectors can be expressed as

$$ {}^B\vec{l}_i = {}^B_P R \, {}^P\vec{p}_i + {}^B\vec{d} - {}^B\vec{b}_i, \tag{3.1} $$

with ${}^B\vec{d} = [x, y, z]^T$ the translated position of frame $\{P\}$, ${}^P\vec{p}_i = [p_{ix}, p_{iy}, p_{iz}]^T$ the vector describing the upper attachment points relative to frame $\{P\}$, ${}^B\vec{b}_i = [b_{ix}, b_{iy}, b_{iz}]^T$ the vector describing the base attachments points relative to frame $\{B\}$ and ${}^B_P R$ the 3x3 matrix defining the rotation of the $\{P\}$ frame referenced to the $\{B\}$ frame. From the basic theory of axis rotation ([48], [49]) the rotation matrices

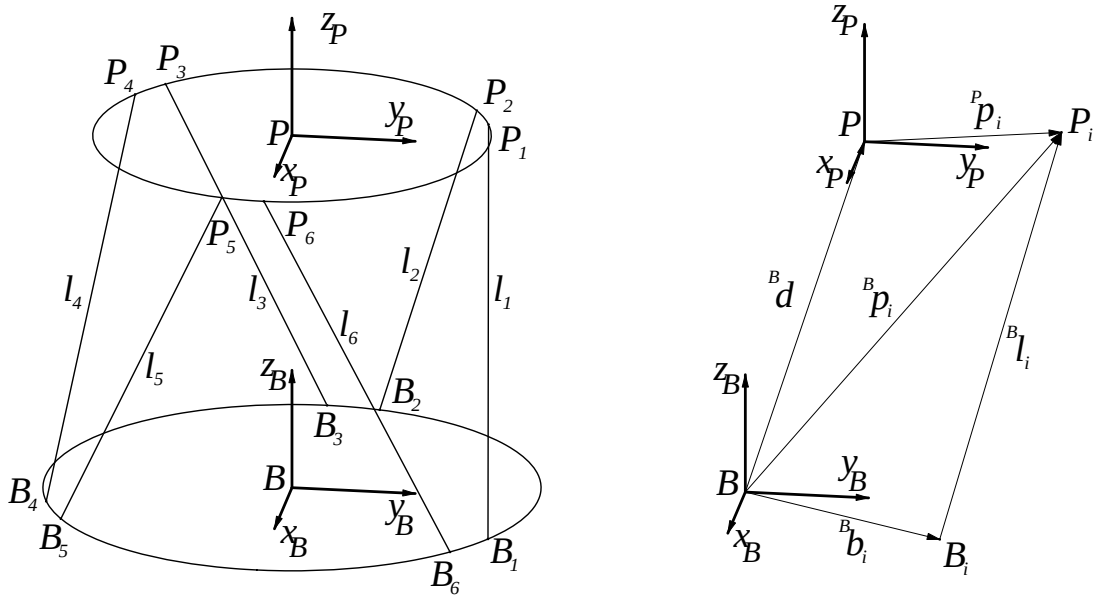

a) b)

Figure 3.2: A General Stewart Platform Configuration with a) the Reference Frames and b) the Vector Diagram for One Leg

are given by

$$R_R = \begin{bmatrix} 1 & 0 & 0 \\ 0 & \cos\alpha & -\sin\alpha \\ 0 & \sin\alpha & \cos\alpha \end{bmatrix}, \tag{3.2}$$

$$R_P = \begin{bmatrix} \cos\beta & 0 & \sin\beta \\ 0 & 1 & 0 \\ -\sin\beta & 0 & \cos\beta \end{bmatrix} \tag{3.3}$$

and

$$R_Y = \begin{bmatrix} \cos\gamma & -\sin\gamma & 0 \\ \sin\gamma & \cos\gamma & 0 \\ 0 & 0 & 1 \end{bmatrix}, \tag{3.4}$$

which when combined, describes the complete rotation of the platform and is expressed as

$$\begin{aligned} {}^{B}_{P}R &= R_Y R_P R_R \\ &= \begin{bmatrix} r_{11} & r_{12} & r_3 \\ r_{21} & r_{22} & r_{23} \\ r_{31} & r_{32} & r_{33} \end{bmatrix} \\ &= \begin{bmatrix} \cos\beta\cos\gamma & \sin\alpha\sin\beta\cos\gamma - \cos\alpha\sin\gamma & \cos\alpha\sin\beta\cos\gamma + \sin\alpha\sin\gamma \\ \cos\beta\sin\gamma & \sin\alpha\sin\beta\sin\gamma + \cos\alpha\cos\gamma & \cos\alpha\sin\beta\sin\gamma - \sin\alpha\cos\gamma \\ -\sin\beta & \sin\alpha\cos\beta & \cos\alpha\cos\beta \end{bmatrix} \end{aligned} \tag{3.5}$$

.

The length of each leg is then, by definition, equal to the Euclidean distance between points B_i and P_i, which can be expressed as $\left\|{}^{B}l_i\right\|^2 = \left({}^{B}l_{ix}^2 + {}^{B}l_{iy}^2 + {}^{B}l_{iz}^2\right)$. After some mathematical simplification, the length of the i^{th} leg of the general Gough-Stewart platform can be described by

$$\begin{aligned} l_i^2 =& x^2 + y^2 + z^2 + r_b^2 + r_p^2 \\ &+ 2\left(p_{ix}r_{11} + p_{iy}r_{12} + p_{iz}r_{13}\right)(x - b_{ix}) \\ &+ 2\left(p_{ix}r_{21} + p_{iy}r_{22} + p_{iz}r_{23}\right)(y - b_{iy}) \\ &+ 2\left(p_{ix}r_{31} + p_{iy}r_{32} + p_{iz}r_{33}\right)(z - b_{iz}) \\ &- 2\left(b_{ix}x + b_{iy}y + b_{iz}z\right) \end{aligned} \tag{3.6}$$

,

where x, y, and z are the coordinate points of the moving platform, r_b is the radius of the circle describing the base joints, assuming a centre point at the origin of the frame $\{B\}$ and r_p is the Euclidean distance from the origin of the frame $\{P\}$ to any point on the circle describing the platform joints. Each of the leg lengths of the Gough-Stewart platform can be calculated as function of the input

angles α (Roll), β (Pitch) and γ (Yaw), as well as the centre point of the platform (x, y and z) by using equation 3.6.

3.2.2 SMS Vector Kinematics

A similar simplification to that of the Gough-Stewart platform was done to the model of SMS. Table 3.2 shows the coordinate points of all the rotary joints (realised in the final construction by rod eyes), which will define the vertices of the simulator.

Table 3.2: Coordinate Points Of The Joints Present In The SMS

Point	Coordinate (x, y, z) m, m, m
B1	(1.365209, 1.193E-005, -0.145639)
B2	(-0.682551, -1.182264, -0.145639)
B3	(-0.682551, 1.182287, -0.145639)
B4	(-0.319907, 0.929612, -5.50E-002)
B5	(0.965021, -0.187758, -5.50E-002)
B6	(-0.645050, -0.741866, -5.5E-002)
P1	(1.214681, 1.19E-005, -0.853818)
P2	(-0.607287, -1.051903, -0.853818)
P3	(-0.607287, 1.051926, -0.853818)
P4	(1.024004, 0.153820, -0.153200)
P5	(-0.378746, -0.963675, -0.153200)
P6	(-0.645150, 0.809890, -0.153200)

A nodal diagram was drawn up of the simulator using the coordinate points and is shown in Figure 3.3. In this diagram the six base points (B_1-B_6) are all grounded points and is always static.

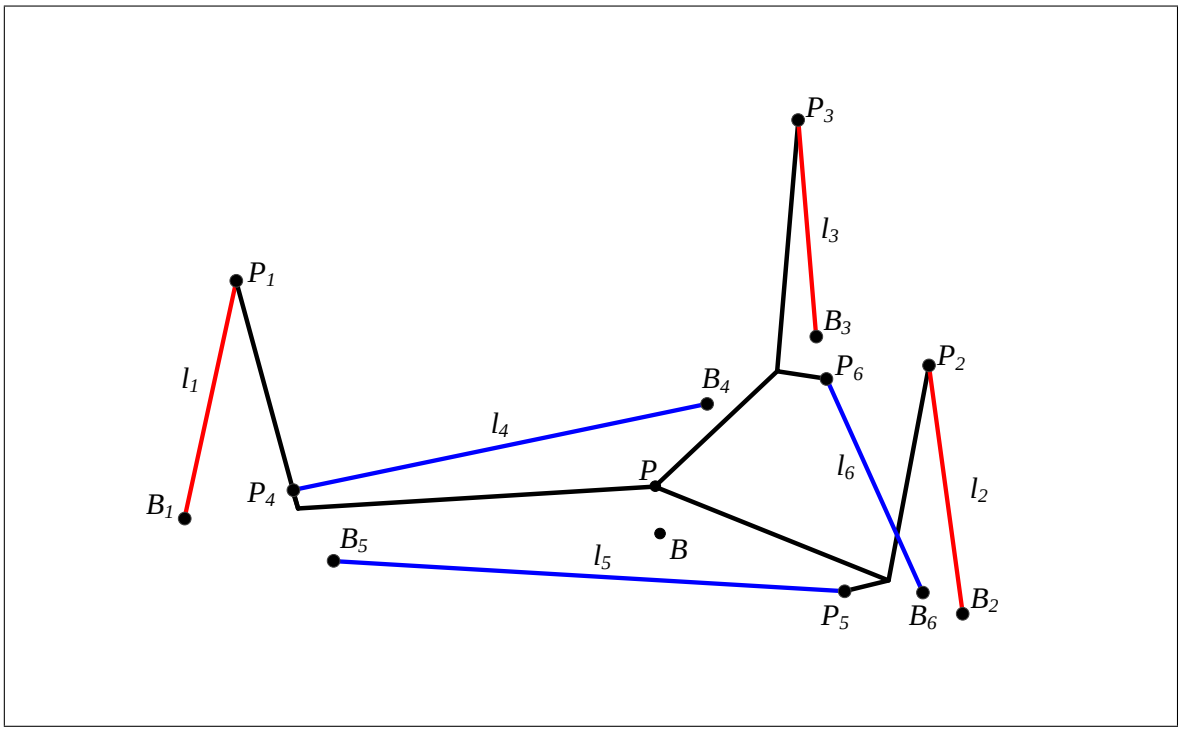

Figure 3.3: A Nodal Diagram of the SMS

The lines connecting points B_4 to P_4, B_5 to P_5 and B_6 to P_6 represent the Panhard rods and have a fixed length of l_4 to l_6. The lines connecting points B_1 to P_1, B_2 to P_2 and B_3 to P_3 represent the pneumatic actuators and have variable lengths l_1, l_2 and l_3. It is important to note that the points describing the platform joints are not all in the same plane or on the same describing circle. The structure connecting all the points labelled P_i form the moving platform of the SMS. These connections have fixed lengths and do not deform under the assumption that they are rigid.

A significant difference between the general Gough-Stewart platform and the SMS is the fact that three leg length constraints are present in the latter. As shown in Figure 3.4 the coordinate transformation to calculate the necessary leg lengths changes from one of pure inverse kinematics in the case of the Gough-Stewart platform (left hand process) to one where the normal inputs (α, β, γ, x, y and z) are dependent on some of the leg lengths in the case of SMS. In this figure the left hand process accepts the six input variables and through the process described in § 3.2.1 the leg lengths l_1 to l_6 are calculated. The right hand process (which is used in the case of the SMS) has roll (α), pitch (β) and

the platform height (z_p) as independent variable inputs, together with the three Panhard rod lengths, l_4 to l_6. The outputs of this system are the three actuator lengths, l_1 to l_3, the parasitic yaw, γ, and the horizontal platform position (x_p and y_p). It is also envisaged that an intermediate step is necessary to first derive the Yaw angle (γ) and the horizontal position (x,y), after which the three unknown actuator lengths are calculated using the result of the intermediate step.

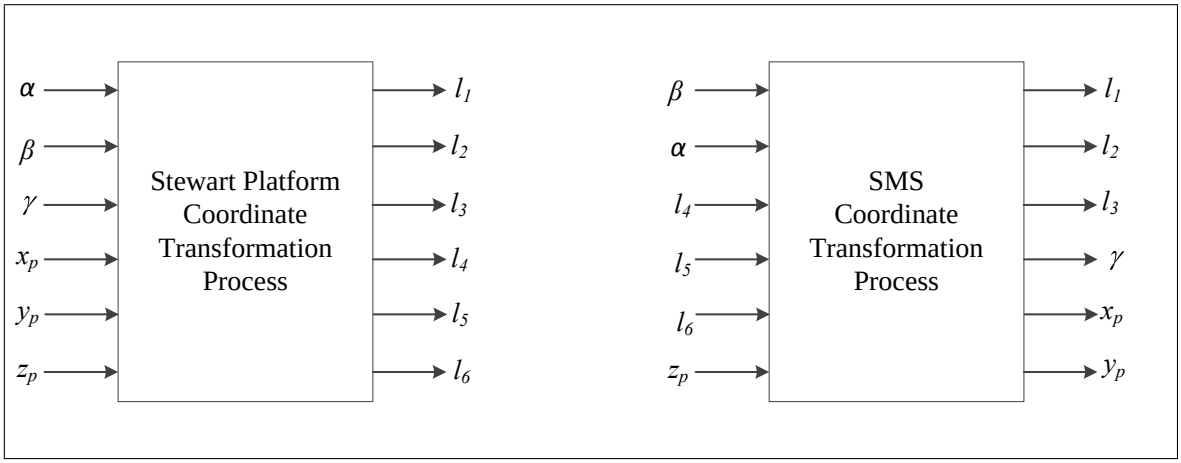

Figure 3.4: A Process Description of the Coordinate to Leg Length Conversion Processes of a Gough-Stewart platform and the SMS

It is because of this constraint that an explicit set of equations have yet to be found or derived to accurately describe the platform kinematics and motion. Various authors such as Qu *et al.* [3] and Chiew *et al.* [2] have reported on the derivation of inverse kinematic equations, all of which are valid for their specific setups, but cannot readily be used on SMS. This is then also the reason that the MBD simulation package, MSC ADAMS® was chosen to generate the necessary motion descriptions for the system analysis, and connect the ADAMS® simulation to that of Matlab® Simulink®.

3.3 MSC ADAMS® MULTI-BODY DYNAMICS

ADAMS® is an acronym for Automated Dynamic Analysis of Mechanical Systems. It was a former proprietary software product of Mechanical Dynamics Incorporation which then was acquired by MSC Software Corporation. ADAMS® is a multi-body dynamics simulation software equipped with Fortran and C++ numerical solvers.

The model building process in MSC ADAMS® involves either using a text driven input, called a .cmd file, a graphical input from the Graphical User Interface (GUI) in AdamsView® or using input

from a CAD or simulation package such as Solidworks® or Rhino®. The physical size of the parts are ignored and the parts are converted to point masses, connected to points and described by inertia and mass properties. In this project, a combination of the GUI and CAD process was used, but the physical properties were transferred from the CAD package according to Tables 3.1 and 3.2. Once the physical parts are placed, the parts need to be linked by means of joints, and movement limited by means of constraints. These are graphically indicated in Figure 3.5.

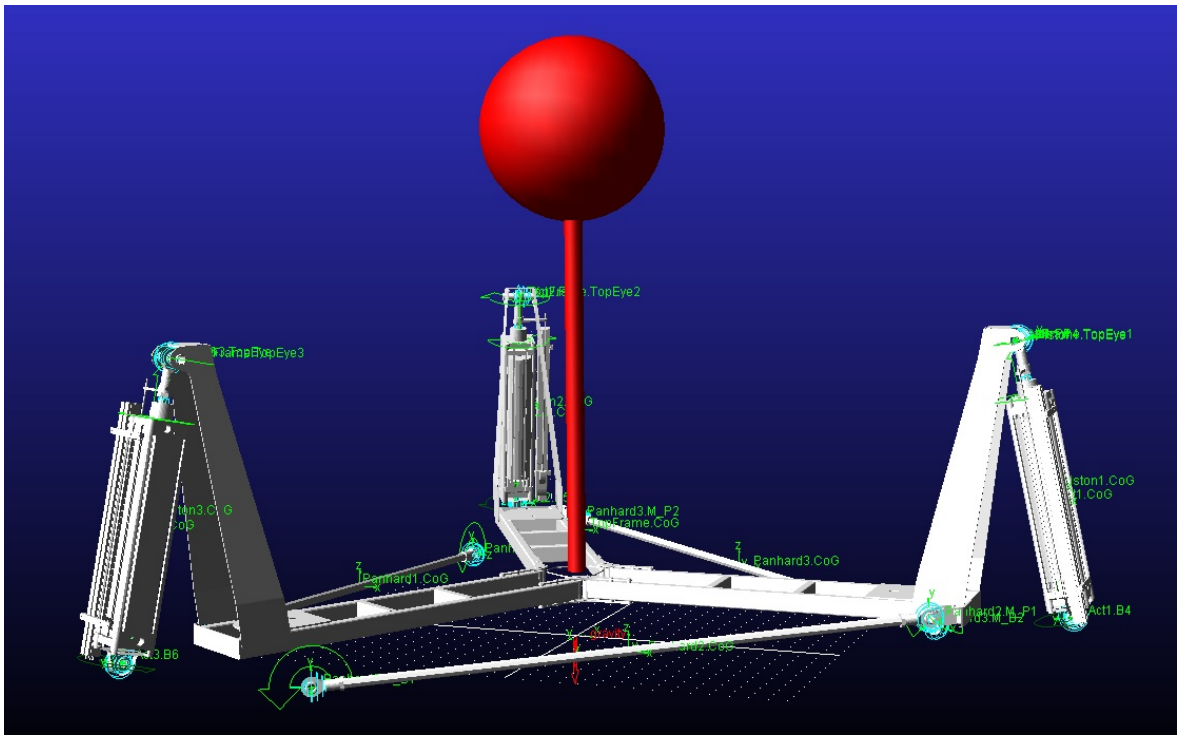

Figure 3.5: The ADAMS® Model with Joints, Constraints, CoGs and Part Names Indicated

The MSC ADAMS® world is fixed and referenced to the "Ground" entity. The Panhard rods and the bottom joints of the actuators are fixed to the "Ground" through spherical joints, with a rotational constraint aligned with the part's main axis, *i.e.* the actuators and rods cannot revolve around their own axes. Spherical joints are also connecting the actuator top joints (on the piston rods) and the Panhard rods to the SMS top frame. No constraints are placed on Panhard rod joints, as they are already constrained by the bottom joints. The piston rods are constrained in rotation, once again to prevent rotation during simulation. The piston and the linear potentiometer slide are merged into one moving part to resemble the real system. The SAT point mass and the connecting rod (red sphere and pole) are connected to the top frame by a fixed joint, simulating the tripod. A cylindrical joint is placed between the piston rod and the actuator body (at the rod seal) to limit movement of the piston

and piston rod in only one direction, once again aligned with the actuator main axis. This joint has the facility to include seal friction, which is not used in the current simulation. A further constraint is placed on every actuator to limit movement past the end stops of the pneumatic actuators. This contact force is placed between the piston and the actuator end stops and acts as an exponentially growing force as a function of depression depth. In the absence of this end stop force, the piston will be able to move past the ends of the actuators.

The actuating forces in the ADAMS® model is placed between the pistons and the relevant actuator bodies and aligned with the axis of movement. These are all single component forces, called "SFORCE_1" to "SFORCE_3". The extension of each actuator is measured as the magnitude of the vector distance between a point on the piston (Piston.CoG) and actuator body (M_Ref), which co-insides with the piston CoG point at zero extension (DM(Act1.M_Ref, Piston1.CoG)). Both the forces and the measurements are placed in the model as state variables.

3.4 INTEGRATION BETWEEN MSC ADAMS® AND MATLAB®

A facility was created in MSC ADAMS® to link other simulation packages to it. This is done by means of ADAMS®' "System Elements" and variables. In order to generate the link between Matlab® and ADAMS®, a force (in the case of actuator 1) will be generated by Simulink® and then passed to the ADAMS® model through a State Variable called "PF1", which is explicitly linked to the one-dimensional force "SFORCE_1". The force is placed in the ADAMS® model between the piston assembly and the actuator body, aligned with the instantaneous coordinates of the top and bottom spherical joints on the actuator (Direction: Between Two Bodies In Line-Of-Sight) and uses a function to update its value (VARVAL(.SMS.PF1)) at every time step.

The evaluation of the runtime expression "DM(Act1.M_Ref, Piston1.CoG)", which determines the extension of the actuator, generates a feedback length, which is passed to State Variable "X1" and can be read by Simulink®.

The Plant Export function (in ADAMS®) is used to generate the nonlinear Simulink® model of the ADAMS® system. In this case a plant was exported with forces ".SMS.PF1", ".SMS.PF2" and ".SMS.PF3" as inputs, and world angles ".SMS.Pitch", ".SMS.Roll" and ".SMS.Yaw" and actuator extensions ".SMS.X1", ".SMS.X2" and ".SMS.X3" as outputs. The other state variables such as $\dot{x}$ and $\ddot{x}$ can also be added to the feedback. The "target" was set as "Matlab" with a "nonlinear" ana-

lysis and a "C++" solver. A model builder script is then generated by ADAMS®, "SMSPlant.m" in this case, which, when run in Matlab®, generates all the Simulink® blocks and environmental variables. The Simulink® block set is available through evaluating the Matlab® variable "adams_sys" in the Matlab® integrated environment. The result of this evaluation is a wrapper containing three Simulink® descriptions of the plant as is shown in fig. 3.6. These descriptions are a Matlab® S-function, a state space block, which is not used in our simulations and a sub-system block containing the same S-function as mentioned earlier, signal multiplexers and some data storage blocks.

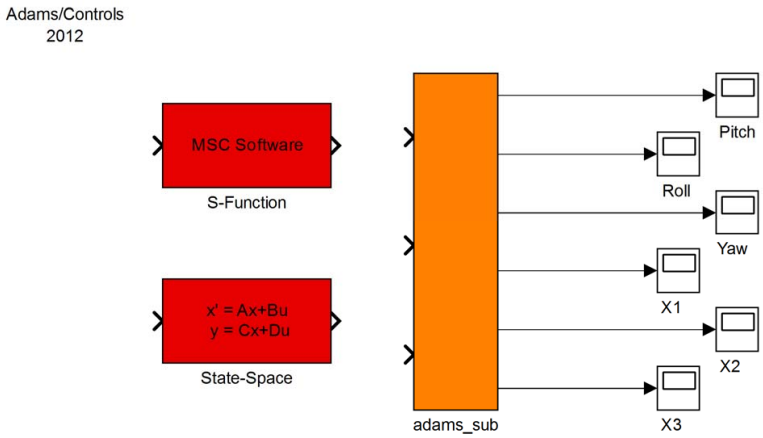

Figure 3.6: The Matlab® Simulink® Block Set of the ADAMS® Generated SMS Plant

By copying and pasting the relevant block into our simulation (adams_sub in this case), either an interactive simulation using the graphics of ADAMS®, or a batch mode, in which only the ADAMS® solver is used, can be run. Control over this and parameters such as the time steps can be found on the mask of the red block called "MSC Software" under the adams_sys (Figure 3.7). Once the "adams_sub" block has been incorporated into a larger Simulink® model, the paths and variable can be accessed by first running the "SMSPlant.m" script and then using the larger model in that environment.

In order to assess the operation of the integration between Matlab® and ADAMS® a simple test system (Figure 3.8) was constructed. In this system the plant is the dynamic model of the SMS without any pneumatic models and only the built-in ADAMS® friction models for the actuators. The inputs to the ADAMS® model are the actuator forces (*PF1* to *PF3*) and the outputs are the leg extensions (*X1*, *X2* and *X3*). It is controlled by a separate PD position controller for each leg using leg extension outputs and the derivatives thereof as feedback. The switches give the user the ability to open the

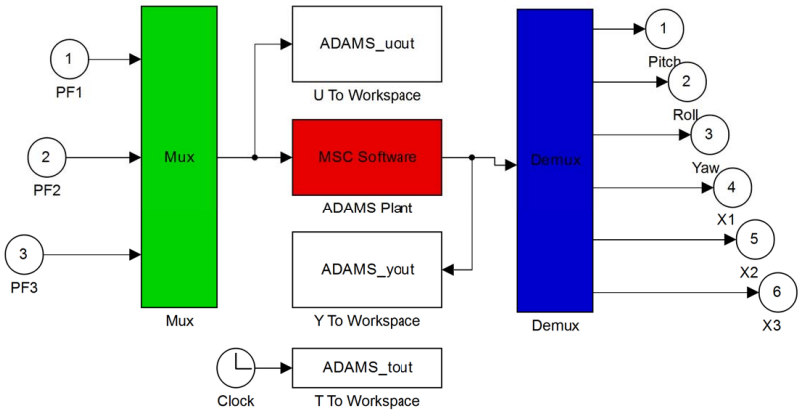

Figure 3.7: The Simulink® Block Describing the SMS Plant Subsystem

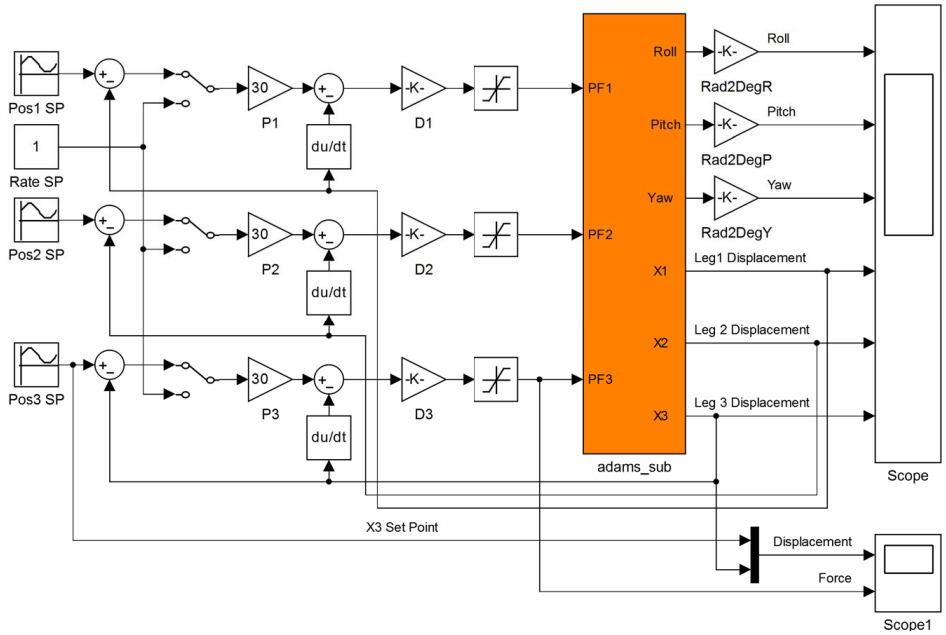

Figure 3.8: A Test System to Evaluate the Integrity of the ADAMS®/Simulink® Integration

position loop, while tuning the rate loop. Once the rate loop is tuned optimally, the position gain can be tweaked to obtain the desired result. The displacement results (Figure 3.9) obtained from the test system simulation indicate a reliable integration with believable results. The graph shows the actuator displacement set point as well as the controlled actuator displacement as a function of time. The transient from the initial condition to the set point and the overshoot with the fast settling time

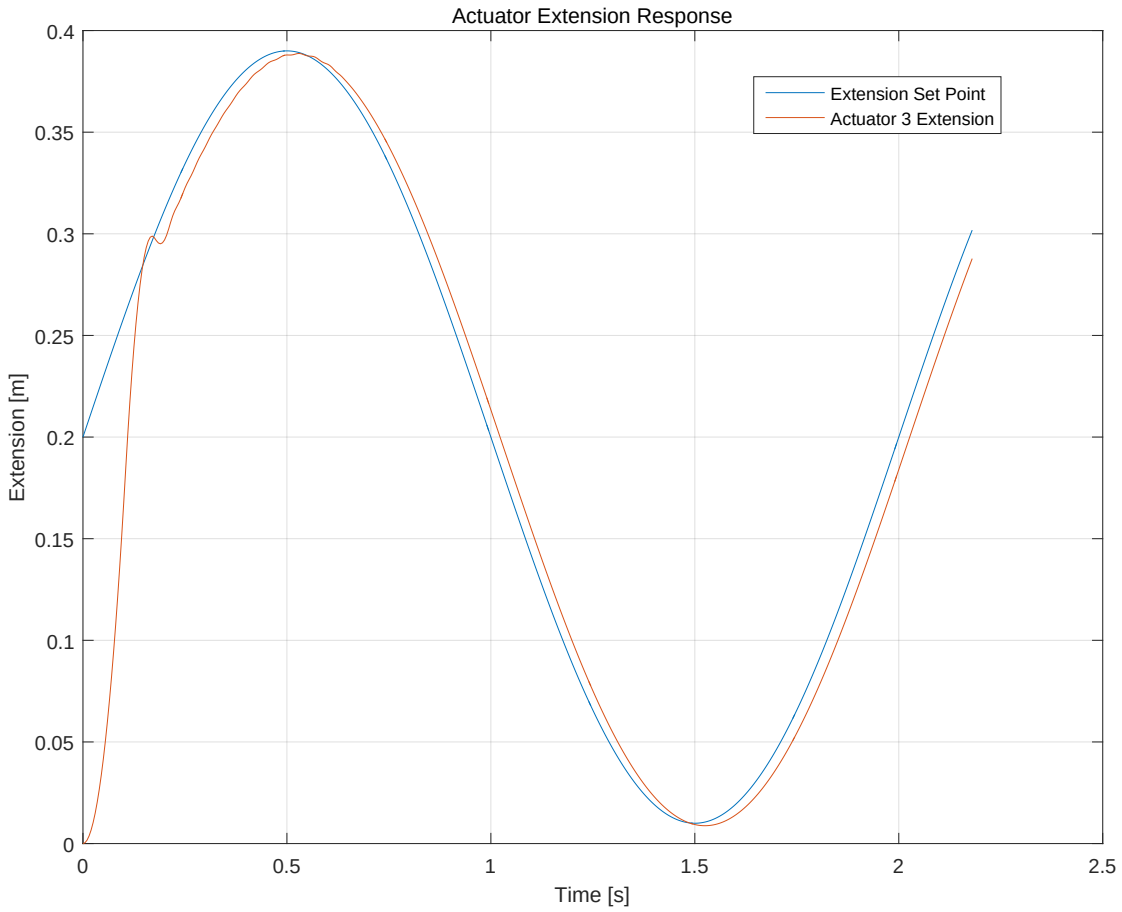

Figure 3.9: The Position Control Response and the Position Set Point of One of the Test System Actuators *vs.* Time

is a sign of a critically damped second order system. A small delay is evident and the result of the ADAMS® friction models. The Figure 3.10 shows the force needed to achieve this result. The force is limited to the theoretical maximum of the pneumatic actuator which is achievable at 0.6 *MPa*. The plant outputs are shown against time in 3.11. The amount of yaw angle variation during the simulation run is noticeable.

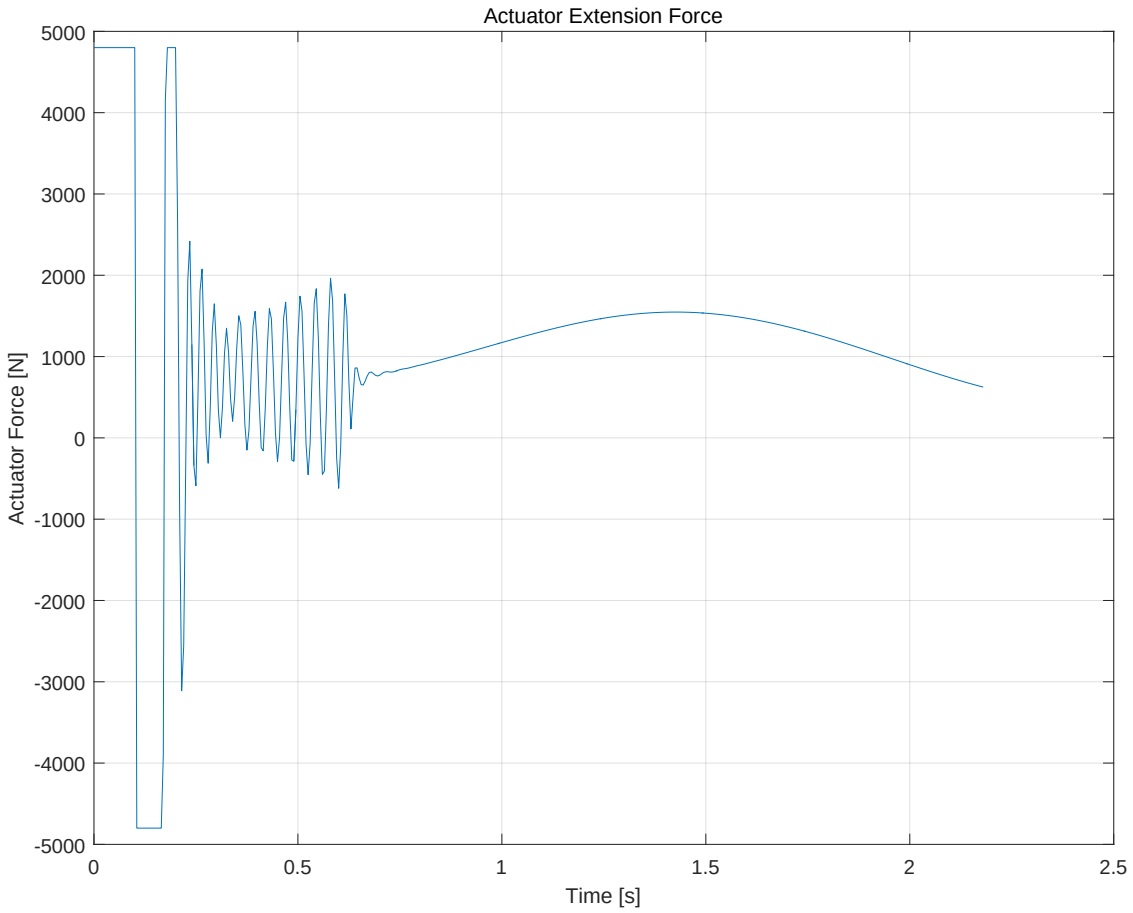

Figure 3.10: The Force Needed to Achieve the Extension Response in Figure 3.9

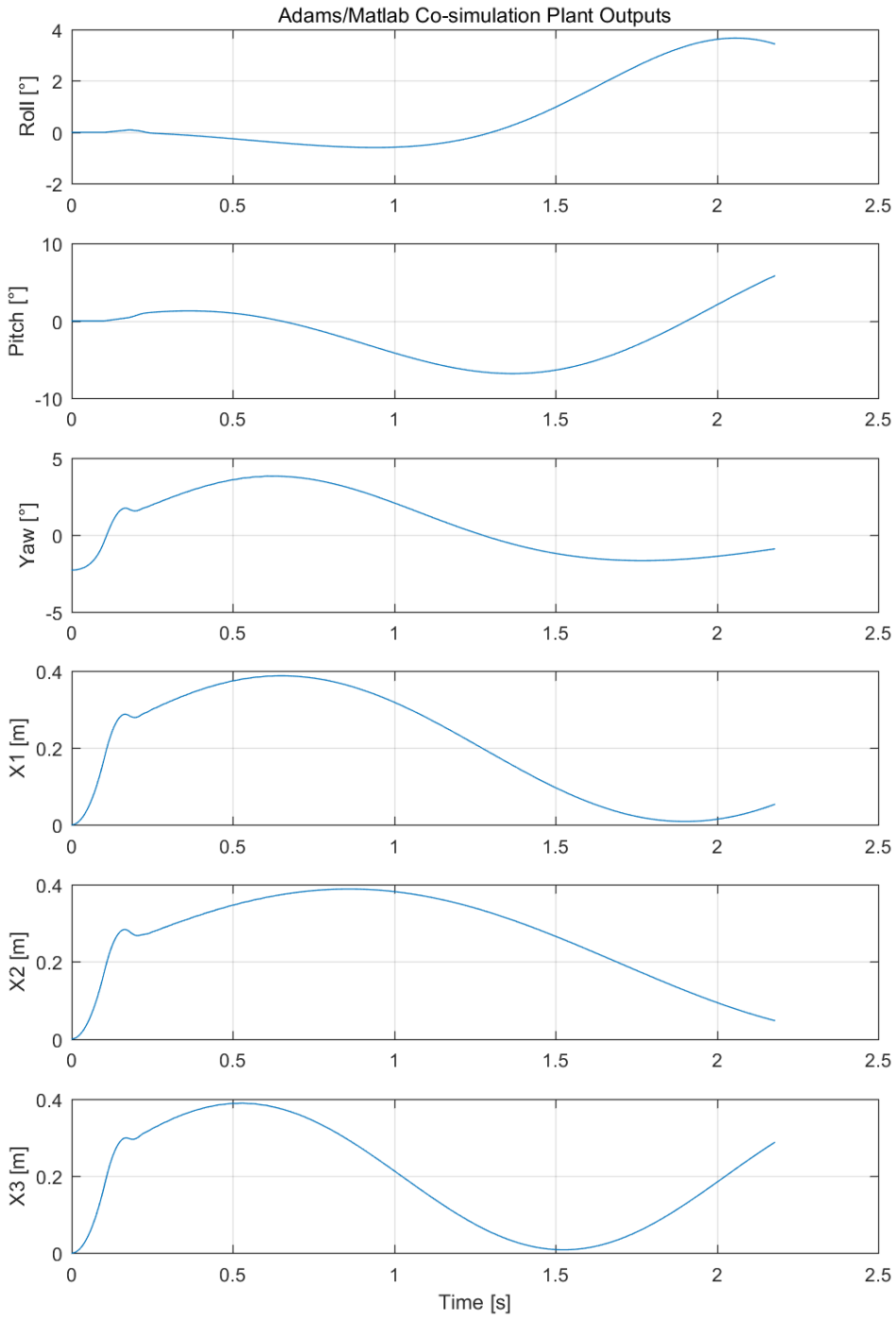

Figure 3.11: The Outputs of the ADAMS® Model

3.5 ADAMS® KINEMATIC SIMULATION

An inverse kinematic solution for the SMS can be found by using a dedicated solver during the operation of the system, which will transform the Pitch and Roll angles of the measured data into actuator lengths. The controller, which is typically not linked with ADAMS®, will then use these actuator lengths as set points to control each leg length. Included in the ADAMS® package is a well developed set of solver algorithms, which can be used in either a non real-time co-simulation or as a pre-process to convert a measured data set, or as a tool to derive a numerical function or lookup table that can be included into the real time simulation. The advantage of the latter is that the time to find a solution for every time step would be the same, as the time taken for the lookup and interpolation functions are deterministic. A second argument to be made for the lookup and interpolation process is that once the function has been defined, ADAMS® is no longer necessary for the operation of the system.

The existing ADAMS® model (as described in §3.3) was modified from one using three forces to effect the orientation of the platform and the SAT to one using a general motion to manipulate the orientation of the platform at a pre-defined working height, solving and exporting the calculated actuator extension lengths.

The changes involved removing the three single component forces ("SFORCE_1" to "SFORCE_3"), freeing up the actuators to translate along their z-axes and adding a general motion onto the platform, aligned with (and moving with) the coordinate system of the platform. Three constraints are placed on the movement, and hence on the CoG of the platform, the first being the height which is maintained at $0.5m$ above the ground, and the other two linked to the input variables "PitchIn" and "RollIn" that govern the platform attitude. Together with the three Panhard Rods, the system is well defined. Output variables "EX1", "EX2" and "EX3" are linked to the translational magnitude between the actuator body reference ("Act1.M_Ref") and the piston CoG ("Pistonx.CoG"), the same variable used for the position control feedback.

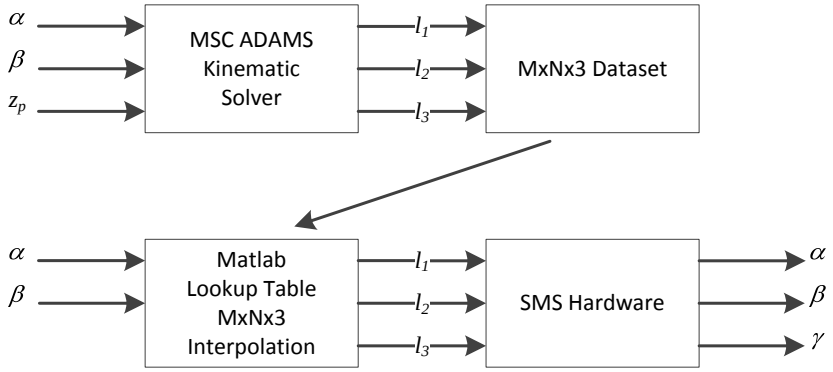

Figure 3.12: The Process to Generate and Test the SMS Kinematic Lookup Table

A matrix of solutions for the actuator lengths was generated by running a kinematic co-simulation with the input pitch angle stepped from -0.1 *rad* (-5.73°) to 0.1 *rad* (5.73°) in steps of 1 *mrad*, and the roll angle stepped over the same range for every step in the pitch angle. The size of the matrix is the determining factor in the step sizes and ranges of sweep, the latter example resulting in a 201x201x3 matrix. A lookup table is thus generated to act as a hard coded conversion for a specific working height, taking the roll and pitch angles (α, β) as inputs and outputting the actuator extension lengths (l_1, l_2, l_3). As the samples are homogenously spaced, an easy linear interpolation can be run to determine conversions that fall between matrix samples. The process is graphically described in Figure 3.12.

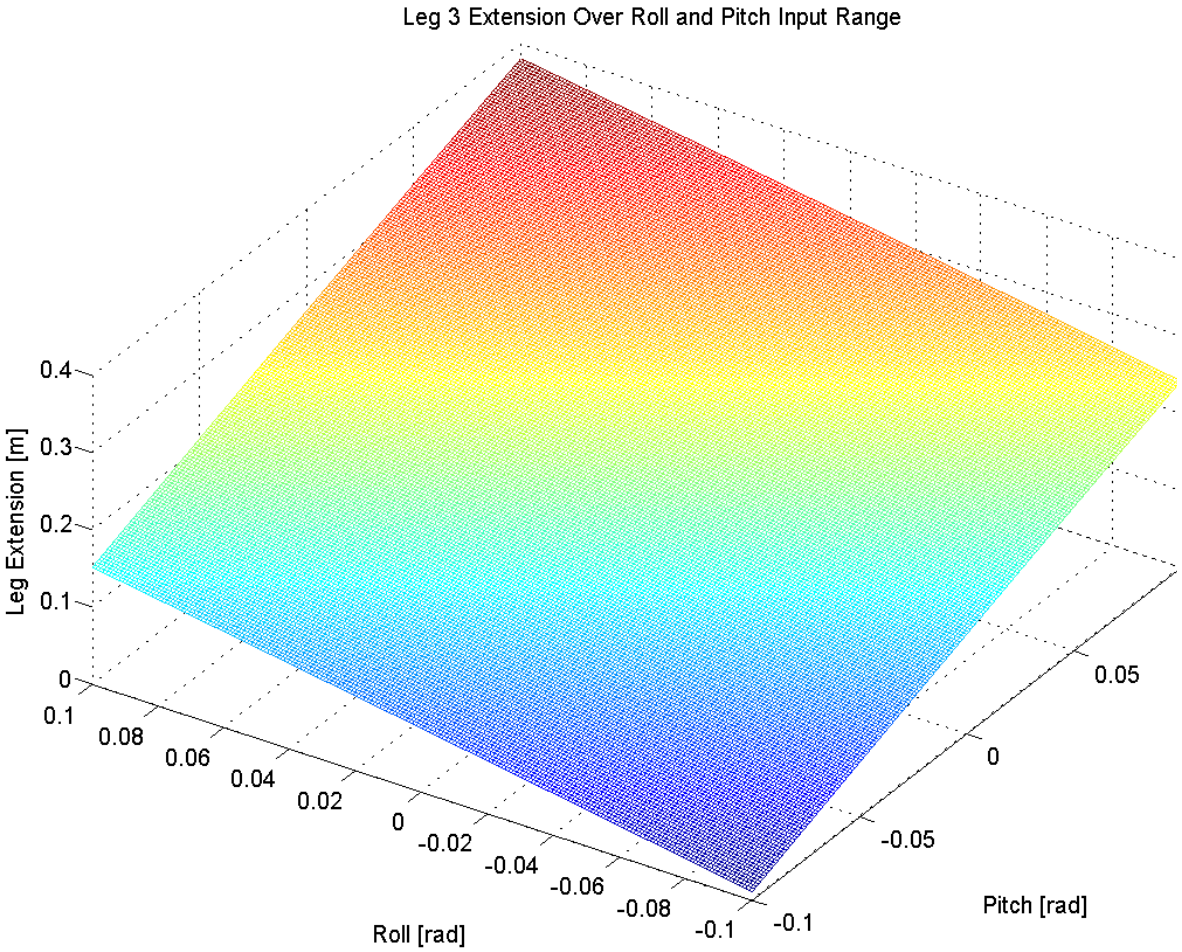

Figure 3.13: Three Dimensional Plot of the Leg 3 Extension Map

To ensure that the lookup table functions as designed a co-simulation was run using randomly generated roll and pitch values and checking that the resulting platform angles tracked the inputs. The ADAMS® model used the actuator lengths as inputs, solving for platform angle and position. The errors derived from this simulation were too small ($< 10^{-9} mm$) to justify any further effort into graphing them. One of the leg extension maps generated with this process is shown in Figure 3.13.

CHAPTER 4

THEORETICAL PNEUMATIC MODELS

The chapter starts off with a description of a pneumatic actuator subsystem. It is then expanded into the different parts, each of which is described in a mathematical form. Each section in this chapter is laid out in three parts, a description of the pneumatic part, a theoretical model of the pneumatic part and the Matlab® Simulink® model of the part.

4.1 PNEUMATIC SYSTEM

The pneumatic system, as previously described in the introduction (§ 2.3) and diagrammatically represented in Figure 2.5 consist of three identical parts, each linked to one of the three legs of the simulator. A schematic representation of one of these pneumatic actuator subsystems is shown in Figure 4.1. The main parts of this subsystem are, starting from the left, the reservoir, the valve, the actuator with the displacement sensor and the load. The latter consists of internal actuator forces, external mass induced forces and external perturbations. Some of the more relevant variables are also shown and will be referred to in more detail in subsequent sections.

As one works towards expressions for the force on the piston rod, which is a function of the pressure in each chamber, it is necessary to derive an expression for the change of pressure in each chamber. By following a process as depicted in Figure 4.2, each section of the pneumatic system can be described from fundamental thermodynamic and physical principles. The input to the system is the valve control voltage V_{vs} (or U_w from the Festo datasheet) in *Volt* which is converted to a valve piston spool displacement x_S in m, which in turn is transformed into a valve port area A_{va} and A_{vb}, both in m^2. The valve port area is used, together with the supply pressure p_s and chamber pressures, p_a and p_b, all in *Pa* to calculate the air mass flow rates, $\dot{m}_a$ and $\dot{m}_b$ in $kg.s^{-1}$ through the valve ports into and out of

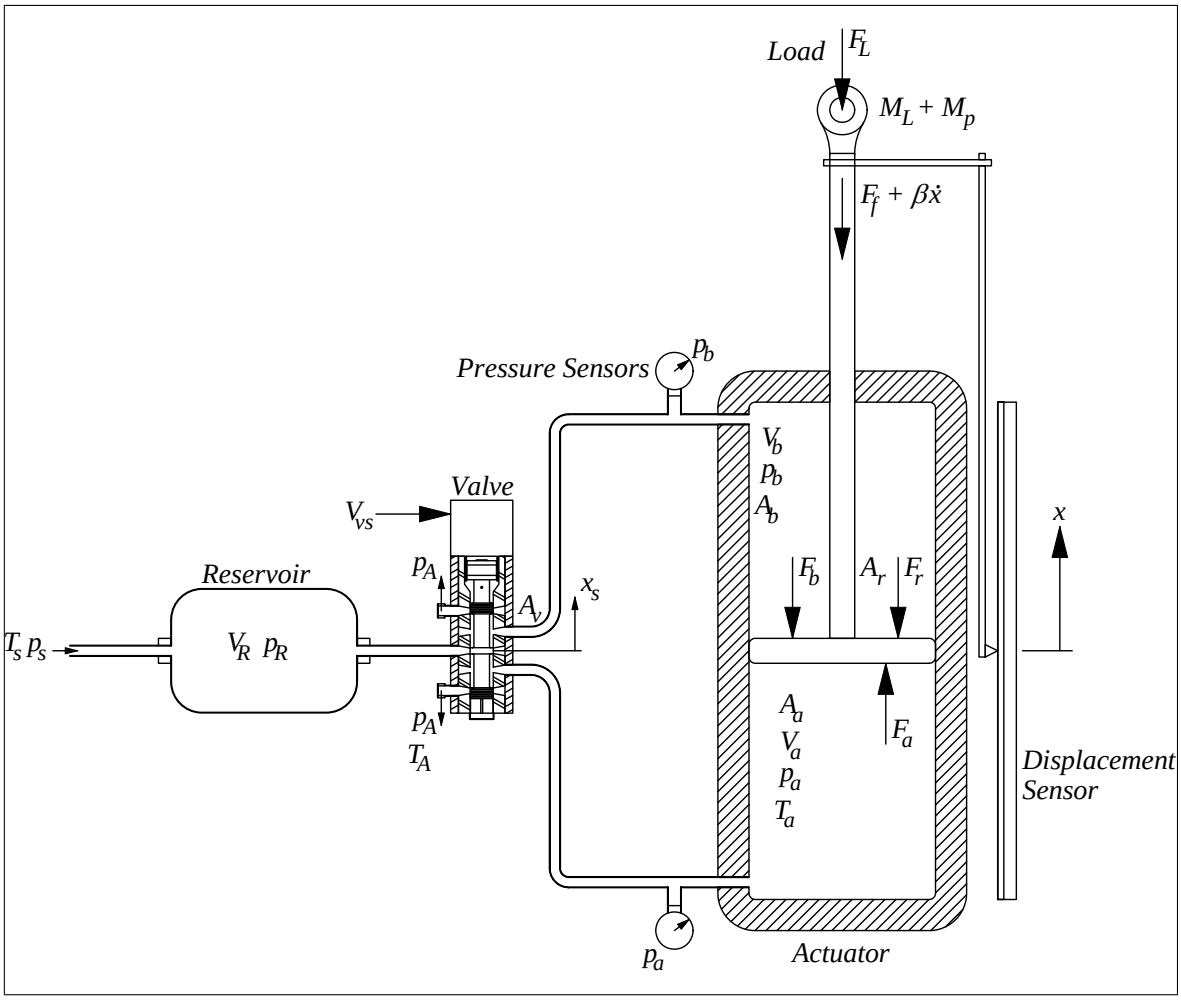

Figure 4.1: A Schematic Representation of the Pneumatic Actuator Subsystem

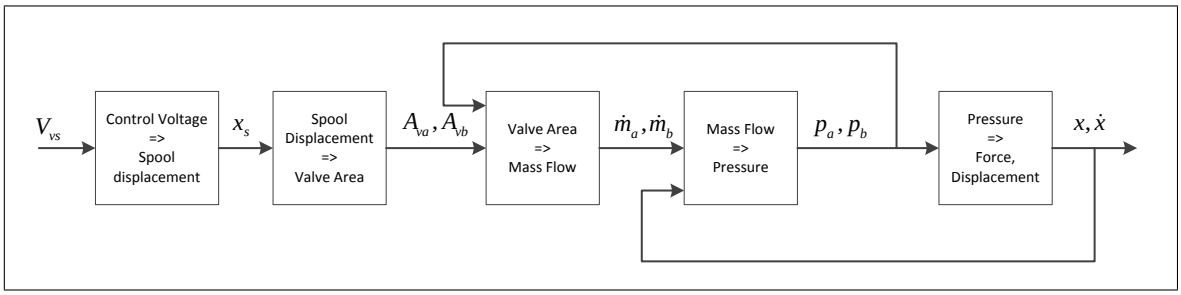

Figure 4.2: Diagram Indicating the Simulation Model Derivation of the Pneumatic Subsystem

the chambers. The mass flow rates of the valve ports, together with the actuator piston displacement x in m and rate $\dot{x}$ in $m.s^{-1}$ are then used to calculate the chamber pressures, the piston forces and the piston displacement.

4.1.1 Pneumatic Actuator Subsystem Matlab® Model

As a whole, the SMS consist of three identical actuator subsystems, each having the same components and hence, the same models. In this case one assumes that each of the three subsystems can be modelled independently and does not have significant cross coupling effects. Following the methodology for the derivation of the pneumatic model as described in Figure 4.2 the Simulink® model for one of the actuator subsystems will have the structure shown in Figure 4.3. This model will be fed by the controller output scaled as a voltage value between 0 V and 10 V. The complete pneumatic model is explained in great detail in the following sections and only a discussion regarding the MSC ADAMS® part is necessary in this section.

The equation of motion (eq 4.34) shows that the forces at play can be grouped as those originating from the pneumatic system (p_aA_a, p_bA_b, p_AA_r, $M_p\ddot{x}$ and F_{fric}), those originating from external perturbations (F_L) and those because of the SMS and MODSAT mass and inertia ($M_L\ddot{x}$). The inputs to the kinematic ADAMS® model are actuator forces and the outputs are the state variables x, $\dot{x}$ and $\ddot{x}$. The result is the model shown in the schematic, where the momentum terms as well as the load forces are included in the ADAMS® model. The piston masses are modelled in ADAMS®.

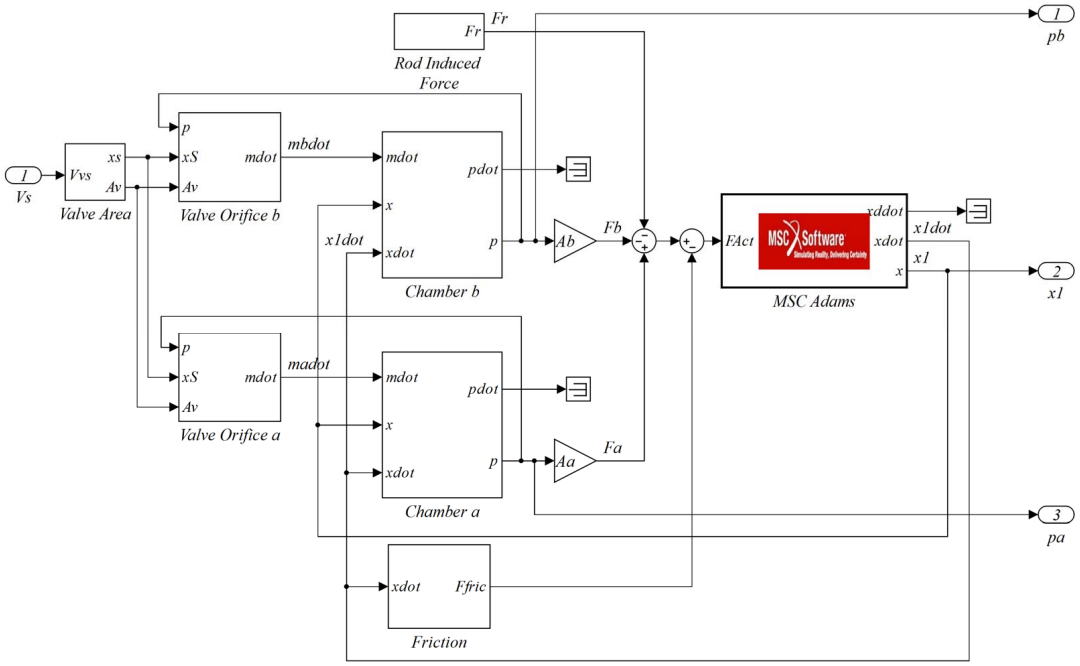

Figure 4.3: The Simulink® Model of One of the Pneumatic Actuators Linked to MSC ADAMS®

4.1.2 Valve

4.1.2.1 Valve Description

The valves used in the SMS are all proportional directional control valves (FESTO MPYE-5-3/8-010-B), with the spool displacement proportional to the input voltage and controlled through a built in controller. A sectional drawing of the valve is shown in Figure 4.4, indicating the structure of the valve. The body is rectangular with the threaded ports on the sides which are connected to a barrel (hatched inner tube) with precision machined port orifices on the circumference of the barrel (five rows of three orifices). Inside the barrel is a spool with three sealing areas closing off the port orifices. Air supply is channeled from *Port* 1 to *Port* 2, and from *Port* 4 to *Port* 5 when the spool is deflected to the left (see fig. 4.5a) by the solenoid driven by the controller during the input of a voltage value smaller than 5 V. During a voltage input of more than 5 V, the spool is driven to the right, connecting *Port* 1 to *Port* 4 and *Port* 2 to *Port* 3 (see fig. 4.5b). When an input voltage of 5 V is applied, all the ports are shut. There is a small overlap (measured as 0.165 *mm*) between the *Port* 1 sealing surface and the port orifice to compensate for manufacturing tolerances and input noise, resulting in a dead band in the middle of the valve travel.

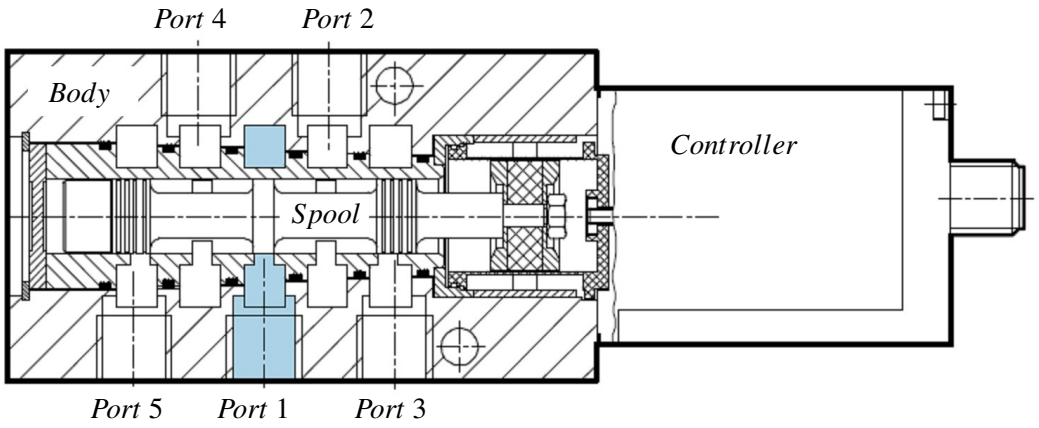

Figure 4.4: Sectional Diagram Of A Festo MPYE-5-3/8-010-B Proportional Directional Control Valve [50]

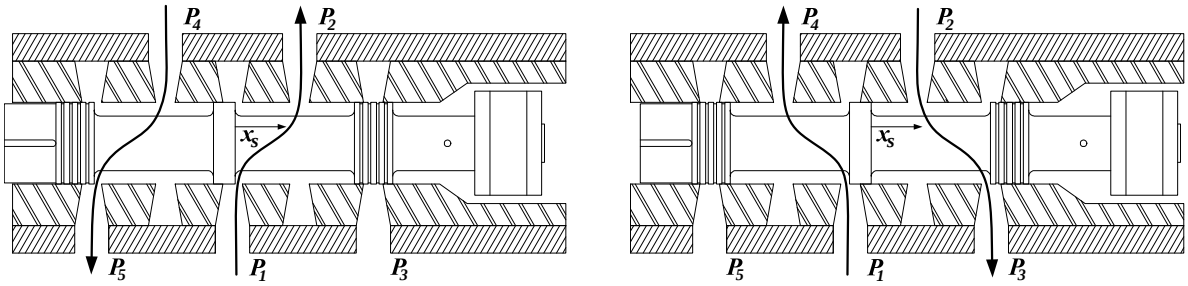

a) b)

Figure 4.5: Festo MPYE-5 Proportional Directional Control Valve with a a) Left Hand Deflection and a b) Right Hand Deflection

4.1.2.2 Valve Theoretical Model

A mathematical model for the pneumatic valve consists (according to Figure 4.2) of a transformation of control voltage V_{vs} to spool displacement x_S, a transformation of the spool displacement to valve orifice area, A_{va} and A_{vb}, and the calculation of the orifice mass flow rates, $\dot{m}_a$ and $\dot{m}_b$, the latter two entities being the same as the mass flow rates in and out of the chambers a and b.

The data sheet of the valve includes a graph of the mass flow rate at a single 0.1 MPa pressure differential (0.6 MPa to 0.5 MPa) as a function of control voltage (Figure 4.6). This graph indicates a percentage of the rated standard nominal volumetric flow rate (q), specified as 2000 $\ell.min^{-1}$ as a function of control voltage (U_w or V_{vs}) for a 0.6 MPa to 0.5 MPa pressure differential. Port connections are also indicated, which is helpful in the construction of a simulation model. This is, however, not enough to build a complete model and a more stringent approach is therefore followed.

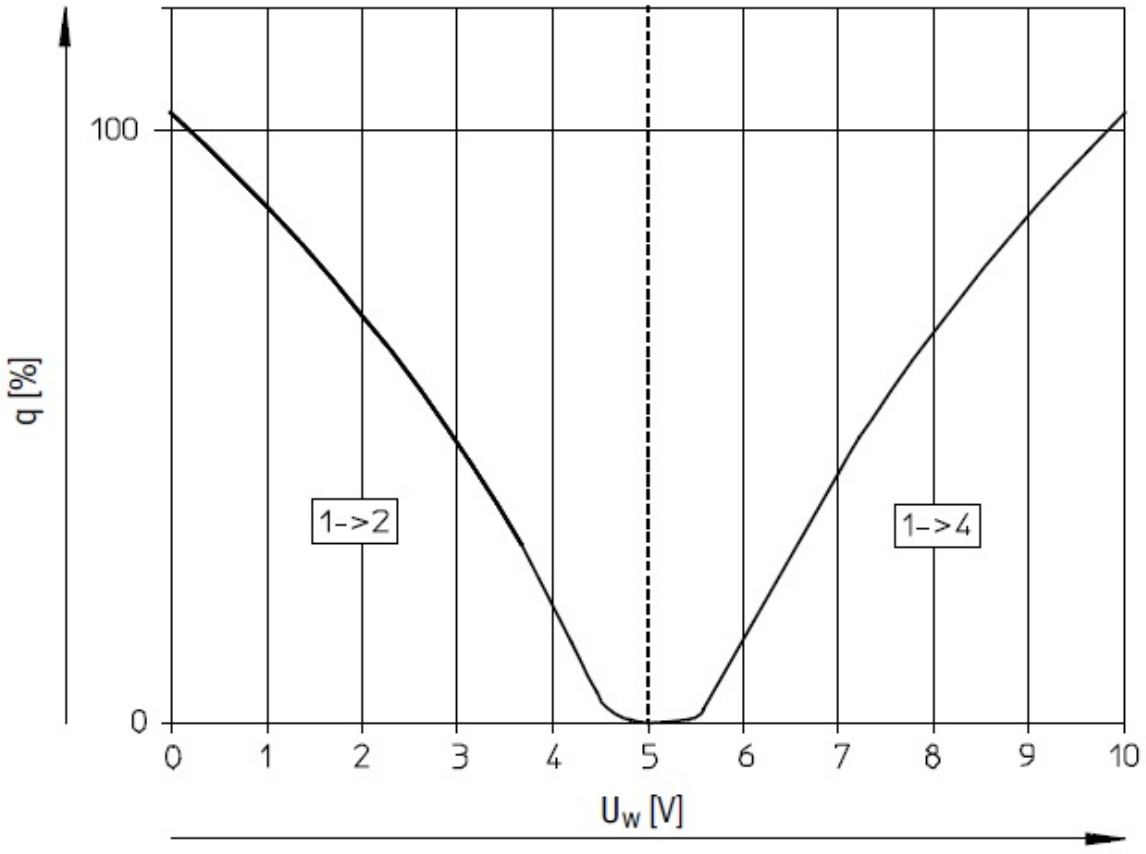

Figure 4.6: The Volumetric Flow Rate of the MPYE-5 Valve [50]

4.1.2.2.1 Valve Spool Deflection An experiment was set up to measure the dependence of the spool deflection on input voltage. A Heidenheim MT30 linear probe was connected to the spool and the deflections measured in both the forward and reverse directions. The control voltage was measured using a calibrated Fluke 289 multimeter. This measurement was done statically to determine the steady-state positioning of the Festo controller and all transients were ignored. The resulting curve of spool displacement *vs.* control voltage (V_{vs}) is shown in Figure 4.7. The top graph shows the measured displacement whereas the bottom graph shows the residual when it is compared with the polynomial approximation (eq. 4.1) as described below. Through a curve fitting process, a third order polynomial was found to describe the gain of the spool with a high enough precision (relative uncertainty is 0.5% (σ) of full scale). The gain of the valve spool plus controller can be expressed as

$$x_s = -0.002V_{vs}^3 + 0.0288V_{vs}^2 + 0.2917V_{vs} - 1.9286, \tag{4.1}$$

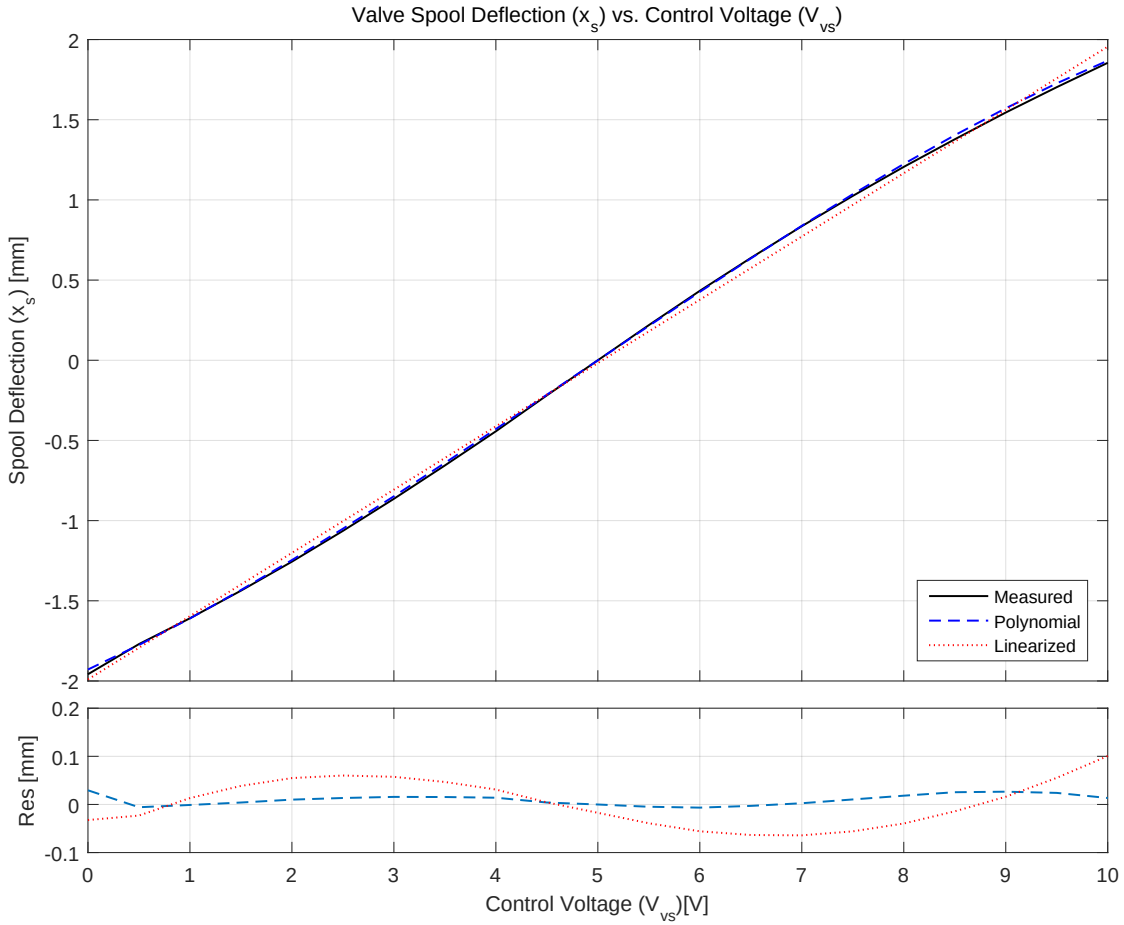

Figure 4.7: Festo MPYE-5 Proportional Directional Control Valve Spool Deflection *vs.* the Input Control Voltage (top graph) and the Residuals after Comparison with the Polynomial and Linear Approximations (bottom graph)

which relates the displacement x_S in *mm* to the input voltage V_{vs} in V. This expression can be simplified into a linear equation, using a least squares fit described by

$$x_s = 0.3946\,V_{vs} - 1.9904, \tag{4.2}$$

which results in a relative uncertainty of 2.6% (σ) of full scale, a precision value quite acceptable in most applications.

4.1.2.2.2 Valve Orifice Area The valve consist of a cylindrical spool in a cylindrical barrel with port orifices in the wall of the barrel. A series of annular feeder channels are machined into the outer surface of the barrel to spread the gas around the spool and utilise the full surface of the inner bore. All the orifices are opened and closed at the same rate during valve operation, as they are all defined

by openings in the valve barrel and the sealing areas on the spool. Noting that all the ports open at the same time (ignoring the microscopic effects of manufacturing tolerance), the cross sectional area of the ports will be equal at any point in time. Also, assuming that the barrel is large enough that the gas flow will be radial from either the annular feeding channels to the spool cavity, or visa versa (see Figure 4.8a) the area of the orifice, and hence the area used in the calculation of the flow, will be the length of the circle segment of the orifice, multiplied by the orifice height.

Similar to the measurement for the spool deflection, a measurement was done on the barrel and spool of the Festo valve to determine the sizes and positions of the orifices, as well as the primary dimensions of the spool. The most important dimensions of the spool for this model are listed in Table 4.1.

Table 4.1: The Primary Descriptors of the Valve Barrel and Spool

Descriptor	Size	Unit	Variable
Barrel Inner Diameter	15	*mm*	d_B
Port Width	3.57	*mm*	w_O
Spool Centre Sealing width	4	*mm*	w_S
Port Angle	1.59	*rad*	θ_S
Spool Maximum Deflection	± 1.9	*mm*	x_{Smax}
Number of Orifices	3		N

From a very simple geometric point of view, the valve orifices can be represented by rectangular holes, as shown in fig. 4.8b. The length of a circle segment can be expressed as $l_S = \theta_S \frac{d_B}{2}$ where $d_B = 2r_B$ is the barrel inner diameter in m and θ_S is the subtending angle of the orifice in rad. From the image in 4.8b it can be shown that the valve area is the product of l_S and x_O. As the spool is wider than the orifice:

$$x_O = x_S + \frac{w_O}{2} - \frac{w_S}{2}, \tag{4.3}$$

where w_O is the width of the orifice in m, w_S is the width of the spool sealing surface in m and x_S is

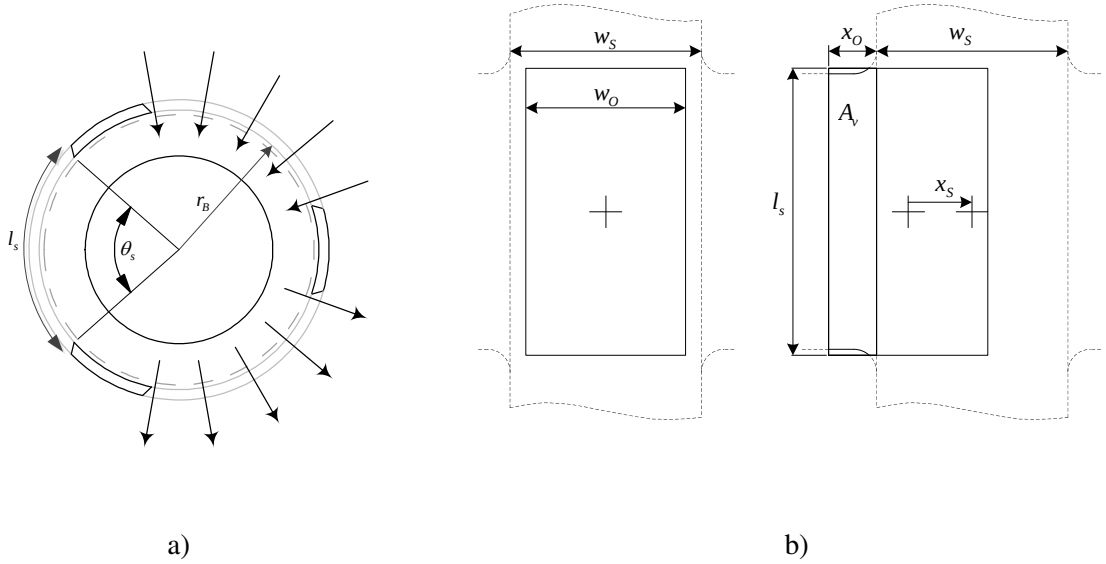

a) b)

Figure 4.8: a) A Section Through the Valve Barrel and Spool Showing the Assumed Radial Flow and b) the Unfolded Orifice Area (solid lines) *vs.* the Valve Spool (dotted lines)

the spool deflection in m. For a barrel design with N slots around the periphery, the valve area can be expressed as

$$A_v = \begin{cases} 0 & \Delta w < x_S < -\Delta w \\ Nl_S\left(|x_S| + \Delta w\right) & -\Delta w \leq |x_S| \leq x_{S\max} \end{cases}, \tag{4.4}$$

with A_v the area in m^2, $\Delta w = \frac{w_O - w_S}{2}$ and the equation is defined for both positive and negative deflections, but undefined for larger deflections than x_{Smax}.

4.1.2.2.3 Valve Mass Flow The mass flow through a valve can, as previously mentioned, be modelled as the mass flow through a variable area orifice, assuming that the gas is ideal and compressible. We also assume that there is no heat transfer in the upstream supply of gas. From the general energy equation derived in § 4.1.3.2, equation 4.26 (see [10, p.22]) can be rewritten in a discrete form, resulting in

$$\dot{Q} - \dot{W}_S = \frac{d}{dt}\int_{cv}\left(\frac{v^2}{2} + gz + u\right)\rho\, dV + \sum_{cs}\dot{m}_o\left(\frac{v_o^2}{2} + gz_o + h_o\right) - \sum_{cs}\dot{m}_i\left(\frac{v_i^2}{2} + gz_i + h_i\right), \tag{4.5}$$

with $\dot{Q}$ the rate of thermal energy entering the system, $\dot{W}_S$ the rate of work done in the system, v the gas velocity, g the gravitational constant, z the height of the system, u the internal energy in the system, $\dot{m}$ the mass flow into and out of the system and h the specific enthalpy of the gas flowing in and

out of the system. If it is assumed that the gas is stationary in the closed volume, the volume does not move, there is no time dependent changes of the internal volumetric energy and the system describes an orifice in which the gas is transformed from state 1 to state 2, the equation can be generalised to

$$Q + \frac{m_1 v_1^2}{2} + m_1 g z_1 + H_1 = W_S + \frac{m_2 v_2^2}{2} + m_2 g z_2 + H_2, \tag{4.6}$$

by integrating with respect to time, rearranging the terms and accepting that the $H = mh$. In such a system without heat transfer ($Q = 0$), the enthalpy difference can be written as

$$H_1 - H_2 = -\int_1^2 V dp \tag{4.7}$$

and by noting that the potential energy of a gas plays an insignificant role, eq. 4.6 will simplify to

$$-\int_1^2 V dp = W_s + \frac{m v_2^2}{2} - \frac{m v_1^2}{2}. \tag{4.8}$$

To derive a relationship (similar to St. Venant and Wantzel, 1839, [10, p.30]) for the mass flow through an orifice, one can start off with a source (reservoir) of gas with infinite volume, with a temperature T_1, a pressure p_1 and a mass of m_1. Venting the gas from the reservoir through a well rounded nozzle, so that no flow contraction occurs, the stationary gas (inside the container) will be accelerated to a gas velocity of v_2. If it is assumed that there is no mechanical work done, and no heat transfer through the vessel's surface ($Q = 0$, and $W_S = 0$), eq. 4.8 will describe the relationship between the energies in the vessel and those in the downstream flow. As previously stated, there is assumed to be no heat exchange, resulting in an adiabatic system for which the relationship

$$p_1 v_1^\kappa = p_2 v_2^\kappa = p v^\kappa, \tag{4.9}$$

holds. Changing the equation to one of "per unit" by using the specific volume ($v = \frac{V}{m}$) and substituting $v = v_1 \left(\frac{p_1}{p}\right)^{\frac{1}{\kappa}}$ from eq 4.9 into the left hand side of the energy equation (eq 4.8), it can be rewritten as

$$-\int_1^2 v dp = -v_1 p_1^{\frac{1}{\kappa}} \int_1^2 p^{\frac{-1}{\kappa}} dp = \frac{v_2^2}{2}, \tag{4.10}$$

which, through integration and some rearranging results in

$$\frac{\kappa}{\kappa - 1}\frac{p_1}{\rho_1} = \frac{v_2^2}{2} + \frac{\kappa}{\kappa - 1}\frac{p_2}{\rho_2}. \tag{4.11}$$

By rearranging eq 4.9 and adding the isothermal relationship, Beater [10] has shown that the velocity of the gas at any cross section of the nozzle at pressure p_2 can be expressed by

$$v_2 = \sqrt{2RT_1 \left(\frac{\kappa}{\kappa - 1}\right)\left[1 - \left(\frac{p_2}{p_1}\right)^{\frac{(\kappa-1)}{\kappa}}\right]}. \tag{4.12}$$

From the continuity equation ($\dot{m} = A_1 v_1 \rho_1 = A_2 v_2 \rho_2 = A v \rho$) and the relationship for the gas density in an isentropic process

$$\rho_2 = \frac{p_1}{RT_1}\left(\frac{p_2}{p_1}\right)^{\frac{1}{\kappa}}, \tag{4.13}$$

the mass flow from the reservoir through the well rounded nozzle can be described as

$$\dot{m} = A p_1 \sqrt{\frac{2}{RT_1}} \sqrt{\left(\frac{\kappa}{\kappa-1}\right)\left[\left(\frac{p_2}{p_1}\right)^{\frac{2}{\kappa}} - \left(\frac{p_2}{p_1}\right)^{(\kappa+1)/\kappa}\right]}. \tag{4.14}$$

A flow function (Ψ) can be defined so that the mass flow can be simplified to

$$\dot{m} = A p_1 \Psi \sqrt{\frac{2}{RT_1}} \tag{4.15}$$

and

$$\Psi = \sqrt{\left(\frac{\kappa}{\kappa-1}\right)\left[\left(\frac{p_2}{p_1}\right)^{\frac{2}{\kappa}} - \left(\frac{p_2}{p_1}\right)^{(\kappa+1)/\kappa}\right]}. \tag{4.16}$$

At this time it is prudent to investigate the flow capacity of a nozzle or orifice. As the pressure differential over the nozzle or orifice increases, the flow of air will increase to a point where the velocity will become supersonic. Any further increase in the upstream pressure, or decrease in downstream pressure will not result in an increase in flow. The maximum flow rate (according to eq 4.14) can be found by evaluating the derivative of the flow function and finding the zero point. One can define a critical pressure ratio $p_{cr} = \frac{p_2}{p_1}$ and substitute it into eq. 4.16, take the derivative of (the square of) the flow function to the critical pressure and the latter is

$$\frac{d\left(\Psi^2\right)}{dp_{cr}} = \frac{\kappa}{\kappa-1}\left(2\frac{p_{cr}^{\frac{2-\kappa}{\kappa}}}{\kappa} - \frac{(\kappa+1)\,p_{cr}^{\frac{1}{\kappa}}}{\kappa}\right). \tag{4.17}$$

The maximum can be shown to be at

$$p_{cr} = \left(\frac{2}{\kappa+1}\right)^{\frac{\kappa}{\kappa-1}}\Bigg|_{\frac{d(\Psi^2)}{dp_{cr}}=0}, \tag{4.18}$$

with a maximum of

$$\Psi_{\max} = \left(\frac{2}{\kappa+1}\right)^{\frac{1}{\kappa-1}} \sqrt{\frac{\kappa}{(\kappa+1)}}\Bigg|_{\frac{p_d}{p_u}=p_{cr}}. \tag{4.19}$$

This derivation is a very ideal situation and can be applied with very small errors on well rounded nozzles with predominantly laminar flow and negligible approach velocity. This is, however, not the case for valves in general. Valves tend to have sharp edges, which will result in turbulent flow and a reduction in mass flow rate due to losses and contraction. It is common, for a compressible fluid such as gas, to define a discharge coefficient C_d which is a function of the pressure ratio [10, p.34], and

include this into the orifice mass flow equation to model the restriction effects. The mass flow through the valve orifice can, if it is assumed that the air temperature does not change during the process, be described with a fair amount of accuracy by

$$\dot{m}_v = \begin{cases} C_1 C_d A_v \frac{p_1}{\sqrt{T}} & \frac{p_2}{p_1} \leq p_{cr} \quad (Choked\ flow) \\ \\ C_2 C_d A_v \frac{p_1}{\sqrt{T}} \left(\frac{p_2}{p_1}\right)^{\frac{1}{\kappa}} \sqrt{\left[1 - \left(\frac{p_2}{p_1}\right)^{(\kappa-1)/\kappa}\right]} & \frac{p_2}{p_1} > p_{cr} \quad (Subsonic\ flow) \end{cases}, \tag{4.20}$$

with

$$C_1 = \sqrt{\frac{\kappa}{R}\left(\frac{2}{\kappa+1}\right)^{\frac{\kappa+1}{\kappa-1}}} \tag{4.21}$$

and

$$C_2 = \sqrt{\frac{2}{R}\left(\frac{\kappa}{\kappa-1}\right)}. \tag{4.22}$$

The gas flow during the small pressure differentials can be described as subsonic flow and the pressure ratio (p_2/p_1) is larger than the critical pressure ratio (p_{cr}) in these equations. $\dot{m}_v$ is the mass flow through the orifice in $kg.s^{-1}$, κ is the specific heat capacity ratio ($\kappa = 1.4$ for air), p_1 is the upstream pressure, p_2 is the downstream pressure, both in Pa, T is the air temperature in K, A_v is the orifice area in m^2 and C_d is a non-dimensional discharge coefficient.

The mass flow through a valve orifice can be simulated using the above model, taking into account that both the charging of the chamber as well as the discharging of the chamber are described by the same equation. For the charging case, the variable p_1 is the supply pressure, and p_2 is the chamber pressure. In the case of discharging, p_1 is used for the chamber pressure and p_2 for the ambient pressure. Valve leakage can also be modelled by selecting the relevant chamber pressures with an arbitrary valve area or discharge coefficient.

4.1.2.3 Valve Matlab® Model

Following the theoretical description of the valve, a process to convert an input voltage to a mass flow has to be realised. Figures 4.9 and 4.10 show the Simulink® models for the valve orifice area and the mass flow through the orifice. These models can also be realised trough Matlab® functions, as is used later in the study. The nonlinear voltage/spool displacement relationship is catered for in the first block, and then subsequently the segment length of the orifice (l_S) as a function of the included

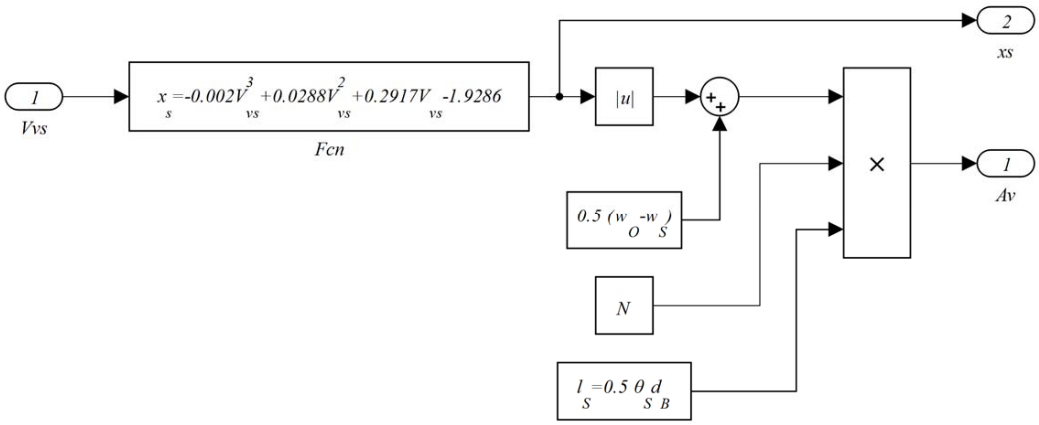

Figure 4.9: The Simulink® Valve Model with Area as a Function of Input Voltage

angle θ_S, the barrel diameter d_B, the widths of the spool sealing area and the orifice. Both the spool displacement and the valve orifice area are presented as outputs, as they form the basis of gas flow and switching logic in the larger model. The mass flow is slightly more complicated, taking into

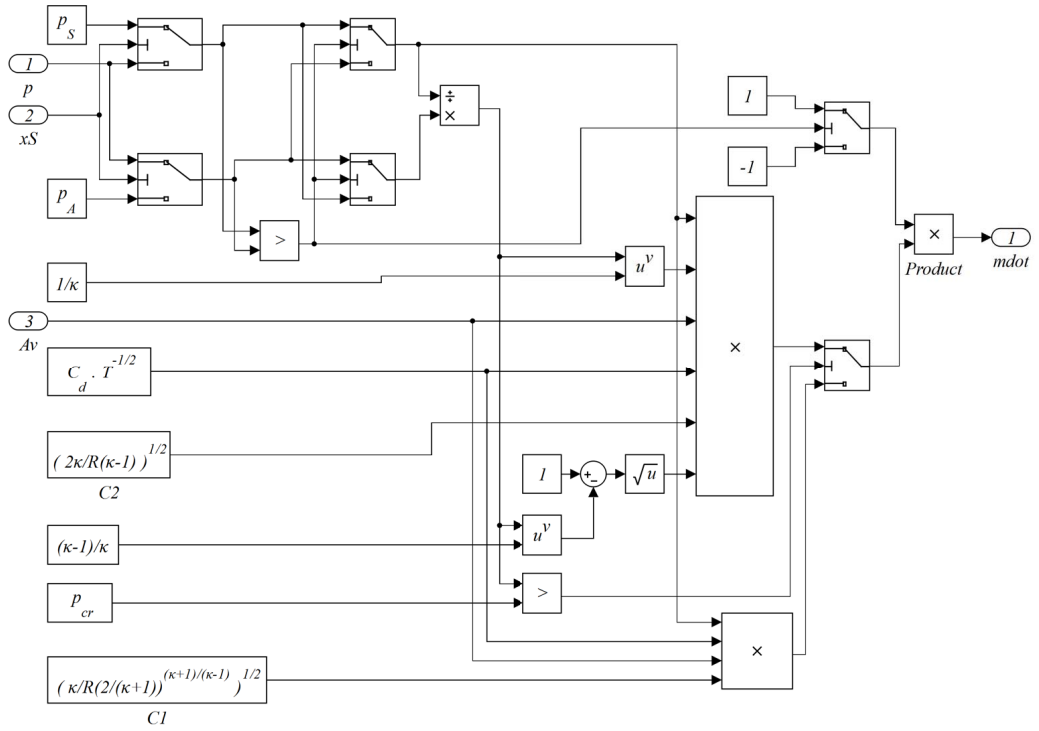

Figure 4.10: The Simulink® Model for the Mass Flow Through the Valve Orifice

account that the flow will either be choked or subsonic, depending on the pressure differential as well

as the fact that the mass flow can become negative in cases where the downstream (chamber) pressure is higher than the supply. The input of the spool displacement is necessary to determine if the process is a charging one or a discharging one.

4.1.3 Actuator

4.1.3.1 Actuator Description

The actuator under investigation is a double acting actuator with adjustable cushioning at the ends. Referring to Figure 4.1, the actuator can be seen to consist of two opposing chambers, separated by the piston which is connected to the actuator rod. The piston displacement is taken to be positive when extending. The two chambers are connected to the supply through tubes and ports, which both have restrictions, hence reduced flow. The main physical descriptors are listed in Table 4.2.

Table 4.2: Physical Descriptors of the Festo DNC-100-400-PPV Actuator

Descriptor	Value	Unit
Piston Diameter	100	mm
Stroke Length	400	mm
Rod Diameter	25	mm
Actuator Mass	11.617	kg
Piston Mass	3.528	kg
Viscous Friction Coefficient	530	$N.s.m^{-1}$

The bottom chamber has a volume of V_a and is filled with dry air at a pressure p_a and temperature T_a. An upward force of F_a is exerted on the bottom of the piston with an area of A_a due to the air pressure p_a. The top chamber has a volume of V_b and is filled with dry air at a pressure of p_b and temperature T_b. A downward force of F_b is exerted on the piston with area A_b due to the air pressure p_b as well as a downward force of F_r due to the ambient pressure p_A on the rod area A_r. External load forces F_L, friction forces F_f and dynamic forces due to the movement of the piston ($\beta\dot{x}$, $M_L +$

$M_p\ddot{x}$) are also indicated. In order to balance the forces and control the piston to a predefined position x, detailed models of the chamber pressures and friction forces will be derived. It is assumed that all the mechanical parts are rigid and will not deform under load or pressure.

4.1.3.2 Theoretical Actuator Model

4.1.3.2.1 Chamber Model The Actuator chambers can be likened with pressure vessels or cylinders with a variable volume and restricted in and outlets. The pneumatic processes involved in the charging and discharging of such cylinders can be described as either adiabatic or isentropic or isothermal. Previous work published on the subject includes that of Ben-Dov [17], McDonnel *et al.* [51] and Ning *et al.* [25], all of which used an adiabatic assumption. Richer [26] used the assumption that the charging process of the cylinder is adiabatic and that the discharging process is isothermal as proposed by Al-Ibrahim [52] in 1992. The latter argued that the charging process is irreversibly adiabatic and the discharging process a better approximation of isothermal than of adiabatic (or isentropic). A derivation by Šitum *et al.* [53] using the energy conservation theorem for a controlled volume of gas was also done with the assumption of an adiabatic process. In most cases the process lies somewhere between adiabatic and isothermal and the polytropic index is assumed to be between 1 and 1.4 (as proposed by Richer [26]) and should be verified during the model validation process.

Using a similar approach to Šitum [53] and Richer [26], basing it on the principle of a control volume (See [8]) with the application of the Reynolds transport theorem, the general energy equation

$$\dot{Q} - \dot{W} = \frac{dU}{dt}, \tag{4.23}$$

can be rewritten as

$$\dot{Q} - \dot{W} = \frac{d}{dt}\int_{cv} e\rho \, dV + \int_{cs} e\rho v \, dA, \tag{4.24}$$

where $\dot{Q}$ is the net rate of thermal energy entering the system, $\dot{W}$ is the net rate at which the system does work, e is the energy per unit mass (specific energy) of the gas, ρ is the gas density, v is the homogenous gas velocity through the control surface and V and A are the volumetric and surface environments respectively. The environment can be likened to the chamber of the actuator. If we assume that the rate of work $\dot{W}$ is the sum of the flow work $\dot{W}_{flow}$ and the mechanical work $\dot{W}_S$, eq. 4.24 can be expanded to

$$\dot{Q} - \dot{W}_S - \int_{cs} \frac{p}{\rho}\rho v \, dA = \frac{d}{dt}\int_{cv} (e_p + e_k + u)\rho \, dV + \int_{cs} (e_p + e_k + u)\rho v \, dA, \tag{4.25}$$

with p the gas pressure, e_p and e_k the potential energy and kinetic energy of the gas respectively and u the specific internal energy of the control volume. By applying the property of enthalpy and assuming that the specific enthalpy is the sum of the internal energy of the system and the product of the pressure and the volume ($h = \frac{p}{\rho} + u$), eq. 4.25 can be expressed as

$$\dot{Q} - \dot{W}_S = \frac{d}{dt}\int_{cv} (e_p + e_k + u)\,\rho\, dV + \int_{cs} (e_p + e_k + h)\,\rho v\, dA. \tag{4.26}$$

Finally, by accepting that the gas in the control volume has no significant movement, hence insignificant kinetic energy and insignificant potential energy, the first two terms in the volumetric integral can be dropped. Similarly the gas passing through the control surface has limited speed, and once again insignificant kinetic energy (less than 2% of the thermal energy at $v = 100\ m.s^{-1}$ and $T = 293\ K$ according to [10, p.114]) and zero potential energy according to the ideal gas law, so that the first two terms in the surface integral can also be left out. If then, the flow across the control surface is through discrete ports and the velocity is uniformly distributed across each port and $u = c_V T$ is substituted, then the energy equation becomes

$$\dot{Q} - \dot{W}_S + \dot{m}_i h_i - \dot{m}_o h_o = \frac{d}{dt}\left(c_V T \rho V\right). \tag{4.27}$$

By substituting $h = c_V T$ (the enthalpy for an ideal gas), the mechanical work ($\dot{W}_S = p\dot{V}$) and $\rho T = \frac{p}{R}$ into eq 4.27, and noting that the thermal exchange through the chamber surface is zero ($\dot{Q} = 0$) the energy equation for an adiabatic process can be expressed as

$$c_p\left(\dot{m}_i T_i - \dot{m}_o T_o\right) = \frac{d}{dt}\left(\frac{c_V p}{R} V\right) + p\dot{V}, \tag{4.28}$$

in which $\dot{m}_i$ and T_i are the mass flow rate and temperature of the gas entering the chamber and $\dot{m}_o$ and T_o are the mass flow rate and temperature of the gas exiting the chamber. c_p is the specific heat capacity of the gas at a constant pressure, c_V is the specific heat capacity of the gas at a constant volume, R is the universal gas constant, p is the chamber pressure and V is the chamber volume. When using the relationships $c_V = \frac{R}{\kappa - 1}$, $c_p = c_V + R$ (Mayer's equation) and $\kappa = \frac{c_p}{c_V}$ and rearranging the terms to express the chamber pressure change, eq 4.28 can be rewritten as

$$\dot{p} = \frac{\kappa R}{V}\left(\dot{m}_i T_i - \dot{m}_o T_o\right) - \kappa \frac{p}{V}\dot{V}. \tag{4.29}$$

This result is the same as that of Richer [26, eq10] and Šitum [53] for an adiabatic process with $T_o = T_i$. It should be noted that the assumption of an irreversible adiabatic process with a κ of 1.4 might need to be amended by rather defining the process as a polytropic one and using different heat capacity ratios depending on the charging/discharging state of the chamber. Therefore, as the heat

capacity ratio can only vary between 1 and 1.4, the correct value can be estimated during a validation process. To enable this feature, eq. 4.29 can be amended to

$$\dot{p} = \frac{R}{V}\left(\alpha_i \dot{m}_i T_i - \alpha_o \dot{m}_o T_o\right) - \alpha \frac{p}{V}\dot{V}, \tag{4.30}$$

where α_i, α_i and α are the heat ratios related to the input mass flow, the output mass flow and the chamber gas. As per the suggestion of Richer, α_i should be close to 1.4 and α_o should be close to 1, with α around 1.2 ([52]).

As the pressure change in the chamber is a function of the change in volume and the volume itself, and the volume in each chamber is linked to the piston position, the volume in the chambers ($i = \{a, b\}$) can be expressed as

$$V_i = V_{di} + A_i\left(\frac{L}{2} \pm x\right) \quad \forall \quad -\frac{L}{2} \leq x \leq \frac{L}{2} \tag{4.31}$$

where V_{di} is the dead (or inactive) volume of each chamber, A_i is the piston area, L is the maximum stroke length and x is the piston displacement relative to the centre of the stroke. This equation is only defined for $-\frac{L}{2} \leq x \leq \frac{L}{2}$. The areas of the piston in the two chambers and hence the volume of the two chambers, are not the same as the top chamber has a reduced volume due to the piston rod. By substituting eq. 4.31 into eq. 4.30 and noting that $\dot{V} = A_i \dot{x}$, the time derivative of the chamber pressures can be rewritten as

$$\dot{p}_i = \frac{R}{V_{di} + A_i\left(\frac{L}{2} \pm x\right)}\left(\alpha_i \dot{m}_i T_i - \alpha_o \dot{m}_o T_o\right) - \frac{\alpha p_i A_i}{V_{di} + A_i\left(\frac{L}{2} \pm x\right)}\dot{x}. \tag{4.32}$$

This equation, as stated by Richer [26], accounts for the change of pressure due to mass flow (air flow) in and out of the ports connected to the chamber (first term) as well as the change of pressure due to the movement of the piston and hence the change in chamber volume (second term). It does not, in its current state, account for leakage of air through the piston seal, which in this study is neglected, as the piston seals are of nitrile rubber and leakage rates are deemed insignificant against the flow rates during operation. If the temperatures of the incoming air, the outgoing air and the chamber is taken to be equal (an isothermal process), the temperature subscripts can be dropped.

4.1.3.2.2 Simple Friction Model In a pneumatic system, the main sources of nonlinearity are the compressible nature of the air (gas), the airflow-pressure relationship and the stick-slip nature of the pneumatic seals. The latter (friction contribution) is under investigation in this section and further expanded in § 6. Various models have been proposed, ranging from "ignoring the problem", the application of the Stribeck stiction model ([53],[23]), some more specific seal models such as

Belforte [35] to very computationally complex descriptions such as that of Swevers *et al.* [32]. It is evident that the actuator friction model will be extremely complex and will most probably become obsolete once the lubrication in the actuator changes. A generalisation can be made (Belforte, 1989) that the friction force grows when the pressure in at least one of the chambers increase, when the extension or contraction velocity increases, when the bore diameter increases or when the lubrication becomes poorer (Raparelli [54]). The most comprehensive model describing friction is the Leuven model presented by Swevers *et al.* [32], which is an improvement of the LuGre [31] model, consisting of a nonlinear state and a velocity dependent friction force component.

Although the LuGre, Dahl and Leuven models account for effects in both the pre-sliding regime and the sliding regime, the present model will be simplified to only include stationary and constant velocity characteristics such as the Stribeck effect. The friction model can be revisited at a later stage to improve the dynamic behaviour.

Similar to Nouri *et al.* [23] and Andrighetto *et al.* [36], the friction force in the actuator can be modelled through

$$F_{fric} = \beta\dot{x} + \left[F_C + (F_S - F_C)\, e^{-\left|\left(\frac{\dot{x}}{\dot{y}_S}\right)\right|^{\delta}}\right] \operatorname{sgn}(\dot{x}), \tag{4.33}$$

with F_{fric} the friction force, β the viscous friction coefficient, x and $\dot{x}$ the actuator displacement and velocity, F_S the static friction force (Stiction force), F_C the Coulomb friction force, $\dot{y}_S$ the Stribeck velocity and δ the Stribeck exponent. A graph indicating a theoretical friction relationship to velocity of an arbitrary system is shown in Figure 4.11. This graph does not indicate the hysteresis present as the velocity decreases, but only a validation process will indicate if it is necessary. It should be noted that this is a very simple friction model and could be improved to resemble the more complete Leuven or LuGre models.

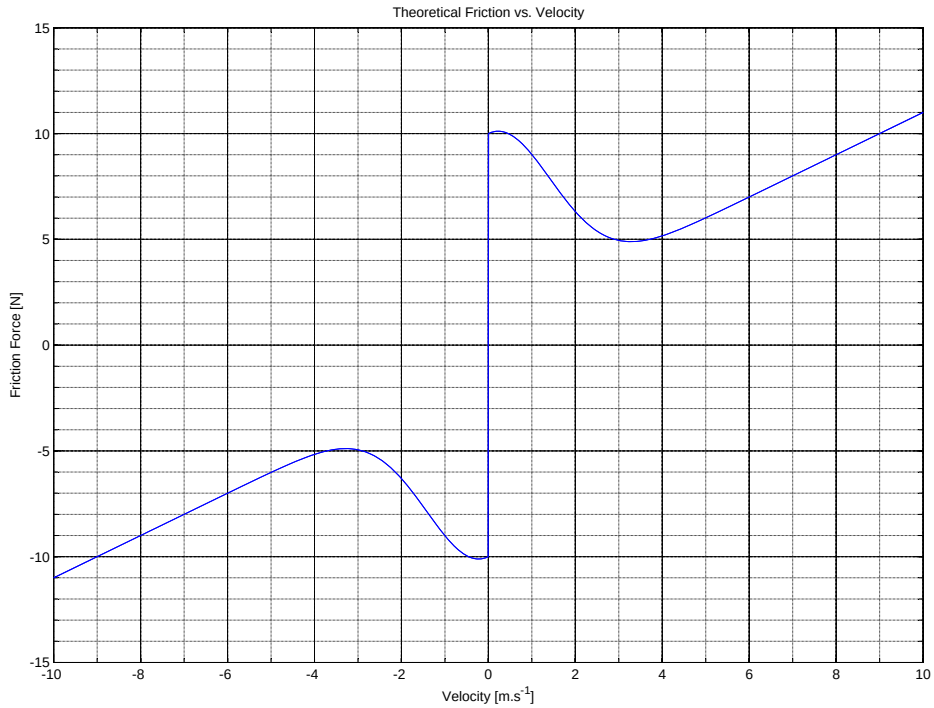

Figure 4.11: The Theoretical Friction Function Based on the Stribeck Friction Model

4.1.3.2.3 Equation of Motion The equation of motion for a single actuator can be defined by using the summation of forces, which consists of the the pneumatic active drive force, which is derived from the pressure difference between the two chambers and the external load forces, which include all dynamic and mechanical forces on the piston rod. As the piston rod and the force is always aligned, scalar entities can be used. The equation of motion can be expressed as

$$p_a A_a - (p_b A_b + p_A A_r) = F_{fric} + F_L + (M_L + M_p)\ddot{x}, \tag{4.34}$$

where p_a, p_b and p_A are the pressure in chamber a, chamber b and ambient pressure; A_a, A_b and A_r are the area of the piston in chamber a, in chamber b and the piston rod area respectively. F_{fric} is the combined friction force, including stiction (static), Coulomb friction and viscous friction (dynamic) (as described in sec. 6.4, eq 4.33). The last two terms, F_L and $M_T\ddot{x} = (M_L + M_p)\ddot{x}$ are describing the external load forces on the actuator and the forces due to inertia. All pressures are in Pa, areas in m^2, forces in N and masses in kg.

4.1.3.3 Actuator Matlab® Model

The actuator consists of two variable volumes separated by a piston. The actuator cylinder volumes are modelled as two separate chambers, labelled with subscripts a (for the bottom chamber) and b (for the top chamber). The leakage of the pneumatic seals are not modelled. The input to the actuator model is the mass flow from the valve ($\dot{m}$) and the output the displacement x, linked through two chamber models and the equation of motion.

4.1.3.3.1 Chamber Model Following the equation for the change of pressure in an actuator chamber, a Simulink® model was composed as shown in Figure 4.12. The inputs are the mass flow ($mdot$), the displacement to modify the chamber volume (x) and the time derivative of the displacement. The output is the chamber pressure that will give rise to force on the piston. The values for α_i, α_o and α can be chosen as $\kappa = 1.4$ for air to approximate an isentropic process or as suggested in par. 4.1.3.2.1. R is the gas constant (288 $J.kg^{-1}.K^{-1}$) and the temperatures of the incoming and exhausting gas is assumed to be equal ($T = 293\ K$). The chamber variables are described in Table 4.2.

4.1.3.3.2 Simple Friction Model As described by sec. 6.4, the simplified friction model for the actuator has been implemented in Matlab® Simulink® using mostly discrete block operators. This model is shown in Figure 4.13. In this image, the top line represents the contribution due to viscous friction, and is dependent on the velocity of the piston, the second line is the nonlinear Stribeck contribution added to the constant Coulomb friction and the last line the function to correct the sign of the friction force. The input to the system is the piston velocity ($\dot{x}$) in $m.s^{-1}$ and the output is the friction force (F_{fric}) in N.

4.1.4 Pneumatic Connections

The reservoirs, the valve units and the actuators are connected via Festo PUN-10x1.5-BL Polyurethane tubing with smooth inner walls. The lengths of the interconnects are typically less than 300 mm, both from the reservoirs to the valve and from the valve to the actuator. Using the model derived by Richer [26], the time delay of a mass of air exiting the tube of 300 mm after entering it under control of a valve, is approximately 870 μs, which can be deemed insignificant in a system using a proportional directional control valve with a critical frequency of 65 Hz (-3dB frequency at the maximum stroke of the valve piston spool). Also, since the reservoirs absorb most of the pressure ripple generated

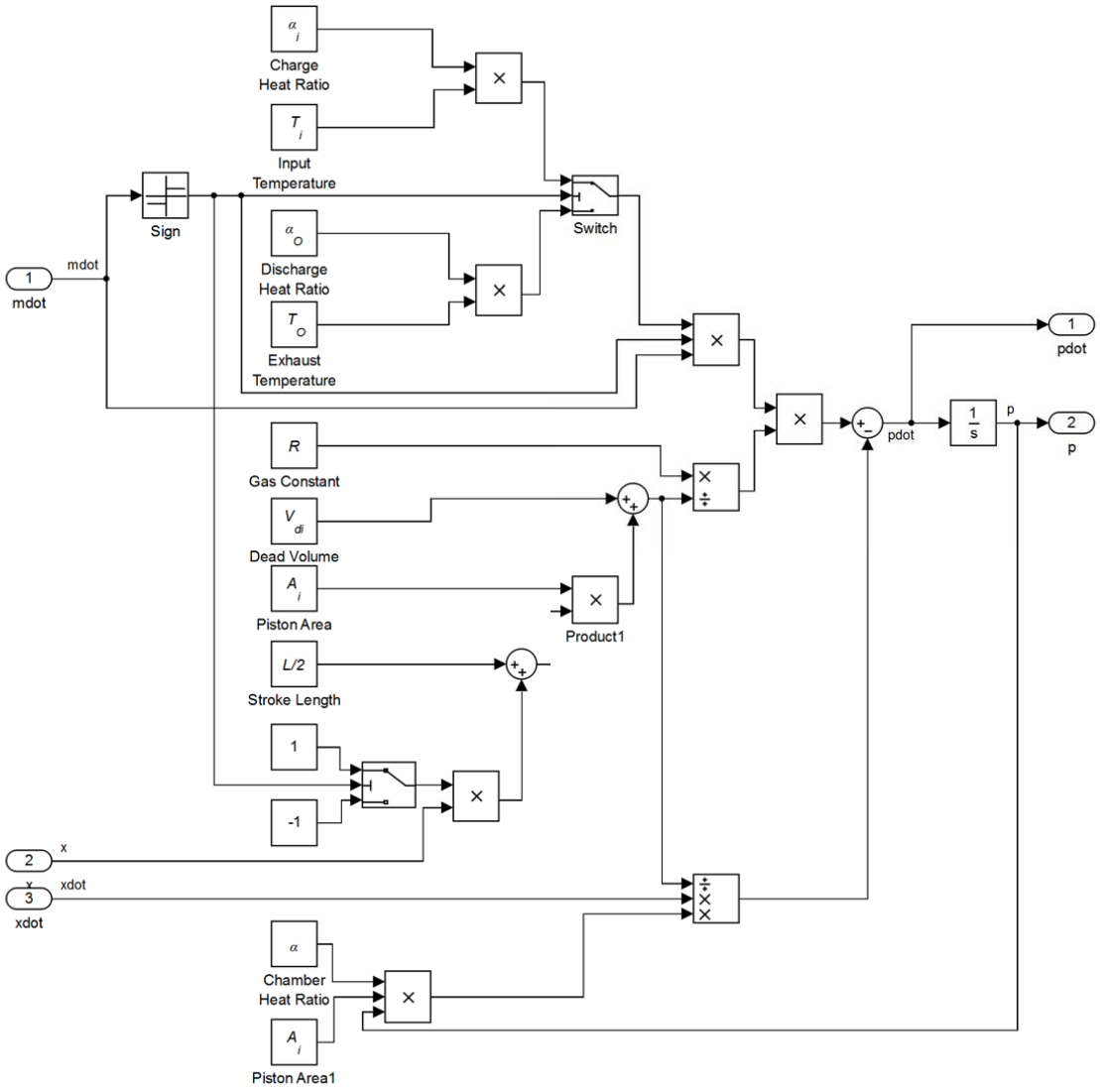

Figure 4.12: The Matlab® Simulink® Model of the Chambers of the Actuator

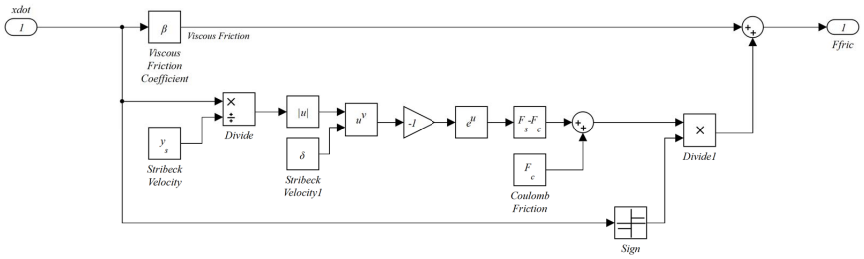

Figure 4.13: The Simplified Matlab® Simulink® Model of the Friction in the Actuator

through the supply tubing and the mass flow rate reduction is only 0.0002%, the tube effects will be ignored.

4.1.5 Pneumatic Reservoir

During an extension or contraction of the actuator, air is being channeled to either of the two actuator chambers. The volume of air used in one full extension-contraction cycle of the actuator equals the maximum combined volume of the two chambers. This air has to be supplied from the pneumatic source, in our case a portable or a permanently installed compressor. Due to the connection from the compressor to the SMS being a tube with a finite inner diameter and due to the friction between the air and the inner pipe surface, a pressure loss and a mass flow rate reduction during dynamic operation is present. This results in fluctuations in the supply pressure to the system.

Analogous to the smoothing effect of a capacitor on the supply voltage of a power supply with a finite resistance, a pneumatic reservoir can smooth out the pressure fluctuations on the supply lines close to the valves and actuators. It is for this reason that a 5ℓ Festo reservoir was added to each of the simulator legs. For the purpose of this document, the reservoirs are not modelled in detail, but the supply pressure is assumed to be smoothed and constant.

CHAPTER 5

MASS FLOW CHARACTERISATION

The control of a pneumatic system is largely dependent on the friction characteristics and the mass flow characteristics of the system. The latter is the subject of this section. A theoretical model was derived from first principles in §4.1 resulting in a model that uses the assumptions of an ideal gas and adiabatic process. The supply pressure is also assumed to be constant.

The mass flow through the valve into and out of the actuator chambers gives rise to the change in pressure and hence the exerted force on the load. It is, therefore, necessary to characterise the mass flow through the controlling unit (*i.e.* the valve and tubes) and to populate the unknown variables in the theoretical model.

The test setup with two reservoirs was used, assuming that a reservoir of a constant volume will have the same temporal pressure response as a chamber of the actuator with the output rod held captive.

5.1 THEORETICAL MODELS

5.1.1 Classic Mass Flow Model

The normal pneumatic system layout using proportional control valves is described graphically in Figure 4.1. The valve and the actuator chambers are connected through lossless tubing. The derivation of the mass flow has been done from first principles in § 4.1.2.2.3 and §4.1.3.2.1. In this derivation we assume that the air supply is at ambient temperature, no change in the supply temperature occurs, and that the process is isentropic.

From this derivation and from various sources in literature (Beater [10], Van der Merwe *et al.* [19] and Šitum [44]) the general form of mass flow through an orifice with a known effective area (A_v), a discharge coefficient of C_d and ideal air flow can be expressed as

$$\dot{m}_v = \begin{cases} C_1 C_d A_v \frac{p_1}{\sqrt{T}} & \frac{p_2}{p_1} \leq p_{cr} \quad (Choked\,flow) \\ C_2 C_d A_v \frac{p_1}{\sqrt{T}} \left(\frac{p_2}{p_1}\right)^{\frac{1}{\kappa}} \sqrt{\left[1 - \left(\frac{p_2}{p_1}\right)^{(\kappa-1)/\kappa}\right]} & \frac{p_2}{p_1} > p_{cr} \quad (Subsonic\,flow), \end{cases} \tag{5.1}$$

with

$$C_1 = \sqrt{\frac{\kappa}{R}\left(\frac{2}{\kappa+1}\right)^{\frac{\kappa+1}{\kappa-1}}}, \tag{5.2}$$

and

$$C_2 = \sqrt{\frac{2}{R}\left(\frac{\kappa}{\kappa-1}\right)}. \tag{5.3}$$

where p_1 is the supply pressure, T is the supply air temperature and κ is the ratio of specific heat capacities of the gas moving through the orifice. p_{cr} is the critical pressure ratio where flow changes from choked to subsonic. This theoretical model assumes no contraction, friction or heat transfer, which will be later shown to influence the shape of the flow function. From equation 4.32, the pressure change in the actuator chambers $\dot{p}_k$ can be expressed as

$$\dot{p}_k = \frac{R}{V_{dk} + A_k\left(\frac{L}{2} \pm x\right)}\left(\alpha_i \dot{m}_i T_i - \alpha_o \dot{m}_o T_o\right) - \frac{\alpha p A_k}{V_{dk} + A_k\left(\frac{L}{2} \pm x\right)}\dot{x}. \tag{5.4}$$

V_{dk} is the dead (or inactive) volume of each chamber, A_k is the piston area, L is the maximum stroke length and x is the piston displacement relative to the centre of the stroke, $\dot{x}$ the rate of displacement, α_i, α_o and α are the heat capacity ratios related to the input mass flow, the output mass flow and the chamber gas, $\dot{m}_i$ and T_i are the mass flow rate and temperature of the gas entering the chamber and $\dot{m}_o$ and T_o are the mass flow rate and temperature of the gas exiting the chamber respectively.

By arguing that the the captive actuator has a constant chamber volume, the actuator can be replaced by a pressure vessel with a constant volume such as an air reservoir. The equation for pressure change in the actuator (eq. 5.4) can be simplified by noting that that the actuator extension rate ($\dot{x}$) is zero and the second term can be ignored. It can also be assumed that the outlet mass flow is insignificant in the case of charging as the upstream pressure is much higher than the chamber pressure. In the discharging case the inlet mass flow approaches zero and the first term can be ignored. The pressure

change in the pressure vessel can then be expressed as

$$\dot{p}_c = \begin{cases} \frac{\alpha_i R T_i \dot{m}_i}{V_c} & for\, charging \\ \frac{-\alpha_o R T_o \dot{m}_o}{V_c} & for\, discharging. \end{cases} \tag{5.5}$$

with α_i and α_o the inlet and outlet heat capacity ratios, R the gas constant, T_i and T_o the inlet and outlet air temperatures, $\dot{m}_i$ and $\dot{m}_o$ the inlet and outlet mass flow rates and V_c the volume of the test chamber.

By combining eq. 5.5 and eq. 5.1 and assuming that the air temperature equals the ambient air temperature, the change in chamber pressure for the charging cycle can be expressed as

$$\dot{p}_c = \begin{cases} C_d A_v C_1 \frac{\alpha_i R \sqrt{T}}{V_c} p_1 & \frac{p_2}{p_1} \leq p_{cr} \\ C_d A_v C_2 \frac{\alpha_i R \sqrt{T} p_1}{V_c} \left(\frac{p_2}{p_1}\right)^{1/\kappa} \sqrt{1 - \left(\frac{p_2}{p_1}\right)^{(\kappa-1)/\kappa}} & \frac{p_2}{p_1} > p_{cr}. \end{cases} \tag{5.6}$$

As proposed by, amongst others, Richer [11] and van der Merwe *et al.* [19] the value for α_i for the charging cycle in an isentropic system is assumed close to the isentropic expansion index $\kappa = 1.4$ for air. For the discharging cycle, α_o is assumed close to one indicating an isothermal process.

The mass flow rate at large pressure differentials is essentially independent of the actual differential, and can therefore be used to calculate the discharge coefficient with reasonable accuracy. By focussing only on the choked flow region, the first term of eq. 5.6 can be rewritten as

$$C_d = \frac{\dot{p}_c V_c}{p_1 \alpha_i A_v C_1 R \sqrt{T},} \tag{5.7}$$

which expresses the discharge coefficient for the specific valve opening. This coefficient is for now assumed to be constant for all pressure differentials.

5.1.2 ISO Mass Flow Model

The simplification of the pneumatic system for valve mass flow model identification (sec 5.1.1) assumes that the orifices are ideal, no contraction is present and that only a single orifice is used. Although a discharge coefficient (C_d) is used, this only adds a linear gain to the system, and does not change the shape of the flow function. In reality, this assumption does not hold as the valve has losses due to friction, turbulent flow, heat transfer and contraction.

A model similar to the previously proposed classic model was devised after observations made by Sanville [15] and by Sanville's generalisation of the work done by Purdue *et al.* [14]. This model later formed the basis for the standard ISO-6358:1989(E) and ISO-6358:2013(E) [12] (quoted from [10]). The ISO valve mass flow model is represented by

$$\dot{m} = \begin{cases} p_1 C \rho_0 \sqrt{\frac{T_0}{T_1}} & \frac{p_2}{p_1} \leq b \\ p_1 C \rho_0 \sqrt{\frac{T_0}{T_1}} \sqrt{1 - \left(\frac{\frac{p_2}{p_1} - b}{1-b} \right)^m} & 0.999 > \frac{p_2}{p_1} > b \\ k_1 p_1 \left(1 - \frac{p_2}{p_1} \right) \sqrt{\frac{T_0}{T_1}} & \frac{p_2}{p_1} \geq 0.999 \quad . \end{cases} \tag{5.8}$$

where

$$k_1 = 1000 C \rho_0 \sqrt{1 - \left(\frac{0.999 - b}{1-b} \right)^m} \tag{5.9}$$

is the linear gain for the laminar flow part of the equation. The laminar flow part (third term of eq. 5.8) is only added for the sake of completeness and is not used in the rest of this study. In this model the discharge coefficient C_d, the valve effective area A_v and a heat capacity ratio dependent function C_1 are lumped together into one coefficient called the sonic conductance (C). The critical pressure (where the flow changes over from subsonic to choked flow) is still defined as a ratio between the upstream and downstream pressures, expressed as b, but is no longer fixed to the value of $b = 0.528$ due to the heat transfer during the process. A third variable (m) called the subsonic index is an exponential index for expressing the characteristic function of the mass flow rate in the subsonic flow region of the flow rate or conductance curve (quoted from [13]). This index changes the shape of the flow function to compensate for concatenated orifices, frictional losses and heat transfer. This variable should not be confused with the air mass which has the same symbol.

If we assume that the mass flow function of the classic model in the choked flow region is the same as that of the ISO model, the sonic conductance can be expressed as

$$C = \frac{A_v C_d}{\rho_0} \sqrt{\frac{\kappa}{R T_0} \left(\frac{2}{\kappa + 1} \right)^{\frac{\kappa+1}{\kappa-1}}} . \tag{5.10}$$

This equation is still dependent on both the discharge coefficient C_d and the heat capacity ratio κ and can only be accurately calculated with the assumption of an isothermal process, using an isothermal chamber ([21], [20]) and no leakage. A possible drawback using this relationship is the difference between the actual geometric valve area (A_v) and the effective valve area (A_{ve}), which is a virtual number derived to account for all leakage and geometric effects. A good approximation is believed

to be reachable with a polytropic assumption as described earlier, using α values between 1 and 1.4. The critical pressure ratio b can only be determined experimentally, and can easily vary up to 50% with little influence on the temporal pressure curves or the mass flow function shape. The subsonic index m is also to be determined experimentally and is determined by the specific test setup.

5.2 VALVE FLOW MEASUREMENTS

In both the theoretical models above, it is difficult to determine the coefficient to populate the models. It is therefore proposed to capture the pressure response of a charging and discharging process and iteratively optimise the values of C_d, C, m and b until the theoretical model temporal pressure response matches the measured temporal pressure response.

5.2.1 Pneumatic Measurement setup

An experimental setup was constructed that used a proportional control valve (Festo MPYE-5-3/8-010-B) as the air switching unit. The outlet ports of the valve were fitted with silencers featuring variable restrictions (Festo GRE-3/8-B), all of which were opened completely. An input reservoir (FESTO CRVZS-5) was used as an on-demand source of air to minimise the effect of pressure drops over the supply line from the compressed air supply point. The reservoir was fed from an air supply port, the pressure was regulated by means of a Festo LFR-3/8-D-0-MIDI filter/regulator and a Festo LOE-3/8-D-MIDI lubricator (no lubrication was used in this experiment). Both the actuator chambers were replaced with similar air tanks, all of which had a fixed volume. None of the chambers were isothermal chambers. In all the chambers, both the pressure and the air temperature was measured using analog pressure sensors (Festo SPTW-P10R-G14-VD-M12) and type K thermocouples. The thermocouple signals were amplified using Analog Devices instrumentation amplifiers and the cold junction temperature measured with a glass/mercury thermometer and logged. All the measured signals were captured with a Data Translation DT9803 USB Analog to Digital Converter (ADC) sampling at 100Hz. The valve was switched from a fully closed condition to a preset open position by varying the input pulse amplitude and offset. In this way the one tank will be at an initial pressure equalling ambient pressure while the other tank will be at an initial pressure equalling the supply pressure. The spool displacement was measured using a calibrated Heidenhain probe to log the steady state position. The spool transient response was ignored. An illustration of the test setup is shown in Figure 5.1 and a photograph of the setup is shown in Figure 5.2. Not visible in this picture is the air

service unit and the signal capture unit (ADC and the Personal Computer (PC)).

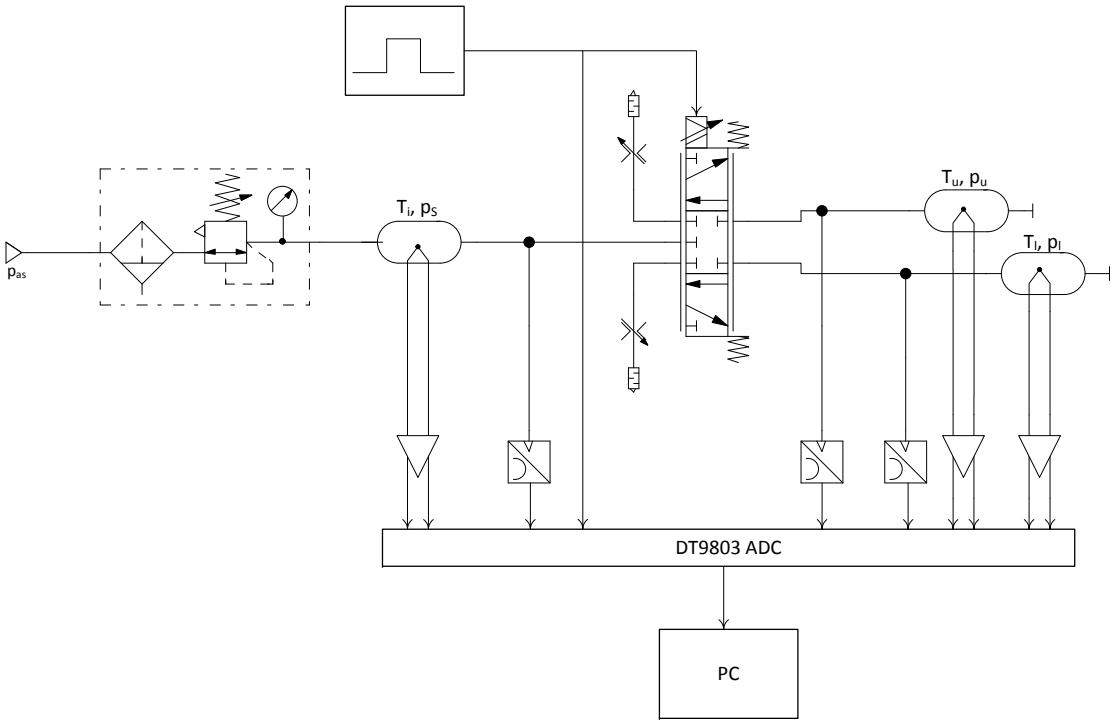

Figure 5.1: Graphical Diagram Of The Valve Flow Characterisation Test Setup

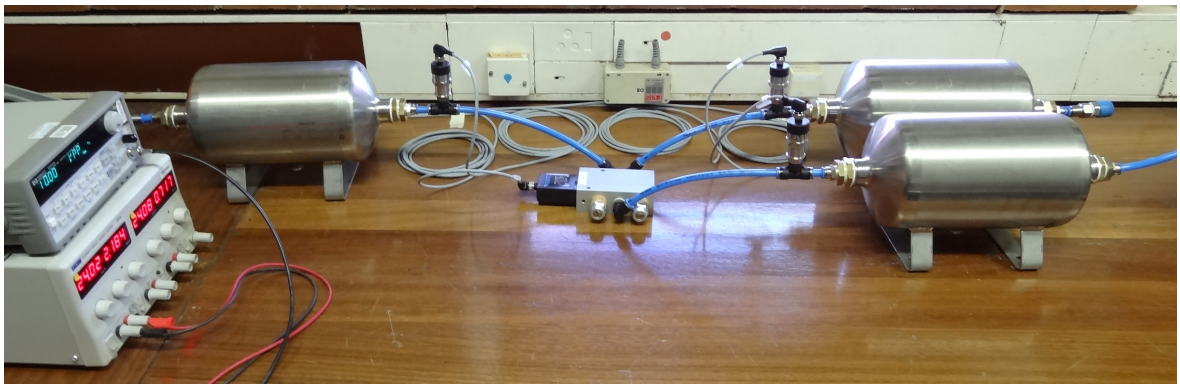

Figure 5.2: Photograph Of The Valve Flow Characterisation Test Setup

5.2.2 Temperature Measurement

Important variables in all pneumatic processes are the air temperature and the change in air temperature. The assumptions of an isothermal process made earlier depend largely on the temperature profile

during the charging and discharging cycles. Should the air temperature stay constant, the processes can be classified as isothermal and the derivations done are all valid. Reality, however, dictates different, and the air temperature does vary to different extents. The air temperature is therefore added to the set of measurement variables and was measured by adding thermocouples to the air reservoirs. The drainage plugs underneath the reservoirs were modified to accept the 1.5mm diameter sheathed type K thermocouples, which were epoxied into the plugs to facilitate an air tight seal. The tips of the thermocouples were placed as close as possible to the centres of the reservoirs. The time constants of the thermocouples were unknown but assumed to be in the order of seconds. A literature search revealed time constant values between 0.4s and 6s for insulated sheathes of 1.5mm diameter depending on the flow and gas conditions. No measurements were taken to determine the time constants due to time constraints. The data gathered by the temperature sensors were therefore used as a global indication of the temperature trends rather than an absolute data set to be used in the calculations. Once the thermocouples are characterised, the measured values can be trusted and used in the analysis.

The thermocouples were connected to Analog Devices instrumentation amplifier circuits (INA110) and set up with a linear gain of 500. The amplifiers were routed differentially to the ADC to minimise the common mode electronic noise. Offsets were assumed to be negligible and the linearity of the amplifiers to be perfect. The cold junction temperature was measured during each experiment and added to the calculated result of the sensors.

According to the National Institute of Standards and Technology (NIST)[55] the temperature of a type K thermocouple relative to the cold junction temperature can be expressed as

$$T_K = \sum_{i=0}^{9} c_i E^i, \tag{5.11}$$

where T_K is the thermocouple temperature in $^\circ C$, c_i are the coefficients for the temperature subrange 0-1372 $^\circ C$ and E is the thermocouple EMF in mV. It should be noted that the measured voltage is the generated thermocouple EMF multiplied by 500 due to the amplifiers. The coefficients are tabulated in Appendix C, Table C.1.

Taking into account that the thermocouple cold junction is at room temperature, the air temperature as measured by the thermocouple is given by

$$T = T_K + T_{CJ}, \tag{5.12}$$

with T_{CJ} the cold junction temperature in $^\circ C$.

5.2.3 Test Matrix

Following the reasoning above, a test matrix was set up to measure the pressure and temperature changes in both the supply line as well as the reservoirs. This was initially done at various valve openings using the previously determined spool deflection vs. input voltage relationship. The fact that the resting position (0V input) of the spool did not coincide with the pneumatic centre point of the spool valve and that the sealing of the spool valve was not perfect (hence leakage) resulted in a change of procedure to use the actual spool deflection as the independent variable. The Heidenhain probe was placed at the end of the spool to measure the steady-state deflection and repeatability of the position with regards to the input voltage, hence determining beforehand the input voltage needed for a specific valve deflection and valve area. The spool deflection was only measured to the one side of the spool travel, making the assumption that the deflection will still be symmetrical around the centre point as indicated by the deflection vs. voltage test. This assumption placed great importance on the determination of the pneumatic centre point. It was noticed that a spool deflection could be found where both the load tanks could be charged to exactly the same pressure, arguing that the charge rates through the two valve sections were of equal magnitudes and the discharge rates (or leakage) were equal. This indicated a centred spool assuming the spool bore tolerance did not change along the length of the spool. This pneumatic centre point was used further on as the zero position for the spool valve. Tests done on two separate days revealed this position to coincide with a voltage input of 4.92V.

The charging and discharging of the load tanks were done with spool deflections from 0.2mm to 1.8mm. The increments were not equal in size, as more detailed measurement was needed around the valve opening point and less detail at large openings. The tests were also done at two input pressures to investigate the effect of the pressure difference. In an application, the valve model will only be populated with values for that specific supply pressure, assuming that the pressure is kept constant.

The method used for all the test was kept the same as not to introduce any unknown artifacts due to a procedural change. The supply pressure was set to the relevant level using the pressure regulator and monitoring the ADC values in real time. Once a steady supply pressure was attained, the temperature probes signals were corrected by adding an offset to the ADC values to compensate for the temperature drift in the instrumentation amplifiers. The cold junction temperature and the ambient air pressure were measured and logged.

The Heidenhain displacement probe was initialised and the pneumatic centre of the spool was found. This was done by finding the input voltage on the valve spool where the steady-state pressure condition in the two downstream tanks were equal. This accounted for equal spool area and equal leakage in and out of the tanks. This position and voltage was then used as the zero point of deflection and input. The Heidenhain probe was then zeroed.

The input signal for the valve was generated with an Agilent Signal generator in triggered one shot mode. Only one excitation pulse of adequate duration was generated for each measurement with a significant time delay between measurements. This was done to minimise the heating of the tank walls, as the assumption of an adiabatic process did not hold. The setup was given time to return to the ambient state, so that all measurements were comparable. The duration of the pulses were long enough to ensure a steady-state condition at the end of it.

For the charging process the initial state of the valve was set to be in a fully open position, venting the pressure container to ambient conditions. For the discharging process the tank was charged up to the supply pressure. During the process itself the valve was opened to the preset deflection value, and the actual deflection checked against the expected value, using the Heidenhain probe.

5.3 VALVE CHARACTERISTICS - PROCESSING

5.3.1 Signal Processing

Using the test setup described in § 5.2.1, a series of charge and discharge cycles were recorded with the ADC. The signals were stored in the Data Translation proprietary format, exported to Microsoft Excel format and then converted to Matlab® data files through the import function in Matlab® . The charge profiles for a supply pressure of 0.4 *MPa* are shown in Figure 5.3 a) and the discharge cycle pressure profiles in Figure 5.3 b). The pressure profiles for a 0.2 *MPa* supply pressure are shown in Figure 5.4 a) for the charging case and b) for the discharge. In both the 0.2 *MPa* and 0.4 *MPa* discharge experiment, the saturation pressure for the pressure sensors can be seen as being around 100 *mbar*, which is the reason that the graphs do not approach 0 *MPa* in the steady state. This saturation effect (lower measurable limit) makes it difficult to fit accurate curves to the measured data, and influences the calculation of the entity m and b in equations 5.8 and 5.9.

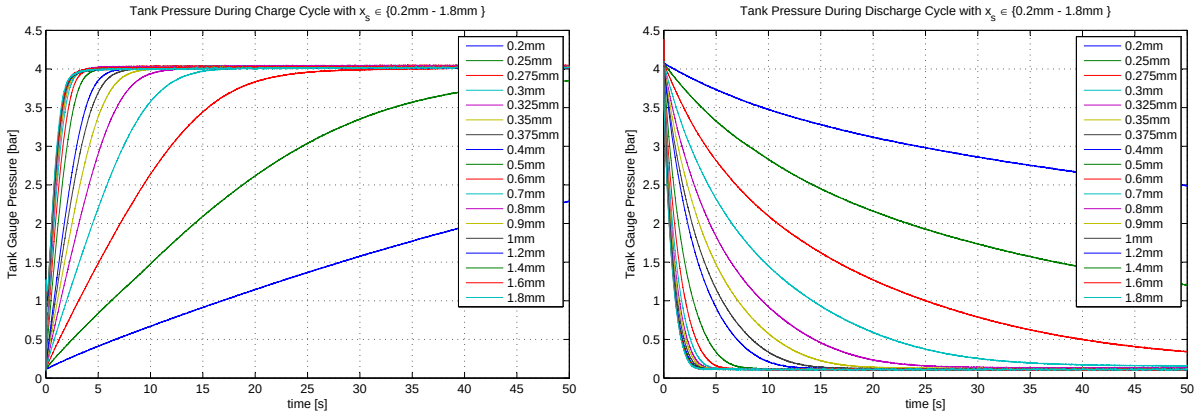

a) b)

Figure 5.3: a) Charge Pressure Profiles for a 0.4 *MPa* Supply Pressure and b) the Discharge Pressure Profiles for a 0.4 *MPa* Supply Pressure

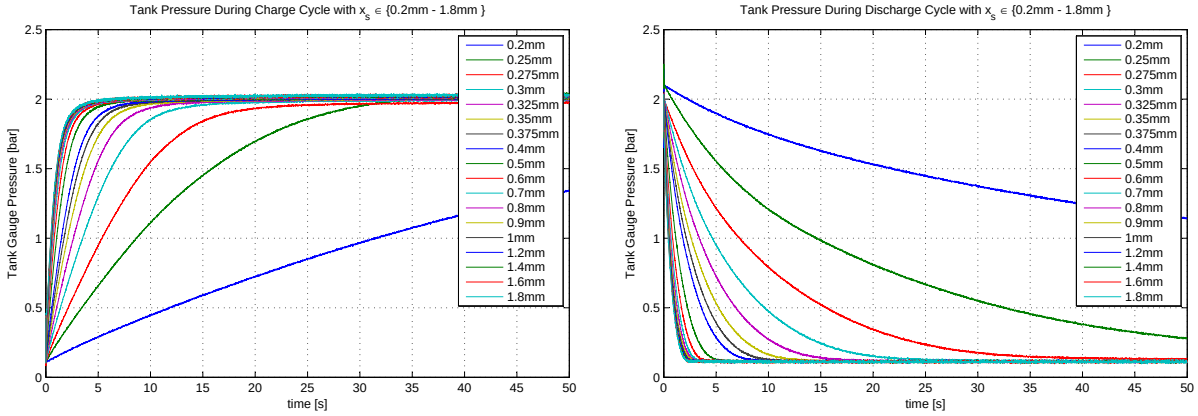

a) b)

Figure 5.4: a) Charge Pressure Profiles for a 0.2 *MPa* Supply Pressure and b) the Discharge Pressure Profiles for a 0.2 *MPa* Supply Pressure

The pressure data captured in raw format is noisy and there are various methods to smooth them out. These include using multiple sample sets and taking the average of the sets, or smoothing the data using observers such as the α-β filter. The latter method was used on all the data captured, as it cut down on the experimental time, at a cost to the data analysis time. The α-β filter assumes an adequately approximated system with two states, the one being the integral of the other. Typical

examples are displacement (x) and speed ($\dot{x}$) in a linear motion system, or in our case, pressure (p) and pressure rate ($\dot{p}$). Both the latter entities are valuable in the later calculation of the flow constants.

In order to determine the applicability of an observer as a filter, the characteristics of the signals had to be known. It was deemed important to determine if the noise contribution had a zero mean, the probability distribution was Gaussian and the noise spectral density approached a constant number (hence white Gaussian noise). The zero mean was a requirement implicitly adhered to by removing all zero frequency biases or trends (discussed later). The analysis was done on all selected experimental runs, and the resulting filtering applied to all the signals. To determine the noise levels on the signals the noise contribution was isolated by using the steady state parts of the captured pressure signals. The case at hand is a 0.4 *MPa* supply pressure case with a spool deflection of 0.5 *mm*. The temporal pressure responses of the supply, the charging tank and the discharging tank is shown in Figure 5.5. After the necessary scaling to convert volts (*bar*) to *Pa*, a section (20 s to 50 s) of the data set was extracted and kurtosis and skewness determined.

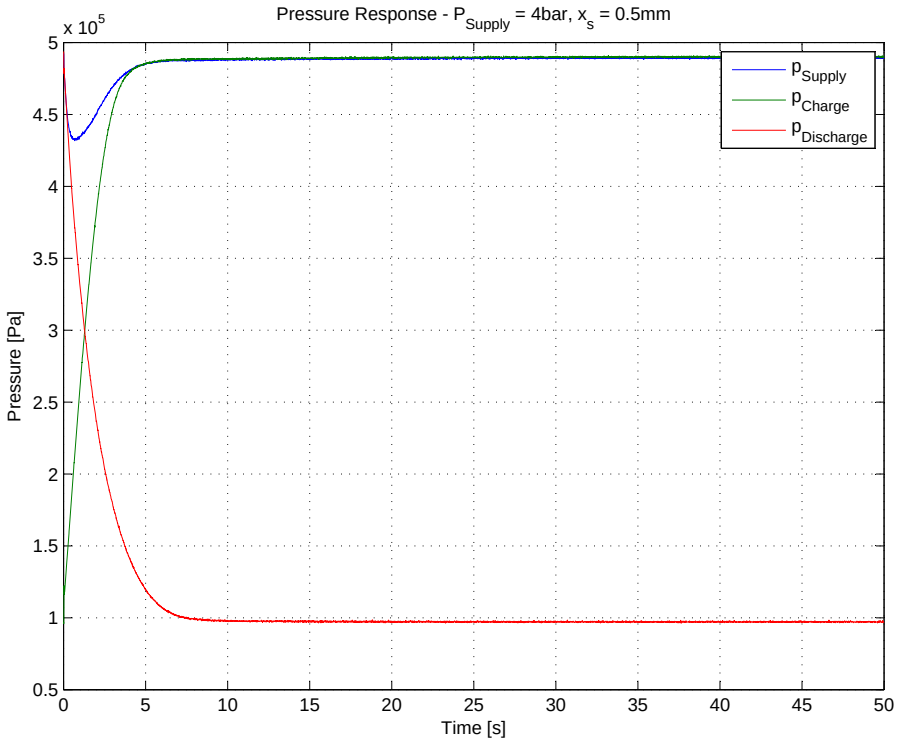

Figure 5.5: Pressure Profiles for a 0.4 *MPa* Supply Pressure

The definition of kurtosis (as described in the "Computational Statistics Handbook with Matlab® " [56]) was used. When normalised to yield a zero value for a normal distribution it can be expressed as

$$\gamma_2 = \frac{\frac{1}{n}\sum_{i=1}^{n}(x_i - \bar{x})^4}{\left(\frac{1}{n}\sum_{i=1}^{n}(x_i - \bar{x})^2\right)^2} - 3, \tag{5.13}$$

where γ_2 is the kurtosis of the data set, n is number of samples in the data set, x_i is the ith value in the set and $\bar{x}$ is the mean value of the data set. It can be seen that a data set without any linear or non-linear trends are important for accurate kurtosis determination. The slightly upwards trend in the charge curve was removed using Matlab® 's "detrend" function. Applying the kurtosis function, values between 0.24 and 1.2 were calculated, suggesting that the distribution is not far from a Gaussian distribution.

A second check was conducted, using a simple histogram analysis, which yielded a similar Gaussian shape. The distribution of the noise on the supply pressure signal is shown in Figure 5.6. Once again, the shape is Gaussian as compared with a scaled Gaussian curve with a σ of 300. Lastly, a

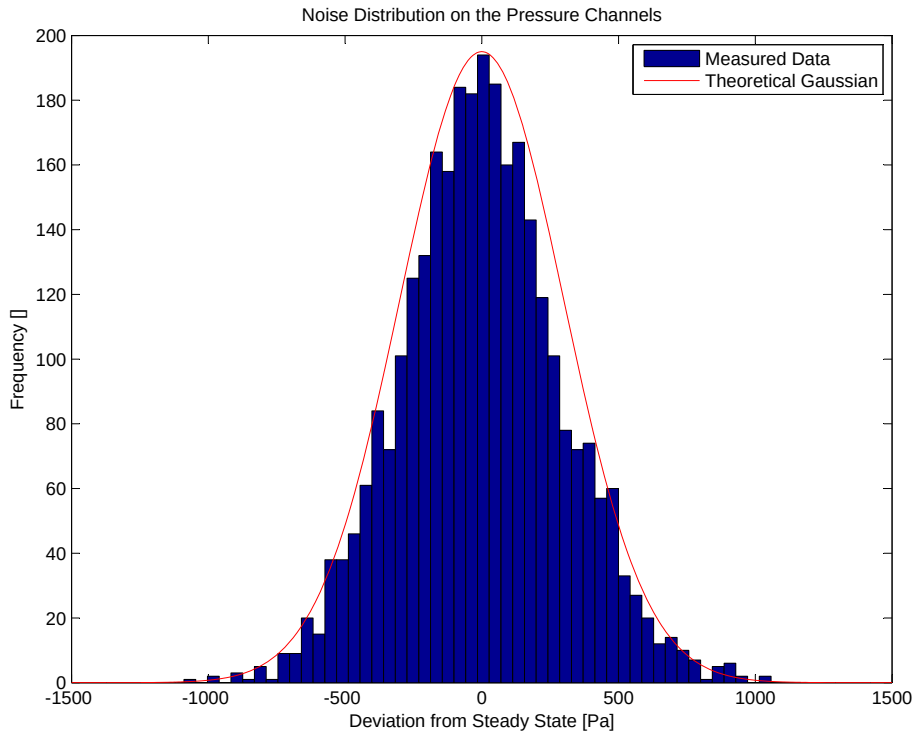

Figure 5.6: Signal Distribution on the Supply Pressure Signal

spectral analysis was conducted on selected sample runs, of which one Power Spectral Density (PSD)

is shown in Figure 5.7. The top graph (blue) labelled "Unfiltered" shows the PSD of the pressure supply signal as captured and scaled to achieve absolute pressure. The signal was analysed without removing any trends or biases and revealed a power noise floor of around 31 $dB.Hz^{-1}$ above 25 Hz. Below 25 Hz there are some features in the signal that defined the temporal response, hence valid data and not noise. The second line (green) indicates the result on the PSD after using the α-β filter, showing a 15 dB reduction in the high frequency noise.

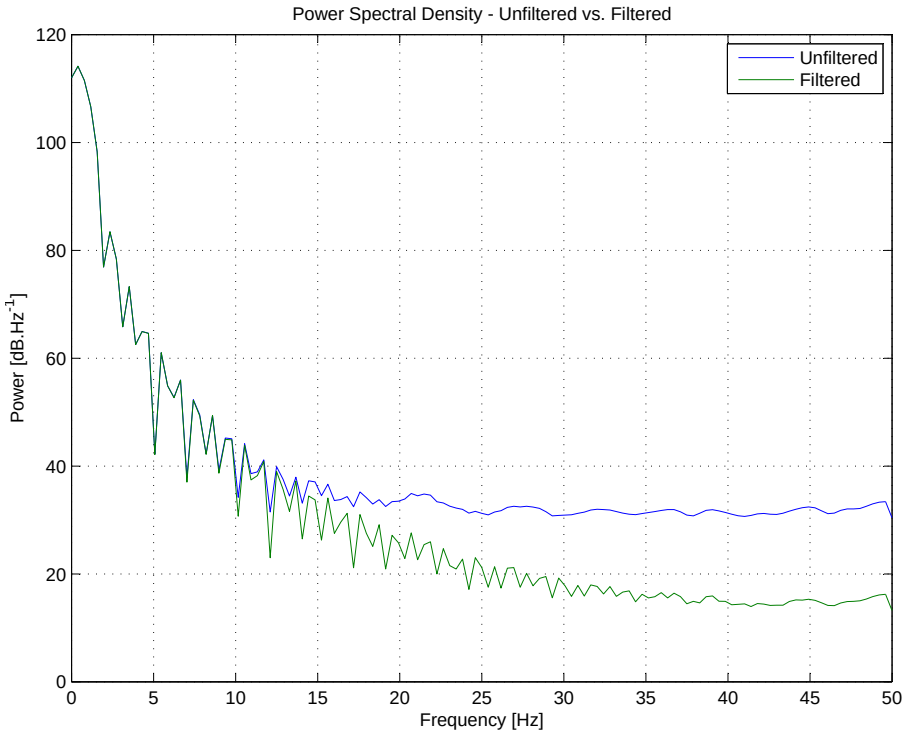

Figure 5.7: Power Spectral Distribution of the Supply Pressure Signal, Raw and Filtered

It can then be safely stated that the noise contribution to the measured pressure signals are Gaussian white noise with a zero mean and a constant spectral nature. The noise could therefore be described by a mean value and a standard deviation value (or variance) which for the case at hand was $\mu = 5 \times 10^{-11}$ Pa and $\sigma = 323.2$ Pa respectively.

The smoothing of the measured data was therefore done using an α-β filter of which the values of α and β was determined iteratively until the RMS noise values were within acceptable margins. These margins were chosen at random, easing the calculation of the flow coefficients. A goal was set to reduce the RMS noise by a factor of two, resulting in a Signal to Noise Ratio (SNR) of larger than

1000. As both the classic and ISO models do not take fast transients into account, the actual measured values displayed features that are not modelled and these were given a low priority. An example of such features is the pressure spike at large pressure ratios and large valve openings. In all the cases the pressure signal was filtered by an α-β filter with $\alpha = 0.25$ and $\beta = 0.02$. The result on the PSD is shown in Figure 5.7 and on the temporal signal in Figure 5.8. From the temporal filtered signal we can calculate the mean to be zero, the standard deviation (σ) to be 187.1 *Pa* and an RMS noise value of 131.4 *Pa*.

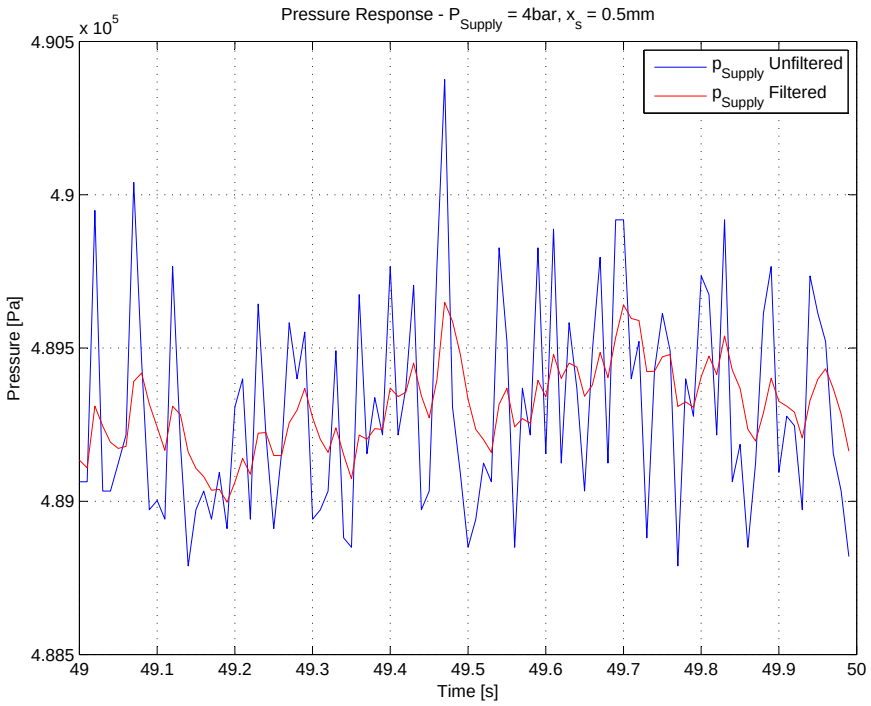

Figure 5.8: Excerpt from the Temporal Pressure Signal of the Supply Pressure, Raw and Filtered

5.3.2 Discharge Coefficient

The discharge coefficient is a critical component of the classic valve model. It essentially determines the gain of the air feed system and influences the dynamic behaviour of the system. There are various schemes published to determine the value and characteristics of the discharge coefficient. Most of these schemes are based on a derivation of the ISO model sonic conductance value ([57] and [21]) and setting the choked flow definition of the classic model and ISO model alike ([19]). According to Van der Merwe *et al.* [19], the manufacturer (Festo) published the discharge coefficient as a constant with a value of 0.575. This number is a characteristic of a specific valve design and is typically

determined by the manufacturer and published as part of a maximum flow rate specification. Also in this publication, the value of C_d was taken to be a constant and the gain varied by changing the valve area to suit the flow rate. This could counter the effects of leakage and effective valve area.

The approach was to use the classic model and the test setup described earlier to determine the value(s) for C_d by doing a series of charge and discharge cycles and then applying the first term of eq. 5.4 by rewriting the expression to isolate the discharge coefficient C_d. The valve area (A_v) was calculated using the geometric layout of the valve as described by Eq. 4.4.

The signals were all smoothed using the α-β filter described earlier, and the pressure and temperature corrected and scaled to absolute pressure and temperature in Pa and K. A by-product of the smoothing process of the chamber pressure data (p_u and p_l) is the rate of pressure change ($\dot{p}_u$ and $\dot{p}_l$). Using the relationship shown in eq. 5.7 the discharge coefficient was calculated with α_i either the inlet or outlet heat ratios, 1.4 and 1 respectively. It should be noted that for the charging case the supply pressure was used for p_1 and the chamber pressure change for $\dot{p}_c$. For the discharging case, the chamber pressure was used for p_1 and the direction of air flow necessitated a negative sign.

An example of the calculated discharge coefficient and the chamber pressure for the charging cycle with a supply pressure of 0.4 MPa and a spool deflection of 0.55 mm is shown in Figure 5.9 and for the discharging cycle in Figure 5.10.

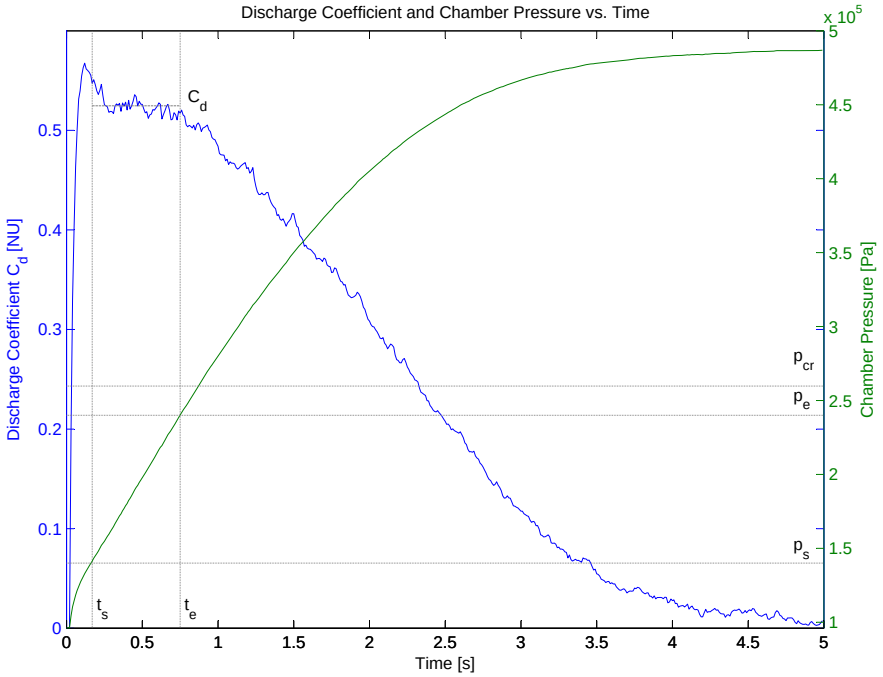

Figure 5.9: Discharge Coefficient and Chamber Pressure Time Response of the Charging Cycle Showing the Choked Flow Region

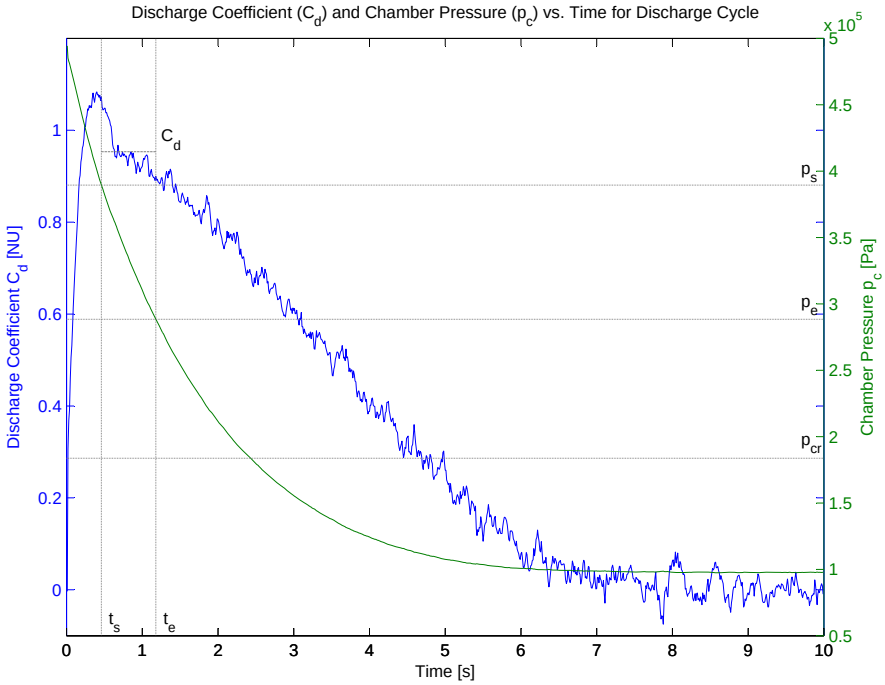

Figure 5.10: Discharge Coefficient and Chamber Pressure Time Response of the Discharging Cycle Showing the Choked Flow Region

A section of the pressure response was selected where we are sure that the flow is choked, *i.e.* where the ratio of the upstream and downstream pressure is larger than 0.528, and where there are no pressure transients such as in the first few tenths of milliseconds ($p_A + 50\ kPa \leq p_c \leq p_A + 150\ kPa$). For the discharging (Figure 5.10), less transient effects were observed and the levels were chosen to be $p_s - 100\ kPa \leq p_c \leq p_s + 200\ kPa$. These are indicated by two limits, t_s and t_e, with corresponding pressures p_s and p_e. It can be be noted that the calculated discharge coefficient is fairly constant over this area and the mean value is taken as a representative value. This approach for selection of choked flow region is also supported by Wang *et al.* [20] and Kawashima [21], although they used the ISO model and isothermal chambers. For this specific sample set the discharge coefficient for charging was calculated to be 0.5247 (Figure 5.9) and for discharging 0.9534 (Figure 5.10).

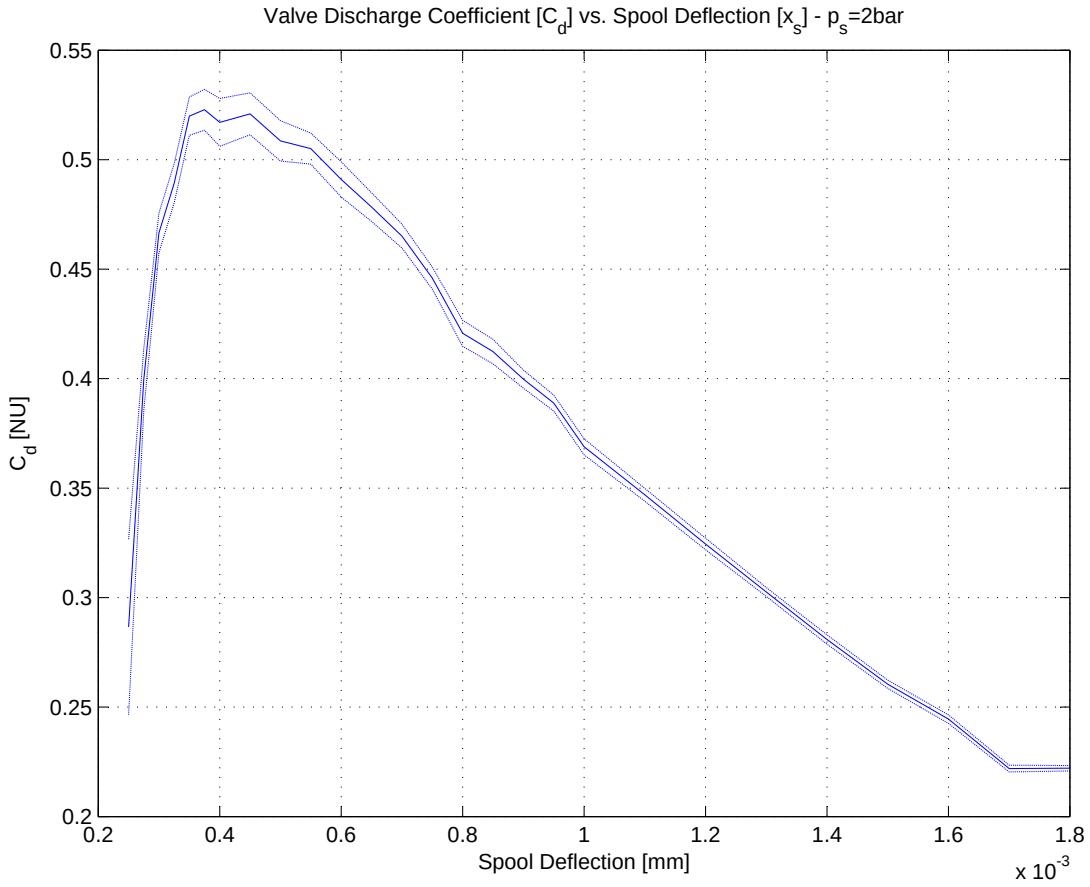

Figure 5.11: Discharge Coefficient Range at $p_s = 0.2\ MPa$

The discharge coefficient can, unfortunately, not be calculated as a single number, as the range of pressure selected for the choked flow region (p_s and p_e above) is a subjective matter. The addition of noise on the measured signal and the choice of the smoothing filter coefficients also contribute

to an unknown variation. The discharge coefficient can then be expressed as a range of possible values, between a minimum and maximum, using the standard deviation (σ) as the limits (Figure 5.11).

To verify that that the varying nature of the discharge coefficient is not a single error in the experiment, the values for both the charge and discharge as well as those for other supply pressure were added on one graph (Figure 5.12).

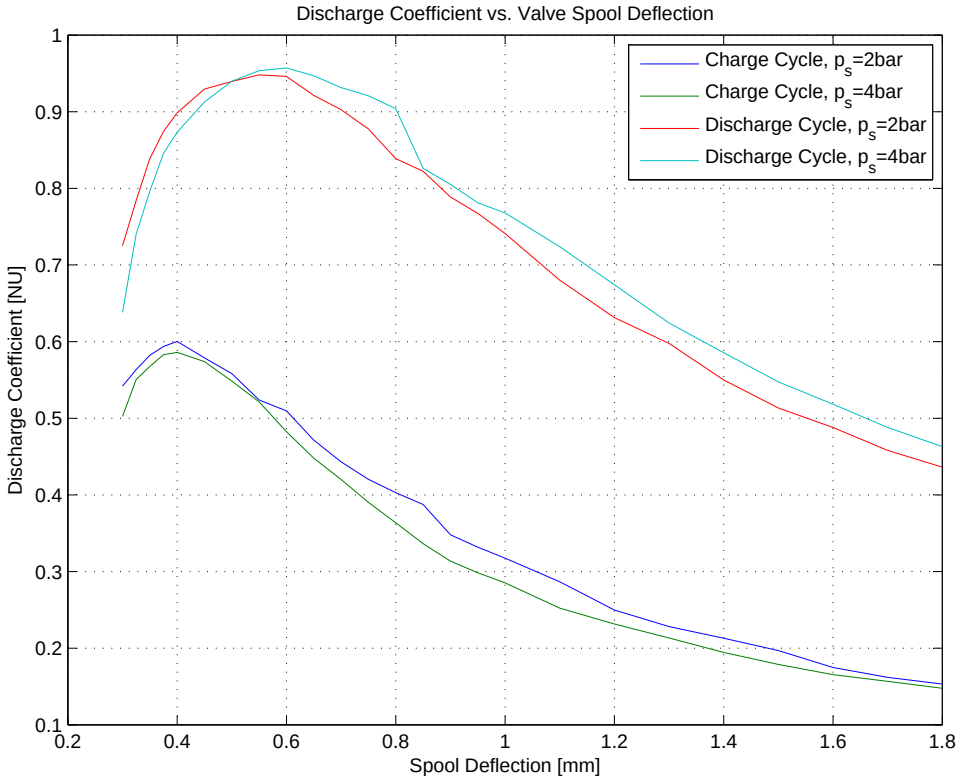

Figure 5.12: Discharge Coefficient for Charge and Discharge Cycles using the Classic Model

From this graph the decreasing trend is evident in all the experiments. As we are mostly focussed on the smaller valve openings, the downward trend of all plots is not a large concern at present. It can also be stated that the C_d values using different supply pressures are not vastly different. They also correspond fairly well in the $0.3mm$ to $0.6mm$ charge region to the advertised C_d value of 0.575 as published by Van der Merwe *et al.* [19], a value specified by Festo.

The large difference between the charge cycle coefficients and the discharge cycle coefficient can at this stage be attributed to the assumption of an isothermal process. The α_o value of 1.0 *vs.* the α_i of

1.4 has a significant effect on the outcome of the calculation. The assumption of an isothermal process assumed that energy had to leave the system. If we revisit that assumption for the determination of the discharge coefficient and we note that the processes at play during the first parts of the test runs (for which the data is used in the above calculation) are short lived, the adiabatic assumption is justified. It can also be observed from the variations in the temperature data that the isothermal behaviour is contradicted. Using an α_o value of 1.4, equal to κ and the inlet heat ratio (α_i), the discharge coefficient values for the discharge cycle can be plotted against the charge cycle values (Figure 5.13), resulting in a much better correlation in the absolute sizes. The discharge coefficient for the discharge cycle (exhaust port), which can only have a value between 0 and 1, is slightly higher than that of the charge cycle (inlet port), a result of the absence of tubing and downstream orifices. The only obstruction in the exhaust line is the (open) variable restriction valve and the silencer.

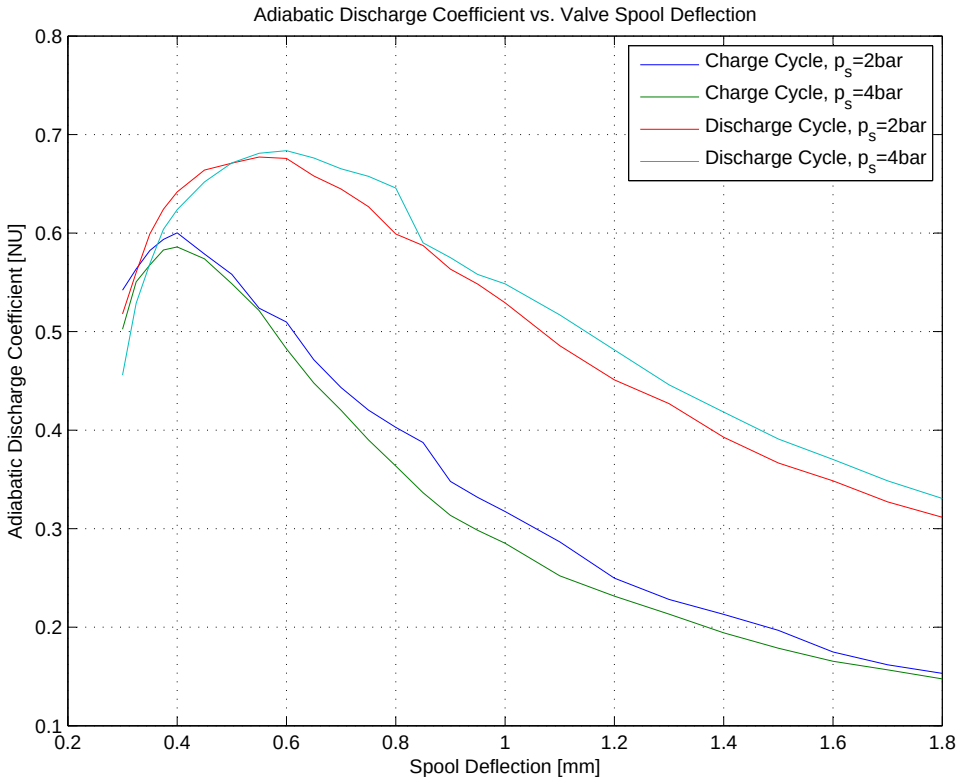

Figure 5.13: Adiabatic Discharge Coefficient for Charge and Discharge Cycles using the Classic Model

5.3.3 Sonic Conductance

Another approach to find the flow coefficients of the valve is to once again use the sampled pressure data and to use the ISO model as described in § 5.1.2, eq. 5.8 together with a parameter estimation algorithm and temporal pressure data from the measurement. Matlab® 's built in version of the Nelder-Mead multidimensional unconstrained nonlinear minimization algorithm was used with b, C and m as the variable parameters. The critical pressure ratio (b) was limited between 0 and 0.528, the sonic conductance (C) between 1×10^{-7} $m^3.Pa^{-1}.s^{-1}$ and 1×10^{-10} $m^3.Pa^{-1}.s^{-1}$ and the sonic index (m) between 0 and 3. The objective function to be minimised was defined as

$$F_o = \sum |p_{est} - p_m|, \tag{5.14}$$

with p_{est} the estimated pressure values and p_m the measured pressure values. This weighted the contribution of the error evenly on all the samples of the test sequence, irrespective of the sign of the error.

For each of the test points the temporal pressure curves for both the charging and discharging cycles were fitted with best fit curves based on the ISO model mass flow. As the mass flow equation is nonlinear in the subsonic flow region, an explicit expression for the pressure-time relationship could not easily be derived. An example of such a relationship can be found in a publication by Kawashima *et al.* [21] which is an effort to approximate the temporal behaviour in the subsonic flow region. It was found that although this might hold for pure isothermal experimentation, the fit on our data was not good.

A numerical method to determine a solution of the differential equation was used to get a theoretical temporal graph of the pressure in the tank. Because the pressure in the tank can be expressed by eq. 5.5 and we can state (also see [19], eq. 7, [21], eq. 1) that

$$\dot{p}_c = \frac{\alpha_i R T_i}{V_c} \dot{m}_i, \tag{5.15}$$

where the subscript i indicates either inlet or exhaust variables . This is in the form $\dot{p}_c = f(p_c, t)$ and the initial value $p_c(t_0) = p_{c0}$ with $\dot{p}_c$ the chamber pressure rate which is a function of the chamber pressure (p_c) and time (t). Using the classical Runge-Kutta (RK4) method with a time step of 10 ms, an initial value of either ambient pressure (charging) or supply pressure (discharging) a temporal solution was generated for a combination of b, C and m parameters. This was then compared with the measured response and the parameters changed to minimise the objective function, hence fitting a curve.

From this process, the sonic conductance values for various valve deflections were obtained, together with the resultant critical pressure ratios and sonic index values. These are shown in Figure 5.14 for sonic conductance (C), Figure 5.15 for critical pressure ratio (b) and Figure 5.16 for sonic index (m).

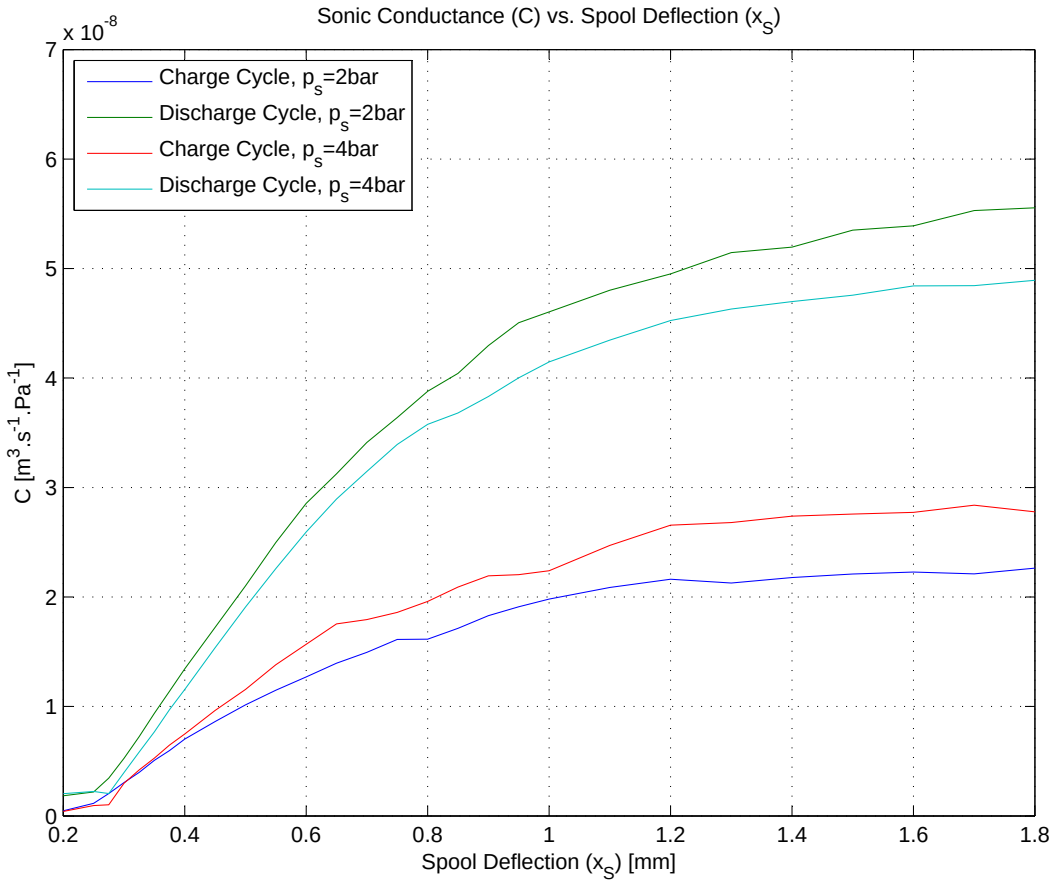

Figure 5.14: Sonic Conductance (C) for Charge and Discharge Cycles at $p_s = 0.2\ MPa$ and $p_s = 0.4\ MPa$ with b Free

The sonic conductance, which is an indication of the lack of resistance the air is subjected to in passing the orifices, has an increase in value as the valve spool is deflected more, due to an increase in the valve area. This is supported by the intuitive feeling that the air has less resistance to escape. The first part of the curve is fairly linear and can be used in a linearisation of the flow for small openings. The curves then flatten off to what seems to be a valve independent static value. At this point in time we can postulate that this is the C value for the open valve and the connecting tubes and orifices, and is related to the maximum flow rate specification of the valve. Another point to note is the significant difference between the charge cycle sonic conductance and that of the discharge cycle, similar to that

derived in § 5.3.2. This can once again be attributed to the use of a unity α_o value which, when changed to 1.4, yields a much closer spacing of the curves as shown in Figure 5.17. This change in value only holds if we make the assumption that the C value is calculated using a part of the temporal data which is still uninfluenced by energy changes, making the process adiabatic.

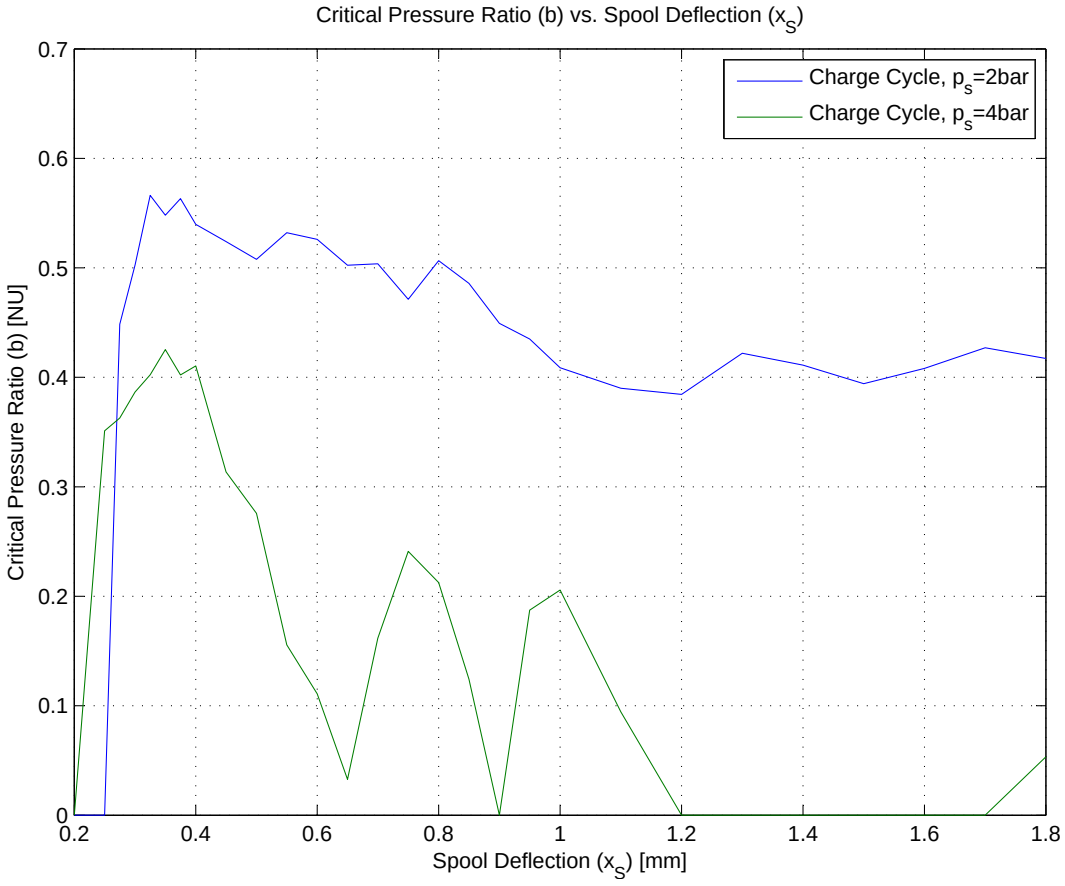

Figure 5.15: Critical Pressure Ratio (b) for Charge and Discharge Cycles at $p_s = 0.2\ MPa$ and $p_s = 0.4\ MPa$

The critical pressure ratio values as calculated by the parameter estimation process are largely inconclusive. For the 0.2 *MPa* charge cycle the values are very close to the expected level of 0.528 or slightly lower. The 0.4 *MPa* charge process delivered a much more erratic behaviour with values ranging from zero to 0.42. Authors like Wang *et al.* [20] assume that b is difficult to determine experimentally and has little effect of the mass flow formulation in the time domain. At the moment we believe that the values of b can be assumed to be close to the theoretical 0.528. All the values derived for the discharge cycles were for all practical purposes zero, and will be used as such further on. The sonic index values are shown in Figure 5.16 and apart from the 0.2 *MPa* charge cycle all fall

close to unity values. All the coefficients derived in this section are used to populate a model that is supposed to mimic a real world system. Irrespective of the actual values, if the temporal response is good enough, the coefficients can be used and the un-modelled effects can be assumed to be included in those values. The fit of the temporal response is outlined in § 5.4.1.

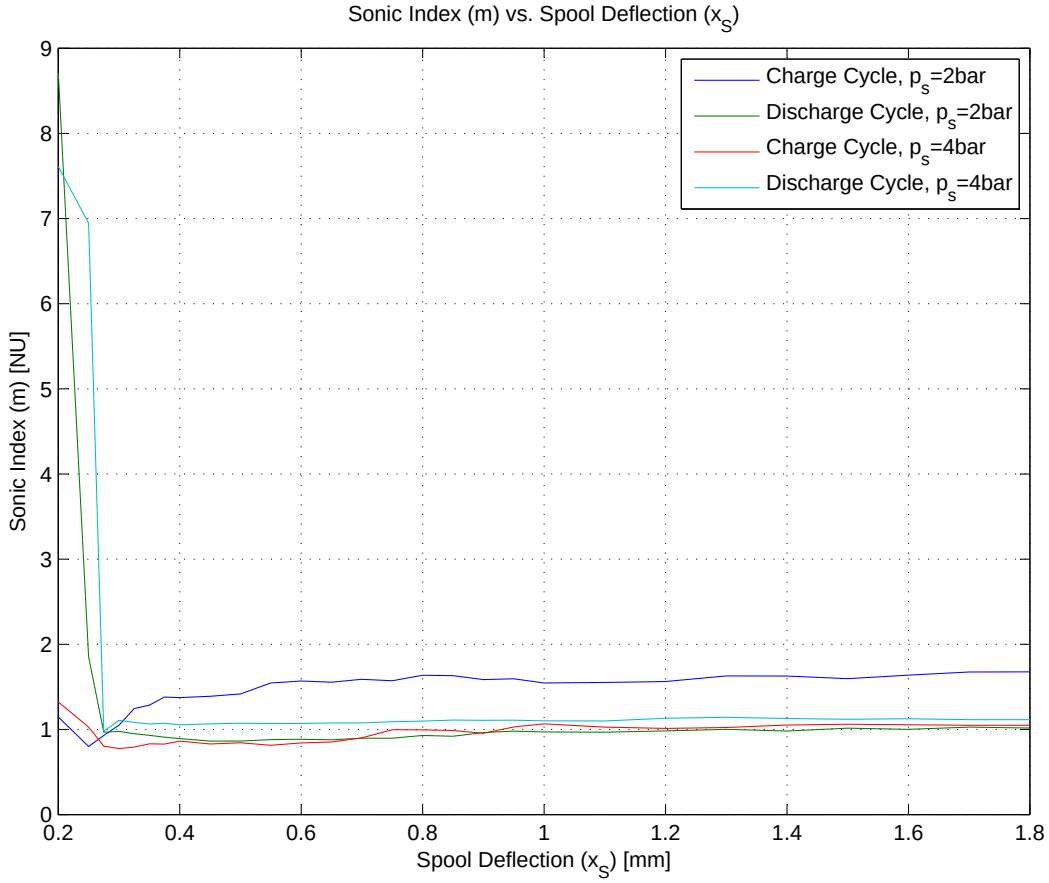

Figure 5.16: Sonic Index (m) for Charge and Discharge Cycles at $p_s = 0.2\ MPa$ and $p_s = 0.4\ MPa$ with b Free

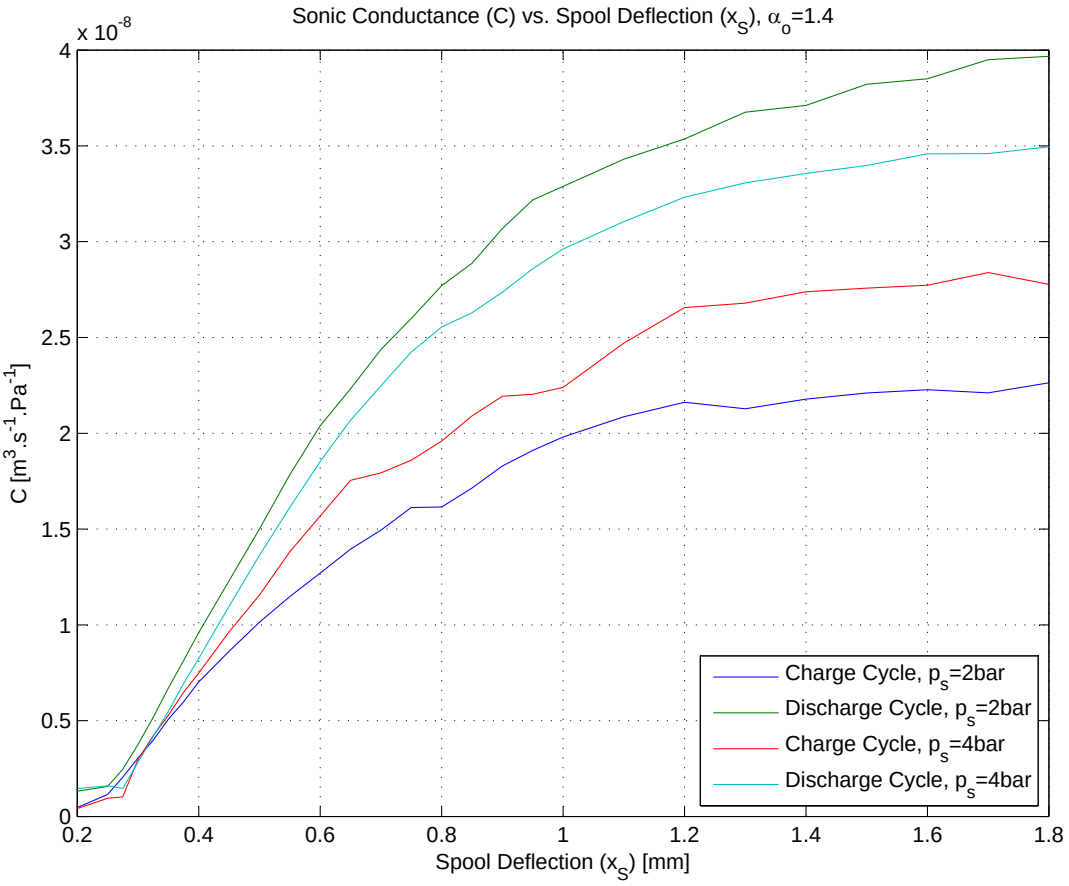

Figure 5.17: Sonic Conductance (C) for Charge and Discharge Cycles at $p_s = 0.2\ MPa$ and $p_s = 0.4\ MPa$ with b Free and an Adiabatic Assumption

As mentioned earlier, the values for the critical pressure are difficult to determine, and should they be assumed to be at a theoretical value of 0.528, the effect on the estimated values of the sonic conductance has to be investigated. This was done by using the same Nelder-Mead minimisation algorithm, but constraining the b values. The result (Figure 5.18) is a decrease in the values of C, and the curves of the two supply pressure experiments moving closer together. The shapes of the curves stayed largely the same, and the decrease of the 0.4 MPa curve is more pronounced than that of the 0.2 MPa experiment. In the latter case, the decrease at small spool deflections is negligible, but increases to approximately 15%, whereas in the 0.4 MPa case the decrease reaches 25%. The statement made by Wang *et al.* [20], *i.e.* "the percentage error of flow rate is very small no matter how much percentage error of b is changed" holds for the smaller spool deflections and valve areas, but deviates at the extremes of the spool travel.

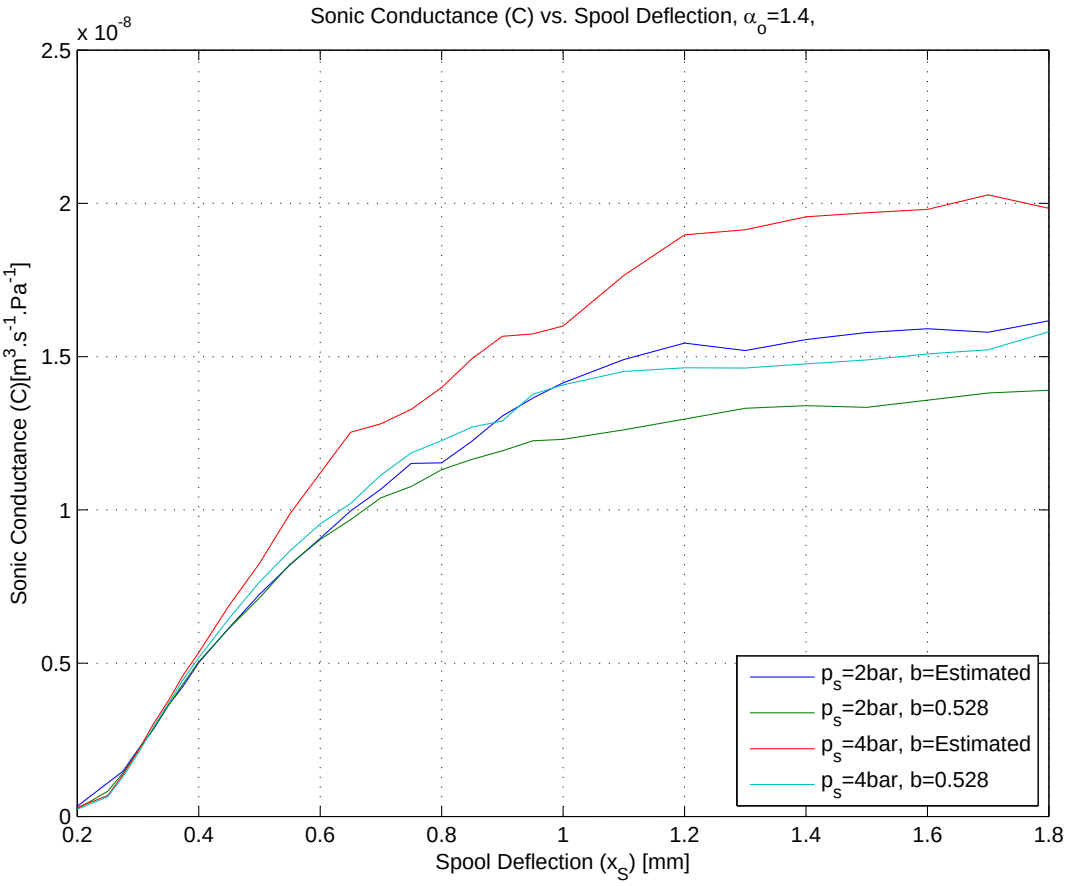

Figure 5.18: Sonic Conductance (C) for Charge Cycles at $p_s = 0.2\ MPa$ and $p_s = 0.4\ MPa$ Indicating the b Dependence

Taking all of the above into account, the Sonic Conductance (C) for a valve with a supply pressure of 0.4 MPa and 0.2 MPa, assuming a fast adiabatic process in both the charge and discharge cycles, can be drawn as shown in Figure 5.19, a) plotted against spool deflection and b) plotted against valve control voltage. A switch-over behaviour between the two supply pressure curves can be seen, *i.e.* for the lower supply pressure the charging conductance has lower values than that of the higher supply pressure, whereas the values for the discharging are the opposite, being higher. The reason for this switch-over is not yet understood. As we will only be using the system at a supply pressure of 0.4 MPa, the 0.2 MPa information is purely for the sake of investigation. Also evident from this graph is the dead band around the centre section where the flow rate is low and the sonic conductance values are low, all a result of the mechanical closure of the valve orifices. In Figure 5.19 b) a line separating the charge and discharge areas is drawn at $V_S = 4.92\ V$ indicating the offset voltage for the zero position.

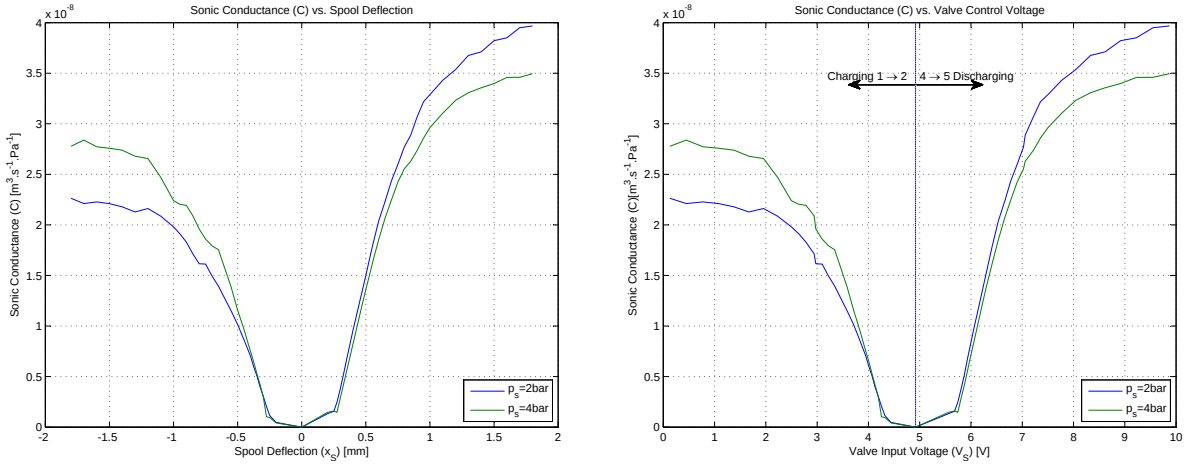

a) b)

Figure 5.19: Estimated Sonic Conductance as a Function of a) Spool Deflection and b) Valve Input Voltage - Derived from Temporal Charge and Discharge Pressure Data, $\alpha_i = 1.4$, $\alpha_o = 1.4$

A point worth noting is the similarity of this figure with the effective area curves in publication by Šitum *et al.* [53] as well as Van der Merwe *et al.* [19].

5.4 COEFFICIENT AND MODEL VALIDITY

A final check for validity of the coefficients is to compare the temporal behaviour of the chamber pressure in a simulated environment with that of the measured pressure data from the experiments and to match the theoretical and measured mass flow through the valve.

The classical model as proposed by, amongst others, Richer [11], Šitum *et al.* [53] as well as the ISO model was used in the validation exercise. The temporal measured data from the two supply pressure tests were compared with the output of the model in which the computed coefficients were used. A metric for the model fit was defined as the Mean Absolute Error (MAE) described by

$$MAE = \frac{1}{n}\sum_{n}|p_t - p_m|, \tag{5.16}$$

where each charge or discharge cycle chamber pressure (p_m) is compared with the theoretical chamber pressure(p_t) and the mean of the absolute error calculated.

Because the amount of test runs are too numerous to plot, only a selection of sample points are shown in the next section. A sample close to the valve opening, one in the middle of the linear region, one

in the middle of the spool travel and one at a fully open point were chosen. The spool deflections are $x_S = 0.3\ mm$, $x_S = 0.5\ mm$, $x_S = 1.0\ mm$ and $x_S = 1.8\ mm$. In the following graphs the temporal chamber pressure is shown against the output of the classical model (using the C_d and A_v variables) and against the output of the ISO model (using b, C and m variables). In all these cases a Runge-Kutta RK4 estimator is used to integrate the pressure rate in the chamber where the chamber is fed by a valve mass flow function as depicted in Figure 5.20.

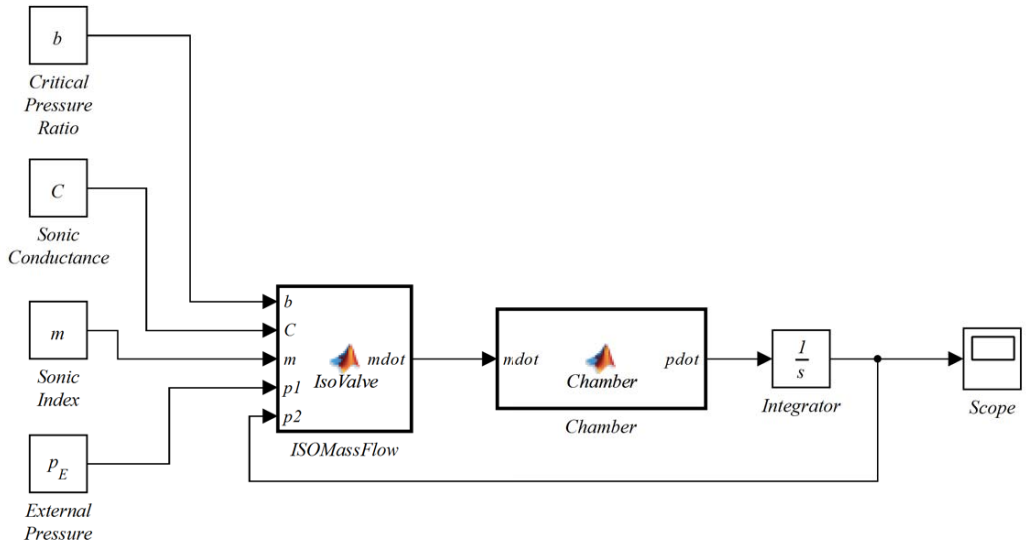

Figure 5.20: Block Diagram of the Valve ISO Model and Chamber Pressure Response Validation - Simulink® Version Shown

In this specific case the model was realised using Matlab® Simulink® with user functions "*ISOMass-Flow*" and "*Chamber*". The inputs to these functions were the coefficients derived in the estimation process together with the environmental conditions. The mass flow is converted into pressure rate and then integrated over time to yield the chamber pressure over time. This result is then compared with the measured data for the specific conditions. The "*ISOMassFlow*" function was written to detect charging and discharging cycles by comparing pressure ratios of the external and internal ports. To ease the comparison, the measured data was truncated to start at the initialisation of the pulse function (from the signal generator), and to end at the end of the pulse. Using the same sampling rate of 100 $S.s^{-1}$, the temporal responses are equivalent.

A similar model to that shown in Figure 5.20 was constructed for the classic model, replacing the "*ISOMassFlow*" function with a "*ClassicMassFlow*" function. During the comparison these models were converted into standard Matlab® scripts, which made it more manageable to handle the various input conditions. The same function blocks were used, and the integrator replaced by the Runge-Kutta integrator.

5.4.1 Classic Model and ISO Model Temporal Pressure Comparison

The classic model (as described above) temporal chamber pressure response, the ISO model response and the measured chamber pressure response curves for a 0.2 *MPa* supply pressure are captured in Figures 5.21 to 5.28.

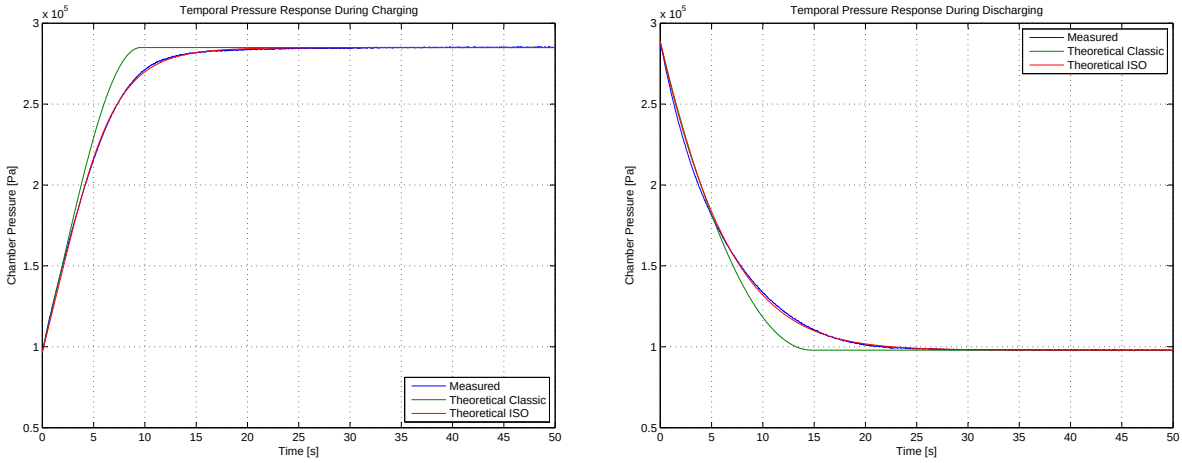

a) b)

Figure 5.21: Chamber Pressure vs. Time Comparison for a 0.2 *MPa* Supply Pressure, $x_S = 0.3$ *mm* Spool Deflection - a) Charging (Port 1 to 2), b) Discharging (Port 4 to 5)

In all these graphs it can be seen that, although the classic model was derived from a choked flow region and with careful choice of measured data, the temporal shape of the classic model output does match the measured data well. The main reason for this is the fact that the temporal pressure response shape over time is not modelled accurately for a setup that is more complex than just a single orifice.

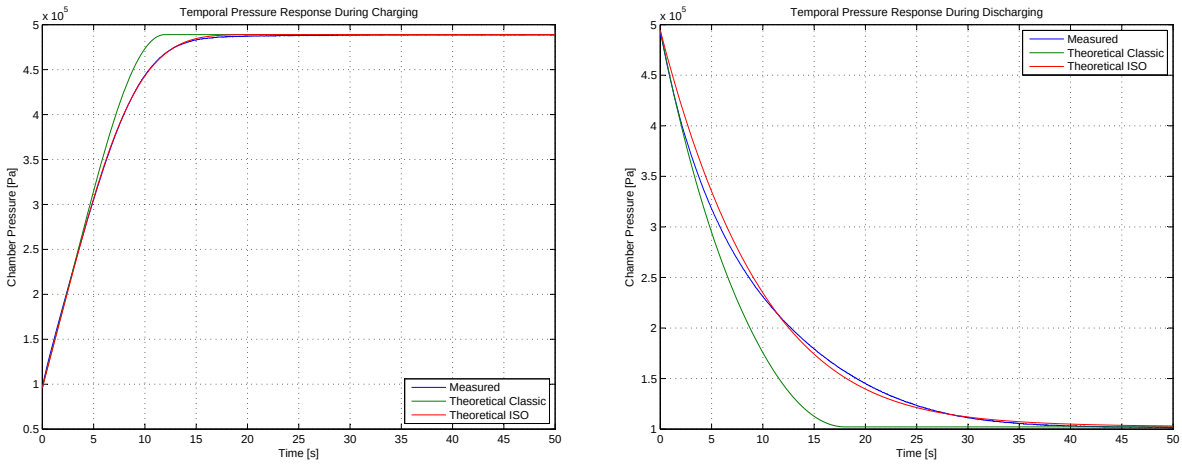

a) b)

Figure 5.22: Chamber Pressure vs. Time Comparison for a 0.4 *MPa* Supply Pressure, $x_S = 0.3$ *mm* Spool Deflection - a) Charging (Port 1 to 2), b) Discharging (Port 4 to 5)

The classic model exhibits a flow rate similar to that of the ISO model and the measured data during the first part of the choked flow region. This corresponds well with the fact that the discharge coefficient was calculated from data in this region. The decrease in the flow rate during the subsonic region is, however, not represented well in the classic model. This gives rise to faster rise and fall times. It can also be seen that the ISO model responses fit the measured data fairly well, with the critical pressure ratio not limited to a single value at 0.528. The sonic index contribution, in many cases larger than 1, shapes the mass flow function to match the measured temporal data.

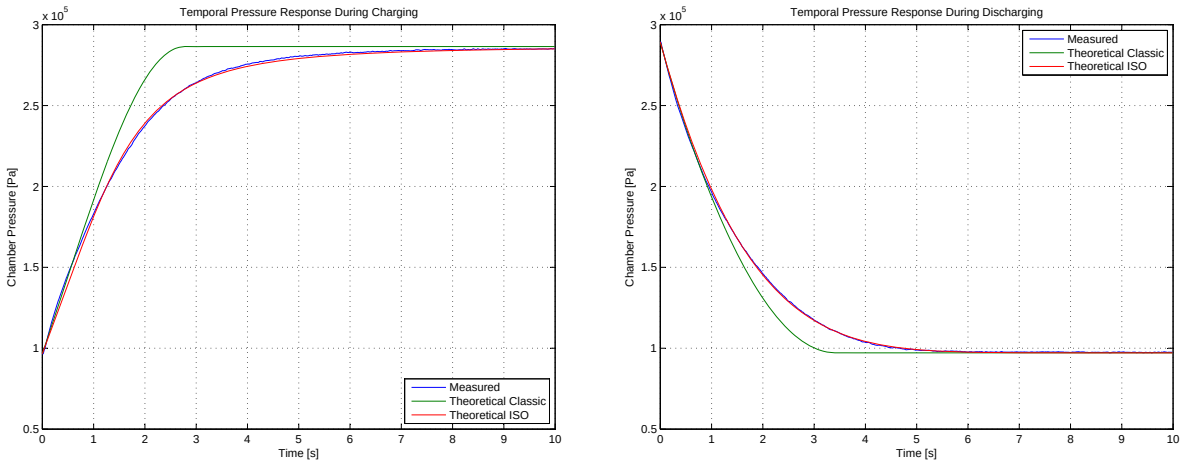

a) b)

Figure 5.23: Chamber Pressure vs. Time Comparison for a 0.2 *MPa* Supply Pressure, $x_S = 0.5$ *mm* Spool Deflection - a) Charging (Port 1 to 2), b) Discharging (Port 4 to 5)

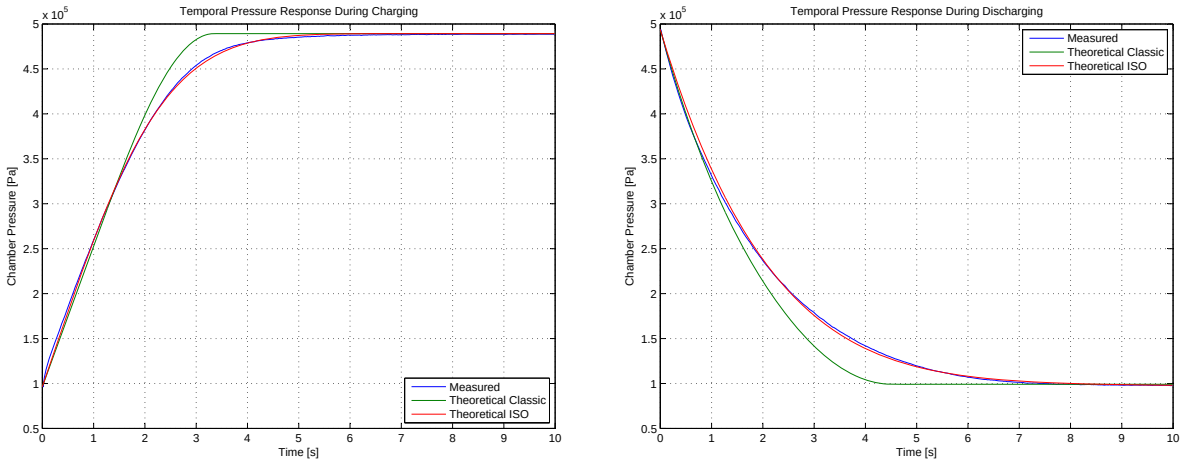

a) b)

Figure 5.24: Chamber Pressure vs. Time Comparison for a 0.4 *MPa* Supply Pressure, $x_S = 0.5$ *mm* Spool Deflection - a) Charging (Port 1 to 2), b) Discharging (Port 4 to 5)

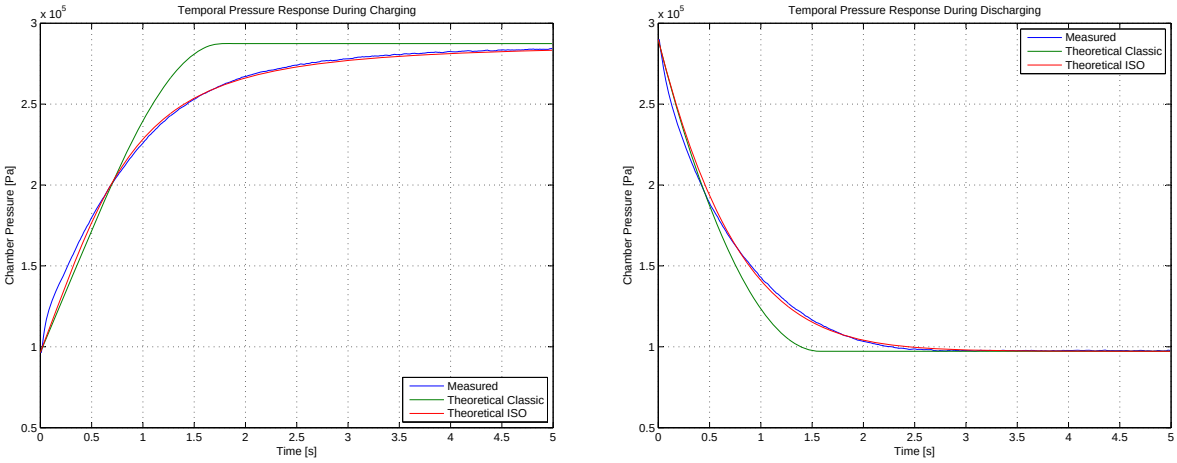

a) b)

Figure 5.25: Chamber Pressure vs. Time Comparison for a 0.2 *MPa* Supply Pressure, $x_S = 1.0$ *mm* Spool Deflection - a) Charging (Port 1 to 2), b) Discharging (Port 4 to 5)

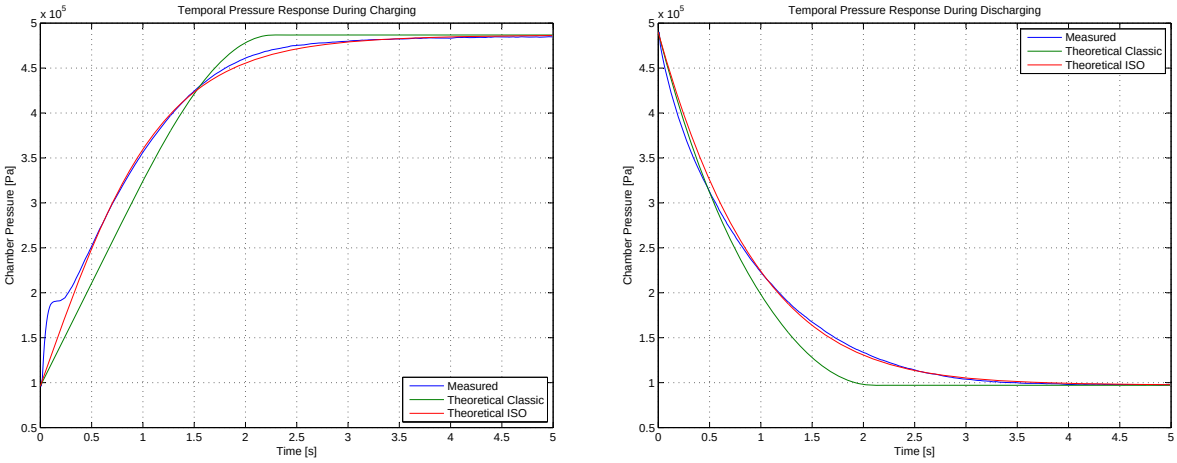

a) b)

Figure 5.26: Chamber Pressure vs. Time Comparison for a 0.4 *MPa* Supply Pressure, $x_S = 1.0$ *mm* Spool Deflection - a) Charging (Port 1 to 2), b) Discharging (Port 4 to 5)

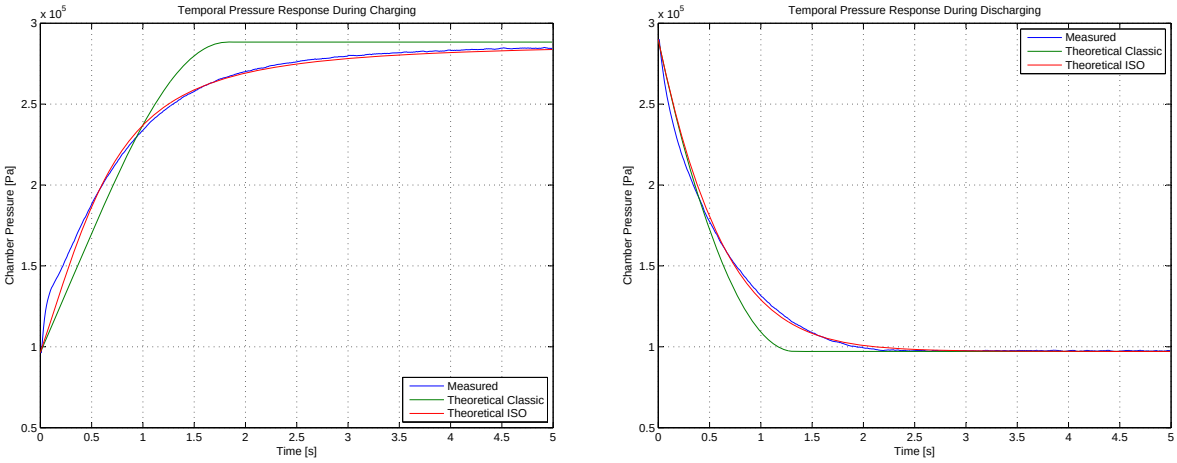

a) b)

Figure 5.27: Chamber Pressure vs. Time Comparison for a 0.2 *MPa* Supply Pressure, $x_S = 1.8$ *mm* Spool Deflection - a) Charging (Port 1 to 2), b) Discharging (Port 4 to 5)

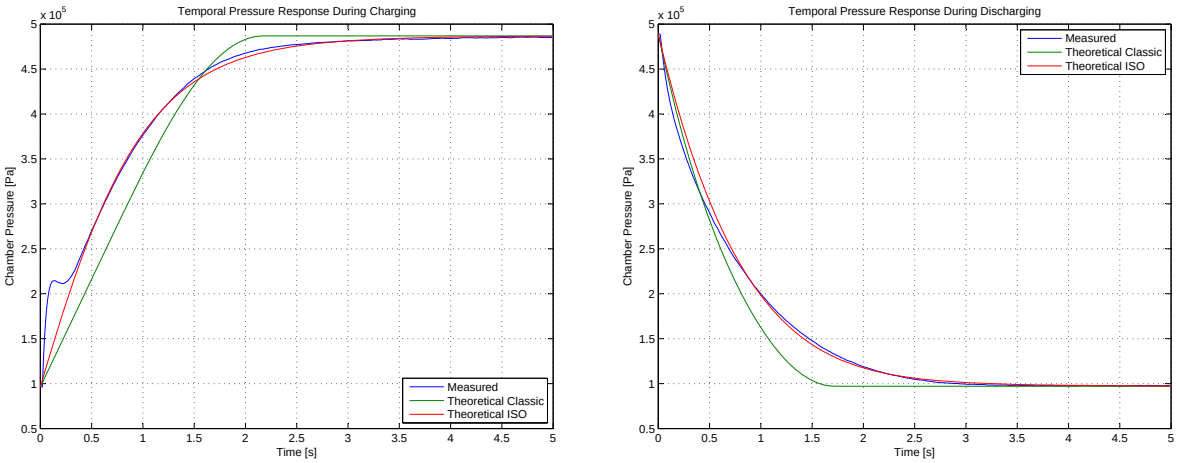

a) b)

Figure 5.28: Chamber Pressure vs. Time Comparison for a 0.4 *MPa* Supply Pressure, $x_S = 1.8$ *mm* Spool Deflection - a) Charging (Port 1 to 2), b) Discharging (Port 4 to 5)

As mentioned earlier (§ 5.3.1), the smoothing (noise reduction) process applied to the data had to reduce the noise but not alter the shape of the low frequency characteristics of the data. The features

or shapes that is referred to are the initial pressure spikes at the start of the charging process that becomes more pronounced with larger pressure differentials. Such features can be seen in Figure 5.26 and in Figure 5.28 between 0 s and 250 ms. For the estimation process for b, C and m, these features were ignored, as indicated by the ISO model's linear increase in pressure in that region.

In § 5.4 the MAE metric was defined and applied to the two models at the two different pressures. The MAE plotted against the spool deflection x_S for the 0.2 MPa data set is shown in Figure 5.29 a) and the MAE for 0.4 MPa in Figure 5.29 b).

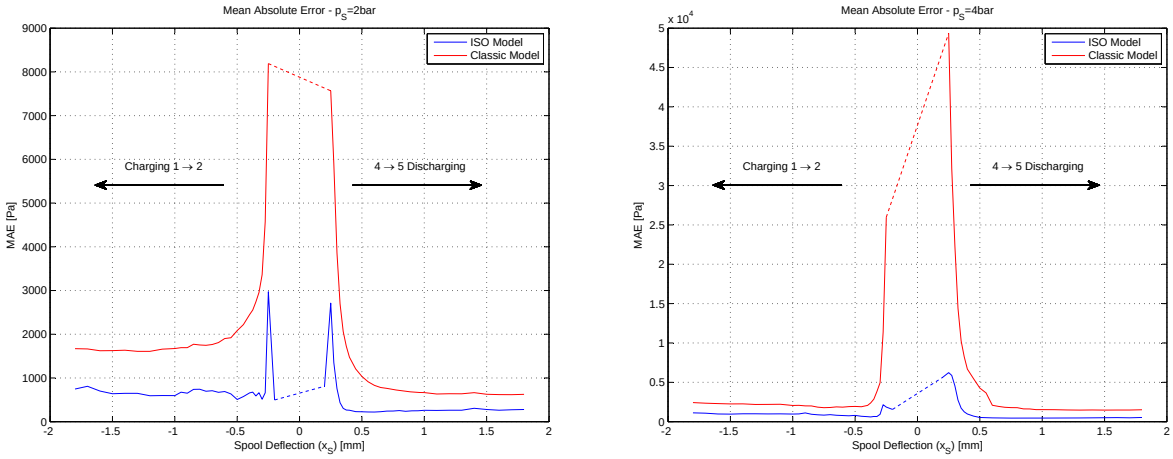

a) b)

Figure 5.29: MAE for the Classic Model and the ISO Model at a) 0.2 MPa and b) 0.4 MPa

The same MAE metric can also be plotted against the valve control voltage V_S and is shown in Figure 5.30 a) in the case of $p_S = 0.2\ MPa$ and and Figure 5.30 b) in the case of $p_S = 0.4\ MPa$.

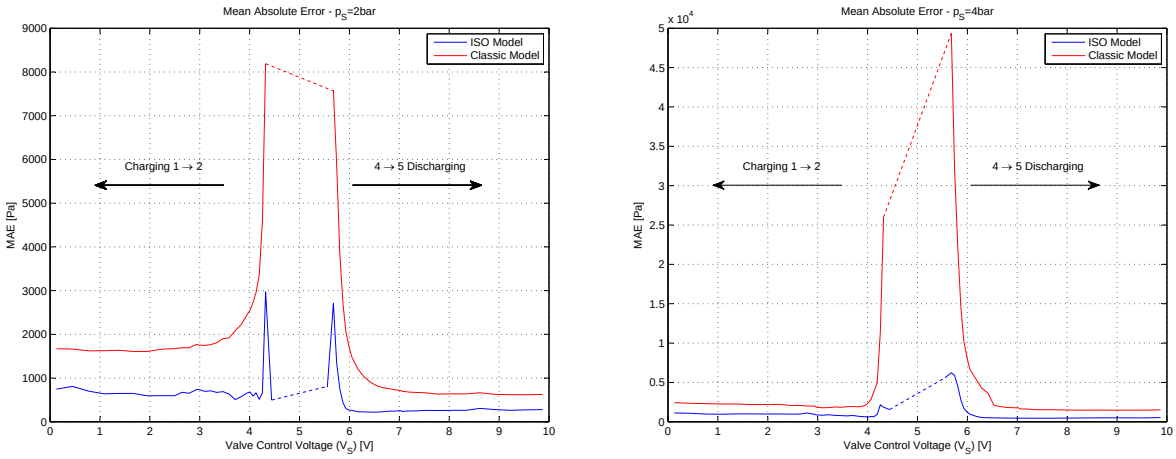

a) b)

Figure 5.30: MAE for the Classic Model and the ISO Model at a) 0.2 *MPa* and b) 0.4 *MPa*

When applied to the data and model outputs a significant difference in the two models can be seen. The previously noticed deviation of the classic model shape to that of the measured data is the cause of a very significant change in the MAE. In both supply pressure cases the MAE of the classic model is at least twice the size of that of the ISO model, confirming that the ISO model is a better fit than the classic model. As there was no data captured in the region between the initial valve openings, no MAE could be computed hence the dashed lines stating a worst case condition.

The classic model is only valid for valve areas larger than 0 m^2 which only occurs at deflections larger than 0.2 *mm*. The region indicated with a dashed line therefore has no values associated with it. A similar argument can be made for the ISO model, in this case no data was captured for the spool deflection smaller than 0.2 *mm*.

If these curves are compared with values reported by Van der Merwe *et al.* [19] the magnitude of the errors are similar (and in most cases smaller), and the model and coefficients are good enough to be representative of a valve and chamber system in real life.

5.4.2 Classic Model and ISO Model Mass Flow Comparison

A frequently posted specification for a valve is the flow rate or mass flow rate. This is usually determined by the manufacturer with great care and describes the valve in enough detail for general usage. If

the valve should be integrated into a system with tubes and silencers, this flow rate curve will change. Following the same process used for the determination of the temporal flow (and pressure) characteristics of the valve in a system, the mass flow rate has been calculated for our test setup. This section acts largely as documentation for the purpose of being thorough. The coefficients derived from the temporal behaviour is used later on in the final pneumatic model, the main reason being that the temporal estimation results in much more accurate values than that of the mass flow. This statement is substantiated by observations during the study and has not been proven empirically.

The following graphs (Figures 5.31 to 5.38) are the results of the coefficient estimation process as described in the above sections. Once again the classic model does not describe the shape of the mass flow accurately, and the magnitude tends to be larger than the measured data. The ISO model, having the sonic index to modify the shape, represents the real life process fairly well and can be used in the modelling of most pneumatic systems with confidence. An anomaly that starts to emanate above spool deflection of x_S 1.0 *mm* is the large mass flow rate between $p_2/p_1 = 0.2$ and $p_2/p_1 = 0.43$ (Figure 5.38). This is not a great concern for the purpose of this study as fully opened valve condition will not be used often. Due to the construction of the test setup, with pressure sensors in the connecting lines, rather than in the chambers, more than a single chamber cavity needs to be modelled to represent the system accurately. It is postulated at present that the large mass flow rate at large pressure differentials is a result of the combined effect of the connecting tubes and pressure sensor cavity charging up and the spool deflection transient. It is therefore seen as an effect typical to this specific test setup and has not been investigated any further.

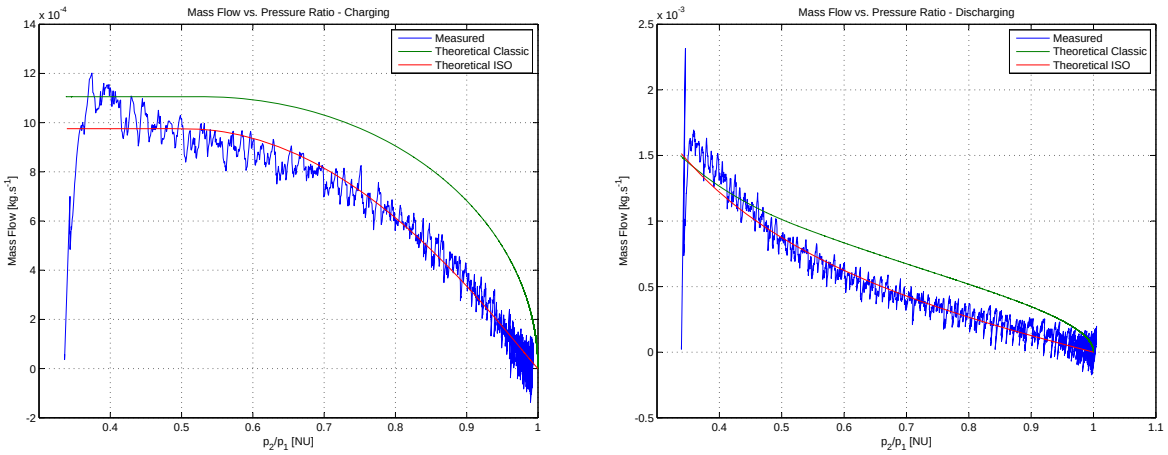

a) b)

Figure 5.31: Mass Flow Rate Measured, Calculated With Classic Model and Calculated With ISO Model for $x_S = 0.3\ mm$ and $p_S = 0.2\ MPa$ during a) Charging and b) Discharging

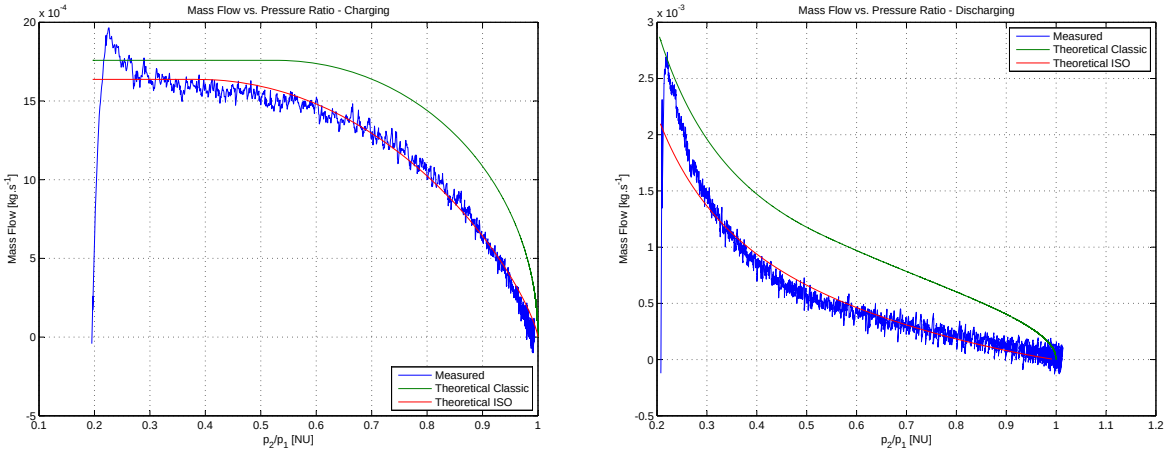

a) b)

Figure 5.32: Mass Flow Rate Measured, Calculated With Classic Model and Calculated With ISO Model for $x_S = 0.3\ mm$ and $p_S = 0.4\ MPa$ during a) Charging and b) Discharging

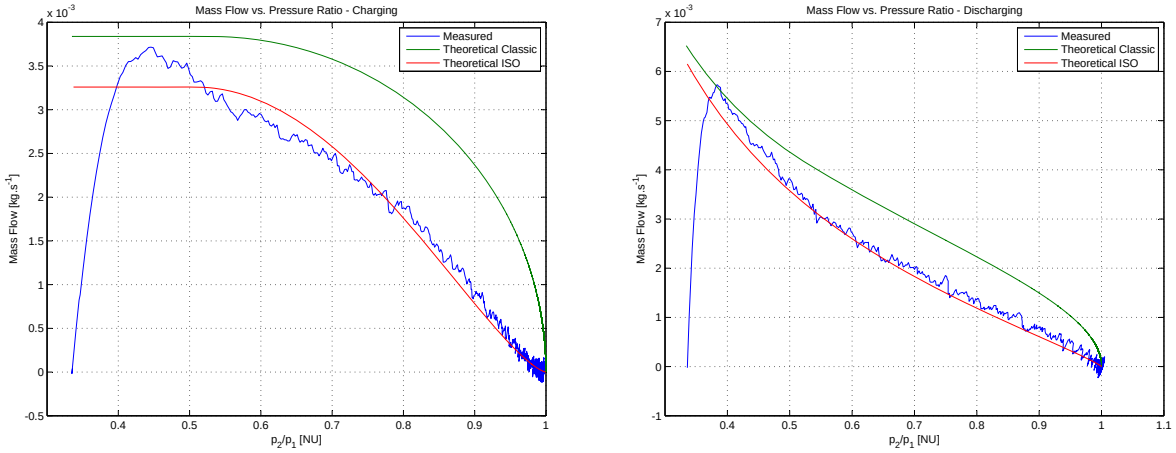

a) b)

Figure 5.33: Mass Flow Rate Measured, Calculated With Classic Model and Calculated With ISO Model for $x_S = 0.5\ mm$ and $p_S = 0.2\ MPa$ during a) Charging and b) Discharging

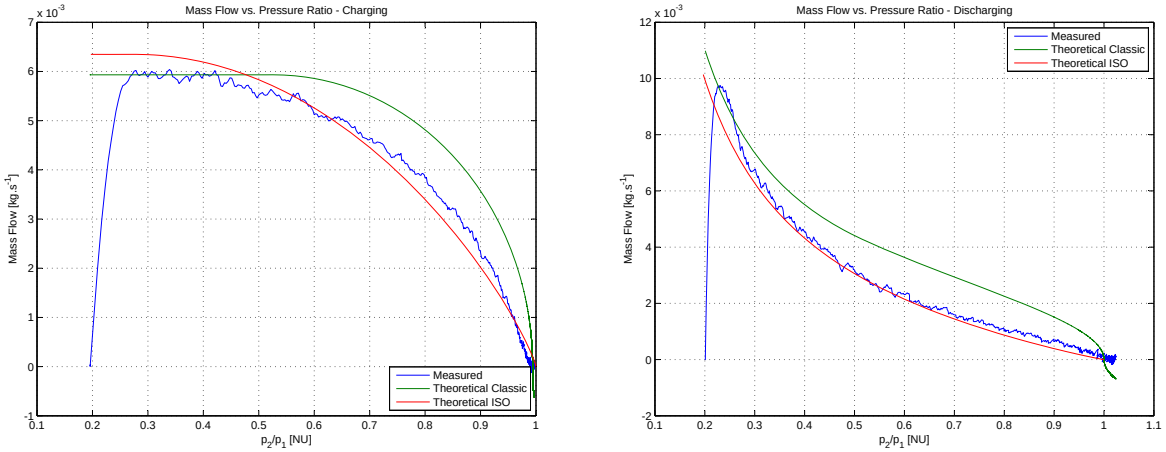

a) b)

Figure 5.34: Mass Flow Rate Measured, Calculated With Classic Model and Calculated With ISO Model for $x_S = 0.5\ mm$ and $p_S = 0.4\ MPa$ during a) Charging and b) Discharging

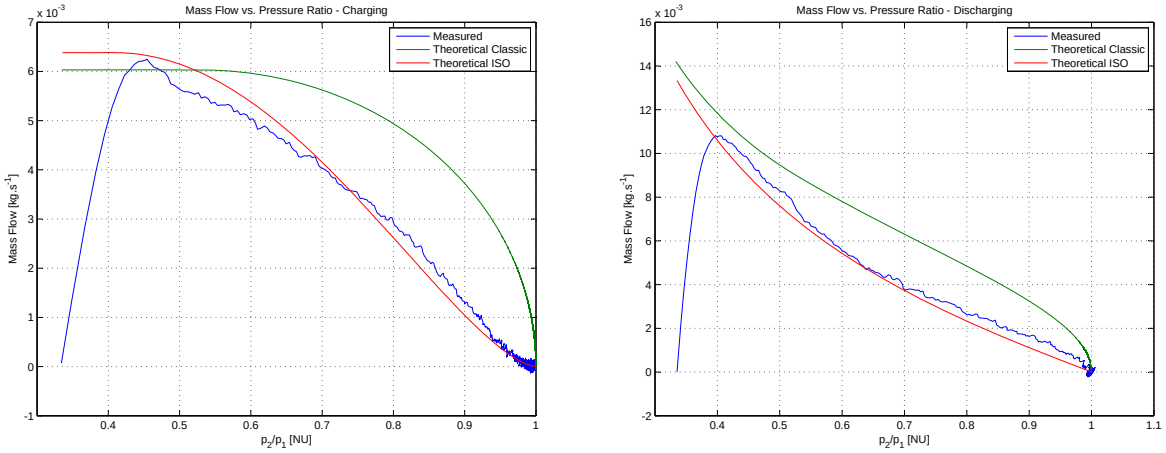

a) b)

Figure 5.35: Mass Flow Rate Measured, Calculated With Classic Model and Calculated With ISO Model for $x_S = 1.0\ mm$ and $p_S = 0.2\ MPa$ during a) Charging and b) Discharging

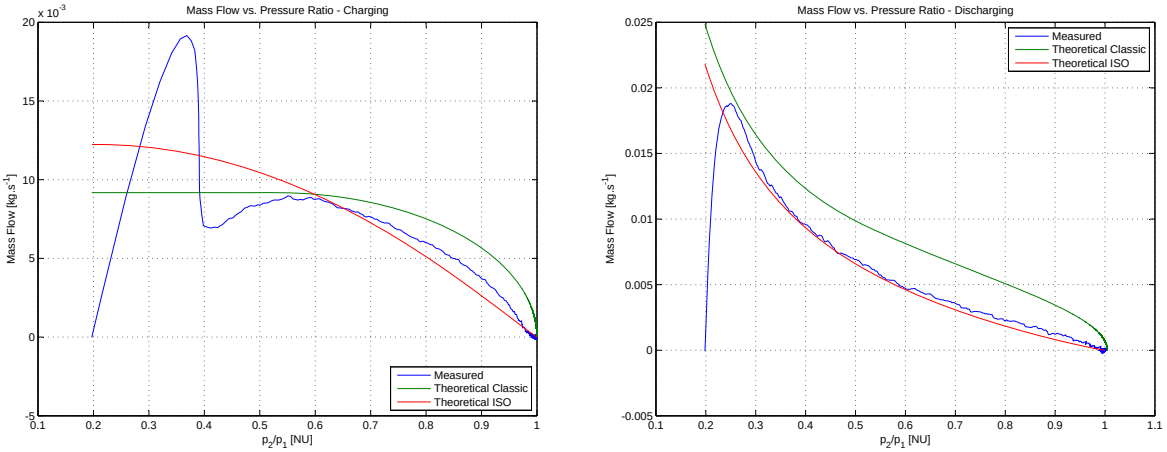

a) b)

Figure 5.36: Mass Flow Rate Measured, Calculated With Classic Model and Calculated With ISO Model for $x_S = 1.0\ mm$ and $p_S = 0.4\ MPa$ during a) Charging and b) Discharging

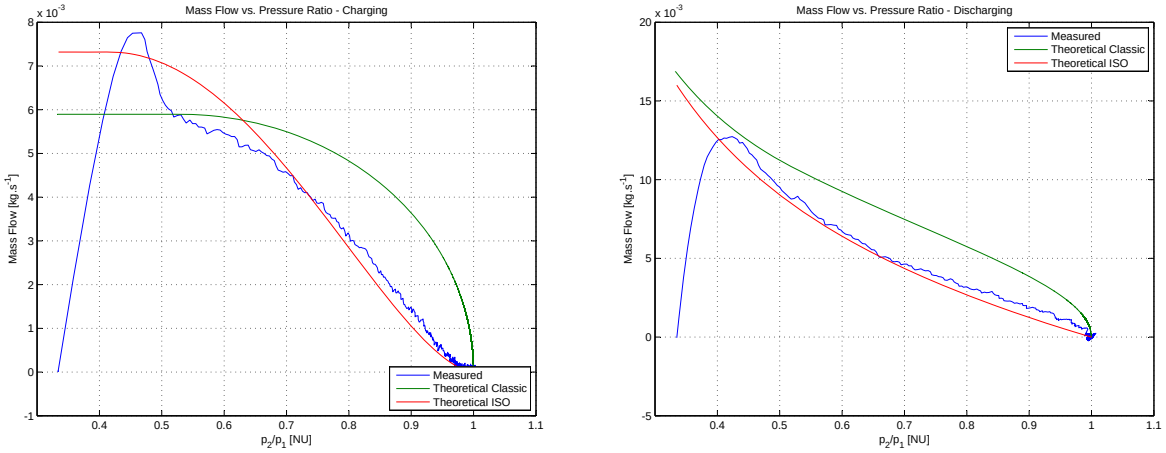

a) b)

Figure 5.37: Mass Flow Rate Measured, Calculated With Classic Model and Calculated With ISO Model for $x_S = 1.8\ mm$ and $p_S = 0.2\ MPa$ during a) Charging and b) Discharging

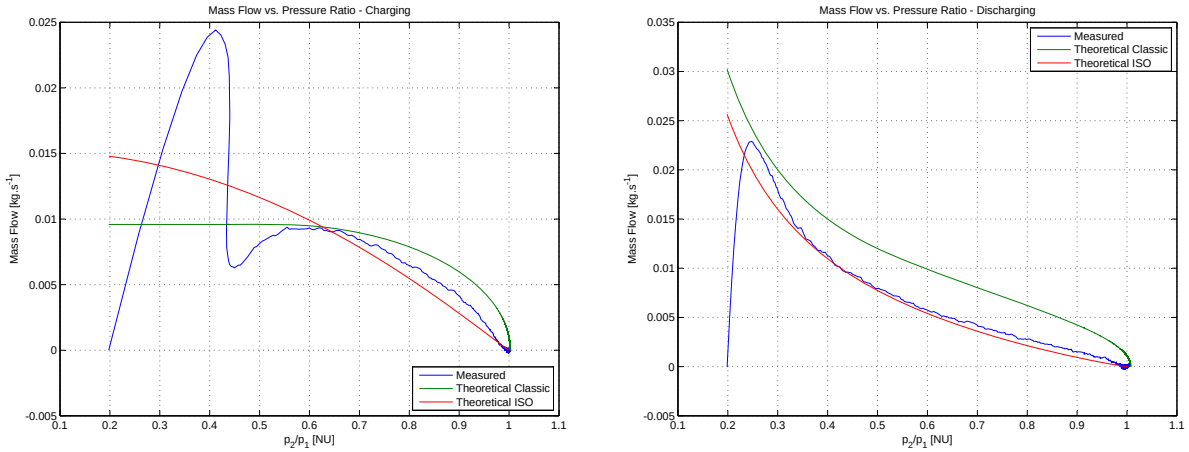

a) b)

Figure 5.38: Mass Flow Rate Measured, Calculated With Classic Model and Calculated With ISO Model for $x_S = 1.8\ mm$ and $p_S = 0.4\ MPa$ during a) Charging and b) Discharging

5.4.3 ISO Model Coefficients

The estimated ISO model coefficients for the FESTO MPYE-5-3/8-010-B proportional directional control valve connected to a 5ℓ pneumatic reservoir through a $10mm$ diameter Festo polyurethane tube are tabulated in Tables 5.1 and 5.2. These coefficients are later used in the analysis of the SMS pneumatic system.

Table 5.1: Estimated ISO Model Coefficients at $p_S = 0.2\ MPa$

		0.2 MPa						
		Charge			Discharge			
Vs	xs	b	C	m	Vs	b	C	m
V	mm	[NU]	$[m^3.s^{-1}.Pa^{-1}]$	[NU]	V	[NU]	$[m^3.s^{-1}.Pa^{-1}]$	[NU]
4.441	0.2	0.00000	4.67829E-10	1.14460	5.55900	0.0	1.84872E-09	8.70985
4.32	0.25	0.52800	1.14592E-09	1.02343	5.68000	0.0	2.18832E-09	1.85216
4.256	0.275	0.45411	2.05111E-09	0.94084	5.74400	0.0	3.45395E-09	1.13042
4.193	0.3	0.50252	3.05117E-09	1.05000	5.80700	0.0	5.26657E-09	0.97695
4.129	0.325	0.56616	3.97483E-09	1.24420	5.87100	0.0	7.24289E-09	0.95078
4.07	0.35	0.54813	5.07362E-09	1.28469	5.93000	0.0	9.37528E-09	0.93096
4.01	0.375	0.56329	5.97613E-09	1.37887	5.99000	0.0	1.13809E-08	0.90829
3.95	0.4	0.53977	7.02421E-09	1.37415	6.05000	0.0	1.34381E-08	0.89166
3.83	0.45	0.52403	8.61646E-09	1.38869	6.17000	0.0	1.72232E-08	0.86220
3.712	0.5	0.50771	1.01400E-08	1.41590	6.28800	0.0	2.10118E-08	0.86208
3.588	0.55	0.53215	1.14766E-08	1.54537	6.41200	0.0	2.49745E-08	0.87975
3.466	0.6	0.52604	1.27028E-08	1.56881	6.53400	0.0	2.85491E-08	0.88402
3.342	0.65	0.50238	1.39482E-08	1.55436	6.65800	0.0	3.12534E-08	0.87880
3.222	0.7	0.50369	1.49419E-08	1.58837	6.77800	0.0	3.41151E-08	0.89642
3.099	0.75	0.47127	1.61256E-08	1.57056	6.90100	0.0	3.63868E-08	0.89611
2.975	0.8	0.50662	1.61491E-08	1.63593	7.02500	0.0	3.87886E-08	0.92820
2.942	0.85	0.48587	1.71400E-08	1.63047	7.05800	0.0	4.04168E-08	0.91945
2.783	0.9	0.44931	1.82898E-08	1.58501	7.21700	0.0	4.29603E-08	0.96196
2.645	0.95	0.43504	1.91040E-08	1.59406	7.35500	0.0	4.50527E-08	0.97925
2.498	1	0.40881	1.98066E-08	1.54601	7.50200	0.0	4.60446E-08	0.96963
2.229	1.1	0.39001	2.08654E-08	1.55158	7.77100	0.0	4.80226E-08	0.96768
1.955	1.2	0.38442	2.16175E-08	1.56279	8.04500	0.0	4.95093E-08	0.98294
1.668	1.3	0.42196	2.12761E-08	1.62850	8.33200	0.0	5.14616E-08	1.00029
1.382	1.4	0.41119	2.17815E-08	1.62668	8.61800	0.0	5.19550E-08	0.98088
1.083	1.5	0.39422	2.21034E-08	1.59652	8.91700	0.0	5.35075E-08	1.01522
0.775	1.6	0.40811	2.22760E-08	1.63694	9.22500	0.0	5.39006E-08	1.00028
0.448	1.7	0.42697	2.21113E-08	1.67392	9.55200	0.0	5.52976E-08	1.02727
0.129	1.8	0.41720	2.26372E-08	1.67511	9.87100	0.0	5.55440E-08	1.01617

Table 5.2: Estimated ISO Model Coefficients at $p_S = 0.4\ MPa$

		0.4 MPa						
		Charge			Discharge			
Vs	xs	b	C	m	Vs	b	C	m
V	mm	[NU]	$[m^3.s^{-1}.Pa^{-1}]$	[NU]	V	[NU]	$[m^3.s^{-1}.Pa^{-1}]$	[NU]
4.441	0.2	0.00000	4.13153E-10	1.32069	5.55900	0.0	2.03974E-09	27.96589
4.32	0.25	0.35113	9.54101E-10	1.02828	5.68000	0.0	2.24115E-09	7.60944
4.256	0.275	0.36722	1.88927E-09	0.81108	5.74400	0.0	2.67314E-09	2.05796
4.193	0.3	0.38654	2.98278E-09	0.77586	5.80700	0.0	3.96533E-09	1.10725
4.129	0.325	0.40237	4.20924E-09	0.79244	5.87100	0.0	5.83896E-09	1.08272
4.07	0.35	0.42538	5.28155E-09	0.83104	5.93000	0.0	7.67732E-09	1.06297
4.01	0.375	0.40221	6.47385E-09	0.82732	5.99000	0.0	9.70005E-09	1.07223
3.95	0.4	0.41039	7.48757E-09	0.86335	6.05000	0.0	1.15534E-08	1.05287
3.83	0.45	0.31360	9.63519E-09	0.82973	6.17000	0.0	1.53640E-08	1.06469
3.712	0.5	0.27569	1.15580E-08	0.84249	6.28800	0.0	1.90852E-08	1.07256
3.588	0.55	0.15562	1.38112E-08	0.81303	6.41200	0.0	2.25872E-08	1.06766
3.466	0.6	0.11088	1.56844E-08	0.84158	6.53400	0.0	2.59436E-08	1.07022
3.342	0.65	0.03272	1.75455E-08	0.85195	6.65800	0.0	2.89451E-08	1.07641
3.222	0.7	0.16173	1.79304E-08	0.90173	6.77800	0.0	3.14588E-08	1.07556
3.099	0.75	0.24108	1.85931E-08	0.99567	6.90100	0.0	3.39272E-08	1.08979
2.975	0.8	0.21249	1.95916E-08	0.99482	7.02500	0.0	3.57637E-08	1.09729
2.942	0.85	0.12419	2.09062E-08	0.98719	7.05800	0.0	3.68020E-08	1.11032
2.783	0.9	0.00005	2.19311E-08	0.95476	7.21700	0.0	3.83088E-08	1.10722
2.645	0.95	0.18729	2.20336E-08	1.02833	7.35500	0.0	4.00182E-08	1.10756
2.498	1	0.20567	2.23970E-08	1.06520	7.50200	0.0	4.14715E-08	1.10078
2.229	1.1	0.09437	2.47077E-08	1.02648	7.77100	0.0	4.34631E-08	1.09848
1.955	1.2	0.00000	2.65640E-08	1.01078	8.04500	0.0	4.52480E-08	1.13117
1.668	1.3	0.00000	2.67936E-08	1.02177	8.33200	0.0	4.63010E-08	1.14242
1.382	1.4	0.00000	2.73834E-08	1.05087	8.61800	0.0	4.69828E-08	1.12868
1.083	1.5	0.00000	2.75736E-08	1.06044	8.91700	0.0	4.75656E-08	1.11906
0.775	1.6	0.00000	2.77285E-08	1.05521	9.22500	0.0	4.84132E-08	1.12569
0.448	1.7	0.00000	2.83859E-08	1.04816	9.55200	0.0	4.84356E-08	1.11487
0.129	1.8	0.05336	2.77726E-08	1.04804	9.87100	0.0	4.89318E-08	1.11471

CHAPTER 6

FRICTION IN PNEUMATIC SYSTEMS

The friction model using only the Stribeck effect or only combinations of Coulomb and viscous friction in general has limitations when used in dynamic systems. These classical models do not describe hysteresis or varying stiction force, nor do they describe the small movements prior to slipping. In the pneumatic system under investigation, the deformation of the pneumatic seals could be lumped with the latter and seen as a pre-sliding elasto-plastic deformation.

Many of the modern friction models are based on the LuGre model [31], which saw the light as a result of a co-operative effort between the Lund Institute of Technology and the Polytechnic of Grenoble. The model combines the Dahl model [30] with the Stribeck steady-state behaviour and describes surfaces as non-uniform on a microscopic level that make contact at a number of asperities. These contacts act similar to elastic bristles or springs that deform linearly under a tangential force and give rise to a friction force. No physical movement on the bristle contacts occur at this stage, although the one surface will move relative to the other. This is also called the pre-sliding regime.

As the force is increased in magnitude a transition regime is entered as some of the bristles will start to slip and in the case of the LuGre model the behaviour of the friction force is based on the average behaviour of the bristles. The system then moves into the sliding regime. The LuGre model has been improved by Swevers *et al.* to incorporate hysteresis [32]. This is known as the Leeuven model. Other models such as Dupont *et al.*'s elasto-plastic models [33] includes a function to minimize drift, and a computationally effective physically motivated general friction model such as the General Maxwell-Slip model [34].

These models have been developed over the last 30 years and can accurately represent various friction systems. As the scope of this study is limited, a detailed model will not be used, but rather one that

will represent more dominant behaviour of the SMS.

We have therefore decided on a point symmetric model with a classic static friction region (F_S) with a very small amount of pre-sliding movement. A constant Coulomb friction component together with a Stribeck function describes the gross-sliding region of the movement. Experimentation will reveal if the decreasing velocity curve will follow the increasing velocity curve, in which case the friction force will be described by

$$F_f = \text{sgn}(v)\left[F_C + (F_S - F_{C1})\, e^{-\left|\frac{v}{v_S}\right|^{\delta}}\right] + \sigma_1 v \tag{6.1}$$

with F_C the Coulomb friction component, F_S the maximum stiction force, v the linear velocity and δ the Stribeck exponent. v_S is the Stribeck velocity and determines the minima of the Stribeck curve. The gradient of the friction curve is defined by σ_1. The Stribeck curve decreases with an increase in velocity and is bounded by the static force (F_S) and the Coulomb force (F_C) as proposed by Armstrong-Hélouvry [38].

A more general model in which the Coulomb friction and the friction slope for the accelerating and decelerating parts of the movement can differ was proposed by Nouri [37] and is given by

$$F_f = \alpha_f \begin{cases} sgn(v)\left[F_{C1} + (F_S - F_{C1})\, e^{-\left|\frac{v}{v_S}\right|^{\delta}}\right] + \sigma_1 v & sgn(a) = sgn(v) \\ sgn(v) F_{C2} + \sigma_2 v & sgn(a) \neq sgn(v) \end{cases} \tag{6.2}$$

where F_{C1} and σ_1 are the Coulomb friction coefficient and viscous friction coefficient for the accelerating travel and F_{C2} and σ_2 are the Coulomb friction coefficient and viscous friction coefficient for the decelerating travel respectively. α_f is a function to model the stick-slip behaviour close to the origin (very low velocities).

6.1 FRICTION IDENTIFICATION TEST SETUP

In order to determine the extent of the contribution of the friction forces in the pneumatic actuators, an investigation into the magnitude and complexity of the friction was done.

Friction attributes such as the Stribeck coefficients, the viscous and Coulomb friction coefficients and hysteresis function of pneumatic actuators can be determined in a few ways. One way is to excite the actuator externally with an instrumented linear exciter (push-pull excitation), thereby accurately determining the static friction force (Stiction), the Coulomb friction, and the rate dependent viscous

and drag friction contributions [35]. This method has some drawbacks such as the effect of the displaced air in the actuator and the effect of pressure on the seals. A similar test can be devised by charging the actuator chambers to a constant pressure, exciting the piston externally and measuring the friction forces. These kind of experiments require specialised equipment, and although it is the more controlled way to approach the problem, it falls outside the scope of this study. A well published method used by others such as Nouri [37] and Andrighetto *et al.* [36] is to excite the actuator with compressed air, capturing the displacement and chamber pressures and using Newton's second law to determine the friction behaviour, *i.e.* the sum of the applied forces (ΔF_p and F_L) equals the "inertia" force ($(M_L + M_p)\ddot{x}$).

It was decided to use the equipment already at hand to model the friction function for the actuators in SMS. A single Festo actuator and a proportional control valve were used in a configuration similar to that described in § 5.2 for the valve characterisation, exchanging the two reservoirs with the actual actuator and position feedback system. It should be noted that the pneumatic variables were not the focus of this investigation, hence no temperature measurements were done. The schematic representation of one of the actuator subsystems is shown in Figure 4.1 and the experimental pneumatic setup in Figure 6.1. A compressed air supply at a gauge pressure (p_S) of 0.4 MPa and a temperature (T_S)

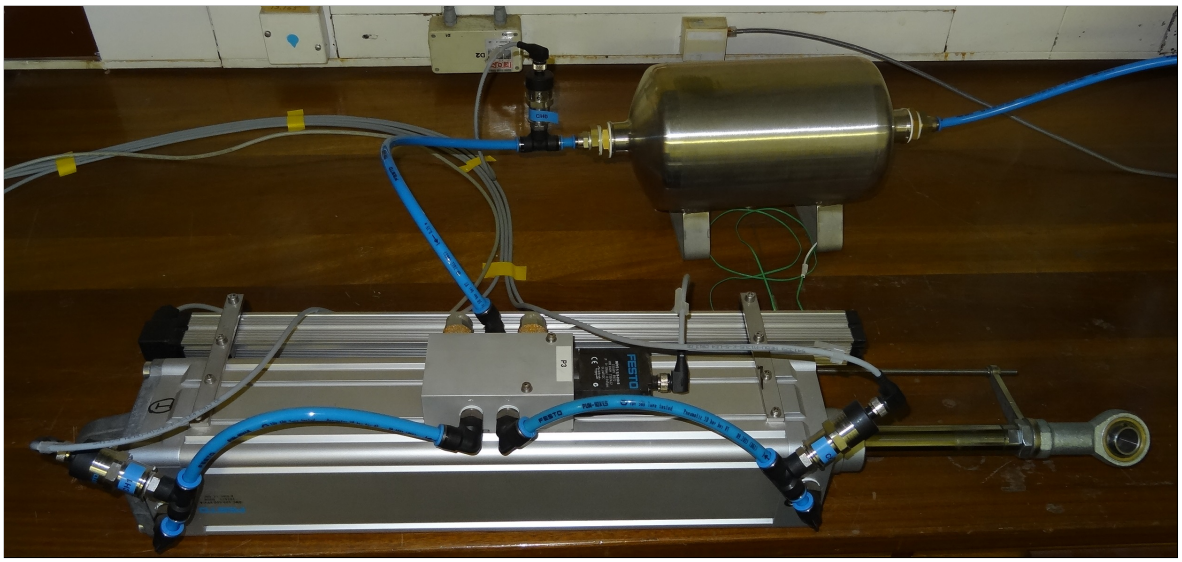

Figure 6.1: The Pneumatic Part of the Friction Identification Setup

of approximately 20 $°C$ - 23 $°C$ was used to test the system. The supply is part of a fixed installation in the laboratory and is therefore prone to pressure drops along lengthy supply lines. A reservoir of volume V_R is used to smooth some of the pressure fluctuations due to the long air lines during peak

air demand and delivers compressed air to the valve and actuator at a pressure of p_R. The Festo 5/3 proportional control valve is energised by a signal generator V_{vs} that can vary the frequency, amplitude, dead-band compensation and centre offset. The waveform can be adjusted to control the rate of actuator movement and the actuator acceleration to suit the experiment at hand. Two Festo pressure sensors convert the instantaneous chamber input pressures (p_a and p_b) to analogue signals that are proportional to the guage pressure at the input ports. Due to physical limitations on the actuator, the pressure sensors had to be mounted on the feed line of the two chambers, and could not be set up to measure the chamber pressures directly. Pressure errors can be expected at high mass flow rates due to the transport delay through the pneumatic junctions and ports. Because of this, the mass flow rate was kept as low as possible and the excitation frequency below 1 Hz.

As the actuator under test had end cushioning, the experimental travel of the actuator was limited to the centre section of the total actuator travel, staying well clear of the last 50 mm at the ends. According to the Festo data sheet, the cushioning length is 32 mm, in which region area and flow characteristics are unknown, and the calculation of the friction can become erroneous.

The actuator is used in a horizontal orientation, driving only the linear displacement sensor wiper through the connecting rod. It is operated without any load in the direction of the movement, *i.e.* $F_L = 0$. The moving mass (M_p) in the actuator consists of the piston, the piston rod, the rod eye with its locking nuts, the displacement sensor connecting rod and its fastening plate, and the displacement sensor wiper block. The friction and the mass of the wiper block has been assumed to be negligible. The masses of these components are tabulated in Table 6.1 and when added up equals approximately 3.64 kg. The piston diameter is 100 mm and the piston rod diameter 25 mm.

The subsystem is connected to a Data Translation DT9803 ADC by which the time domain signals can be captured. A sampling rate of 1 $kS.s^{-1}$ is used to ensure resolution of fast transients of the pressure signals. Signals measured in these experiments are the supply pressure (p_S), the valve excitation voltage (V_{vs}), the chamber pressures (p_a and p_b) and the linear resistive displacement sensor voltage (V_x) translated to displacement (x).

Table 6.1: Theoretical Mass Of The Moving Components

Component	Mass [kg]
Piston and Rod	3.064
Rod Eye and Nut	0.432
Connecting Hardware	0.143
	3.639

6.2 FRICTION IDENTIFICATION PROCEDURE

Referring to the setup described in § 6.1, Newton's second law can be written in terms of the applied and net forces on the piston as

$$(M_L + M_p)\ddot{x} = F_a - F_b - F_r - F_L - F_f \tag{6.3}$$

where F_a is the pneumatic force on the lower face of the piston, F_b is the pneumatic force on the top surface of the piston, and F_r is the force due to the ambient air pressure on the rod; all in N. F_L represents the load and is assumed to be equal to zero. The friction force counteracting the piston movement is denoted by F_f and will be expressed as a complex non-linear function which is dependent on the piston position (x), the piston rate ($\dot{x}$), the piston acceleration ($\ddot{x}$), the chamber pressures (p_a and p_b [37]), and the state of lubrication, amongst others. The dynamic force due to the mass of the piston balances the equation when the load is removed ($M_L = 0$). The force terms can further be expressed as

$$M_p\ddot{x} = p_a A_a - (p_b A_b + p_A A_r) - F_f \tag{6.4}$$

where p_a and p_b are the instantaneous chamber pressures in Pa, A_a and A_b are the two piston areas respectively in m^2, p_A is the ambient pressure in Pa, and A_r is the rod area in m^2.

As described in § 6.1, the signals derived from the setup are captured with a Data Translation DT9803 ADC, transformed into comma delimited text data with the Data Translation "QuickDAQ 2013" software and imported into Matlab®. As the data acquisition process and the sensors are the same as that used in the valve characterisation process (§ 5.3.1) the kurtosis and skewness can be assumed to be the same as in that experiment. The noise component of the signals can therefore be assumed to be white Gaussian noise with a zero mean, a Gaussian probability distribution and a noise spectral dens-

ity approaching uniformity. With that in mind, an α-β filter can be used as an observer to smooth the signals and reduce the noise. The processing on every one of the measurement sets follows the same flow, *i.e.* capture the signals, convert and import the data into Matlab®, smooth out the noise, check that the filtered signals match the original signals close enough by monitoring the standard deviation, calculate the linear rate ($\dot{x}$) and linear acceleration ($\ddot{x}$) using α-β filters, and determine the friction force *vs.* rate maps using eq. 6.4. When the friction plots are known, the friction model coefficients are identified to fit the maps as accurately as possible.

Authors such as Andrighetto [36] populated the friction *vs.* rate map using constant rate values, ignoring the transients at acceleration and the effects of cycle frequency. This method also requires a vast amount of sample sets to populate the map accurately as each set only defines one point on the curve. A more complete picture is seen when the excitation is done at various frequencies and rates, as well as at non-zero acceleration. The excitation of the valve is done in such a manner that the travel is limited to the non-cushioned region, and the frequency adjusted so that multiple complete cycles of displacement can be measured. The bias offset is adjustable to keep the actuator in the centre of the travel.

6.3 FRICTION IDENTIFICATION DATA SETS

A complete friction model would require a large number of modelled features, each identified by a range of tests. Hysteresis, lubrication effects, asperity modelling, pressure and frequency dependencies can be ignored in this simplified friction model. The test matrix used for this study was set up to include a variation of supply pressures from 0.05 MPa to 0.4 MPa, and cycle frequencies from 0.1 Hz to 10 Hz. The valve openings were adjusted to meet the actuator travel criteria laid out in the previous section. An assessment of the usefulness of the data was conducted after initial processing and sample sets were discarded that had piston movement into the cushioning section of the actuator and where the excitation frequency or maximum linear velocity surpassed the working range of the simulator.

A kinematic analysis of the SMS using MSC ADAMS® and Matlab® Simulink® was done to determine the maximum linear velocity and linear acceleration that can be expected during the simulation of frigate deck motion. These variables are then used to limit the data sets for friction model identification. The specification as outlined in Table 2.1 defined the angular rate limits for Roll and Pitch rates as $6\,^{\circ}.s^{-1}$ and $4\,^{\circ}.s^{-1}$ respectively, derived from the maritime vessel Inertial Navigation System

(INS) data collected at Arniston on 27 March, 2006 and False bay on 20 February, 2008 . As the roll and the pitch axes are orthogonal, the worst case actuator linear velocity would be in the event of a full pitch change coinciding with a full roll change.

Using the leg extension lookup table as defined in § 3.5 together with the ADAMS®/Matlab® co-simulation and the INS data as inputs, the actuator maximum linear velocity was determined to be $v_{max} = 0.13\ m.s^{-1}$. The data set which was used included angular deflections of 10.2° which fall outside the mechanical range of the simulator, but indicates a worst case scenario in terms of velocity requirements. To support this method, the maximum frequency at a full extension of any actuator (*i.e.* $0.4\ m$) can be defined as $f_{max} = 0.22583\ Hz$ to match the 95% PSD spectral power point as defined from the spectral analysis of the measured maritime vessel data. In this case the maximum possible linear velocity for any actuator was calculated as $v_{max} = 0.2728\ m.s^{-1}$. As this is a statistically derived value, and the probability of full deflection cycles at f_{max} is low, the velocity limit was chosen to be $v_{max} = 0.2\ m.s^{-1}$ and the friction identification input data sets limited to ones which were excited at that rate.

The measured data from a typical test set is shown in Figures 6.2 to 6.6 and the process described below is used on all the sample sets. The system is supplied with compressed air and regulated at a pressure of $0.4\ MPa$. The frequency of the signal generator is arbitrarily set at $0.1\ Hz$ and the amplitude adjusted to give the desired actuator travel. Exciting the system with a voltage as shown in Figure 6.2 resulted in the linear displacement of the actuator which was captured over approximately five and a half cycles and is shown in Figure 6.3. These graphs also show the $\alpha - \beta$ filtered signals. Using the displacement data with an α of 0.1 and a β of 0.005, the observer output included both the filtered displacement signal as well as the estimated rate as shown in Figure 6.4. Comparing the unfiltered displacement signal with the estimated displacement signal, the standard deviation of the point to point difference (residuals) was calculated to be $\sigma_x = 3.75 \times 10^{-5}\ m$ and the mean $\mu_x = 5.416 \times 10^{-7}\ m$. This indicated that the filter did not change the characteristic shape of the signal. Figures 6.4 and 6.5 show the velocity and chamber pressures respectively. The standard deviations of the difference between the raw signals (the output of the displacement estimator in the case of velocity) and filtered signals are $\sigma_v = 0.0019\ m.s^{-1}$, $\sigma_{p1} = 261.8\ Pa$ and $\sigma_{p2} = 277.2\ Pa$ respectively. The mean values for the differences are $\mu_v = -2.28 \times 10^{-5}\ m.s^{-1}$, $\mu_{p1} = -0.85\ Pa$ and $\mu_{p2} = 0.43\ Pa$, all insignificant relative to the signal they represent. The acceleration graph is not shown due to the limited use in putting it to paper.

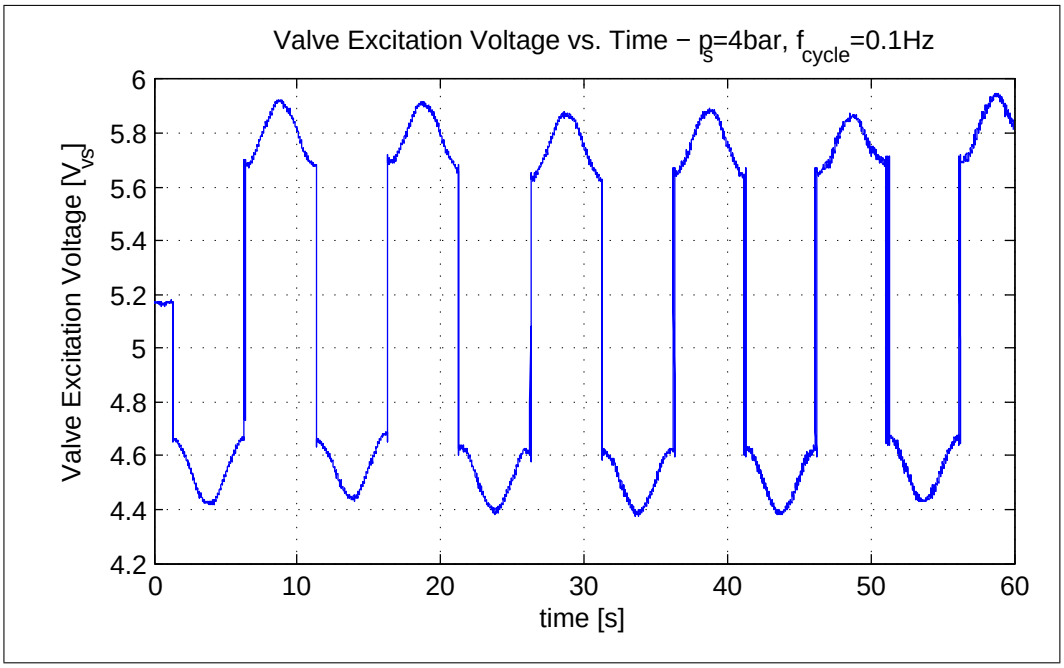

Figure 6.2: Valve Excitation Signal for Friction Characterisation - $p_s = 0.4\ MPa$, $f_{cycle} = 0.1\ Hz$

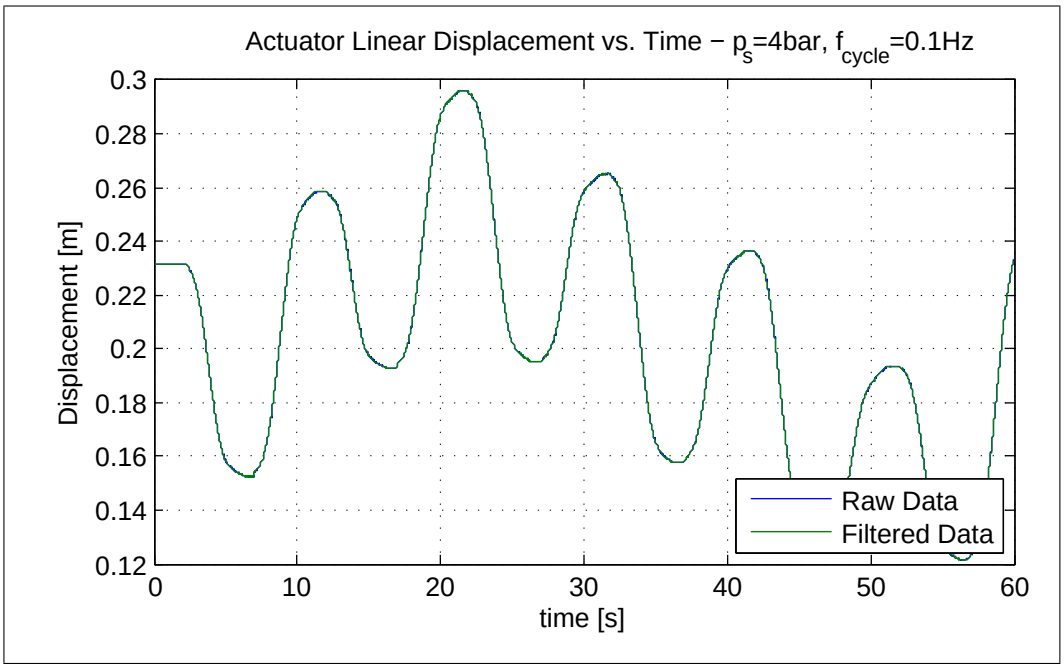

Figure 6.3: Pneumatic Actuator Linear Displacement for Friction Characterisation Compared with the Estimated Displacement from the α-β Filter - $p_s = 0.4\ MPa$, $f_{cycle} = 0.1\ Hz$

After pre-processing the measured data, and using Eq. 6.4, the friction force (F_f) *vs.* velocity (v) map was calculated and is shown in Figure 6.6. From this graph it can be seen that there is a very

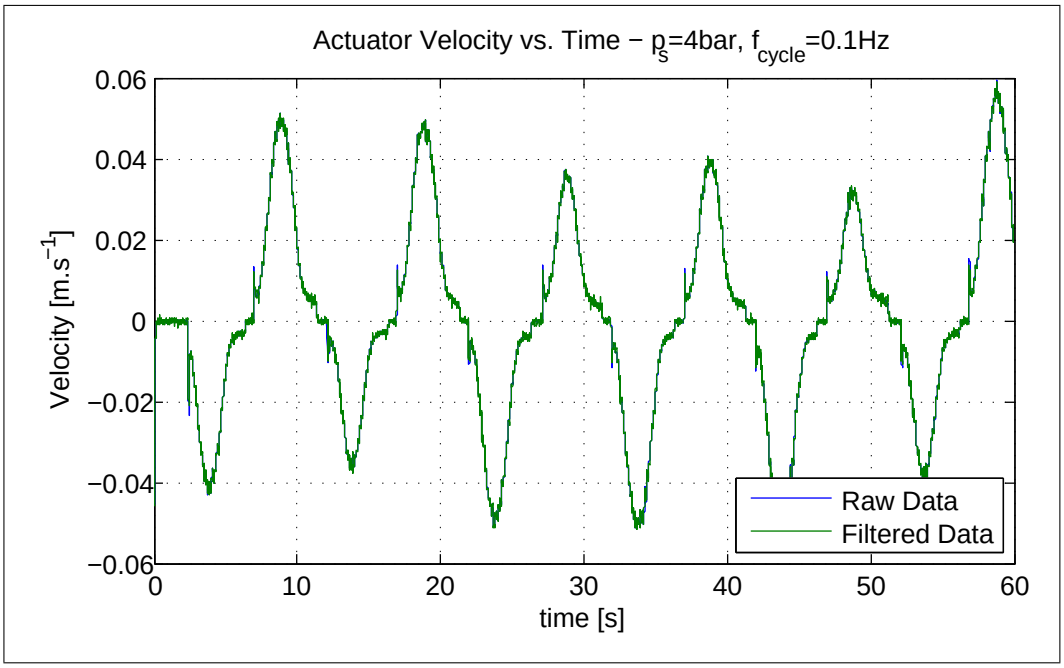

Figure 6.4: Pneumatic Actuator Velocity Derived From the α-β Filter Displacement Estimation Compared with the Velocity from the Velocity Estimation - $p_s = 0.4\ MPa$, $f_{cycle} = 0.1\ Hz$

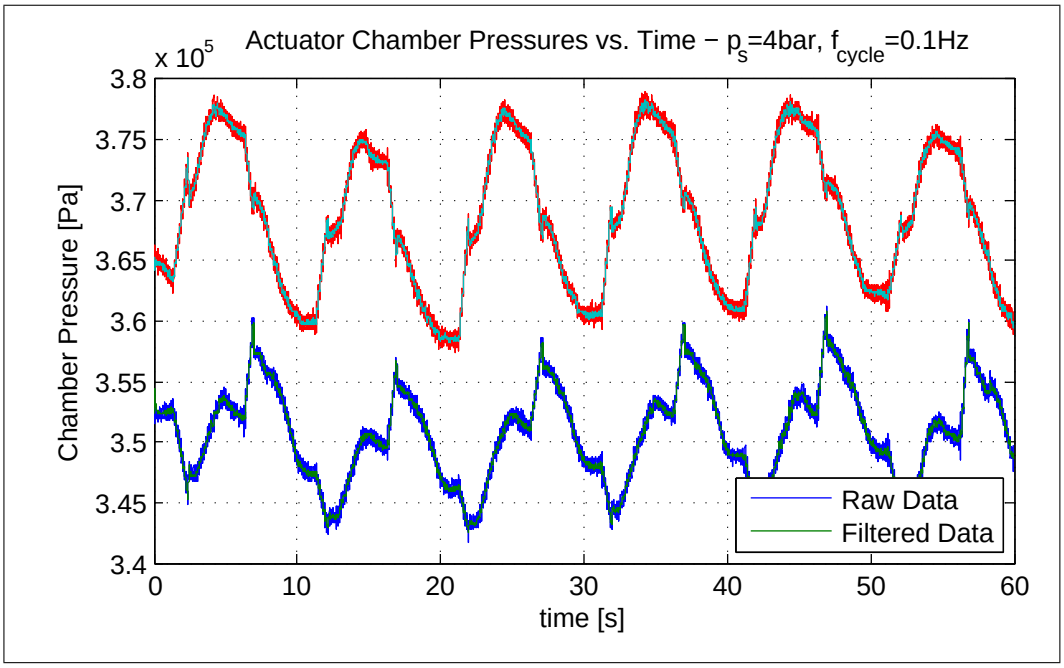

Figure 6.5: Pneumatic Actuator Pressure Compared with the Estimated Pressure from the α-β Filter Estimation - $p_s = 0.4\ MPa$, $f_{cycle} = 0.1\ Hz$

distinct Stiction (Static friction) component with a breakaway force of around 70 N, a constant offset from zero attributed to Coulomb friction, and a velocity dependent component attributed to viscous friction. The difference in friction force for an increasing velocity (positive acceleration) to that of a decreasing velocity (deceleration) is unclear in the figure. A temporal animation reveals that the friction force follows the upper path with acceleration and it follows the lower stiction-less path with deceleration.

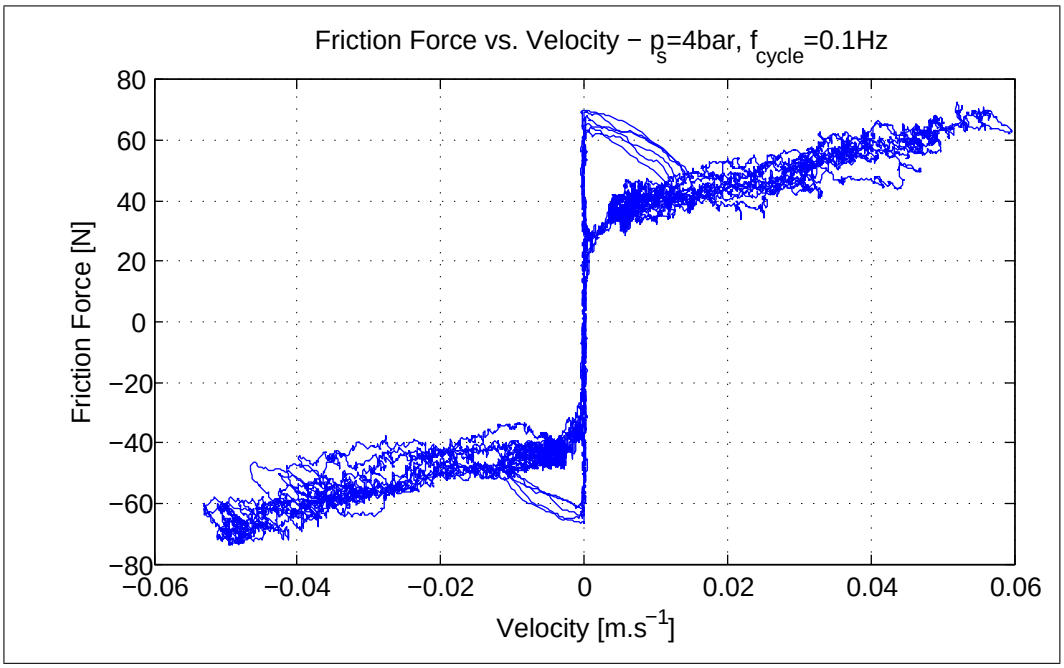

Figure 6.6: Pneumatic Actuator Friction Force as Function of the Velocity - $p_s = 0.4\ MPa$, $f_{cycle} = 0.1\ Hz$

No significant hysteresis is observed at low rates and low accelerations (*i.e.* low cycle frequencies), but it does become evident at higher rates and higher accelerations, becoming pronounced above $a_{RMS} > 0.19\ m.s^{-2}$. This manifests itself such that the decelerating part of the friction curve and the accelerating part of the friction curve no longer follow the same viscous friction profile in the gross sliding regime. An example of such hysteresis can be seen in a test sample shown in Figure 6.7. Another effect is an exponential increase in the friction force and a deviation from the theoretical linear trend of viscous friction with an increase in velocity (Figure 6.8). This sample has been excluded from the identification process due to the velocity range being too large and the presence of unmodelled dynamics. The exponential increase in friction force at higher velocities has been modeled as an extra term in the friction function, but the effect on the friction at the velocities of interest is negligible.(See

§ 6.4).

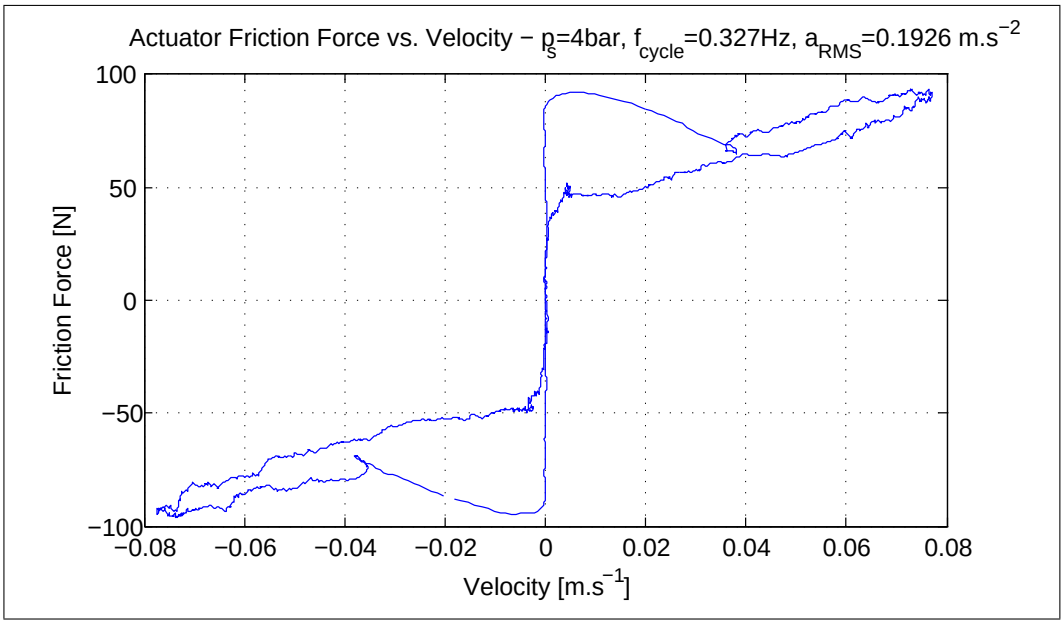

Figure 6.7: Pneumatic Actuator Friction Force as Function of the Velocity - $p_s = 0.4\ MPa$, $f_{cycle} = 0.327\ Hz$, $a_{RMS} = 0.1926\ m.s^{-2}$

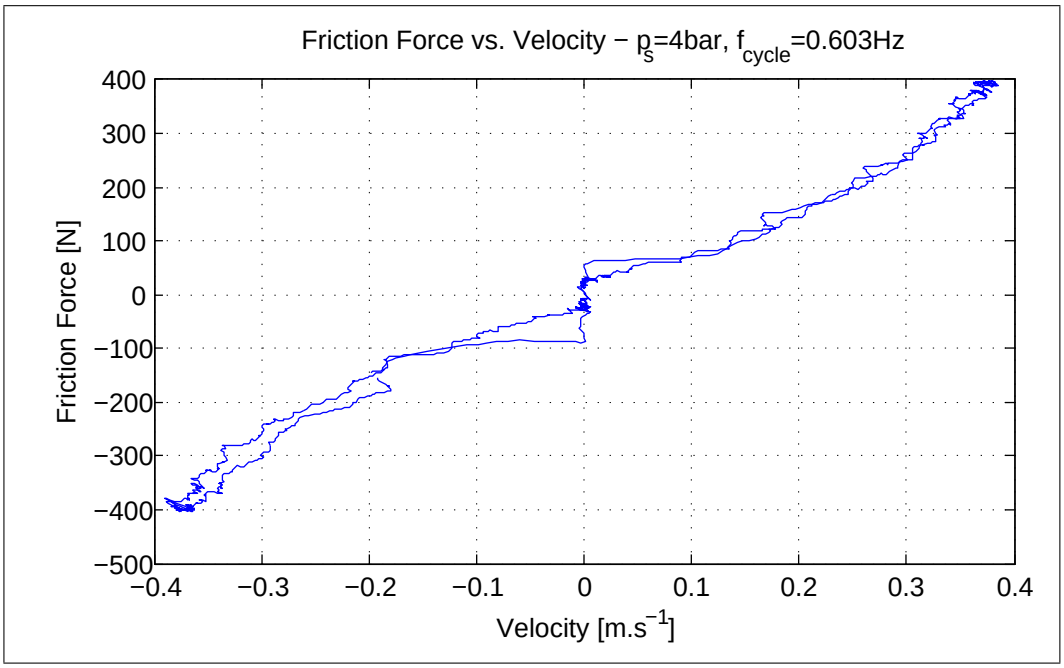

Figure 6.8: Pneumatic Actuator Friction Force as Function of the Velocity Showing the Force Deviation From the Linear Viscous Friction Trend - $p_s = 0.4\ MPa$, $f_{cycle} = 0.603\ Hz$

Taking all the measurement data sets and processing the data as described above produced a combined

friction *vs.* velocity map as presented in Figure 6.9. Here it can clearly be seen that the Stribeck velocity changes between different runs. After a rigorous analysis of various possible causes, it is postulated that the controlling effect is the acceleration of the movement. The physical cause is not yet understood, but for the sake of a representative model it was included as a modified Stribeck velocity.

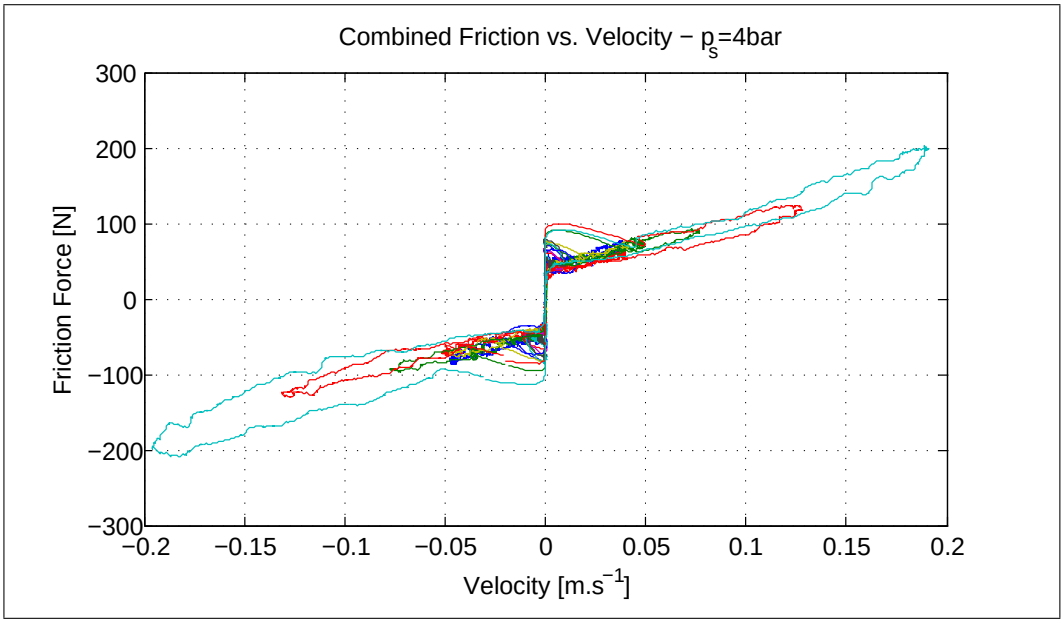

Figure 6.9: Pneumatic Actuator Friction Force as Function of the Velocity - $p_s = 0.4\ MPa$ for Different Maximum Velocities / Stroke Sizes.

6.4 FRICTION MODEL

Many friction models have been investigated and it was decided to limit the complexity of the model and exclude hysteresis in the pre-sliding regime. Another exclusion is the hysteresis in the gross sliding regime as described by the LuGre model.

Adopting the friction model used by Nouri [23] as the basis for the SMS model it can be stated that the model will have three dominant states, these being a pre-sliding state, a gross sliding accelerating state and a gross sliding decelerating state. The friction *vs.* velocity maps of the theoretical model for three different cycle frequencies are shown in Figure 6.10 with a more detailed plot of the lower velocity region shown in Figure 6.11.

As the velocity increases from zero to the maximum velocity ($v_{max} = 0.2\ m.s^{-1}$ in this example), the

friction force initially increases to a large value according to the stiction force. The modern friction models use the concept of an average asperity contact deflection that is initially elastic in nature, gradually starts slipping (a smooth transient - a combination of elastic and plastic slippage) and enter the gross sliding regime which is in theory purely plastic in nature.

In the SMS model the initial pre-sliding regime is simplified to a smooth transient between two stiction limits (ε_f, see Figures 6.10 to 6.12) that reach a peak of F_S. The friction function follows the top of the curve for increasing velocity and the bottom curve for decreasing velocity. Below the stiction limit (ε_f) the curve will transition back to a friction force of zero at zero velocity. The function is point symmetrical (or an "odd function") and the reverse will occur during the negative velocity cycle. At the end of the transient region the friction decreases with an increase in velocity which is described by the Stribeck function. Acceleration dependent friction together with the linear viscous friction component (F_V) and the constant Coulomb friction component (F_{C1}) give the curve its characteristic form. In its pure form, the friction function will be asymptotic to a line crossing the y-axis at F_{C1} and a gradient of σ_1. A similar line can be constructed for the decreasing velocity crossing the y-axis at F_{C2} and having a gradient of σ_2.

From some of the experiments, a deviation from the pure linear form was observed, forcing the model to include an exponential term to account for the deviation. The offset (ΔF_f) from the linear curve is attributed to unmodelled effects, the cause of which cannot be explained at present, but makes the model more representative. At low velocities the exponential term has very little effect, but becomes prominent at higher velocities. The SMS operating velocities fall outside the exponential region.

Detailed plots close to the origin are shown in Figures 6.11 and 6.12 (Note that the three curves in this plot are identical in the pre-sliding region and are congruent).

The friction model is then described by a direction determined point symmetric function F_f described by

$$F_f = \alpha_f \begin{cases} sgn(v)\left[F_{C1} + (F_S - F_{C1})\, e^{-\left(\left|\frac{v}{a\zeta v_S}\right|^{\delta}\right)} + F_{UE}\left(e^{(\gamma_f|v|)} - 1\right)\right] + \sigma_1 v & sgn(a) = sgn(v) \\ sgn(v)\left[F_{C2} + F_{UE}\left(e^{(\gamma_f|v|)} - 1\right)\right] + \sigma_2 v & sgn(a) \neq sgn(v) \end{cases} \tag{6.5}$$

with F_{C1} and F_{C2} the Coulomb friction (in N) y-intercepts respectively, F_S the maximum Stiction force (in N), v the linear velocity in $m.s^{-1}$, a the linear acceleration in $m.s^{-2}$ and δ the Stribeck exponent.

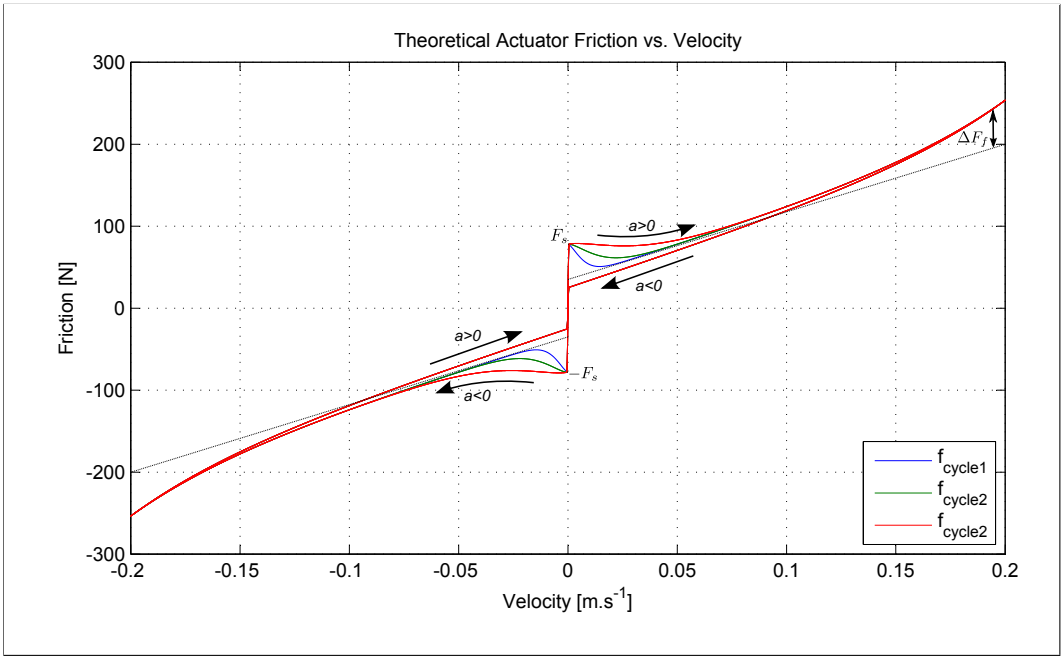

Figure 6.10: Pneumatic Actuator Theoretical Friction Force as Function of the Velocity at Three Different Cycle Frequencies

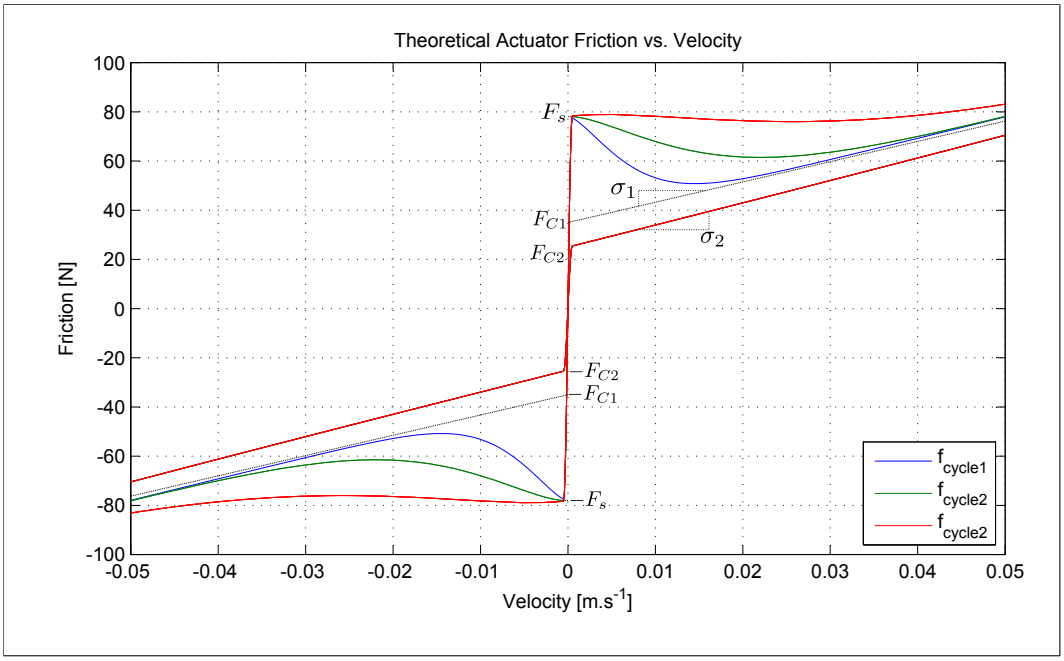

Figure 6.11: Low Velocity Region of the Pneumatic Actuator Theoretical Friction Force as Function of the Velocity at Three Different Cycle Frequencies

v_S is the Stribeck velocity and is modified by the instantaneous acceleration and the modification constant ζ. The gradients of the ascending and descending velocity curves are expressed as σ_1 and σ_2, both in $N.s.m^{-1}$. The unmodelled friction effects (ΔF_f) that cause the exponential increase at higher velocities are represented by a maximum deviation F_{UE} N, and the form function governed by γ_f which is an arbitrary constant in $s.m^{-1}$ found by system identification. The force deviation term is expressed as

$$\Delta F_f = F_{UE}\left(e^{(\gamma_f|v|)} - 1\right). \tag{6.6}$$

The friction force will quickly increase to a maximum value equal to the static friction F_s during pre-sliding. Although this model does not account for the asperity deflection theory, a discontinuity from $-F_S$ to $+F_S$ will generate large transients during simulation and a better behaved function was introduced to represent the transition across the origin. The stiction limits ε_f are chosen to be small relative to the identified Stribeck velocity of the system. Between the two limits the friction force will follow a curve described by the normal Stribeck function weighted by a sinusoidally varying function α_f, having a zero value at $v = 0$ and a value of 1 at $v = \varepsilon_f$. This velocity dependent function can be expressed as

$$\alpha_f = \begin{cases} \sin\left(\frac{\pi|v|}{2\varepsilon_f}\right) & |v| < \varepsilon_f \\ 1 & otherwise \end{cases} \tag{6.7}$$

with v the velocity in $m.s^{-1}$ and ε_f the stiction limit in $m.s^{-1}$.

6.5 FESTO ACTUATOR FRICTION MODEL

By using the measurements described in § 6.2, filtering the data and using a model estimation process, the average, best fit model for the SMS specific Festo actuator was determined. From Figure 6.9 it can be seen that the stiction value is not the same for all the experiments. The model estimation process showed that the sample mean of the stiction force is $\mu_{F_S} = 77.27\ N$ with a standard deviation of $\sigma_{F_S} = 4.67\ N$. If it is assumed that the stiction force (F_S) is a constant for a system with a specific lubrication and physical condition, and that these conditions do not change quickly, then an average stiction value can be used in the model and the variations from the experiments can be attributed to measurement errors, measurement noise and other uncertainties. All the other variable estimates converged to their final values very quickly. These are:

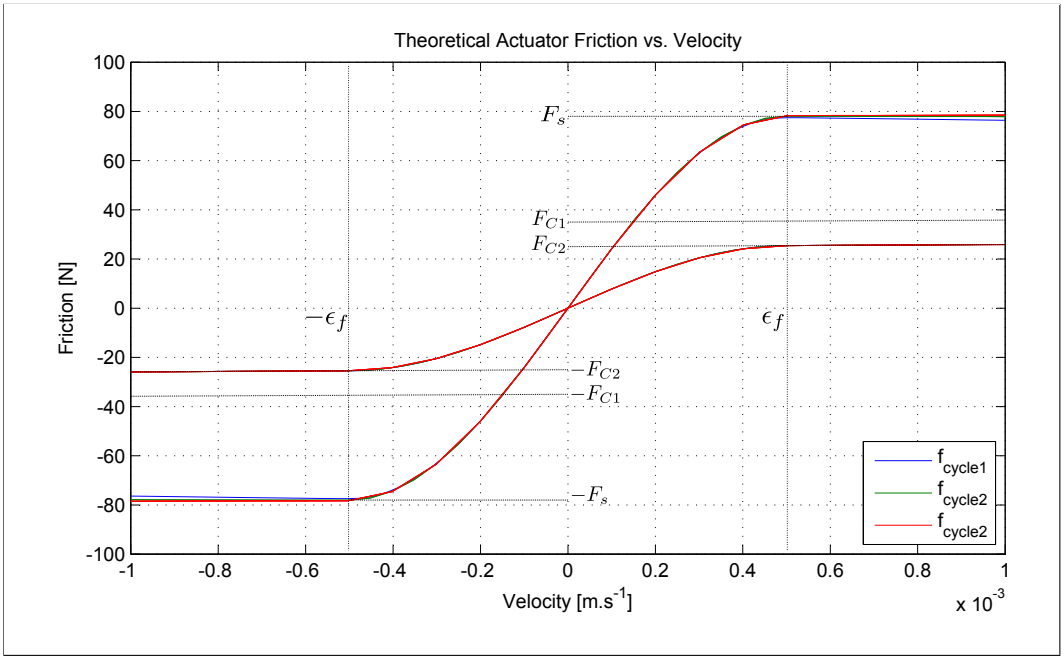

Figure 6.12: Pneumatic Actuator Theoretical Friction Force Inside the Stiction Region as Function of the Velocity at Three Different Cycle Frequencies.

- *Static Force:* $F_S = 77.27\ N$
- *Coulomb Friction ascending:* $F_{C1} = 38\ N$
- *Coulomb Friction descending:* $F_{C2} = 38\ N$
- *Viscous Friction Coefficient ascending:* $\sigma_1 = 530\ N.s.m^{-1}$
- *Viscous Friction Coefficient descending:* $\sigma_2 = 530\ N.s.m^{-1}$
- *Stribeck Velocity:* $v_S = 0.05\ m.s^{-1}$
- *Stribeck Exponent:* $\delta = 1.4$
- *Stribeck Velocity adjustment Constant:* $\zeta = 0.9\ s^2.m^{-1}$
- *Exponential form function exponent:* $\gamma_f = 13\ s.m^{-1}$.
- *Stiction Limit:* $\varepsilon_f = 0.005\ m.s^{-1}$

By using equation 6.5 and the variables listed above, the model fit was evaluated by applying the model to the measured linear displacement data. Three sets of data were selected to represent a low speed, a medium speed and a high speed, all falling in the actuator (and SMS) operational region. The measured friction *vs.* velocity maps are shown in Figures 6.13 to 6.15. In all three figures the blue trace represent the measured data and the green trace represent the output of the friction model using the measured velocity as an input. From these traces it can be seen that the theoretical

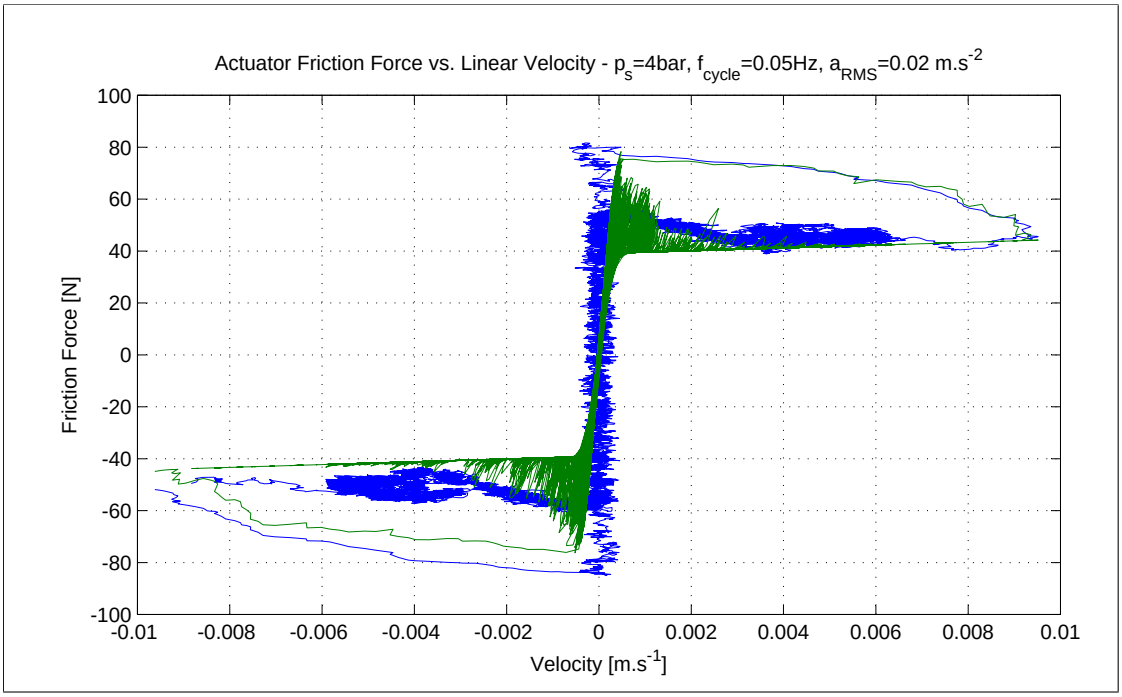

Figure 6.13: Pneumatic Actuator Friction Force as Function of the Velocity - Low Speed (Blue Trace - Measured Data, Green trace - Friction Model)

model reproduces the measured system fairly well. The low speed friction response visually fits the measured data very well. At the higher rates a much larger hysteresis can be seen which is not modelled in the friction model. We can therefore assume that the theoretical model as described by equation 6.5 represent the friction in the system adequately for controller design.

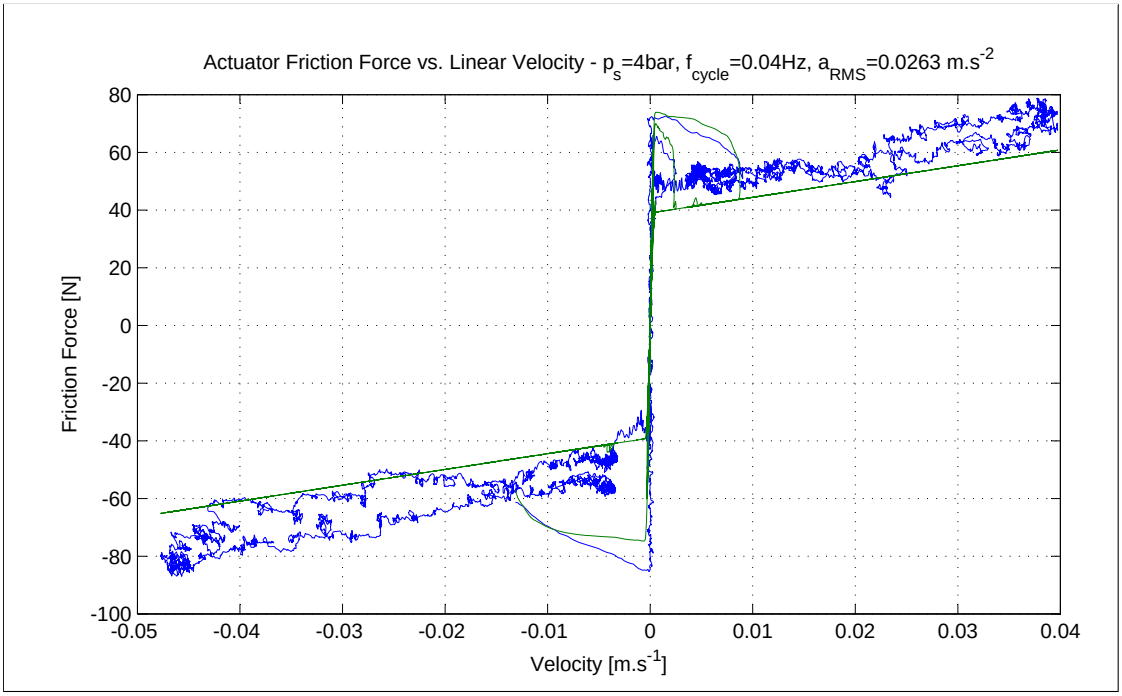

Figure 6.14: Pneumatic Actuator Friction Force as Function of the Velocity - Medium Speed (Blue Trace - Measured Data, Green trace - Friction Model)

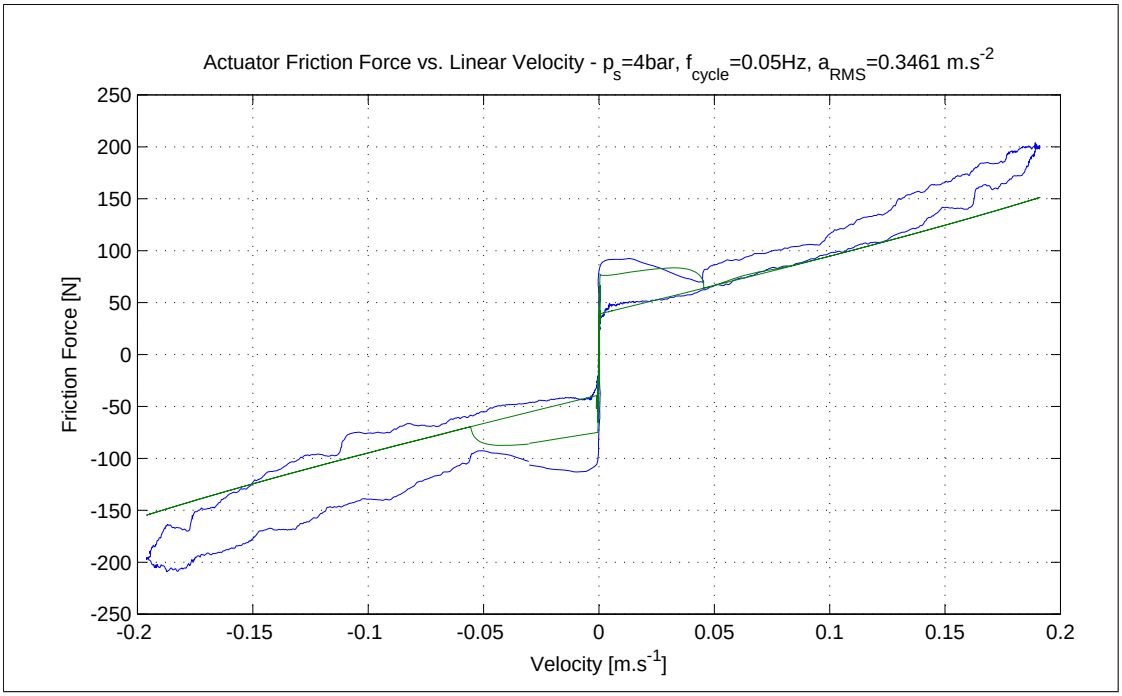

Figure 6.15: Pneumatic Actuator Friction Force as Function of the Velocity - High Speed (Blue Trace - Measured Data, Green trace - Friction Model)

CHAPTER 7

SIMULATION MODEL VALIDATION

The pneumatic system model, the kinematic and dynamic model in ADAMS®, and the friction model developed in the previous stages of the study have to be validated to ensure a reliable rendition of reality. As the system model complexity increases, and lower level models are combined into a larger higher level model and the effects of unmodelled phenomena accumulate. The specific contribution of those effects on the results become unclear making the validation process difficult and fault finding impossible.

A Matlab® Simulink® simulation of one of the actuators was compiled and various scenarios executed to assess the reliability of the models. These scenarios were similar to the actuator friction identification process, chosen to fall within the operational domain of the SMS. The same experimental configuration used for the friction identification (§ 6.1) was used in the validation of the actuator model. Once the pure theoretical model was validated the simulation was expanded to an ADAMS®/Matlab® Simulink® co-simulation. The pneumatic and friction models were tested against the experimental data by initially using a single actuator model and subsequently the full SMS model. A series of open-loop and closed-loop experiments were designed and executed and a comparison done between the measured data and the simulated data.

7.1 FESTO ACTUATOR MODEL VALIDATION

7.1.1 Matlab® Simulink® Model Description

The test setup as described in § 6.1 was used and a series of additional tests were conducted with varying frequencies over a range of 0.1 Hz to 1 Hz and an amplitude range of 0 V to 2 V. The

limitation on the open-loop excitation of the actuator is the available actuator travel which results in a frequency-amplitude trade-off. As the frequencies are reduced, the amplitudes can be increased and *visa versa*. Modifications to the excitation signals were 1) the addition of an arbitrary offset to make the piston movements more symmetrical and 2) a deadband compensation to quickly traverse the central working area of low air flow. Though these modifications are not particularly important they do, however, make for easier data analysis. As both the simulation and the experiment used the same input signal, the comparison is valid in any of the cases.

The simulation model compiled in Matlab® from the pneumatic model identification and the friction model identification processes is shown in Figure 7.1. This is a purely mathematical simulation run in Matlab® using the actual measured solenoid input signal as the input and outputting the chamber pressures, chamber volumes and actuator displacement. Referring to the block diagram the pneumatic

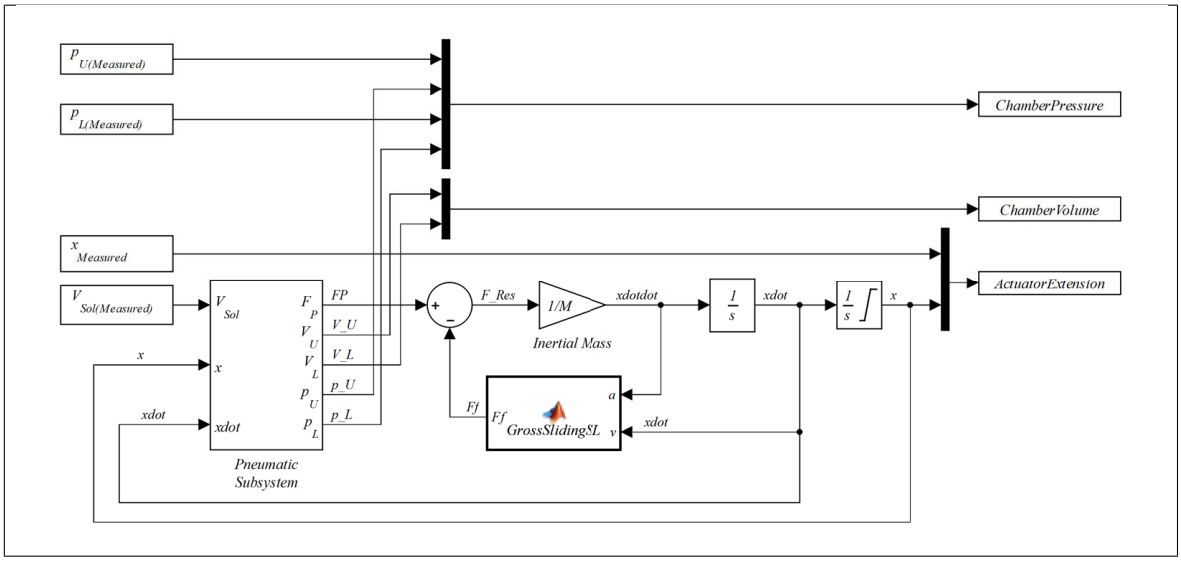

Figure 7.1: Actuator Matlab® Simulink® Model used for Actuator Model Validation

model is compiled as a "per-actuator" entity, as is the friction model. This can easily be expanded to a model with multiple actuators at a later stage. No stochastic behaviour such as random offsets, changing coefficients in the friction model or noise has been built into the model. All copies of the actuator will therefore function exactly the same with the same input.

The pneumatic model has the measured solenoid signal ($V_{Sol(Measured)}$) and the fed back piston displacement (x) and velocity ($xdot$) as inputs. Of the latter two, only the displacement is a directly measurable entity. The pneumatic force (F_P), the upper and lower chamber volumes (V_U and V_L) and

the upper and lower chamber pressures (p_U and p_L) are obtained from the model. In this model the lower chamber is equivalent to chamber a and the upper chamber to chamber b in Figure 4.1. This makes it easier when referring to the physical assembly of the SMS. The pneumatic model block diagram is shown in Figure 7.2. In this model the solenoid voltage (V_S) determines the mass flow

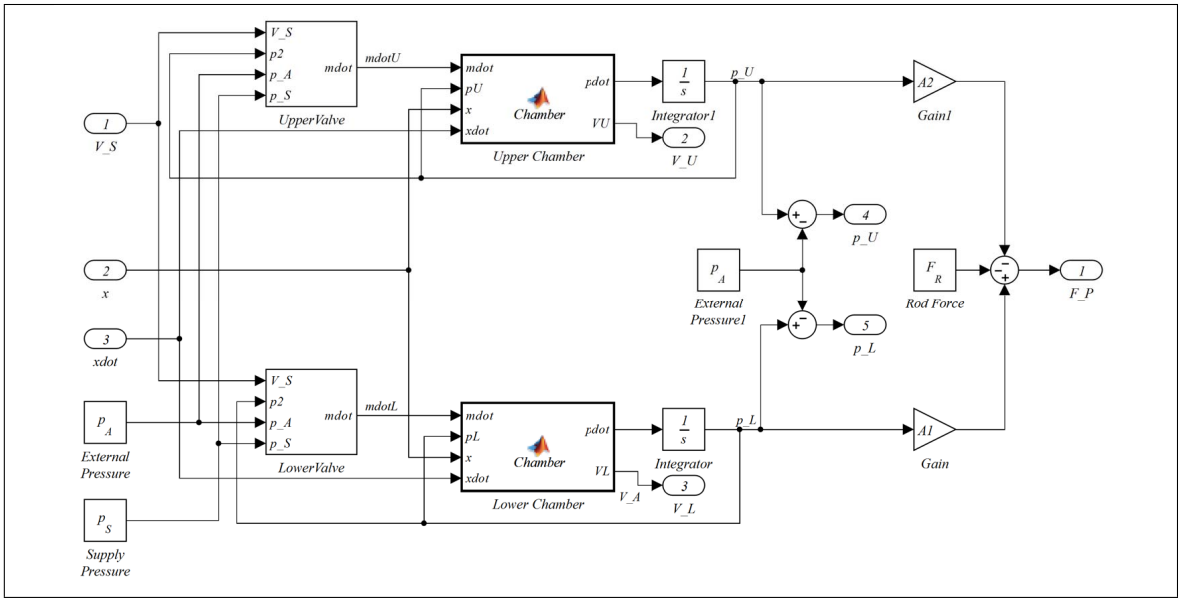

Figure 7.2: Pneumatic Subsystem Matlab® Simulink® Model Used for Actuator Model Validation

through the valve using the ISO valve model compiled in § 5.1.2 and a switching function to determine the voltage dependent source and sink pressures. For a valve spool deflection in one direction the source pressure would be the high pressure feed to the system and the sink pressure would be the actuator chamber pressure. A deflection in the opposite direction will result in the source pressure being the actuator chamber pressure and the sink pressure the outside vented ambient pressure. A valve orifice per actuator chamber is used and labelled "UpperValve" and "LowerValve". The lookup tables derived from the model identification and the switching function are shown in Figure 7.3. The outputs of the valve models are the mass flow rates through the valve orifices and hence into or out of the actuator chambers. A gain had to be applied to the mass flow rate to compensate for the change in the air flow characteristics from the reservoirs to the actuator, in effect a change in the α_i and α_o coefficients. Experimental iterations revealed these gains to be between 1.5 and 1.65 in both the upper and lower pneumatic circuits.

The upper and lower chamber models are directly derived from the pressure rate equation for a pressure chamber (eq. 5.4). It consists of two terms, one describing the pressure change due to the in and

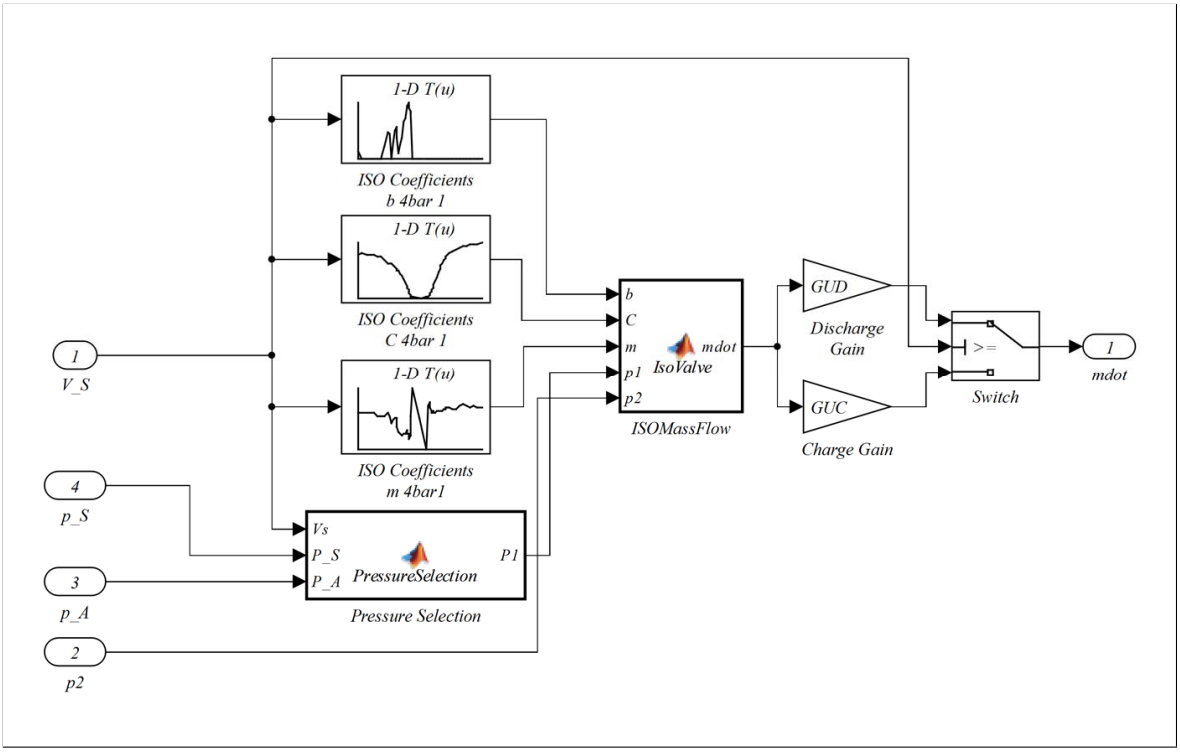

Figure 7.3: Upper Valve Mass Flow Matlab® Simulink® Model Used for Actuator Model Validation

out flow of air, and the other describing the pressure changes due to volume changes as the piston moves. The integrated output of the chamber pressure will then act directly on the two piston surface areas and result in the pneumatic related force (F_P) exerted by the piston. The difference between this force (F_P) and the friction force (F_f) will be the resultant force (F_{Res}) acting on the moving mass.

The simple dynamic model is realised with a single gain to account for the linear momentum followed by two integrators for model state changes. The last integrator is limited in output to the travel length of the actuator. All the displacement values are centre zero in $[m]$ (a value of zero at the centre of the actuator travel) and all the pressures absolute in $[Pa]$.

The friction model is implemented as a Matlab® function described by equations 6.5 and 6.7 in § 6.4.

In order to compare the theoretical Matlab® Simulink® model with the actual hardware, the measured data for a specific experiment is evaluated against the model output for that experiment, specifically the displacement and pressures. The initial conditions for the simulation are derived from the meas-

ured data.

7.1.2 Matlab®/ADAMS® Actuator Model Description

As an interim step in the building of the Matlab®/ADAMS® co-simulation of the SMS a model of a single actuator was compiled. This could be verified directly with the Matlab® Simulink® actuator model and the measured bench top experimental data. The block diagram of the Festo actuator

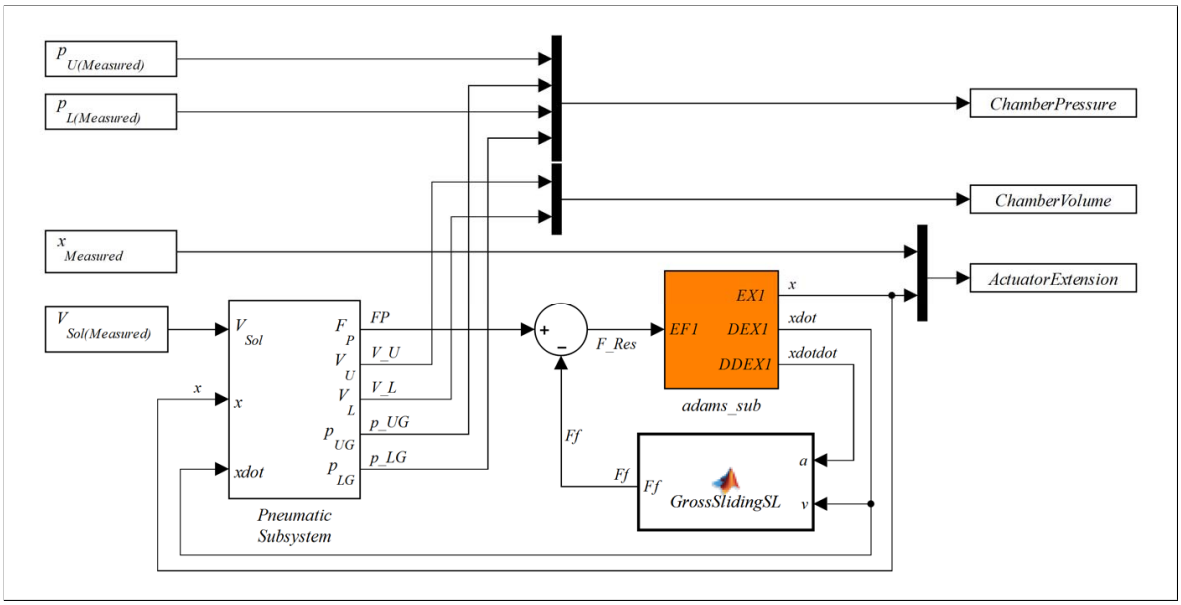

Figure 7.4: Matlab® Simulink®/ADAMS® Model Used for Actuator Model Validation

secured to a firm base as exported from Matlab® Simulink® is shown in Figure 7.4. The dynamic functions of the model such as momentum and external force perturbations are added by ADAMS® and the pneumatic and friction functions are added by Matlab®. The block named "*adams_sub*" has a force input and a displacement, velocity and acceleration output. An important part of this test is to confirm the correct integration between ADAMS® and Matlab®. The ADAMS® model is shown in Figure 7.5. On the left hand side of the image the fixed connection to the simulation ground entity is indicated as a lock icon. This connection anchors the cylinder to the ground reference. A cylindrical connection with insignificant friction is placed between the cylinder and the piston, thereby constraining the piston movement in the x-direction. An extra limitation is placed on the rotation of the piston. To connect the model to Matlab®, an ADAMS® "controls plant" was generated with a single component force parametrically aligned with the two bearing centres as input, and three dimensional system elements ($EX1$, $DEX1$, $DDEX1$) as the output states. The outputs are

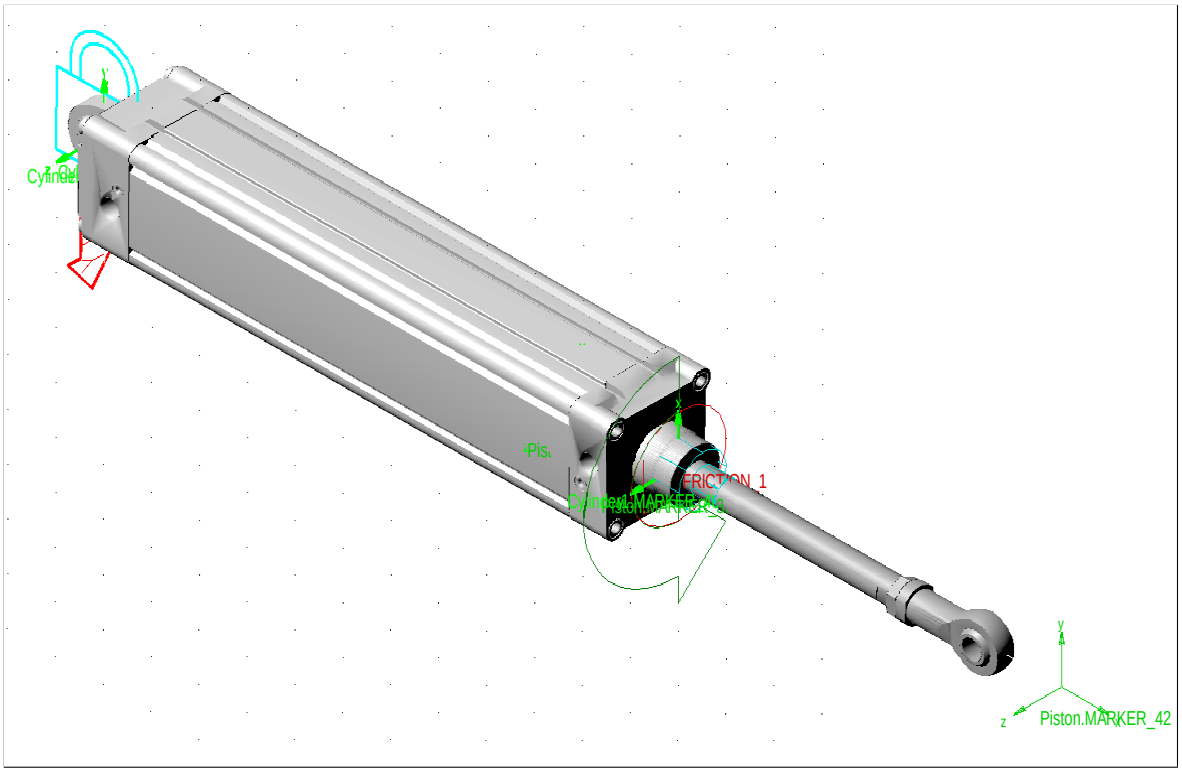

Figure 7.5: ADAMS® Model Used for Actuator Model Validation (”*adams_sub*”)

also aligned with the two bearing centres. Although the acceleration and velocity are not measurable entities in the real system, the output of these variables from ADAMS® is necessary for the inputs to the friction model.

7.2 ACTUATOR MODEL VALIDATION

As mentioned in the introduction, the actuator hardware responses were compared with the simulation model through a series of experiments. The amplitude and frequency of the excitation signal were varied across the useable range of the actuator, taking the mechanical travel of the actuator into account. All the validation experiments were done with a source pressure of 0.4 *MPa*.

The correlation between the measured data and the simulated data varied and some of the experiments delivered better fits than others. In general it was found that the fit was better at larger valve openings than smaller ones. This was attributed to the accuracy of the friction model and the pneumatic model relative to the changing lubrications and air temperatures. It was also noted that the model was very sensitive to variations in the initial conditions of the states and particularly their first and second

derivatives.

The characteristics of the system used for a first order validation in the case of both the Matlab® Simulink® and Simulink®/ADAMS® co-simulation were the tracking of the piston extension (x) and the chamber pressures (p_U and p_L). It should be noted that due to the extent of this series of experiments, only a first order validation was done. One examples is shown for the purpose of completeness.

A signal centred around an arbitrary point close to 5 V was generated as an input to the proportional valve. This signal is shown in Figure 7.6. The offset from 5 V is added to ensure that the physical movement of the piston stays symmetrical and that there is little drift from the initial position. In the first example the offset to achieve zero average drift of the actuator piston was 0.165 V. The initial signal is a sine wave with an amplitude of 0.54 V and a frequency of 0.328 Hz. A $\pm$0.5 V offset was added to the centre of the signal to compensate for the mechanical valve orifice overlap and reduced flow region. The resultant piston displacement from both the simulation as well as

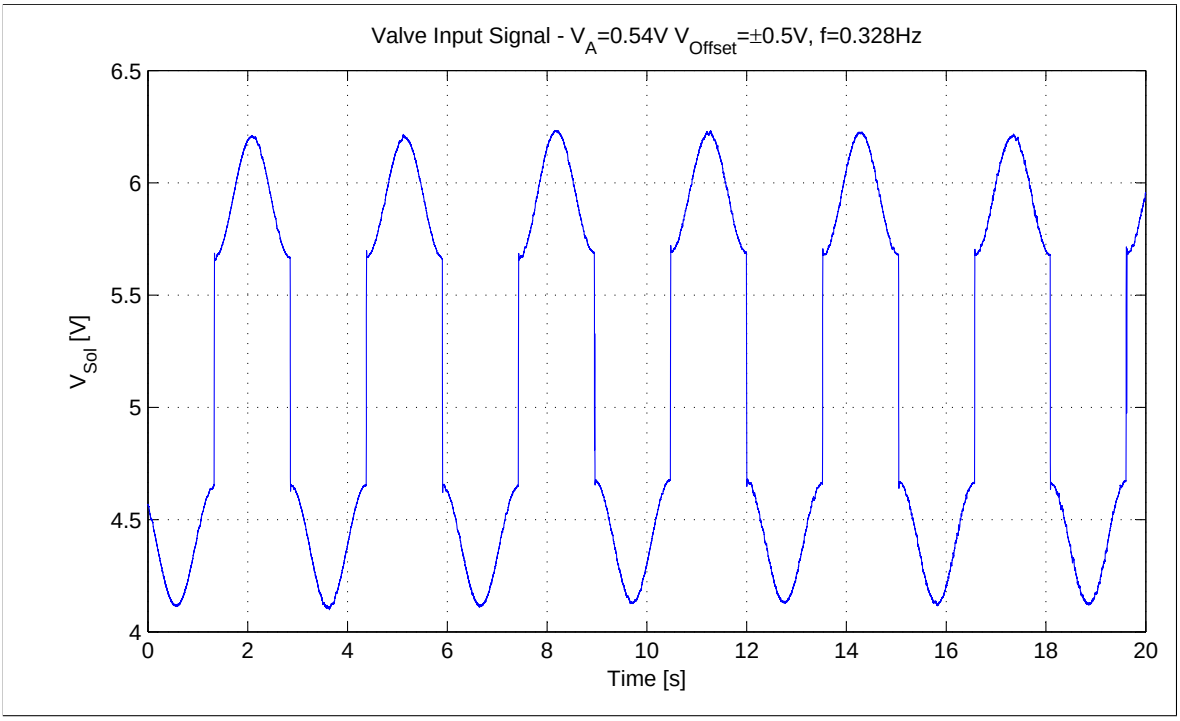

Figure 7.6: Input Signal (V_{Sol}) for Matlab® Simulink® Actuator Model Experiment

the measurements is shown in Figure 7.7. Comparing the two traces two major things are evident. Firstly, the amplitude of the simulated signal is a close match to that of the the measured signal. The measured signal has an approximate travel of 81 mm_{p-p}, whereas the simulated displacement

is around 87 mm_{p-p}. The simulated travel is approximately 7% larger than the measured travel. Secondly, the low frequency trend, although not exactly the same in both cases, follows the same basic form. On the downside and immediately noticeable is the apparent delay in the simulated displacement relative to the measured signals. The delay is around 200 *ms* and does not change with different input conditions. It is postulated that this is due to the lack of translational movement in the friction model as the pneumatic seals deform immediately prior to moving into the gross sliding regime. In reality the seal elastic deformation allows a movement of the piston without the sealing surface actually moving, a characteristic that is not modelled in the current model. If the chamber

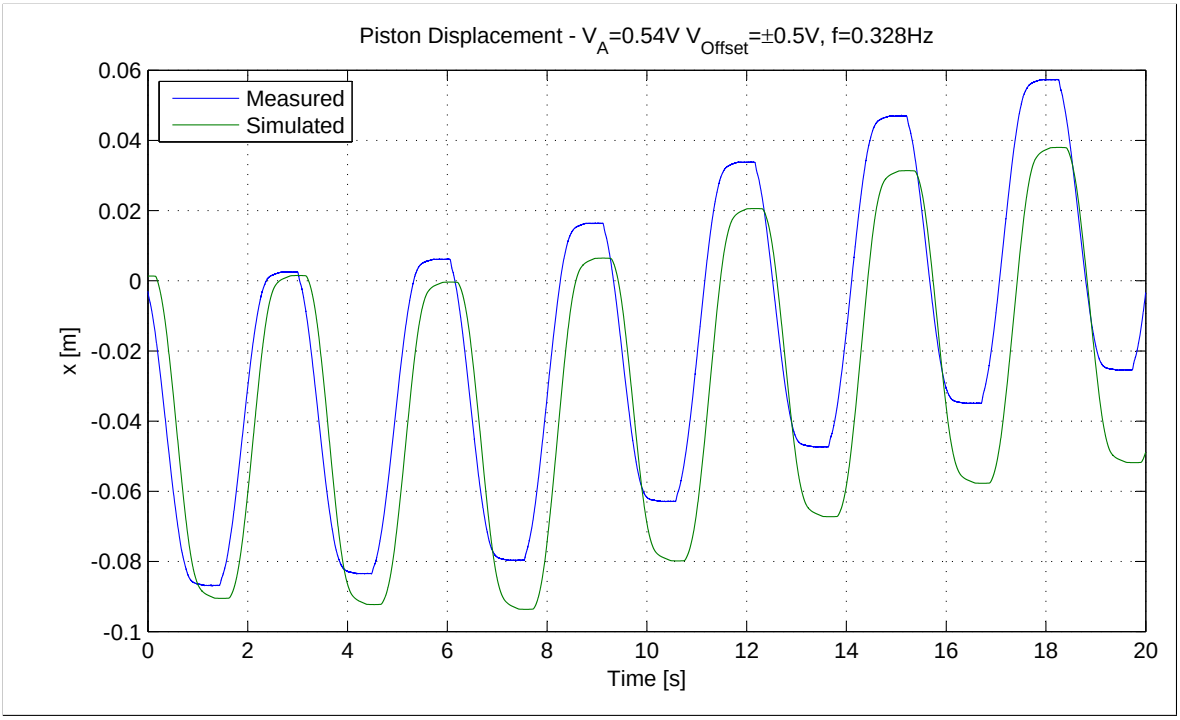

Figure 7.7: Actuator Linear Displacement (x_1 and $x_{1(Measured)}$) for the Matlab® Simulink® Actuator Model Experiment

pressures of the simulated system are compared with that of the real system (as shown in Figures 7.8 and 7.9), they are very similar. Keeping in mind that the chamber pressures are very dependent on the instantaneous volume as well as the volumetric rate of change of the chamber, small deviations are to be expected. The simulated output tracks the measured data with adequate precision for the scope of this study. Slight roundedness of the simulated output on the upper peaks of the upper chamber pressure (Figure 7.8) and delayed pressure reduction immediately after the peaks correlate to the slower and delayed piston movement indicated in the displacement graphs. The same phenomena are present in the lower chamber bottom peaks. In both of the chamber pressure graphs, the primary

frequency of the signal is well presented, as is the rate of change of the pressures. Once again the initial conditions play a major role in the transients of the model as noticed from the experimental data. These experiments show that the model of the actuator is an adequate representation of the real world actuator if used within the $0-1$ Hz frequency range and at a supply pressure of 0.4 MPa.

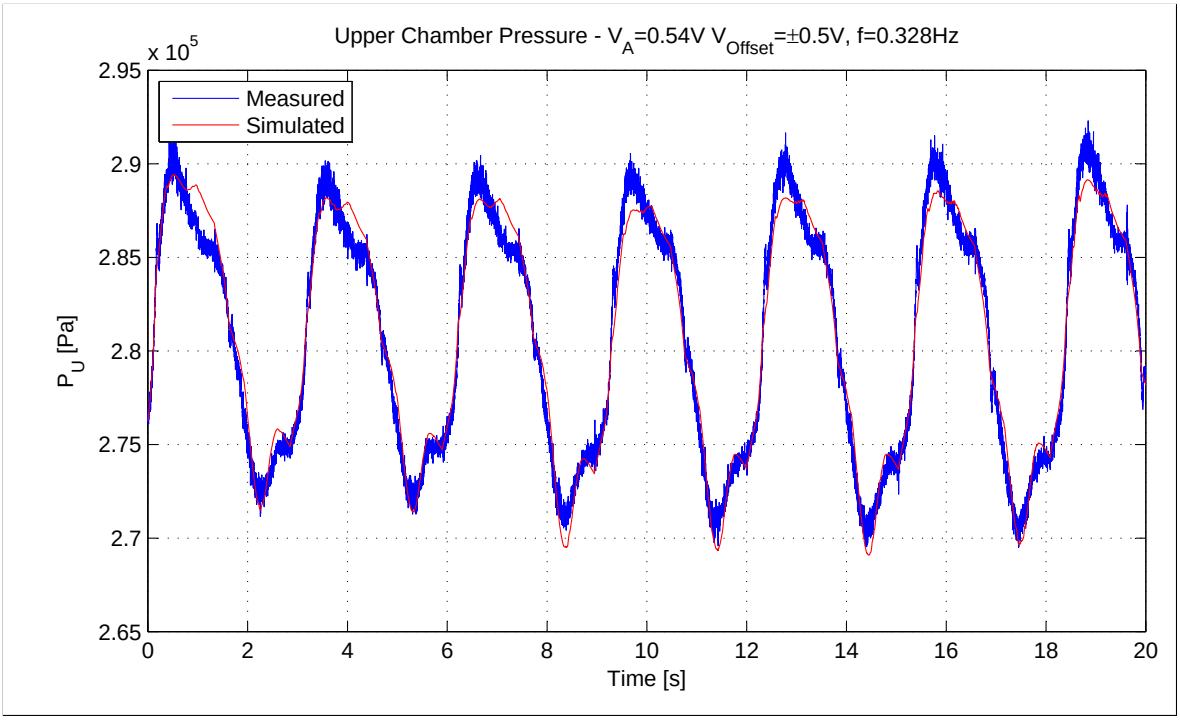

Figure 7.8: Upper Chamber Pressure (p_U and $p_{U(Measured)}$) for the Matlab® Simulink® Actuator Model Experiment

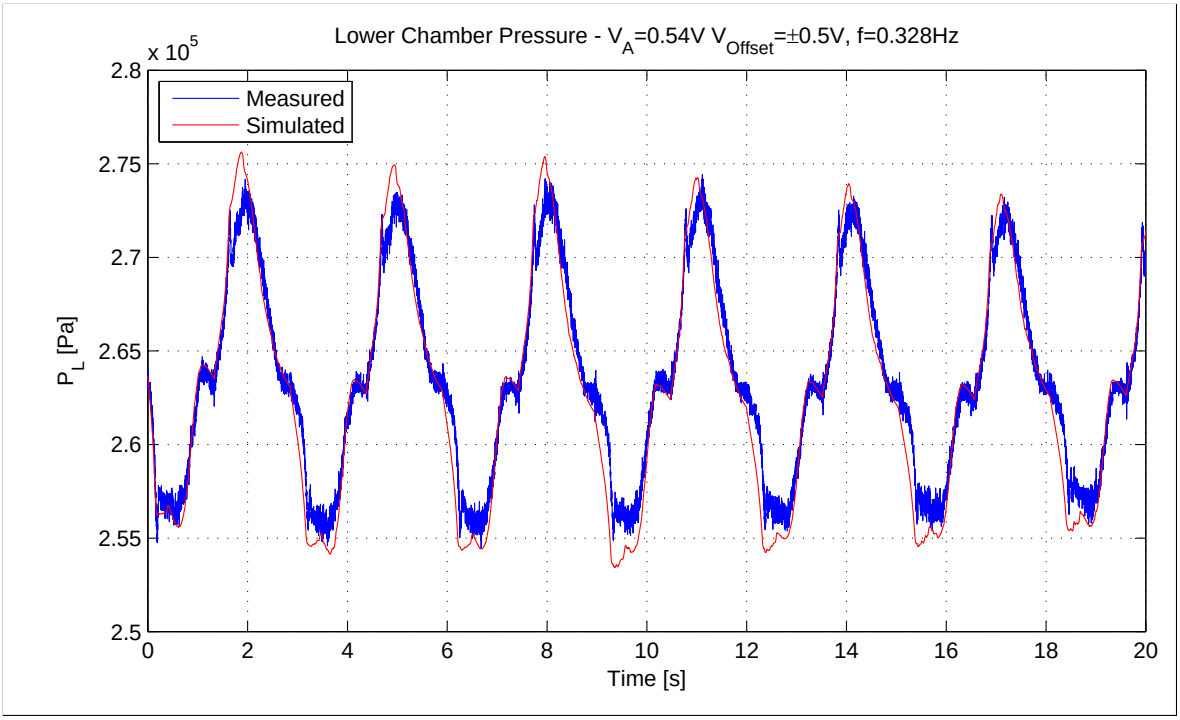

Figure 7.9: Lower Chamber Pressure (p_L and $p_{L(Measured)}$) for the Matlab® Simulink® Actuator Model Experiment

7.3 SMS MODEL VALIDATION

The model of the actuator using Matlab® Simulink® and ADAMS® in a co-simulation has been shown to be of adequate accuracy and represents the primary characteristics of the real actuator under the conditions it was tested under. In order to simulate the complete SMS system, a similar validation process needs to be run. The dominant characteristic of the pneumatic actuator is similar to an integrator, resulting in a constant extension with a step input in valve opening. The value of open-loop step and impulse response tests is deemed to be limited. As the system is clearly a nonlinear system, even closed-loop step and impulse responses have questionable usefulness.

Two experiments of the complete system were therefore defined. The first is an open-loop test about the midpoint of the actuator travel with a sinusoidal input variation. The second experiment is a closed-loop test with an Amplitude Modulated Pseudo-Random Binary Signal (APRBS) input. In both of the above-mentioned tests, the input signal which was used to excite the experiment will also be used to excite the Matlab® Simulink®/ADAMS® simulation. Both the actuator extension output and the chamber pressure outputs from both the experiment and the model will subsequently

be compared.

7.3.1 SMS Matlab® Simulink® Model

The complete SMS dynamic system was initially defined in Figure 3.8 as a Simulink® S-function addressing the "adams_plant" defined in the MSC ADAMS® SMS model. It had three single component forces (PF_1, PF_2 and PF_3) - aligned with the three actuator piston rods - as inputs and a linear state (x_i) and the platform angles (roll, pitch and yaw) as outputs. This model has subsequently been updated for the purpose of validation to include all the linear states, *i.e.* the actuator extension (x_i), the actuator extension rate ($\dot{x}_i$) and the extension acceleration ($\ddot{x}_i$). The new SMS model, including a signal generator and simple controller for the open-loop validation is shown in Figure 7.10. As in the actuator validation model, the friction and pneumatic functions are modelled in Matlab®, whereas the kinematics and some of the dynamics are modelled in ADAMS®. The three actuators are copies of the same model, with the same coefficients, inputs and outputs. Each of the pneumatic subsystems are

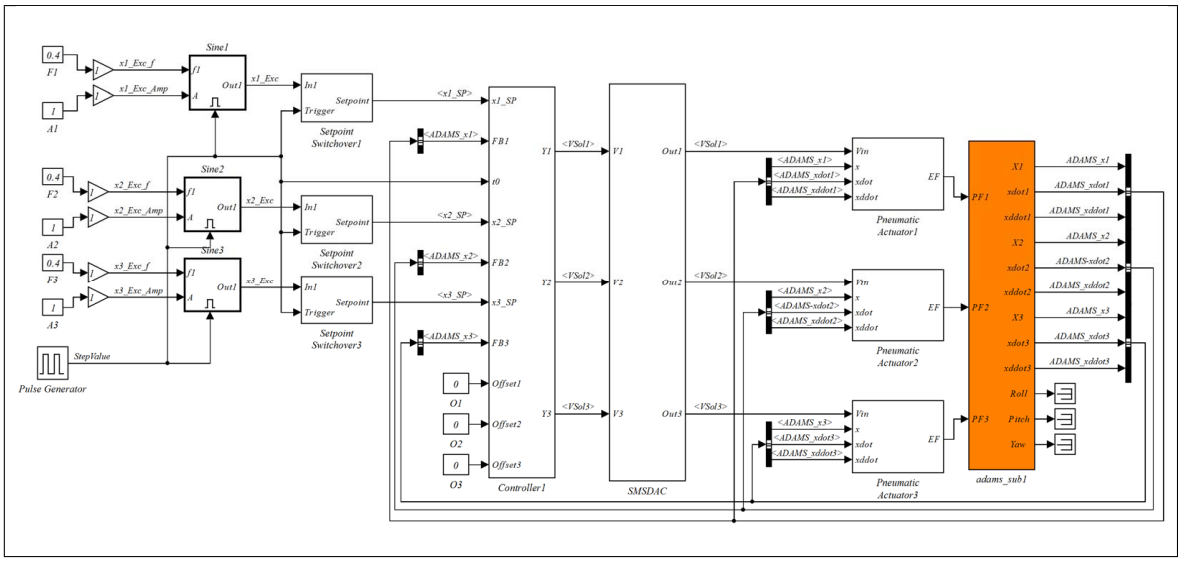

Figure 7.10: SMS Model Block Diagram Used For Simulink®/ADAMS® Simulation Open-Loop Simulations

controlled by a voltage input to the proportional control valves indicated by signals *VSOL1* to *VSOL3*. The force output is passed on to ADAMS® via the three system elements *PF1* to *PF3* and the states fed back to the pneumatic models for the determination of chamber volume, volumetric rate and the friction forces. The physical hardware includes all these blocks in the final system. In the real world system the interface to the valves is realised by DACs fed into low-pass filters. In the Matlab® envir-

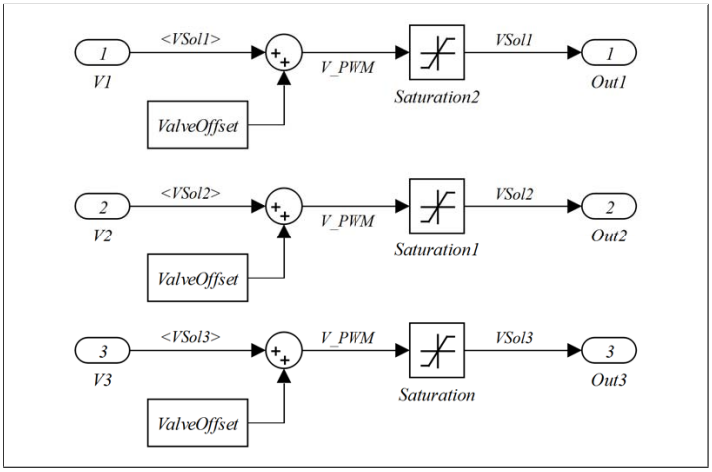

Figure 7.11: Digital to Analog Converter (DAC) Model Used For Matlab® Simulink® Simulation

onment this is redundant and the interface is modelled as an ideal DAC with a voltage range of 0 V to 10 V (See Figure 7.11). A 5 V valve offset (*ValveOffset*) is added to shift the zero centered output of the controller to the midpoint of the valves, translating a zero command signal into a zero air flow condition. The open-loop experiments are designed to level the SMS off at mid-height ($x = 0$) under

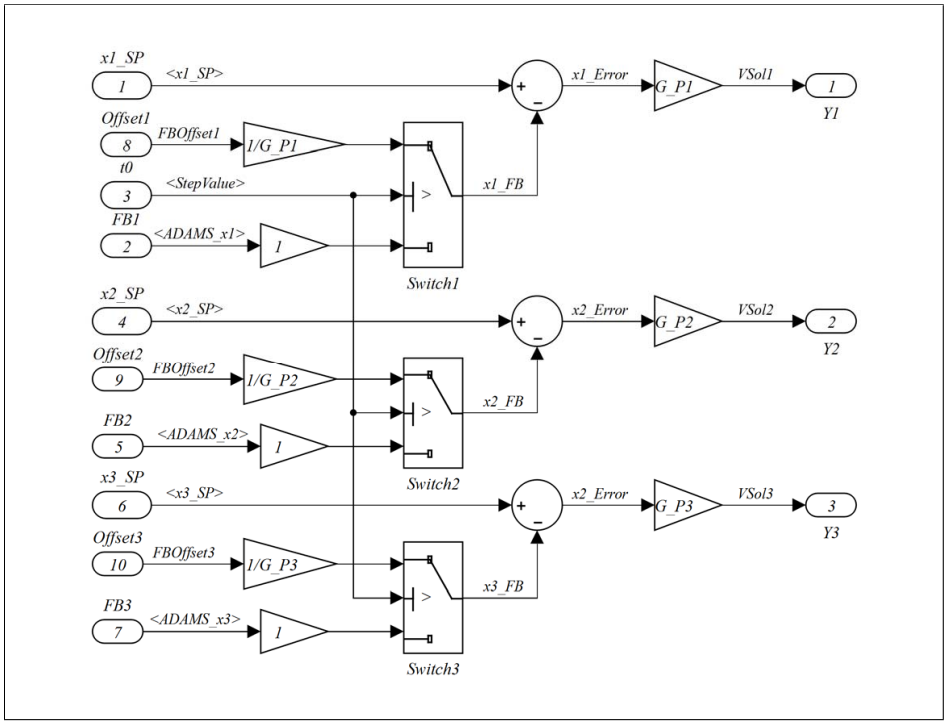

Figure 7.12: Controller Used For Matlab® Simulink® Simulation

closed-loop control with a low gain proportional controller and then starting the open-loop sinusoidal

excitation when the system has settled. To achieve this a changeover is needed which is generated by the "*Pulse Generator*" function. A settling time of 2 seconds is used for the closed-loop and is governed by the variable "*StepValue*". This variable is used as an input to the function generator, the setpoint changeover functions and the controller (Figure 7.12).

When the "*StepValue*" is zero, the feedback from the linear displacement system elements in ADAMS® (<*ADAMS_xi*>) are used to close the loops through the "*Switch1*" to "*Switch3*" switches, generating the error signals '*x1_Error*" to "*x3_Error*". The forward gains of the controller are depicted by "*G_P1*" to "*G_P3*" and were fixed at a value of 50 through iterative experimentation. This value delivers acceptable settling times and adequate control for the experiment.

When the "*StepValue*" is changed to one, the feedback loops are broken and an offset corrected by the inverse of the forward gain is subtracted from the setpoint signal. The setpoint signal is then changed from a constant value of (in this case) zero to a time varying sinusoidal signal.

The signal management part of the model (blocks to the left of "*Controller1*") will be discussed in § 7.3.4.

7.3.2 Real Time Work Shop (RTW) Controller

A very similar block diagram (Figure 7.13) represents the embedded code that will run on the controller hardware described in § 7.3.3. This block diagram is a copy of the central part of the Simulink® model (Figure 7.12). The power of Real Time Work Shop (RTW) comes into play with this transfer of systems, giving the firmware developer the ability to reuse a Simulink® model in the actual hardware design. The process of transferring the Simulink® generated code into CCS is described in full detail in Appendix B. The main idea behind the Matlab® embedded coder is to design firmware through a graphical interface, generate the C-code and compile and download the firmware onto a suitable platform. The code generated through the embedded coder mostly runs in a real time mode with a predetermined sampling rate. All general blocks in Simulink® are therefore executed periodically at the defined time intervals set by the the main timer. In the case of the Texas Instruments (TI) TMS320F28335 processor, this is realised by a timer overflow generated interrupt routine and task scheduling at multiples of the base sampling rate. All the peripheral systems such as the ADC, Pulse Width Modulation (PWM), timers, clock speed and communication ports (Serial Communication Interface (SCI), Controller Area Network (CAN)) are initialised by a "*Target Preferences*" block

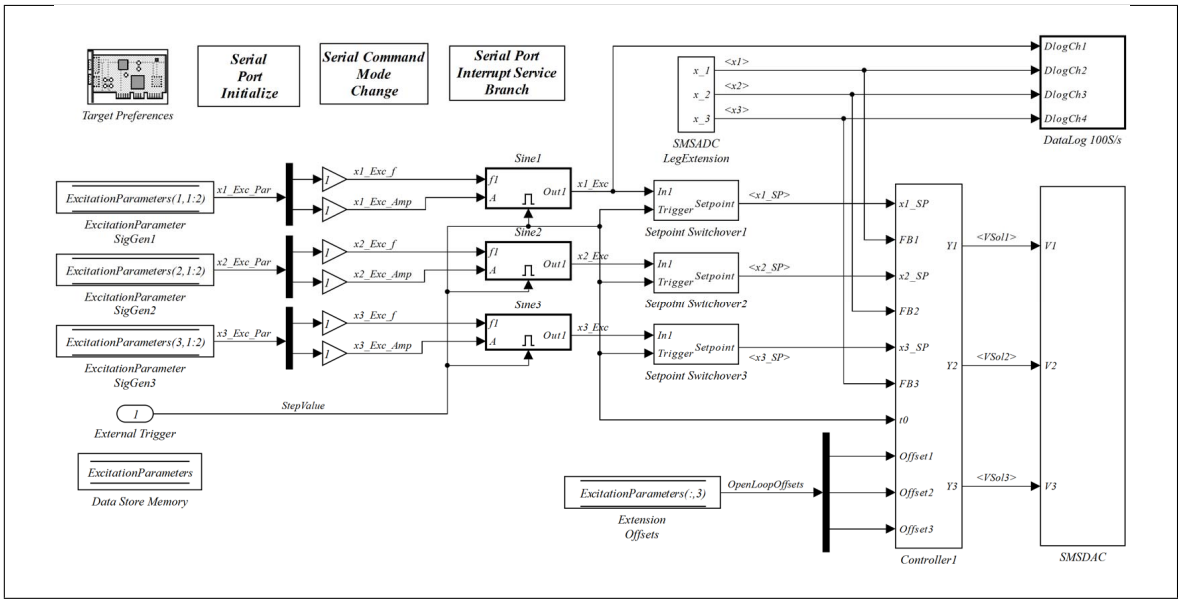

Figure 7.13: Controller Used For Matlab® Simulink® Simulation

definition specific to the processor (top left corner).

As part of the model initialisation, user generated custom code can be added through the "*Configuration Parameters*" menu. This includes code that will be added in the source file, header file, program initialisation functions and program termination functions. This code is executed only once and used for setup and variables which are not accessible through Simulink® blocks.

The built in serial port protocol in Simulink® was found to be very problematic and did not synchronise well on message packets. A replacement protocol was written in CCS and transferred to the "System Initialize Function Custom Code" block named "*Serial Port Initialize*" for initialisation and the "System Update Function Custom Code" block named "*Serial Command Mode Change*" for the periodic execution of code to manage the input commands and input parameters from the console.

The next function added to the main structure is the "*Serial Port Interrupt Service Branch*" which contains the built in *IRQ9* SCI-B Receive (RX) peripheral interrupt enable and request flags with some custom code to execute the serial reading and string parsing routine. This last function is a pure interrupt driven function based on received data from the console.

The one main disadvantage of the RTW embedded coder is the fact that external variables are not

easily defined and used in the machine generated code.

A data memory space called "*ExcitationParameters*" reserves space and defines the input variables for the signal generators used in "*Sine1*" to "*Sine3*". These are the frequencies ("*xi_Exec_f*"), the amplitudes ("*xi_Exec_Amp*") and the offsets ("*OpenLoopOffsets*"). These variables can then be accessed through the serial port routines to modify the system operation. Another method to transfer variable information is to define an input port such as port 1, "*External Trigger*", and define the signal from that port as, for instance, "*StepValue*" with a "SimulinkGlobal" storage class under the "Signal Properties" "Code Generation" tab.

The real world interfaces of this controller is still the ADCs ("*SMSADC LegExtension*") for the actuator displacements and the PWM modules ("*SMSDAC*") for the output valve commands. The actuator positions are derived from the 12 bit ADC value corrected by the calibration values obtained from the measurement of the minimum and maximum positions scaled to the actual travel between these positions. The fact that the travel is only 400 *mm* but the sensor has a full scale over 450 *mm* is taken into account in this correction. Also, according to the wiring of the sensors, the position values have to be subtracted from the full deflection and an arbitrary offset to get the actual centre zero position. These values are then labeled $x1$, $x2$ and $x3$. The PWM hardware is a well developed module on

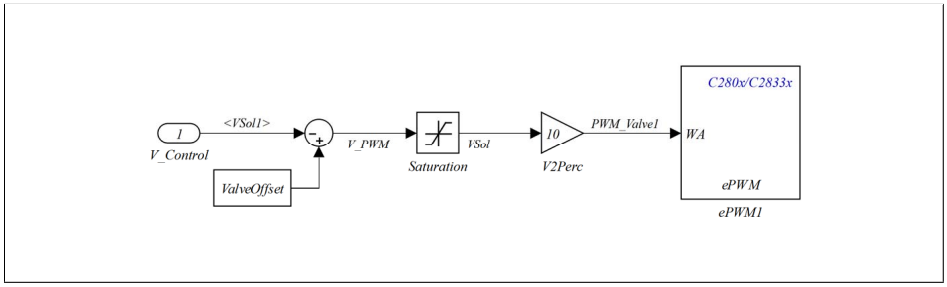

Figure 7.14: The PWM Output Used For The Valve Signal DAC

the TI processors, with many configuration parameter. This module was set up with a 50 kHz base frequency and a percentage of full scale control input. This means that a 0% duty cycle will output 0 V and a 100% duty cycle will output 10 V. The counter base is set up to do both up and down counts, effectively doubling the timer period that is set to 10 μs to achieve the 50 kHz target. The solenoid drive block diagram is shown in Figure 7.14. The control signal is offset to the centre of the valve excitation range and limited to 10 V (as was done in the case of the simulation model) and then multiplied by a factor of 10 to achieve a percentage of full scale for the PWM module. Together with

the filter described in § 7.3.3 this forms a very efficient DAC.

The main controller block (”*Controller1*”) and the signal generator blocks (”*Sine1*” to ”*Sine3*”) are exact copies of the pure Matlab® Simulink® model. A data logging and transfer function was added to monitor the simulation internal signals from the CCS V5 debugging interface. The sampling rate on the data logging is only 100 $S.s^{-1}$ and is triggered by a zero transition on channel 1 (”*DlogCh1*”), similar to an oscilloscope. The values for 200 samples per channel are stored in memory and then transferred to the debug interface via the Joint Test Action Group (JTAG) adapter.

The signal management part of the model (Blocks to the left of ”*Controller1*”) will be discussed in § 7.3.4.

7.3.3 SMS Controller Hardware

In the actuator friction experiments, the actuator validation experiment, the SMS system validation experiments, and the final SMS system, a digital controller connected to a PC and interfaced to the relevant SMS parts were used. This is the same controller hardware with different embedded software builds for the different tasks at hand. The controller hardware consists of an enclosure with a mains voltage power supply, a TI TMS320F28335 floating point microcontroller in a TI control card format running at 150 MHz and an analog interface module. Connectors and cable looms connect the controller with the relevant valves and potentiometers. The electronic system schematic is shown in Figure 7.15.

The controller has been designed to control all of the functions of the simulator and to be able to run without a PC connected to it, should the need arise. However, the PC still forms an integral part of the system as long as data need to be captured. The serial interface to the PC is an RS422 physical layer running a standard 8-bit serial protocol (8 data bits, no Parity, 1 stop bit) at 115200 $b.s^{-1}$. The protocol is a combination of control characters to determine if a message is a command or data, the relevant data, and terminated with a carriage return. At present, no error checking or checksums are added. A Universal Serial Bus (USB) to RS422 converter (RS422 Interface) is used between the PC and the SMS controller. A master "Enable/Disable" switch (P1) has also been added to the controller to prevent the system from being accidentally activated. This switch disconnects the proportional directional valve power supplies from the main power supply, rendering them inactive.

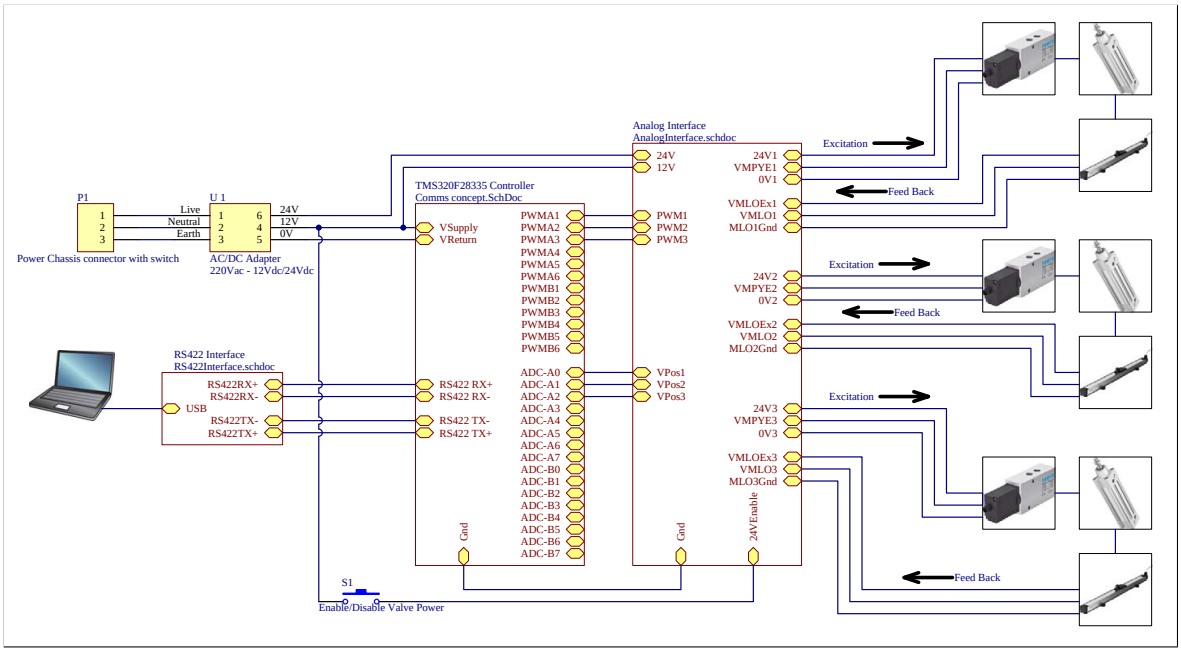

Figure 7.15: SMS Controller Electronic Hardware Schematic

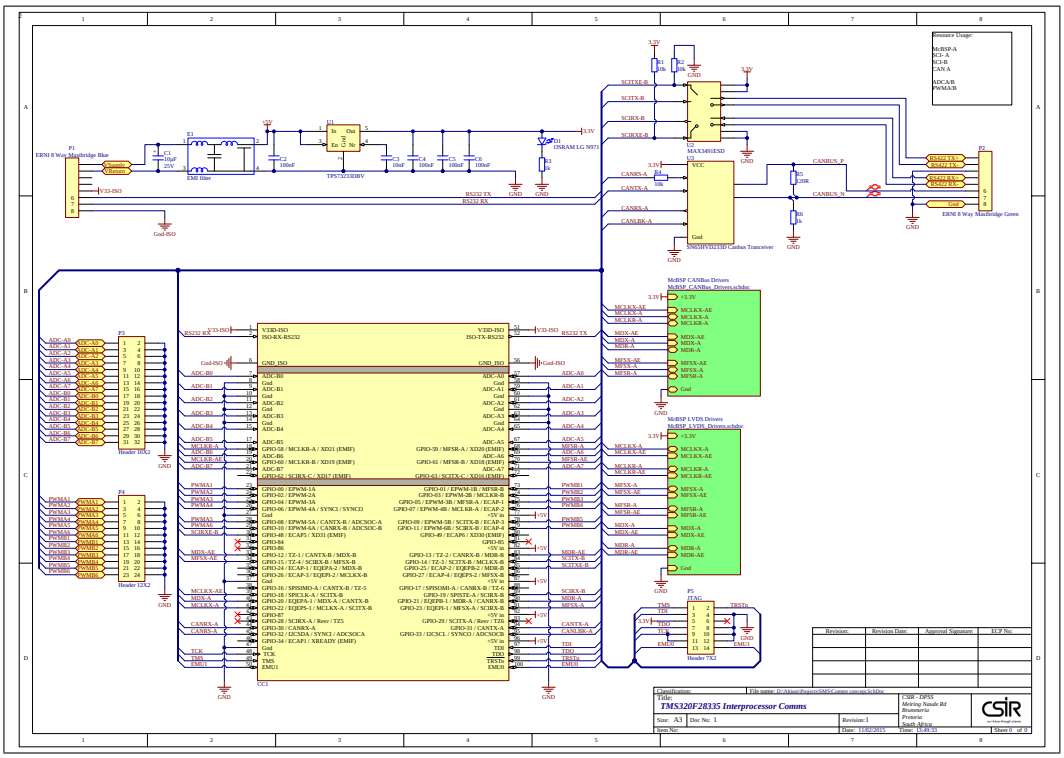

Figure 7.16: SMS Controller Processor Schematic

The mains power supply (U1) is a standard 220 Vac to 12 Vdc and 24 Vdc switched mode power supply with an illuminated "On/Off" switch (S1).

The simulator controller has a TI TMS320F28335 microcontroller that runs the whole system, including the communication and the control loops. The commands such as setpoints or gains are sent from the PC and interpreted by the microcontroller. The computed valve signals are generated by means of the PWM hardware (PWMA1, PWMA2 and PWMA3) and passed on to the analog interface where they are low-pass filtered. The PWM period as set up in the Matlab® RTW domain is 10 μs resulting in a 50 kHz base frequency. Three 2^{nd} order Sallen-Key Butterworth low-pass filters (U4A, U5A and U6A in Figure 7.17) with a -3 dB bandwidth of 98 Hz is used with adjustable output non-inverting amplifiers (U4B, U5B and U6B) at the output to scale the valve signals to the correct values between 0 V and 10 V. Little effort was made to limit the amount of output noise as the input to the valves are also band limited by the input filters of the valve controllers, as well as the valve spool movement.

As part of the same analog interface there are three 1^{st} order active Butterworth RC low-pass filters (U7B, U8B and U9B) with unity gain and -3 dB bandwidths of 482 Hz for the 1 $kS.s^{-1}$ case and 48 Hz for the 100 $S.s^{-1}$ case. These filters act as anti-aliasing filters for the ADC inputs of the controller. The ADC is used to convert the output voltage of the three linear potentiometers mounted on the pneumatic actuators to equivalent actuator extensions. The potentiometers are energised by a 3 V supply rail generated by the voltage regulator (VR1). Because the input range of the TMS320F28335 ADC is 3 V, and the linear potentiometers measure over a range of 450 mm, but the actuators only travel 400 mm, measurements of the extensions can be made with accuracy in a region above the amplifier lower saturation voltage by setting up the mechanical fixtures to have a small offset from the potentiometer end points. A calibration of the end points and measured voltages, together with an offset voltage can then correct for any assembly variation. The buffer amplifiers (U7A, U8A and U9A) ensure that the impedance of the measurement circuit is high enough so that the potentiometer circuits are not loaded. The returned signals are passed to the microcontroller through ADC ports ADC-A0 to ADC-A2.

The TMS320F28335 and its supporting circuitry are shown in Figure 7.16.

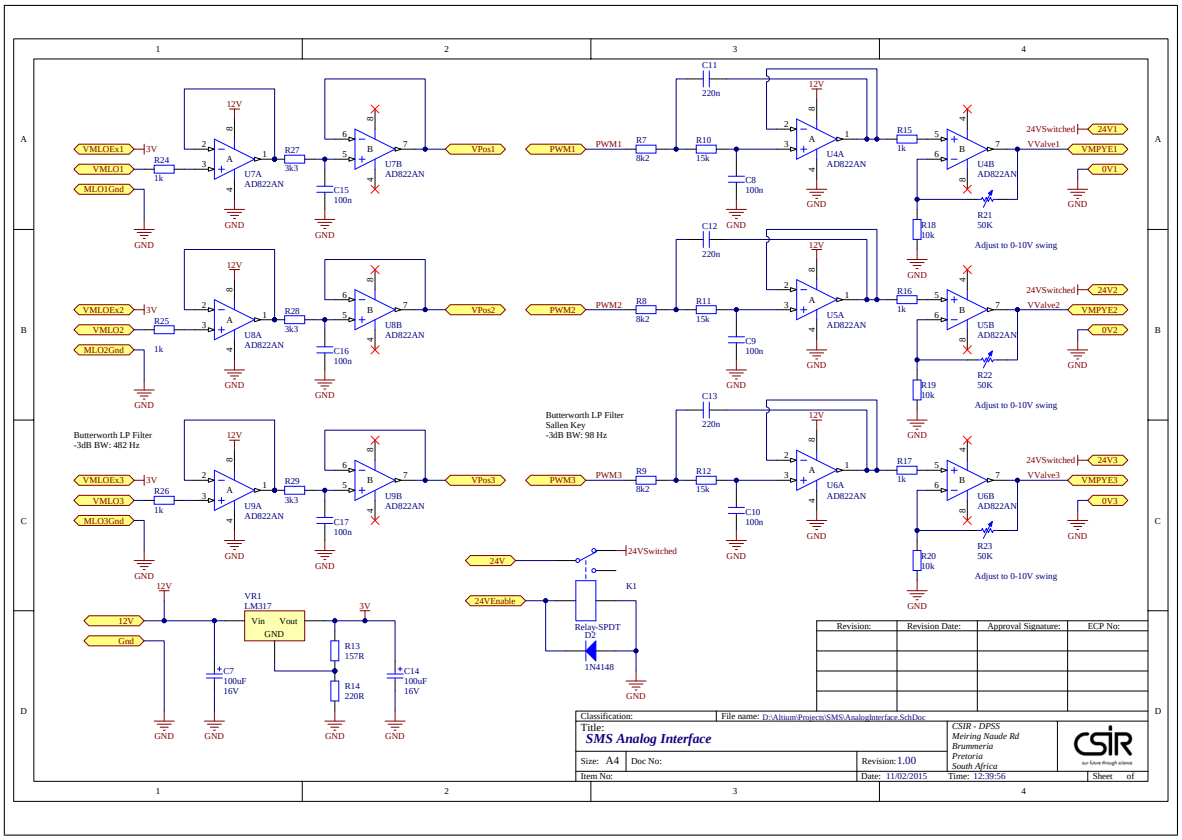

Figure 7.17: SMS Controller Analog Interface Schematic

7.3.4 Open-Loop Tests

As mentioned earlier in the report, the open-loop tests are performed at a specific work point, which in this case is the midpoint of the actuator travel and also the theoretical level position of the SMS platform. Referring to Figures 7.13 and 7.18 a) an enabled subsystem is used to initiate the open-loop excitation. Once the "*StepValue*" variable is changed from the zero to the one state, the subsystem is activated and all the time dependent variables such as "*Time*" are reset. The sine function has a defined starting state in every experiment and will run until the controlling signal disables the subsystem. The output generated by the block is a sine wave with a frequency of "<*x1_Exc_f*>" and an amplitude (in *V*) of "<*x1_Ecx_Amp*>". This sine wave is modified with a linear gain "*1/G_P1*" (Figure 7.18 b)) to compensate for the controller forward gain and is presented as one of two possible setpoint values to the controller. The setpoint is selected by the same "<*StepValue*>" variable that started the sine generator. A zero state will select a constant actuator setpoint of 0 *m*, which will be tracked by the proportional controller. A one state will signal the start of the open-loop experiment and select the modified sine wave as an open-loop excitation for the duration of the experiment. After

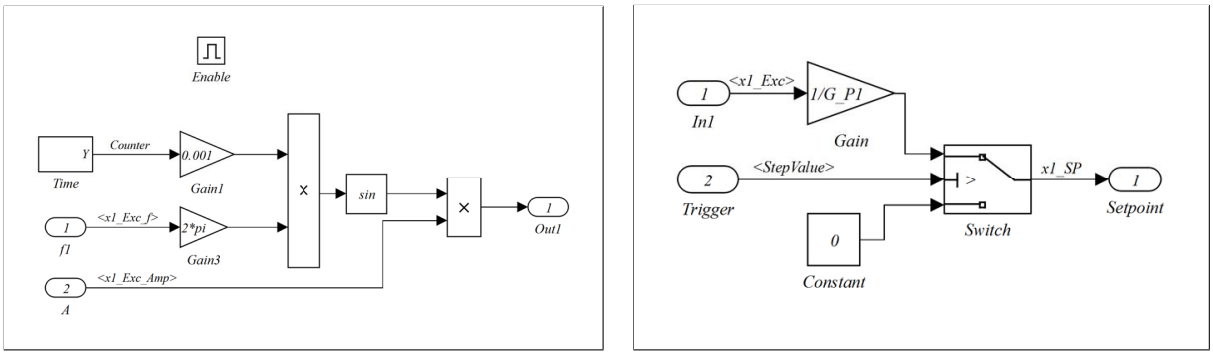

a) b)

Figure 7.18: a) SMS Open-Loop Sine Generator Function and b) Set Point Switch over Function

the experiment is stopped by the console input, or timed out by the pulse generator, the closed-loop setpoint and proportional controller are enabled.

Three distinct channels of signal flow can be observed in the model. Each of these channels represent one of the pneumatic actuators, each with a set of variables to control the frequency, offset and amplitude of the excitation. This enables one to excite the system in pure lifting modes as well as roll and pitch modes with different frequencies.

The SMS system together with the complete SAT was prepared in the DPSS Rooflab for the open-loop and closed-loop experiments. The base of the SMS was bolted to plates installed in the floor, the SAT feet removed and bolted to the SMS top plate, service air supplied to the system and the controller flashed with the RTW controller.

7.3.4.1 Open-loop Results

A series of open-loop tests were conducted with the complete system. The supply pressure was regulated down to 0.4 MPa to match the mass flow models. The tests were divided into two groups, the first being tests with all three actuators receiving in phase signals and therefore only lifting and lowering the SAT, the second being out of phase actuation to roll and pitch the payload. For the sake of brevity the frequencies (F_i) used were limited to only three discrete frequencies, 0.3 Hz, 0.5 Hz and 0.8 Hz and the valve voltage amplitudes (A_i) to 0.7V , 0.8 V and 0.9 V. A total of 18 test runs were completed and compared with simulation results with the same input parameters.

The system was elevated close to the actuator midpoints by means of a simple proportional controller

with a safe proportional gain of 10. Experimentation showed that gains above 40 resulted in instability. Because of the limited flow close to the midpoint of the valve travel a steady-state error was always present.

Once the system was elevated the open-loop tests were run for 10 s. A small offset was needed on the inputs to counter the valve leakage and to prevent the loaded platform from dropping into the buffer zone. Similar offsets were used in the simulation, but as valve leakage was ignored in the model, they differed from the measurement values.

As an example of an open-loop test a roll actuated experimental run is presented. Actuating the system to generate a platform roll action was achieved by using a zero amplitude input signal on the bow actuator (Actuator 1) aligned with the positive x-axis and positive and negative amplitudes of 0.9 V and -0.9 V on actuators 2 and 3 respectively. The valve input signals for actuator 2 to achieve roll actuation are shown in Figure 7.19. As the measured signal is asynchronously captured, a time correction was applied to align the start of the open-loop sections of the two signals as can be seen by the difference in length of the trailing end data (after 10.73 s). The portion of the signal from 0 to

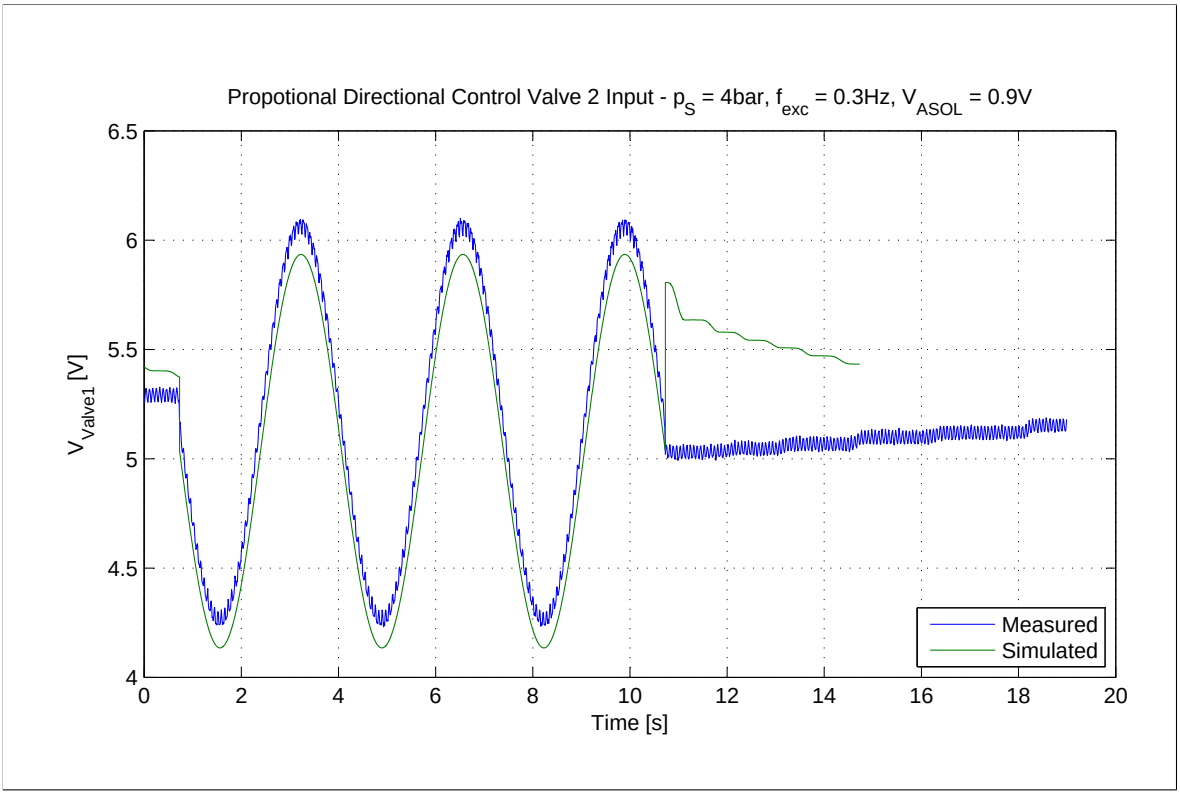

Figure 7.19: Proportional Directional Control Valve 2 Input Voltages, Measured and Simulated

730 *ms* represents the proportional position controlled part of the experiment prior to the 10*s* open-loop test. The difference in the two signals can be attributed to variances in the steady state error and the leakage that influences that error in the real system. At the 10.73 *s* point a very large transient can be observed. This is due to the switch from the open-loop test domain back to the closed-loop domain. In the simulation the controller variables are not zeroed after the switching to the open-loop domain, resulting in a large commanded transient at this point.

The same position error can be seen in Figure 7.20, although much smaller, as this is the output from the position controlled part of the signal. Similar to the the actuator model validation process, the initial conditions for the system plays a large role in the instantaneous absolute values of the chamber pressures and the actuator positions. The focus for comparison is therefore on trends rather than absolute instantaneous values. It was also found that the experimental setup, having many cycles of complete actuation before a measurement is done, initially had different steady-state values as opposed to the simulation. Running the simulation for at least two full cycles solved that problem and the steady-state values approach each other asymptotically.

In the 10*s* of open-loop excitation the sine shaped signals of the simulated run and the experimental run are the same except for the difference in the leakage compensation offset. Once the controller is reactivated (10.73 *s*) the valve voltage values of the model *vs.* the real actuator are different as a result of different actuator positions at that time. The offset added to the open-loop section was chosen to prevent the position to drop too far, hence a small position error and the actuator being close to the desired setpoint at the end of the open-loop excitation. The actuator travel is less during the simulation, resulting in a larger position error at the end of the excitation, hence a larger control signal when the loop is closed.

The rise time (t_{rs}, time from 10% to 90%) of the the simulated displacement signal at the first positive flank (at approximately 3 *s*) is $t_r = 0.509$ *s* whereas the measured rise time (t_{rm}) for the same feature is 0.6 *s*. The rest of the features have very similar rise and fall times, with a typical ratio of measured to simulated time of $t_m/t_s \approx 0.85$. On the rising flanks of the measured displacement plot an overshoot is clearly visible, whereas on the simulated system the displacement overshoot is not as dominant as in the real system. The load (SAT) has high inertia caused by its distant CoG relative to the SMS. This causes overshoot at the end of a decelerating cycle. Since the system is excited at much higher rates than expected, the small overshoot does not disqualify the system validity. The presence of the overshoot indicates an unmodelled higher order effect.

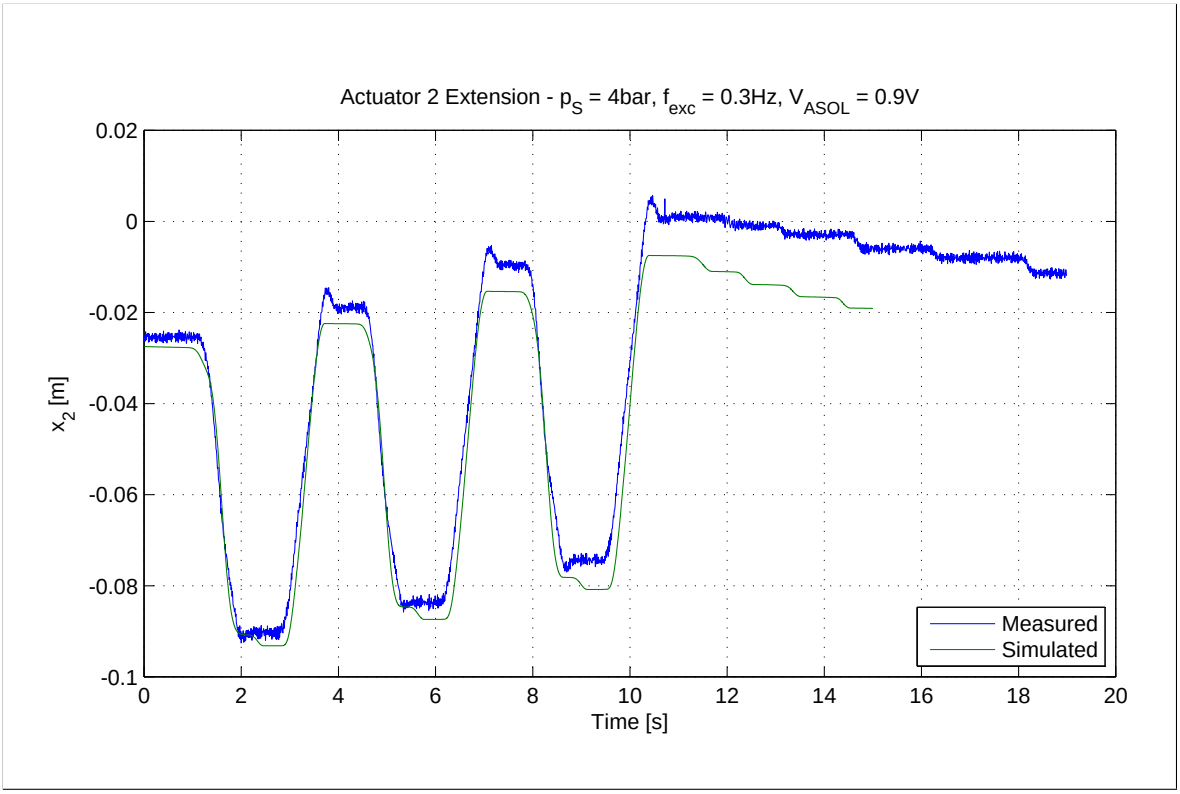

Figure 7.20: Actuator 2 Extension Distances, Measured and Simulated

After the restart of the controlled region ($\approx 11.5\ s$) a slow stepwise drop in the extension can be seen. The cycle time per step for the simulated system is around 1 *s* whereas the cycle time per step for the real world system is around 1.6 *s* - 2 *s*. This difference is due to the valve offsets and the size of the position error, coupled with the "deadband" in the middle of the valve travel. A better optimised controller will solve the steady-state errors; this is therefore not a great concern at present.

Lastly, the chamber pressures of the two cases need to be compared. For the measurement of the chamber pressures the same pressure sensors (Festo SPTW-P10R-G14-VD-M12) were used in the determination of the pneumatic model, the friction model and the actuator model. The sensors were placed as close as possible to the entry ports of the actuators to measure the best possible representation of the chamber pressures. Figures 7.21 and 7.22 show the measured and simulated chamber pressures of the "port" side actuator (Actuator 2). Once again the initial conditions at the start of the simulation played a large role in the absolute values of the signals. The results shown in the graphs are for the second simulation cycle (as explained above) with small differences in the steady-state chamber pressures during the controlled phase. Once the open-loop excitation starts, the trends of the traces track each other with acceptable accuracy, taking into account the multitude of simulation

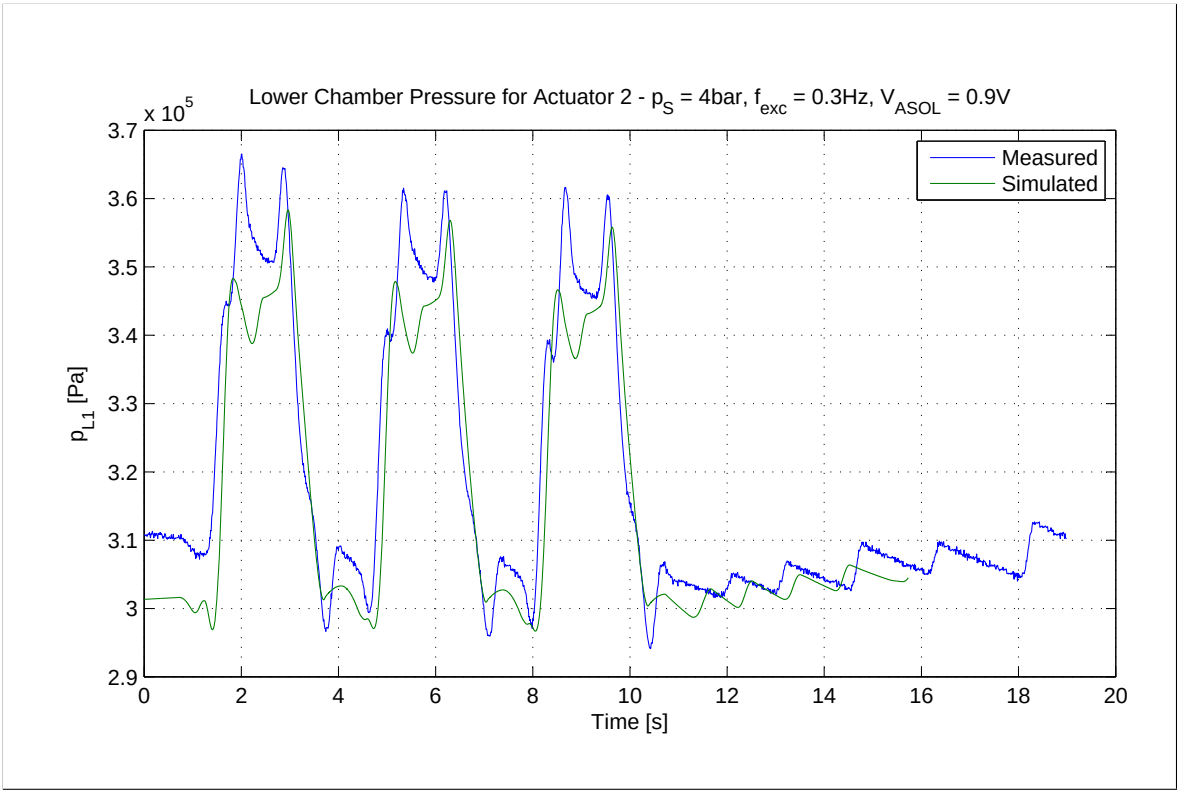

Figure 7.21: Actuator 2 Lower Chamber Pressure, Measured and Simulated

errors that accumulate. Although all the high frequency components are not modelled, the behaviour is the same, and there is not significant delays or instabilities. The simulated system also seems to have a more damped response than the real system, as the ringing at the end of the cycles are less pronounced. This behaviour will need to be taken into account once the controller stability comes into play. A controller that synthesises a marginally stable simulated system could cause instability in the real hardware.

Taking the experimental results of the open-loop tests and comparing them visually with that of the model, a high level of similarity can be seen. A reinforcing of the test of ”likeness” is the use of the normalised cross-correlation operation and the determining of the cross-correlation coefficient. Per definition this is a value between -1 and 1 where 1 means a perfect fit, zero means no correlation at all and -1 means an anti-correlation. We will therefore strive for a value as close as possible to one. Using Matlab’s definition of normalised cross-correlation as shown in eq. 7.2 and using the zero lag

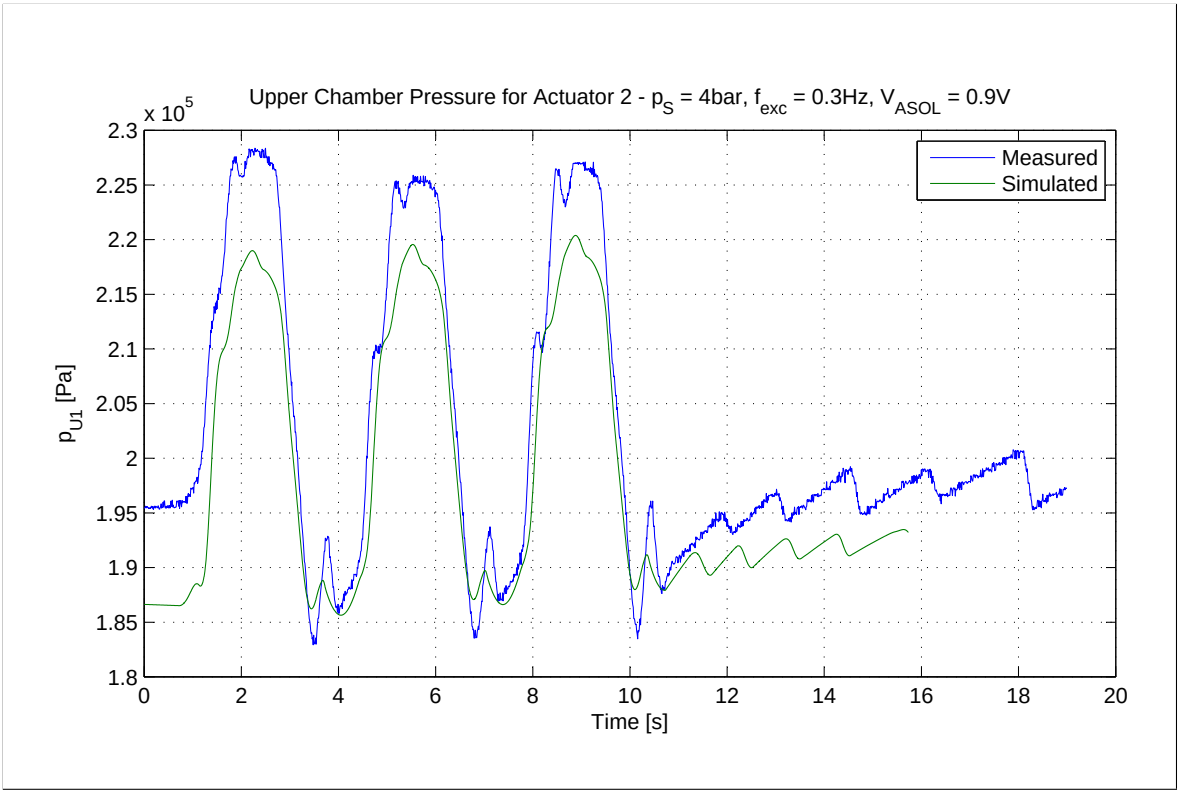

Figure 7.22: Actuator 2 Upper Chamber Pressure, Measured and Simulated

value as a measure of "likeness" this can be achieved.

$$\hat{R}_{xy}(m) = \begin{cases} \sum_{n=0}^{N-m-1} x_{n+m} y_n^* & m \geqslant 0 \\ \hat{R}_{yx}^*(-m) & m < 0 \end{cases} \tag{7.1}$$

$$c(m) = \frac{\hat{R}_{xy}(m-N)}{\sqrt{\sum_n |x_n|^2 \sum_n |y_n|^2}} \quad m = 1,2 \ldots 2N-1 \tag{7.2}$$

Without going into the mechanics of the cross-correlation function the normalised cross-correlation coefficient was determined by using the Matlab® command "c=xcorr(x,y,0,'coeff')" with signals x and y. These signals had their offsets stripped off through the "detrend()" function. The result for the upper chamber pressure (Figure 7.22) is a value of $c_{p_U}(N/2) = 0.9745$ and a value of $c_{p_L}(N/2) = 0.9355$ for the lower chamber pressure (Figure 7.21). This indicates that the correlation between the measured pressure signals and the model derived pressure signals are very good and that the model is accurate in the open-loop domain.

7.3.5 Closed-loop Tests

To complete the simulation model validation process, a series of closed-loop tests were performed that would excite both the simulation model and the real SMS system. The results of the tests were then compared to assess if the simulation model is an acceptable representation of the real system.

To fully validate such a model an extensive test campaign would be needed to ensure that all the possible combinations and permutations of movement are covered and all the possible modes excited. This would be an equally large task compared to building the models. Only two types of excitation inputs were therefore set up to complete the tests in a sensible time period. The first type only lifted and lowered the complete SMS by controlling the actuator extensions with the same setpoint signals. In these tests the torque generated by the elevated centre of gravity of the SMS during non-zero roll and pitch angles and hence the force generated on the actuators during these conditions were negligible. The second type of excitation used generated roll and pitch angles respectively by exciting the actuators out of phase. In this case the payload induced torque is included in the validation process. For ease of post analysis the roll and pitch modes were not mixed into complex movements but kept separated.

A new top level structure for the simulated system was implemented and is shown in Figure 7.23. The most pertinent changes were the addition of chirp signal generators to drive the setpoints (visible on the left-hand side of the system labelled *Excitation*$_i$), PID controllers in the *Controller* subsystem and deadband compensation in the *SMSDAC* subsystem. Firstly, the time dependent setpoints

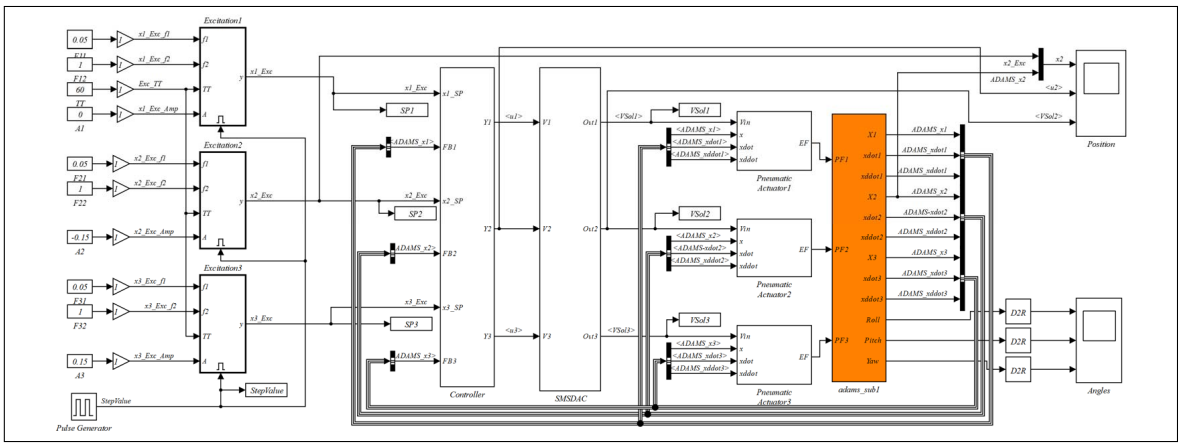

Figure 7.23: Simulink® Model Used in the Closed-loop Validation

($Excitation_i$ in m) are chirp signals described by

$$Excitation_i = A \sin\left[2\pi\left(\frac{(f_2 - f_1)}{2t_{Target}}t + f_1\right)t\right] \tag{7.3}$$

where f_1 and f_2 are the start and end frequencies in Hz respectively, t_{Target} is the duration of the chirp in s, t is time in s and A is the amplitude in m. The generator adds a time dependent frequency offset ($\delta f = \left(\frac{f_2 - f_1}{2t_{Target}}\right)t$) to the initial frequency (f_1) to determine the instantaneous frequency of the signal. The Matlab® Simulink® subsystem describing this is shown in Figure 7.24. Secondly, the

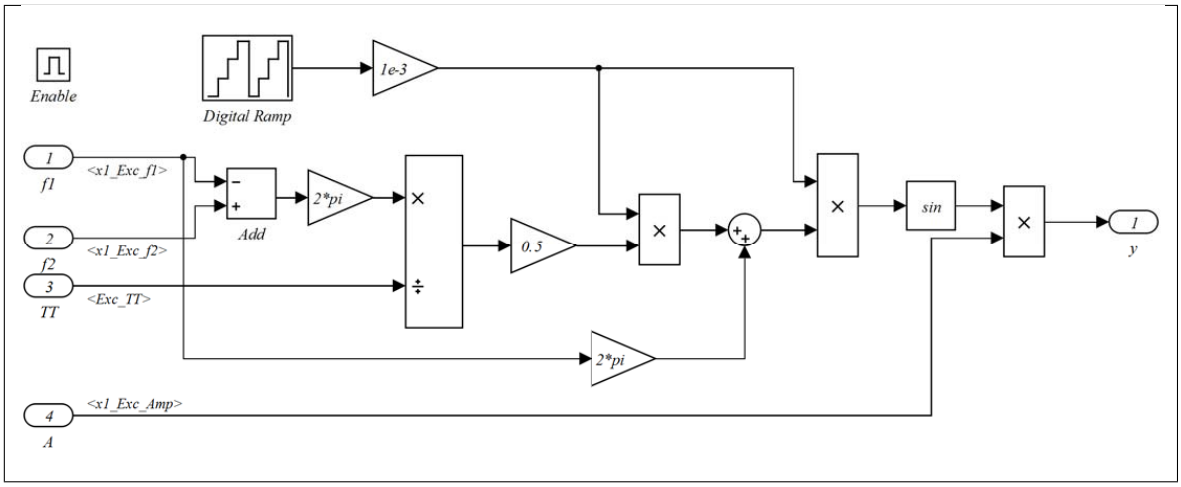

Figure 7.24: Simulink® Model of the Chirp Signal Generator Used in the Closed-loop Validation

PID controllers are placed in the *Controller* subsystem which features a standard parallel structure with three separate branches which are not influenced by the other gains. A low-pass filter is inserted into the differential branch to limit the effects of high frequency noise from the feedback path of the system which are positions measured by the linear potentiometers in this case. The controller transfer function, using a trapezoidal integration method and a Tustin bilinear approximation, can be described by

$$C(z) = G_P + G_I\frac{T_s}{2}\frac{z+1}{z-1} + G_D\frac{N}{1 + N\frac{T_s}{2}\frac{z+1}{z-1}} \tag{7.4}$$

where G_P, G_I and G_D are the proportional, the integral and the differential gains respectively, T_s is the sampling time and N the forward gain of the low-pass filter. The corner frequency of the differential branch is given by N in $rad.s^{-1}$ which rolls off at 20 $dB/decade$.

Lastly, the dead band presented by the very limited flow region (due to mechanical overlap in the valve) in the centre of the pneumatic valve travel needed to be alleviated. A function to ”skip” over that region was prepared keeping in mind that sudden discontinuities will further complicate the

design of the controller. Based on a multi-stage gain function and trying to use built in mathematical functions of the TI controller, the function used in the closed-loop tests is formulated as

$$V_o = a_{DB}V_i + \frac{2b_{DB}}{\pi}\tan^{-1}\left(c_{DB}V_i\right) \tag{7.5}$$

The function is placed between the controller output (Figure 7.14, <*VSol1*>) and the summation of the *ValveOffset*. The output of the function (V_o) is determined by three coefficients, the large signal gain coefficient (a_{DB}), the y-intercept (b_{DB}) and the gain changeover coefficient (c_{DB}). Choosing b_{DB} and c_{DB}, a_{DB} is calculated using

$$a_{DB} = \frac{1}{V_{i\max}}\left(V_{o\max} - \frac{2b_{DB}}{\pi}\tan^{-1}\left(c_{DB}V_{i\max}\right)\right) \tag{7.6}$$

where V_{imax} is the maximum input voltage ($5V$ in this case), and V_{omax} is the maximum output voltage (also $5\,V$). The y-intercept is chosen to enable the controller to overcome the dead band area with very small error signals, reducing the steady-state errors. A value of $b_{DB} = 0.8$ was used in the validation. The gain changeover coefficient (c_{DB}) is chosen large to move the changeover point towards the $V_i = 0$ point and smaller to move it further out. In the validation process a value of $c_{DB} = 100$ was used. The resulting function is shown in Figure 7.25 a).

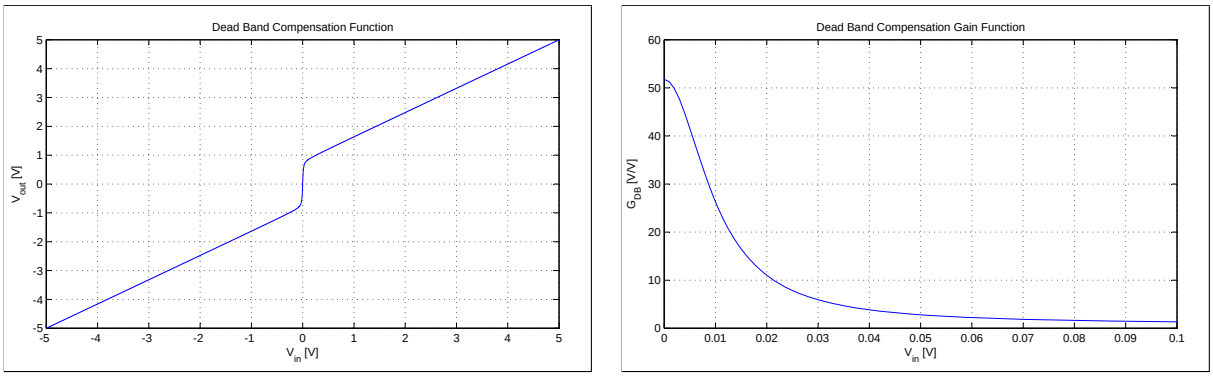

a) b)

Figure 7.25: a) Deadband Compensation Function and b) Gain of the Deadband Compensation function with $a_{DB} = 0.8402$, $b_{DB} = 0.8$ and $c_{DB} = 100$

The gain of the function equals the derivative of the function over input voltage, and can be expressed as

$$G_{DB} = \frac{dV_0}{dV_i} = a_{DB} + \frac{2b_{DB}c_{DB}}{\pi\left(c_{DB}^2V_i^2 + 1\right)}. \tag{7.7}$$

Using this function, the gain at low input values will decrease "exponentially" from a peak value of $G_{DB}|_{V_i=0} = 51.7698$ and approach $a_{DB} = 0.8402$ asymptotically as the input gets larger. The gain *vs.* input magnitude is shown in Figure 7.25 b). Other deadband compensation functions that will linearise the system better can be derived and used, but is seen as future work and is not addressed in this document.

7.3.6 Closed-loop Results

As described in § 7.3.5, only two possible scenarios were tested for model validation. These are lifting and lowering of the SMS (heave) by actuating all three actuators with the same input chirp signal, and roll and pitch movements by actuating out of phase. Actuator 1 was held at midpoint and actuators 2 and 3 were driven out of phase for roll, whereas actuator 1 was driven out of phase with actuators 2 and 3 for pitch.

The heave tests were mainly used to make sure that the system is stable and to find suitable proportional gains for the system. An analysis was done, however, on these results to reinforce the validity argument. An important fact to keep in mind is that the aim of these experiments is to determine validity, not to identify the model. Very little spectral information is present in the lower frequency parts of the excitation due to the long cycle times, but the correlation between the simulated and experimental results needs to be good for model validity.

Once again, actuator 2 positions were used for comparison, mainly because this actuator is always excited with non-zero setpoints. The excitation signal (setpoint) used to simulate heave (all three actuators lifting at the same time) together with the measured and simulated actuator 2 positions are shown in Figure 7.26. The frequency of the setpoint was increased from 0.05 Hz to 1 Hz over a period of 60 s and the actuator displacement was selected at $\pm\Delta x = 0.15$ m. It can be seen that both the Matlab®/ADAMS® co-simulated and the experimental systems perform similarly to the setpoint values. In both cases a delay is present and in both cases a reduction in the amplitude can be seen. This frequency dependent reduction is what will define the bandwidth of the system when a simple proportional controller is used. Figure 7.27 shows the trends between 8 and 17 seconds which indicates that there is a shape difference between the two output signals. The simulation model seems to have a slower charging cycle than the real system which also manifests in a slightly lower bandwidth at a controller gain of $G_P = 2$. Also noticeable on the measured signal is a more prominent friction induced shudder on the downward (retracting) flanks. This phenomenon was not present in

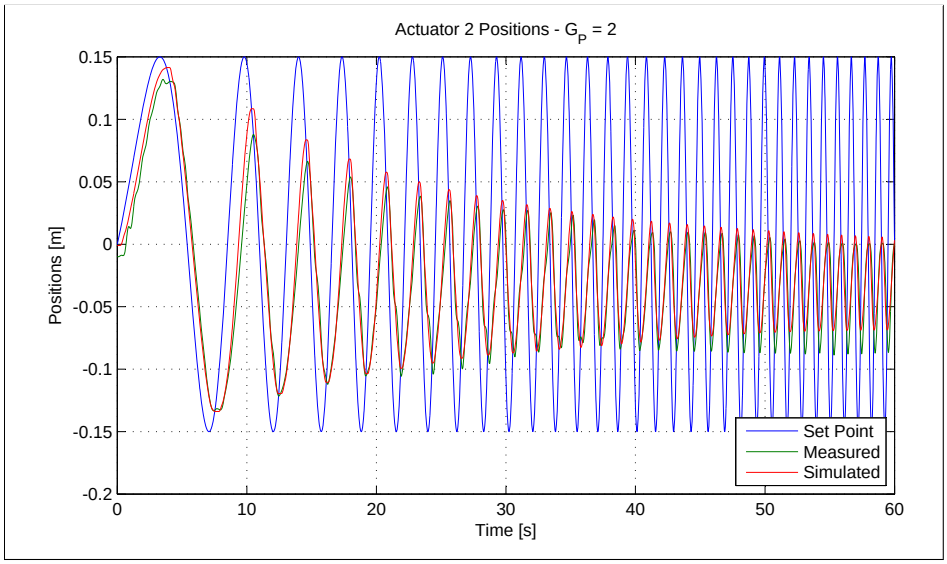

Figure 7.26: Excitation and Actuator 2 Positions as Function of Time in a Closed-loop Experiment With $G_P = 2$ in a Heave Mode

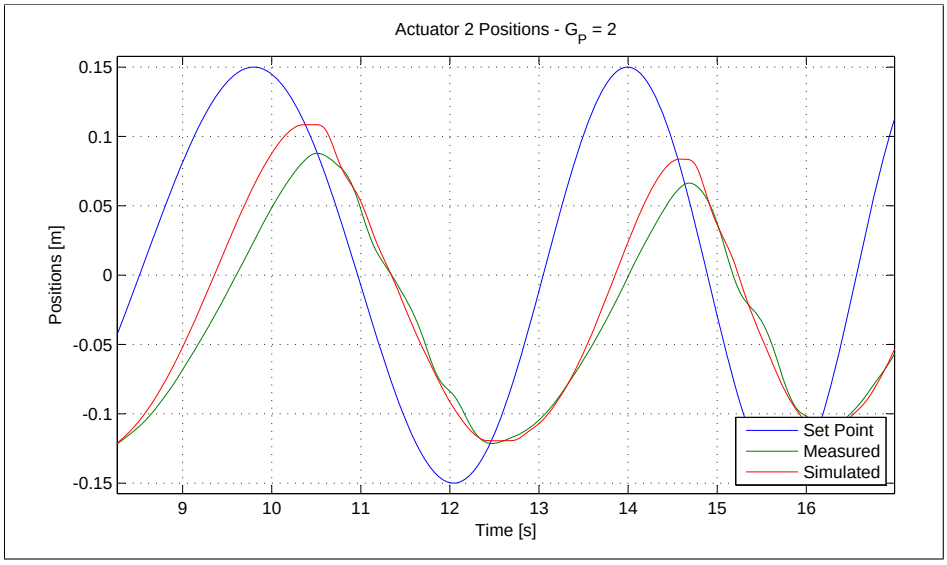

Figure 7.27: Detailed Plot of Excitation and Actuator 2 Positions as Function of Time in a Closed-loop Experiment With $G_P = 2$ in a Heave Mode

all of the experimental runs and is currently attributed to changes in the lubrication, the state of the actuator seals and air supply quality.

By investigating the frequency spectra of the different signals, a good correlation between the real system and the model can be observed. All the signals are processed using complex Fourier analysis

without any windowing functions. Once again, a validation is done and not a system identification. A digital Fourier transform is done on the setpoint and two output signals. The spectral content is shown in Figure 7.28. The setpoint signal spectrum has a very uniform input spectral content from

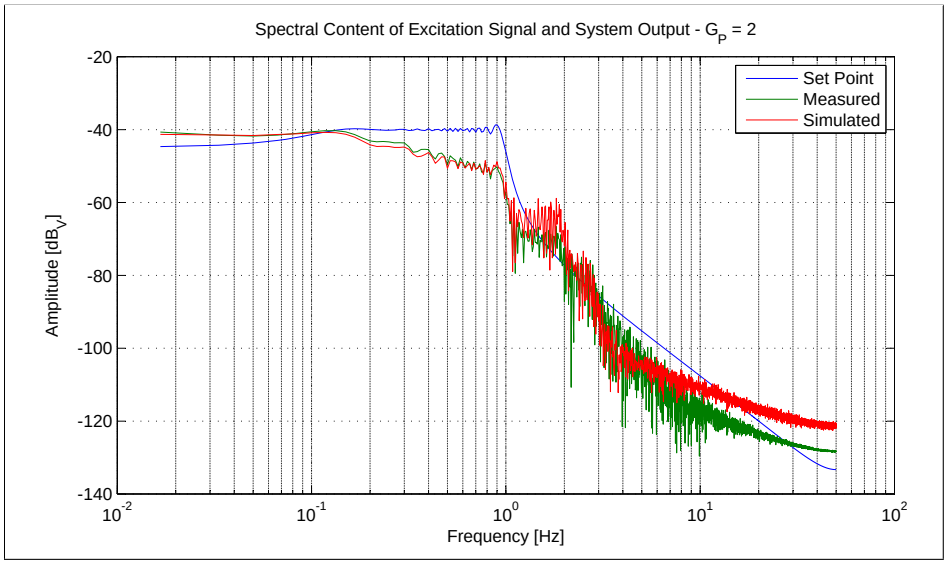

Figure 7.28: Spectral Content of the Actuator 2 Signal in the Heave Mode

around 0.1 Hz to 1 Hz where it starts to drop off very quickly. The slow increase of content below 0.1 Hz is due to the limited amount of cycles at that frequency as defined by the chirp generator (eq. 7.3). The output signals do show some activity in the very low frequency region and a slow drop off toward 1 Hz due to the system bandwidth. In both the measured and simulated systems there are some additional components between 1 Hz and 3 Hz (Figure 7.29). These signal components are not excited by the set point inputs, but added by the system structure, they are more prominent in the measured system than the simulated system and is linked to shudder as described above. By using the spectra of the input and output signals, a first order system frequency response can be drafted and is shown in Figure 7.29. The phase is dominated by spurious noise and shudder induced components above 1 Hz together with measurement noise which is amplified by the small input signal magnitudes at those frequencies. For validation purposes the model response agrees well with the actual system response, but for all practical purposes the frequency range will be limited to 0.05 Hz to 1 Hz (as shown in Figure 7.30). From a controller design perspective it is valuable to know that the system has an inherent pure delay as can be seen by the constant decline of the phase. Once the out-of-band noise is ignored (Figure 7.30) a good correlation between the two systems can be observed. Although there is a small difference in both the gain and phase plots, the trend of the curves are the same and within the same order of magnitude. The gain at the lower frequencies is not a concern as the spectral

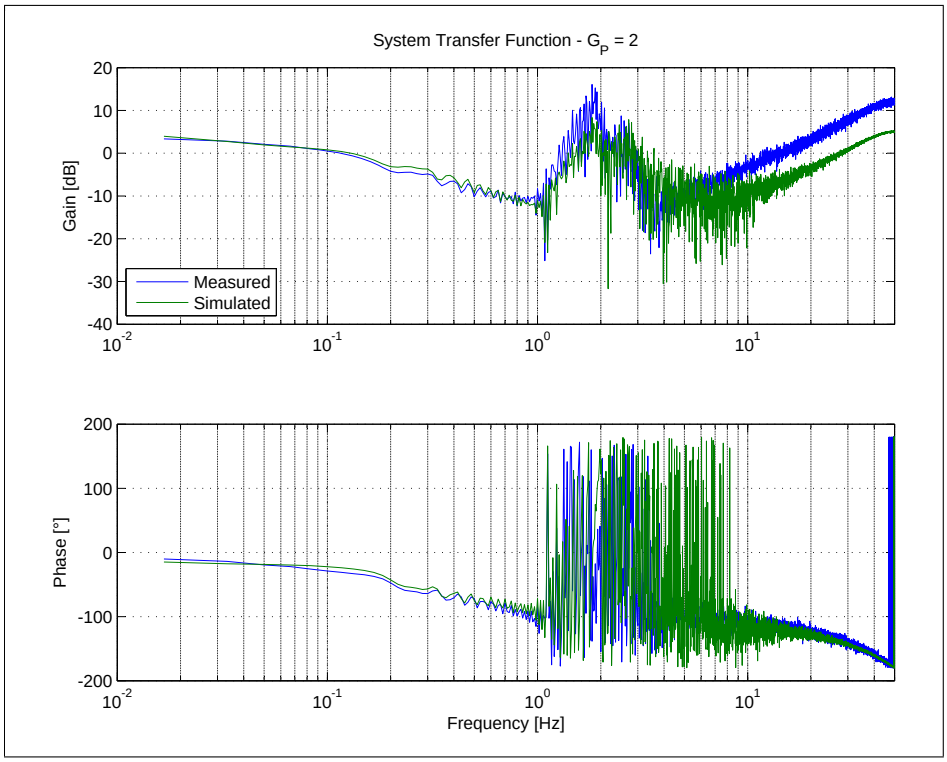

Figure 7.29: Frequency Response of the Actuator 2 Signal in the Heave Mode

components in that region are very limited (as explained above).

It can therefore be stated that the Matlab®/ADAMS® co-simulation model of the SMS developed in the course of this study is a "good enough" representation of the real system which can be used for controller design and evaluation. It should also be taken into account that any controller designed using this model will need to be carefully tested on the real system to allow for variations in the conditions of the pneumatic components.

Further improvements on the model can include an expansion of the input pressure range modelling, a better stick-slip friction model and a more thorough validation. From the model it should be possible to determine the nonlinear transfer function and hence the control systems plant model, and possibly a linearised system model.

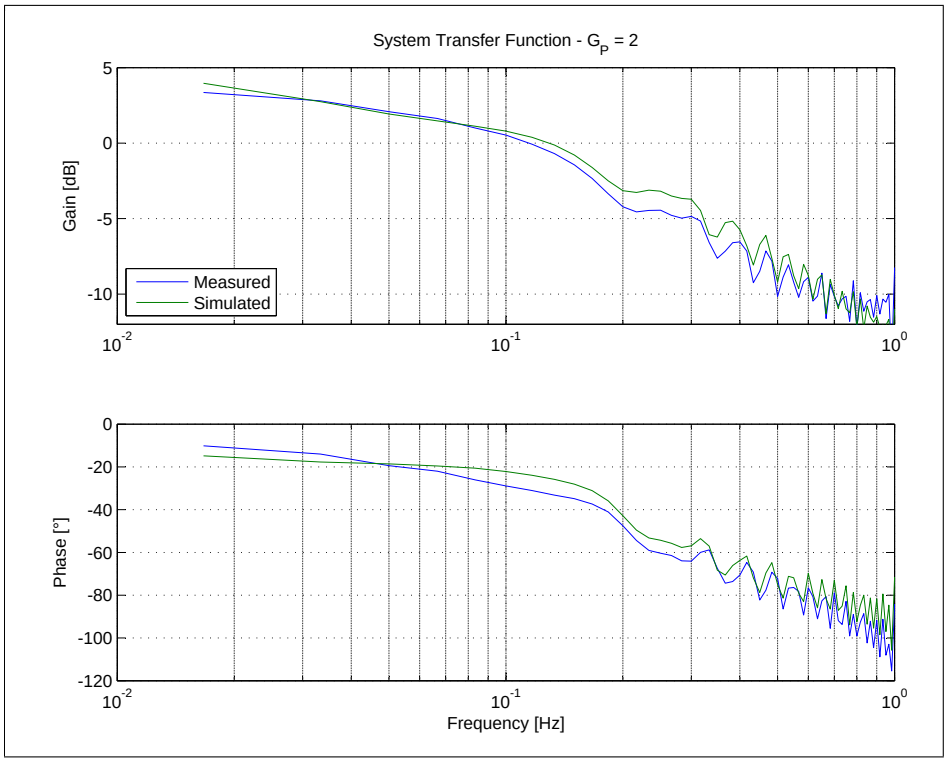

Figure 7.30: Band Limited Frequency Response of the Actuator 2 Signal in the Heave Mode

CHAPTER 8

SMS CONTROLLER

The mathematical model for the SMS system carrying a payload similar to the SAT was derived from first principles in chapters 3 to 6. This model was validated in chapter 7.3 and can be described as an acceptable representation of the real system. The high fidelity model is too complex for the purpose of classical controller design and has to be simplified to a characteristic level. A controller can be designed with this simple model to reach the specification set out at the start of the study. It can then be tested with the high fidelity Matlab®/ADAMS® model and then transferred to the real system once stability has been achieved. This method has been adopted to protect the equipment on the SAT during controller development.

This chapter details the simplified SMS model with some assumptions, the design of controllers using the root locus design method as well as state feedback compensation and some simulation results.

8.1 SIMPLIFIED PLANT MODEL

Refer back to the closed-loop frequency response curve of the SMS (Figure 7.29) obtained from a chirp input signal and a proportional controlled system with a controller gain of two. The shape of the response is characteristic of a system with a flat low frequency response that drops off at approximately 10 dB per decade from 0.1 Hz to 1 Hz. The phase decreases monotonically from around -20° at 0.05 Hz down to -100° at 1 Hz. A lack of excitation frequency components above 1 Hz makes it impossible to determine the high frequency gain or phase roll-off.

A simple characteristic model is proposed by Šitum *et al.* [16] that describes the pneumatic actuator and load as a mass and double spring system with viscous friction and it is shown in Figure 8.1.

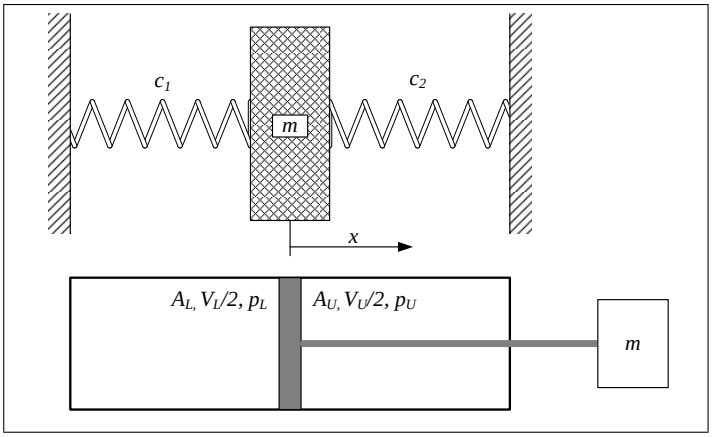

Figure 8.1: Simplified Double Mass-Spring Model for the Pneumatic Actuator with a Load

The system comprises of a mass connected to two springs with spring constants of c_1 and c_2. A viscous friction component related to the velocity of the mass by a coefficient b_f is added to dampen the system. This system is assumed to be a simplified analogy to the shown pneumatic system that has two volumes filled with a compressible fluid (air) connected to a mass m through an infinitely thin rigid rod. Šitum *et al.* derived a third order transfer function for this simplified model with a characteristic (natural) frequency of ω_s and a damping ratio of ζ_f. The transfer function is

$$G(s) = \frac{X(s)}{U(s)} = \frac{k_m C_0 \omega_s^2}{s(s^2 + 2\zeta_f \omega_s s + \omega_s^2)} \tag{8.1}$$

where C_0 is the open-loop forward gain, k_m is an adjustment gain for matching the measured system to the model, $X(s)$ is the position of the piston and $U(s)$ is the valve input voltage. The natural frequency is described by

$$\omega_s = \sqrt{\frac{c}{m}} = \sqrt{\frac{4\kappa \bar{p} A^2}{mV}} \tag{8.2}$$

with κ the specific heat ratio for air, $\bar{p} = (p_U + p_L)/2$ the average absolute chamber pressure at the work point, $A = A_L = A_U$ the effective surface area of the piston (assuming a zero rod thickness) and $V = V_U + V_L$ the total actuator volume. Analogous to the mechanical model the spring constant is $c = c_1 + c_2$ and the total moving mass (one third of the SAT mass) is m. The damping ratio is given by

$$\zeta_f = \frac{b_f}{2m\omega_s} \tag{8.3}$$

where $b_f = 530\ N.s.m^{-1}$ is the viscous friction coefficient as derived in § 6.4 and § 6.5.

A series of open-loop tests were performed with the Matlab®/ADAMS® simulation and the forward gain (C_0) determined from the resulting data. The nonlinear nature of the system came to the forefront as the gain value varied from $C_0 = 0.1\ m.s^{-1}.V^{-1}$ for an input voltage of $u = 5\ V$ to $C_0 = 0.85\ m.s^{-1}.V^{-1}$ for a voltage of $u = 0.5\ V$. As the system will mostly be controlled in close proximity of the setpoint (assuming decent setpoint tracking) the valve control voltages will be closer to the lower limit of $u = 0.5\ V$ and therefore a C_0 value of $0.85\ m.s^{-1}.V^{-1}$ was used. Smaller values will put the system in the nonlinear region of the deadband compensation function and complicate the simplified model.

Using the values determined in the pneumatic and friction modelling portions of the study the unknown values for the model were determined (values shown in Appendix D, Table D.1) and the transfer function populated. In order to compare the simplified model with the validated model the loop was closed with a forward controller gain of $K_p = 2$ and the closed-loop transfer function derived as

$$T(s) = \frac{X(s)}{R(s)} = \frac{K_p G}{1 + K_p G} = \frac{K_p C_0 \omega_s^2}{s\left(s^2 + 2\zeta_f \omega_s s + \omega_s^2\right) + K_p C_0 \omega_s^2.} \tag{8.4}$$

The gain and the phase of the simplified model frequency response was compared with the gain and phase of the measured data frequency response, as well as the high-fidelity simulation model frequency responses; all at 1 Hz. The adjustment gain (k_m) was iteratively changed until a representative closed-loop model could be derived. It turned out that the adjustment gain was redundant and settled on values close to $k_m = 1$. Comparing the frequency response of the complete nonlinear actuator model and the that of the simplified model as shown in Figure 8.2, the gain in the nonlinear systems (the real system and the Matlab®/ADAMS® model) is higher than 0 dB (as discussed in section 7.3.6) and higher than that of the linear simplified model, but in both the systems it rolls off from approximately $-1\ dB$ at 0.1 Hz to approximately $-11\ dB$ at 1 Hz. The resonant peak in the simplified model is situated at $\approx 4\ Hz$ and cannot be compared to the nonlinear system due to the excitation bandwidth limitation. The phase in both models is around -20° at the low frequencies and settles at around -80° at 1 Hz.

From this comparison one can deduce that the simplified model has value in the design of a controller for the SMS, and this will be discussed in the next section.

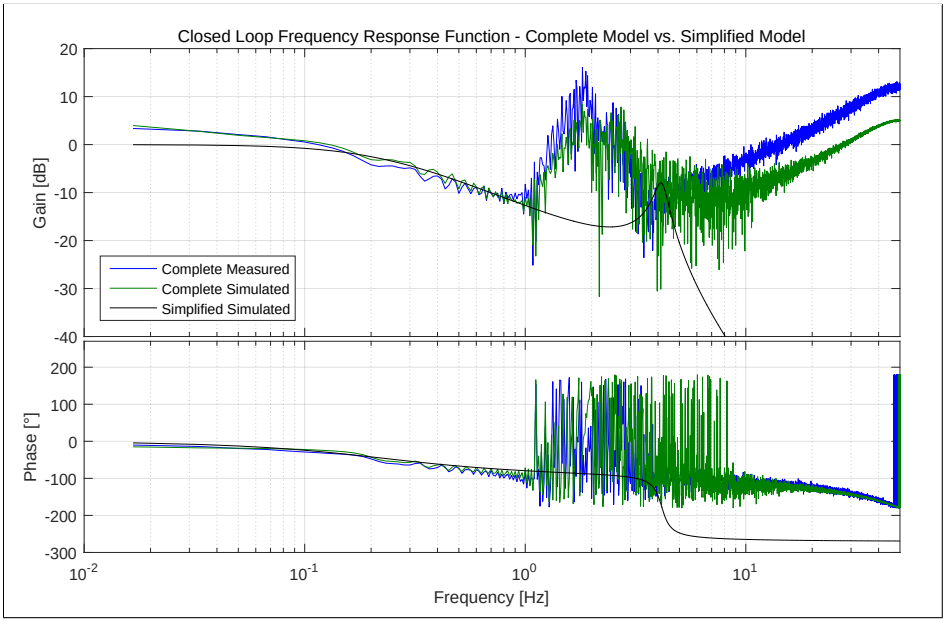

Figure 8.2: Comparison of the Closed-loop Frequency Response of the 3^{rd} Order Simplified Actuator Model with the Closed-loop Frequency Response of the Complete Nonlinear Actuator Model with a Gain of $K_p = 2$

8.2 STATE FEEDBACK COMPENSATION

Apart from the simplified model, Šitum *et al.* also proposed a State Feedback (SF) controller. The SF controller uses position, velocity and acceleration feedback. Only the position feedback is directly measured in the way the SMS controller is set up. This forces the generation of the velocity and acceleration feedback through direct differentiation of the position signal or using observers. This is not a unique problem only for the SMS but was also the case in the servo drive presented by Šitum. To reduce spurious noise in the state feedback paths, the differentiators have a low-pass filter embedded in the structure which is similar to the transfer function used for the PID controller (eq. 7.4). The differentiation to obtain the rate and acceleration introduces a phase shift at higher frequencies and this shift would need to be monitored.

The structure for the SF controller is shown in Figure 8.3 with the proportional gain acting on the position error signal and the velocity and acceleration gains acting on the first and second derivatives of the position signal. Using the transfer function of the simplified model in eq. 8.1 as the plant transfer function $G(s)$ and the control structure proposed above, the closed-loop transfer function

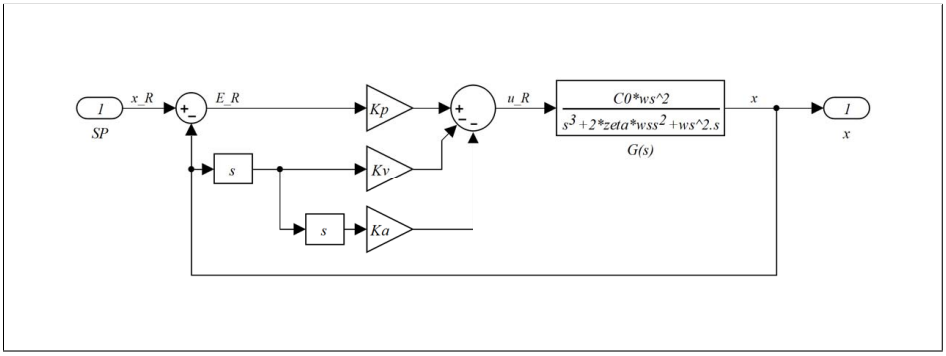

Figure 8.3: State Feedback Controller Structure as Proposed by Šitum *et al.*

$T(s)$ for the system can be derived and is described by

$$T(s) = \frac{X(s)}{R(s)} = \frac{K_p C_0 \omega_s^2}{s^3 + (2\zeta_f \omega_s + K_a C_0 \omega_s^2) s^2 + (\omega_s^2 + K_v C_0 \omega_s^2) s + K_p C_0 \omega_s^2} \tag{8.5}$$

where K_p, K_v and K_a are the state controller gains. The structure of this transfer function is similar to the 3^{rd}-order function of the plant and can be simplified to

$$T(s) = \frac{K_p C_0 \omega_s^2}{s^3 + 2\zeta_c \omega_c s^2 + \omega_c^2 s + K_p C_0 \omega_s^2} \tag{8.6}$$

with ζ_c the closed-loop system damping ratio and ω_c the closed-loop system natural frequency. Re-writing the closed-loop transfer function in terms of poles and zeros with the three poles at p_1, p_2 and p_3 will lead to

$$T(s) = \frac{K_p C_0 \omega_s^2}{(s+p_1)(s+p_2)(s+p_3)} \tag{8.7}$$

By expanding the denominator and factorising with respect to powers of s, the three gain values can be obtained. When assuming that $\alpha_c = \omega_c/\omega_s = 1.5$ and the closed-loop poles are placed at $p_i = \omega_c/2$, these are:

$$K_p = \frac{p_1 p_2 p_3}{C_0 \omega_s^2} = \frac{\alpha_c^3 \omega_s}{8 C_0} \tag{8.8}$$

$$K_v = \frac{(p_1 p_2 + p_2 p_3 + p_1 p_3) - \omega_s^2}{C_0 \omega_s^2} = \frac{3(\alpha_c^2 - 1)}{4 C_0} \tag{8.9}$$

$$K_a = \frac{(p_1 + p_2 + p_3) - 2\zeta_f \omega_s}{C_0 \omega_s^2} = \frac{3\alpha_c - 4\zeta_f}{2 C_0 \omega_s} \tag{8.10}$$

Using the system bandwidth requirement a slightly different approach can be used (called the Specification Based Design (SBD) approach for ease of identification). As this is a 3^{rd}-order system, the

$-3dB$ point for this closed-loop system is situated at approximately $0.5088 p_i \; rad.s^{-1}$ if all three poles (p_i) are placed at the same location. The natural frequency ($\omega_c = p_i\sqrt{3}$) is then chosen to achieve a bandwidth of 1 Hz in this case. From the generic 3^{rd}-order system transfer functions (8.6 and 8.7) the natural frequency is

$$\omega_c = p_i\sqrt{3} \tag{8.11}$$

and the damping ratio as

$$\zeta = \frac{3p_i}{2\omega_c}. \tag{8.12}$$

The equation for the calculation of the gains changes slightly, mainly due to the assumption on α_c. The new set of equations for K_p, K_v and K_a is shown in equations 8.13 to 8.15.

$$K_p = \frac{\alpha_c^3 \omega_s}{3\sqrt{3}C_0} \tag{8.13}$$

$$K_v = \frac{\alpha_c^2 - 1}{C_0} \tag{8.14}$$

$$K_a = \frac{\sqrt{3}\alpha_c - 2\zeta}{C_0 \omega_s} \tag{8.15}$$

Both methods described above were used to determine the gain values for a SF controller which was then used in both the simplified model simulation and the Matlab®/ADAMS® co-simulation to determine usefulness. The values of the controllers and models used are given in appendix E, Table E.1. The fact that the K_v value for the SBD method turned out to be negative is noticeable in the table. Without doing a stability analysis on the gain values they were substituted into the model (Figure 8.3) and a large signal step response simulation was run. The step was chosen to match the size of deflections used in determining the forward gain value (C_0) of the plant, *i.e.* ± 0.1 m. The step response and controller output are shown in Figures 8.4 a) and b).

In both cases the system was stable and performed with responses comparable with the design criteria. The Šitum SF controller generated a response with a rise time of $t_R = 0.255$ s and an overshoot of 0.51 %, whereas the SBD controller gave a rise time of $t_R = 0.33$ s and an overshoot of 2.58 %. If one assumes the bandwidth/rise time relationship to be $BW = 2.2/t_R \; rad.s^{-1}$ for a step response, the

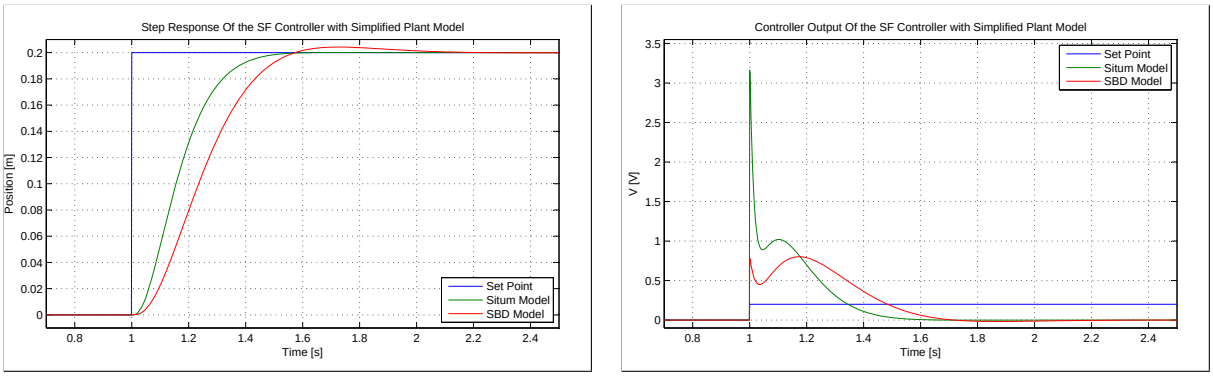

a) b)

Figure 8.4: a) Step Response and b) Controller Output Response of the State Feedback (SF) Controller Closed-loop System

bandwidth of the Šitum controller system is 1.37 Hz and that of the SBD controller system is 1.06 Hz, which corresponds well with the design criteria and the frequency analysis of the systems.

A high fidelity simulation of the controller in the Simulink®/ADAMS® SMS model was implemented by replacing the controller as described in section 7.3.5 with the new SF controller and making sure the system performs as expected. An additional loop gain value (K_c) was inserted to study the effects of the loop gain on system stability. In both cases of the SF controller the simulation resulted in unstable closed-loop systems with the actuators extending uncontrollably to their maximum extension limits. It was obvious that the simplified model did not account for enough characteristics present in the nonlinear system to be used for linearised controller design. Although it can be argued that the simplified model was derived for small signal use only, the controllers designed were excited in both the small signal linear regime as well as the large signal nonlinear regime and fared equally poor.

It was found that by reducing the K_a value dramatically, the stability improved, although the response became slow and sluggish. The values quoted by Šitum *et al.* revealed a very sluggish but stable system and also revealed that the controller structure does have merit. The ratios between the K_p and K_v values of the Šitum *et al.* were similar to the values found in this study, but the K_a value of Šitum *et al.* was much smaller. The system could be made stable by reducing the acceleration contribution, although it resulted in a very acceleration sensitive system. By removing the acceleration feedback (making $K_a = 0$), a marginally stable system with a steady-state limit cycle could be achieved. The limit cycle could be minimised by reducing the overall loop gain.

The led to the belief that a negative K_a could be found that will result in a stable system with small steady-state errors and an acceptable bandwidth. The gain values converged to $K_p = 40$, $K_v = 1$ and $K_a = -0.005$ with numerous iterative experiments which gave a system that is both stable for positive and negative step inputs of $\delta x_R = 0.1\ m$. The system is stable for loop gain variations up to 15 times ($K_c = 15$) the normal value with rise times of $t_R = 0.5672\ s$ and zero overshoot. The rise time is limited by the charging rate of the actuator and hence the value of C_0. This equates to a large signal bandwidth of 0.617 Hz which is acceptable for emulating the platform motion, but not exactly up to the (unreachable) 1 Hz bandwidth. The step responses of both a positive step as well as a

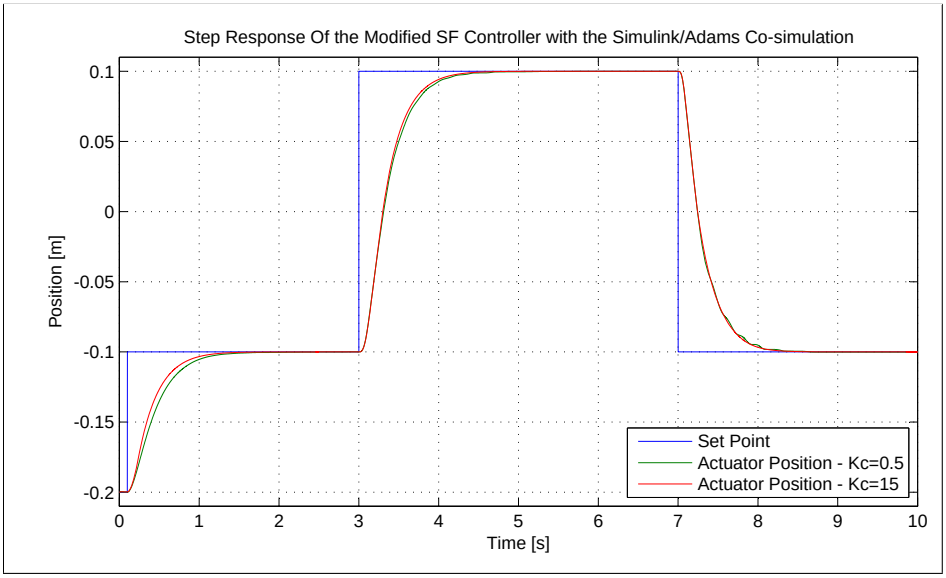

Figure 8.5: Step Response of State Feedback (SF) Controlled Simulink®/ADAMS® System with Modified Gains

negative step are shown in Figure 8.5. The valve input voltage is shown in Figure 8.6 and from this plot it can be seen that during a large part of the large scale actuator movement, the valve input is saturated and the maximum possible air flow is generated. With these high gains it can also be seen that the steady-state regions of the step functions are dominated by (very noisy) reversals in the valve positions which will generate vibration in the structure. This has not been modelled and can be a possible problem due to frame resonance. The step responses show that the rise times for the loop gain extremes ($0.5 < Kc < 15$) do not differ substantially from each other. A higher gain in the loop reduces the small oscillations on the downward flanks of the actuator position. In the case of $K_c = 0.5$ (Figure 8.6 a), the control signal to the valves can be seen to be in an unsaturated state all the time. The valve is therefore not completely open and the flow is not at its maximum level (assuming the

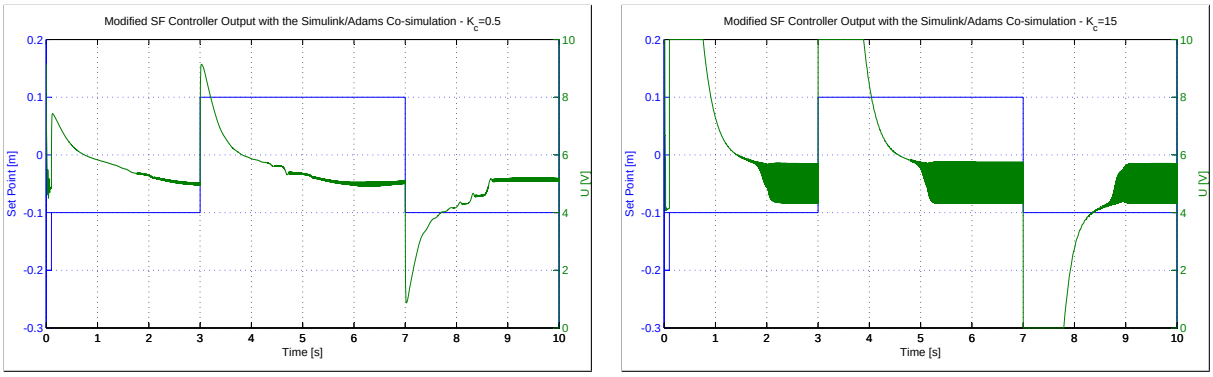

a) b)

Figure 8.6: a) Controller Output with a) $K_c = 0.5$ and b) $K_c = 15$. The Blue Traces Indicate the Input Setpoints and the Green Traces Indicate the Valve Control Voltage

possibility of subsonic flow). Once the loop is increased to the maximum level (K_c=15), the valves are fully open for a much longer period of time and the air flow is theoretically at its maximum possible level for a longer period of time, which should result in a faster response. This faster response does not materialise and there was only a significant change of rise time observed below K_c values of one. The system is therefore seen as stable with little sensitivity to loop gain changes. The effects of the acceleration contribution through the K_a value is substantial and the system is extremely sensitive to changes in the K_a value. Noise immunity has not been investigated as is the system robustness.

CHAPTER 9

CONCLUSION

9.1 SUMMARY

The precursor to this Master's degree study was the design and building of a Ship Motion Simulator (SMS) by the personnel of CSIR - DPSS to excite the inertial sensors of an optical tracker (SAT). The simulator was designed to be portable, clean in operation by using compressed air, and capable of manipulating the mass of the tracker in a similar fashion as the deck of a maritime vessel. The simulator was designed in the form of a modified Gough-Stewart platform, but exchanging three of the normal actuators with Panhard rods. It was to be used with random, open-loop excitation, but that changed to a requirement for traceable closed-loop excitation.

The SMS was consequently made available for this study into the behaviour and performance of pneumatic actuators as well as the geometry of this specific version of modified Gough-Stewart platform. It started with an analysis of the requirements of the system, using actual measured maritime vessel deck motion to compile specifications. The supplied SMS was tested against this requirement throughout the study to assess if the basic design complies. A geometric description derived from CAD models together with mass, moments of inertia, and operational limitations was compiled. The supplied pneumatic subsystem was described and a first iteration simulation done using Festo Fluidsim®. The subsequent phases of the study covered the kinematics of the system, the integration of ADAMS® and Matlab®, the theoretical and validated pneumatic models, an analysis of the noise on the measurement process, the friction models, both theoretical and validated, the SMS system model validation, and a first order controller design.

The following sections contain a concise description of the results of the various stages of the

study.

9.1.1 Kinematics

A geometric model was derived for the simulator by using the theory of axis transformation through rotation matrixes. The inverse kinematics (the equations that define the actuator extensions for a required platform orientation) was derived, but in the absence of an explicit set of equations for the inverse kinematics of the system a process was devised to calculate a lookup table with the orientation angles as indices with the output being the actuator extensions. This process used the solvers in MSC ADAMS® in a co-simulation between MSC ADAMS® and Matlab® Simulink®. A test for correctness of the lookup table was done by reversing the process and measuring the platform orientation given a series of input angles. This process returned infinitely small errors on the orientation.

9.1.2 Pneumatic Models and Mass Flow Characterisation

The modelling of the pneumatic subsystems was approached by assessing what has been published in the scientific domain in the form of text books, papers, and theses and then building on that. Theoretical mass flow models, based on the work of Beater [10], Richer [26] and Šitum [53] was derived from first principles, resulting in (what is referred to as) the classic pneumatic model. The linearity of the valve spool deflection *vs.* the input control voltage was measured and described by a third order polynomial (eq. 4.1). It was also found that the relationship between the geometric valve orifice area and the spool deflection differed from the published circular orifice model used by Richer *et al.* [26] and Smit [1] and was deemed not to be applicable in the valves used in this system. A linear area derivation was done to replace the circular area description. The combination of the above two equations gave rise to an accurate valve input *vs.* geometric area model.

A second valve mass flow model proposed by Beater [10] was implemented and called the ISO model. The classic model and the ISO model parameters were identified through a series of experiments as described in § 5.2 and a comparison made to determine the fit to real data. In order to apply an observer (α - β filter) to reduce the measurement noise, the measurement noise characteristics (mean value, probability distribution, spectral density) were analysed to confirm if the noise is white Gaussian noise. The kurtosis and the skewness as well as a histogram analysis confirm the latter.

In the case of the classic model, the discharge coefficient as a function of the spool deflection was

the identified entity. The discharge coefficient together with the geometric orifice area have the same meaning as the effective area stated by Van der Merwe *et al.* [19] who used a constant value for the discharge coefficient. A comparison was made between the two models and it was found that the ISO model represented the actual system better in both the charging and discharging cycles. The mass flow through the valve is shown in Figures 5.31 to 5.38. The ISO model includes modifiers to account for fluid contraction and compounded restrictions of flow which were excluded from the classic model by assumption. The most dominant variable in the ISO model is the sonic conductance which has an input voltage relationship graphically illustrated in Figure 5.19b and tabulated in Table 5.2. It has also been shown that the MAE of the ISO model (Figure 5.30b) is significantly lower than that of the classic model.

9.1.3 Friction Model and Friction Identification

The friction modelling of a pneumatic system is a study domain on its own and can be done to different levels of precision. The friction in these systems are always nonlinear and in most cases exhibit some form of hysteresis. As explain in detail in Chapter 6, the friction models developed in the last 20 years have increased in dimension, making them accurate but computationally costly. The goal was to find a reasonable friction model to reproduce the shuddering observed on the real SMS. The decision was made to use a simple stick-slip model identified over the operational range of the SMS, rather than a complex LuGre model or the Leeuven model, both modelling pre-sliding and hysteresis.

A friction model based on a small pre-sliding regime bounded by a peak static friction force at the moment when sliding starts, a constant Coulomb friction component, and an increasing viscous friction sliding regime modified by the Stribeck curve was adopted. The model is based on the work of Nouri [23] and offers the freedom to have different viscous friction coefficients for increasing and decreasing velocities. The typical friction *vs.* velocity relationship is shown in Figure 6.10. A series of experiments were conducted to explore the friction problem, gather data to identify the friction parameters, and to validate the friction model. During this process two very important factors emerged, the first being the fact that the viscous friction increases exponentially at higher velocities and the second being that the Stribeck curve and Stribeck velocity are modified by the acceleration of the actuator. These two phenomena were introduced into the friction model as an acceleration dependent Stribeck velocity scaled by a modification constant ζ and an exponential viscous friction.

The friction function derived from the system identification process as described in § 6.5 is expressed

by Eqs. 6.5 and 6.7. The result is a model that produced a friction behaviour that closely resembled that of the actual measured data, as shown in Figure 6.14.

A friction validation process was run to ensure that the model produced the same results as the real system. During the model validation process it became evident that the quality of the air supply and the level of lubrication of the actuator changed the friction behaviour dramatically. With that said, the validation still produced very good correlation between the model and the real system, reinforcing the trust level in the friction model. As will be covered later on, the friction model and the compressibility of the fluid generated very true to life instabilities and limit cycles in the complete system simulation.

9.1.4 SMS Model Validation

A validation process was necessary to assess the quality of the simulation model. The validation was approached from a subsystem level all the way to the complete SMS and SAT. Throughout the study, when a model for a single component was proposed, a validation was done to ensure that the model could be trusted. This was done for the valve mass flow model and the friction model after the identification processes as was shown in previous two sections. When combining these models into a larger scale model, the errors and unmodelled effects accumulate and the actual causes of error becomes unknown.

To minimise this accumulation of errors, the final validation was broken up in phases starting from subsystem to system level. Initially a pure Matlab® Simulink® simulation using a model of a single actuator without any external load was run, ensuring that the Matlab®/ADAMS® co-simulation is functional and correct. Then a series of open-loop tests are done with the full SMS system, replicating the conditions and scenarios in simulation, and comparing the results. Finally, a series of closed-loop tests are done in the same fashion, comparing the simulation results with that of the real system.

Once the experiments are migrated towards the complete SMS system, laboratory instrumentation had some shortcomings and the necessity arose for a dedicated system controller which is described in § 7.3.3. Additional signals were also captured for model validation purposes using the same Data Translation ADC as in the initial tests.

The results of the validation tests were extremely favourable and gave a high level of confidence

in the models. The Matlab®/ADAMS® actuator simulation produced extension rates and chamber pressures that tracked the measured data very well. Initial conditions for the test runs have a large influence on the absolute signals, as expected for nonlinear systems, but using the measured initial pressures and extensions in the simulation resulted in a very good correlation. There were high frequency differences that were attributed to unmodelled effects, but even with these differences the visual correlation was good enough not to justify any further processing. An example of the actuator extension and the chamber pressure comparisons for the no-load condition are shown in Figures 7.7 to 7.9.

Once the full system validation was started, the tests were executed in such a manner as to ensure the safety of the mounted optical equipment. Instability that manifests itself in the shaking of the SMS can result in the failure of the leveling mechanisms of the SAT, a condition that needs to be avoided at all cost. The initial simulation runs to test the controller identified the margins of stability, gave a feel for the controller gains, and minimised unstable situations on the real system. The open-loop tests were conducted from a central working point after leveling the SMS off with a simple proportional controller. Once again the correlation between the simulation model and the real measured signals were very good. The tracking of the signals, as the example shown in Figure 7.20 and Figure 7.21, from the two scenarios (simulation *vs.* actual) was not as good as in the case of the single actuator, mainly due to accumulated unmodelled effects, and justified an analysis of the fit. The coefficients of cross-correlation between the chamber pressures of the simulation and the real system (see § 7.3.4.1) was above $c_p(N/2) = 0.935$ for all the test runs, resulting in a high probability that the model is accurate enough for control. An arbitrary threshold for similarity used so far in this study is a correlation figure larger than 0.8.

The excitation used was either a chirp signal with a frequency range of 0.05 Hz to 1 Hz or a single frequency sine wave. Out of the open-loop tests it became apparent that dead-band compensation would be necessary and was added for the closed-loop tests. The dead-band compensation ensured significant excitation in the small signal region when linear controllers were used. Heave and roll tests for closed-loop response were conducted, and revealed a system with a large signal bandwidth of no more than 0.617 Hz, which is limited by the mass flow rate at 0.4 MPa.

Similar to the open-loop tests, the closed-loop tests produced outputs with great similarity between the simulated and the actual signals. A temporal comparison (Figure 7.27) revealed that the simulated system signals once again tracked those of the real measured system, albeit with a 14% reduction in

peak to peak amplitude and rise time. The actual system has a more pronounced friction induced shudder on the retraction phase, a slower charge rate and, hence, a lower overall bandwidth. The closed-loop spectral response of the system (Figure 7.30) confirmed the reduction in bandwidth for an arbitrary proportional gain. Similar uncontrolled effects in both the real system and the simulated system around the 2 Hz point could also be observed (Figure 7.29) and showed that the model is an acceptable representation of the the real system in the closed-loop.

9.1.5 Simplified Plant Model and Control

Because the main purpose of this engineering study is to find a realistic model for the SMS for the purpose of controller design, a controller design exercise was added. The controller used for the model validation was a generic PID controller that was implemented as a proportional controller due to the integration and derivative gains being zero. An expansion of this study, as will be mentioned in § 9.3, is the design of nonlinear controllers such as sliding mode controllers as used by Smit [1] or reduced order controllers as used by Richer *et al.* [11].

In this study a simplified model of a pneumatic actuator was devised similar to that which is described by Šitum *et al.* [16]. This model is described (§ 8.1) by a third order transfer function with a natural frequency (ω_s) and a damping coefficient (ζ_f). A closed-loop transfer function was derived and described by eq. 8.4

It was shown that the simplified model exhibited the same low pass characteristics as the complex SMS system model and thus the real system. A state feedback controller was designed from the chosen ratio ($\alpha_c = 1.5$) between the open-loop natural frequency and the closed-loop natural frequency, placing the closed-loop poles at half the desired closed-loop natural frequency and calculating the gain values for the controller. This method focused mainly on stability and the suppression of the resonance. A second approach was investigated in which the system bandwidth requirement was used to place the poles, *i.e.* at the -3 dB point of the resulting 3^{rd}-order system.

In both cases the step responses were favourable when tested with both large and small step sizes. The magnitudes of the solenoid valve inputs in both cases were within physical bounds and the systems were stable in both cases. The Šitum controller resulted in a system rise time of $t_R = 0.255\ s$ and a bandwidth of 1.37 Hz, whereas the SBD based controller gave a rise time of $t_R = 0.33\ s$ and a bandwidth of 1.06 Hz.

This turned out to be only half of the truth as only the extending actuator movement was assessed and the stiction coupled with the compressibility of the air resulted in feedback of the high acceleration values not catered for in the simplified model. The latter became apparent when the high fidelity simulation model was used to ensure the stability of the controller. It became evident that the positive feedback of the acceleration (due to a positive value for K_a) was at the core of the problem, and once corrected by using negative values for K_a, resulted in a controlled system with adequate bandwidth ($BW > 0.5\ Hz$) and stability. The bandwidth is ultimately limited by the mass flow of the charging circuit, and the system stability is insensitive to changes to the loop gain because of this limitation.

9.2 EVALUATION OF OBJECTIVES

A very ambitious engineering study to understand the domain of pneumatic system modelling and control was undertaken. An in depth study of the academic domain as well the published literature domain was done and more information was found than what could be assimilated in the duration of this study. Various formal texts in terms of books were found on the subject, a few which were chosen to feed the initial introduction on pneumatic systems and compressible fluids. A vast number of papers from reputable sources were scoured for information pertaining to similar systems, structures processes, and designs. There is also an unfathomable amount of information available from online sources, many of which add to the confusion in the domain. From all these sources, a selection of relevant publications and information sources were made and the theoretical knowledge on the pneumatic domain built up from a rudimentary level to a level of acceptable understanding.

The first objective was just that, finding relevant information to expedite the development of a controlled SMS system.

The second objective was the generation of a detailed model of the SMS system so that it can be used for controller development and controller testing. It is fair to say that the task of the model development has been executed in a methodical and systematic fashion. As this is an engineering problem, the use of advanced tools made for faster progress, such as the determination of the inverse kinematics and the co-simulation between Matlab® and MSC ADAMS®. Commercially accepted standards such as the ISO-6358 model of the valve flow represented the actual flow phenomena better than the classical physics based models, although the latter was the starting point of most of the pneumatic studies found in literature.

In modeling the mechanical structure, some limitations in the typical design philosophy of cost effective systems came to the forefront, *i.e.* that component cost saving can result in large development time spending. That said, if the system was designed as a Gough-Stewart platform and the inverse kinematics were explicitly defined, the use and integration of ADAMS® would have been of a lower priority and the development of the dynamic simulation could have taken much longer with poor results.

The knowledge of transforming physical mechanical structures into simulation models in ADAMS® resulted in a steep learning curve. Once mastered, the power of high level simulation has great value. A Matlab® Simulink®/ADAMS® co-simulation was realised and used for finding the solution to the inverse kinematic problem and to link Matlab® Simulink® pneumatic models, friction models and controllers to ADAMS®.

The flow of air through a pneumatic system with the accompanying thermal changes in the air properties due to the rate at which pressure changes occur, all formed part of the domain of pneumatic system modelling. As mentioned in the summary section (§ 9.1) of the project, a pneumatic model of the actuators used in the SMS was modelled through a combination of first principle derivations and models presented as part of the ISO-6358 standard. The latter became important during the mass flow validation process in which it was found that the classic model did not represent the valve adequately. The coefficients pertaining to this specific case of actuator were obtained through experimentation and published inference techniques.

A deviation from the normally accepted classical flow models was made in the sense that the orifice (or valve) area was kept constant and the changing variable was the discharge coefficient. Normally, the area would be lumped into an effective area and the discharge coefficient would be kept constant. Computationally, the two methods are equivalent, producing the same results. Another deviation was the choice of the isentropic constant for the identification process. It was chosen to be the same for both the charging and discharging processes, assuming that the model uses the same structure in validation and simulation. The effect of the choice of constants is therefore cancelled through other lumped and some unmodelled effects during coefficient identification.

The friction behaviour of the actuator was modelled using a much simpler model than is available. The time constraints on the project as well as the possible gain in complicating the model was taken into account and a model with limited hysteresis and a simple smoothed stick-slip transient was

defined, identified, and validated. An exponential viscous friction component was identified and added to the model. The contribution in the final model of this exponential term is unknown, as is the reason for this extra term. A general shortcoming in the process of both the pneumatic identification and the friction identification is the limited cycles or test points used in the process, as well as the limited variation in the different types of excitation. In the case of the friction model as well the pneumatic model, the same instrumentation was used for the System Identification (SID) and the validation process. This could potentially introduce instrumentation induced errors that is common to both the processes and cancel each other. An independent instrumentation calibration and validation process could prevent this from happening. It can, however, be stated that the final model validation revealed no significant un-modelled effects, which would ease the mind on the errors induced by the instrumentation.

As mentioned earlier, the integration of Matlab® Simulink® and ADAMS® was successfully completed and the co-simulation delivered similar characteristics as the actual system. This gives great confidence in the validity of the simulation system as a controller development environment. As a main objective, the validation of the system was done in the open-loop as well as in a closed-loop mode. In both cases the simulated response correlated well with reality which means that the objective has been reached.

Controller design for a nonlinear system such as the SMS is a non-trivial task that will consume a lot of effort and time. At the start of the larger project, the scope of the nonlinear effects was grossly underestimated. An effort was made to use the newly developed simulation environment for controller design with reasonable results. A simplified linear model was derived for the actuators using published techniques and a state feedback controller designed for it. The response of the controller was acceptable, falling within the bandwidth requirement set at the start of the study. The platform angular tracking of the setpoints also fell within the requirements. The controller turned out to be robust under the test conditions, which excluded external disturbances or SAT payload movements. A limitation was found in the maximum angular rate (large signal response) limited by the maximum flow rate of the pneumatic system, hence limiting the bandwidth and any higher bandwidth developments. Due to the lack of a suitable sensor and time limitations, the accuracy of the platform movement was not verified through measurement.

9.3 FUTURE WORK

As time and budget is played off against accuracy and fidelity, a project or a study needs to be confined to only the necessary work and effort. Such was the case with the characterisation, modelling, and control of the SMS. The output of the study adhered well to the initial requirements and the objectives were reached, some with some assumptions. In all the disciplines covered in this study more work and expansion is possible and in some cases necessary. Herewith an assessment of further work that should be undertaken.

From a requirements perspective, more real world measurements should be done on a variety of maritime vessels of various size classes to fully populate the data set for deck motion requirements. At the moment the SMS is a single vessel simulator that can manage up to sea state 4. Higher number sea states will necessitate higher bandwidth and larger absolute angular range on the platform, which in turn will result in a redesign of the mechanical structure. This will be best realised through a parallel manipulator such as a full complement Gough-Stewart platform or a hexapod. Another expansion would be that of simulating smaller vessels with higher natural frequencies, hence the same angular range but with larger bandwidth. Linked to the mechanical structure and the electronic controller is the inverse kinematic model that has further investigation possibilities. A real-time solver for the geometry or an explicit description of the geometry, if it exists, would ease the preparation time for lookup tables and can be implemented in the embedded controller or the maritime deck data source.

The pneumatic model of the actuator is well developed in structure, but can be expanded to simulate deck motion with other source pressures. This would entail model identification over lower as well as higher than the current 0.2 MPa and 0.4 MPa source pressures. It would be time consuming to identify the flow coefficients over a large range of pressures, in which case better system identification techniques could be employed. An ambitious continuation of the pneumatic problem would be a component parameter based model definition. Similar functionality can be found in software packages such as Festo's Fluidsim, with the drawback that only a few parameters are adjustable and the simulator cannot be integrated with other packages such as MBD simulators (MSC ADAMS®) or Matlab®.

A vast amount of work is still possible on the friction behaviour of pneumatic seals and actuators. The most prominent is the inclusion of hysteresis and lubrication effects on the dynamic friction models.

Also, the effect of pressure on the sealing force between the piston and the cylinder is only touched on in a few publications. A factor found specifically in this study is the effect of the instrumentation quality in terms of accuracy and noise figures and suitability of the sensors in terms of bandwidth, reliability, and accuracy. An analysis of these effects would be worthwhile to do.

In the controller domain, the environment for developing the controller has been put in place with a first iteration of linearized controller design completed. The use of nonlinear controller techniques as well as additional sensor feedback for Multi Input Single Output (MISO) control is a natural progression from this study.

REFERENCES

[1] P. E. Smit, "Development of a 3-DoF motion simulation platform," Thesis, Stellenbosch : University of Stellenbosch, 2010. [Online]. Available: http://hdl.handle.net/10019.1/4155

[2] Y. Chiew, M. Abdul Jalil, and M. Hussein, "Kinematic modeling of driving simulator motion platform," in *Proc. 2008 Innovative Technologies in Intelligent Systems and Industrial Applications IEEE Conf.*, July 2008, pp. 30–34.

[3] Z. Qu and Z. Ye, "Kinematics analysis of certain novel 3-DoF parallel manipulator," in *Proc. 2011 3rd Pacific-Asia Conference on Circuits, Communications and System*, July 2011, pp. 1–3.

[4] V. E. Gough and S. Whitehall, "Universal tyre test machine," *Proc. 9th International Technical Congress F.I.S.I.T.A.*, vol. 117, pp. 117–137, 1962.

[5] D. Stewart, "A platform with six degrees of freedom," *Proc. Institute of Mechanical Engineers*, vol. 180, no. 1, pp. 371–386, 1965.

[6] T. Brezina, Z. Hadas, and J. Vetiska, "Using of co-simulation ADAMS-Simulink for development of mechatronic systems," in *Mechatronika 14th Int Symp.*, June 2011, pp. 59–64.

[7] D. Baran and W. Lisowski, "Numerical simulation and co-simulation in analysis of manipulators' dynamics," *AGH Journal on Mechanics and Control*, vol. 32, no. 4, pp. 129–135, 2013.

[8] C.T. Crowe *et al.*, *Engineering Fluid Mechanics*, 9th ed. John Wiley & Sons, 2009.

[9] B. Andersen, *The Analysis and Design of Pneumatic Systems*. Krieger Publishing Company, 2001.

[10] P. Beater, *Pneumatic Drives: System Design, Modelling and Control*. Springer-Verlag, Berlin,

Heidelberg, 2007.

[11] E. Richer and Y. Hurmuzlu, "A high performance pneumatic force actuator system: Part 2 – nonlinear controller design," *Journal of Dynamic Systems, Measurement, and Control*, vol. 122, no. 3, pp. 426–434, Jun. 1999.

[12] ISO 6358-1:2013(EN), *Pneumatic fluid power – Determination of flow-rate characteristics of components using compressible fluids – Part 1: General rules and test methods for steady-state flow*, Std. ISO 6358-1:2013(EN), 2013.

[13] ISO 6358-2:2013(EN), *Pneumatic fluid power – Determination of flow-rate characteristics of components using compressible fluids – Part 2: Alternative test methods*, Std. ISO 6358-2:2013(EN), 2013.

[14] D. Purdue, D. Wood, and M. M.J. Townsley, "The design of pneumatic circuits," *Fluid Power International*, pp. 27–36, 1969.

[15] Sanville, F. E., "A new method of specifying the flow capacity of pneumatic fluid power valves," in *Proc. 2nd Int. Fluid Power Symposium*, BHRA, Ed. Guildford, England: BHRA, 1971, pp. 37–47.

[16] Ž. Šitum and J. Petrić, "Modeling and control of servopneumatic drive," *Strojarstvo*, vol. 43, no. 1-3, pp. 29–39, 2001.

[17] D. Ben-Dov and S. Salcudean, "A force-controlled pneumatic actuator," *IEEE Trans. Robot. Autom.*, vol. 11, no. 6, pp. 906 –911, Dec 1995.

[18] B. M. Y. Nouri and M. B. Y. Saudi, "Experimental modelling and identification of compressible flow through proportional directional control valves," *Universal Journal of Control and Automation*, vol. 2, pp. 4–13, 2014.

[19] J. Van der Merwe, J. H. Muller, and C. Scheffer, "Parameter identification and evaluation of a proportional directional flow control valve model," *R & D J SAIMECHE*, vol. 29, pp. 18–25, 2013.

[20] T. Wang, L. Zhao, T. Zhao, T. Kagawa, and W. Fan, "Determination of flow rate characteristics

for pneumatic components during isothermal discharge by integral algorithm," *J Dyn Syst-T ASME*, vol. 134, no. 6, pp. 061 005–1–061 005–8, Sept 2012.

[21] K. Kawashima, Y. Ishii, T. Funaki, and T. Kagawa, "Determination of flow rate characteristics of pneumatic solenoid valves using an isothermal chamber," *J Fluid Eng*, vol. 126, no. 2, pp. 273–279, May 2004.

[22] K. Kawashima, T. Kagawa, and T. Fujita, "Instantaneous flow rate measurement of ideal gases," *Journal of dynamic systems, measurement, and control*, vol. 122, no. 1, pp. 174–178, 2000.

[23] B. Nouri, F. Al-Bender, J. Swevers, P. Vanherek, and H. V. Brussel, "Modelling a pneumatic servo positioning system with friction," in *Proc. 2000 American Control Conference*, vol. 2, 2000, pp. 1067–1071.

[24] C. Fleck and M. Meuser, "New servo-control concept for pneumatic drives which are subject to strong friction forces," *O+P Journal ï£¡lhydraulik und Pneumatik 47*, no. 8, pp. 548–554, 2003.

[25] S. Ning and G. Bone, "Development of a nonlinear dynamic model for a servo pneumatic positioning system," in *Proc. IEEE Int Conf. Mechatronics & Automation*, vol. 1, July 2005, pp. 43–48.

[26] E. Richer and Y. Hurmuzlu, "A high performance pneumatic force actuator system: Part 1 – nonlinear mathematical model," *J Dyn Syst-T ASME*, vol. 122, no. 3, pp. 416–425, Jun. 1999.

[27] F. Najafi, M. Fathi, and M. Saadat, "Dynamic modelling of servo pneumatic actuators with cushioning," *The International Journal of Advanced Manufacturing Technology*, vol. 42, pp. 757–765, June 2009.

[28] X. B. Tran and H. Yanada, "Dynamic friction behaviors of pneumatic cylinders," *Intelligent Control and Automation*, vol. 4, pp. 180–190, May 2013.

[29] K. Khayati, P. Bigras, and L.-A. Dessaint, "Lugre model-based friction compensation and positioning control for a pneumatic actuator using multi-objective output-feedback control via LMI optimization," *Elsevier Mechatronics*, vol. 19, no. 4, pp. 535–547, 2009.

[30] P. Dahl, "A solid friction model," DTIC Document, Tech. Rep. TOR-0158(3107-18)-1, May

1968.

[31] C. Canudas de Wit, H. Olsson, K. J. Åström, and P. Lischinsky, "A new model for control of systems with friction," *IEEE Transactions on Automatic Control*, vol. 40, no. 3, pp. 419–425, March 1995.

[32] J. Swevers, F. Al-Bender, C. Ganseman, and T. Projogo, "An integrated friction model structure with improved presliding behavior for accurate friction compensation," *IEEE Transactions on Automatic Control*, vol. 45, no. 4, pp. 675–686, April 2000.

[33] P. Dupont, V. Hayward, B. Armstrong, and F. Altpeter, "Single state elastoplastic friction models," *IEEE Transactions on Automatic Control*, vol. 47, no. 5, pp. 787–792, 2002.

[34] V. Lampaert, J. Swevers, and F. Al-Bender, "Modification of the Leuven integrated friction model structure," *IEEE Transactions on Automatic Control*, vol. 47, no. 4, pp. 683–687, April 2002.

[35] G. Belforte, G. Mattiazzo, S. Mauro, and L. R. Tokashiki, "Measurement of friction force in pneumatic cylinders," *Tribotest Journal*, vol. 10, no. 1, pp. 33–48, Sept. 2003.

[36] P. L. Andrighetto, A. C. Valdiero, and L. Carlotto, "Study of the friction behavior in industrial pneumatic actuators," in *ABCM Symposium Series in Mechatronics*, vol. 2, 2006, pp. 369–376.

[37] B. M. Nouri, "Friction identification in mechatronic systems," *ISA transactions*, vol. 43, no. 2, pp. 205–216, 2004.

[38] B. Armstrong-Hélouvry, *Control of Machines with Friction*, ser. The Kluwer International Series in Engineering and Computer Science: Robotics : vision, manipulation and sensors. Springer US, 1991.

[39] J. Slotine and W. Li, *Applied Nonlinear Control*. Prentice Hall, 1991.

[40] S. Laghrouche, M. Smaoui, X. Brun, and F. Plestan, "Robust second order sliding mode controller for electropneumatic actuator," in *Proc. 2004 American Control Conference*, vol. 6, 2004, pp. 5090–5095.

[41] P. Bigras, "Sliding-mode observer as a time-variant estimator for control of pneumatic systems,"

Journal of Dynamic Systems, Measurement, and Control, vol. 127, no. 3, pp. 499–502, Aug. 2004.

[42] G. Bone and S. Ning, "Experimental comparison of position tracking control algorithms for pneumatic cylinder actuators," *IEEE/ASME Transactions on Mechatronics*, vol. 12, no. 5, pp. 557–561, Oct 2007.

[43] X. Yu, "Study on servo control strategy for pneumatic manipulator," in *2010 International Conference on Measuring Technology and Mechatronics Automation (ICMTMA)*, vol. 3, March 2010, pp. 641–644.

[44] Z. Šitum, D. Pavkovič, and B. Novakovič, "Servo pneumatic position control using fuzzy PID gain scheduling," *Journal of dynamic systems, measurement, and control*, vol. 126, no. 2, pp. 376–387, 2004.

[45] K. Hamiti, A. Voda-Besançon, and H. Roux-Buisson, "Position control of a pneumatic actuator under the influence of stiction," *Control Engineering Practice*, vol. 4, no. 8, pp. 1079–1088, 1996.

[46] J. Wang, J. Pu, and P. Moore, "A practical control strategy for servo-pneumatic actuator systems," *Control Engineering Practice*, vol. 7, no. 12, pp. 1483–1488, 1999.

[47] L. J. du Plessis, "Design and optimum operation of a re-configurable planar Gough-Stewart machining platform," Doctoral Thesis, University of Pretoria, 2001.

[48] E. W. Weisstein, "Euler angles," accessed 2013.02.07. [Online]. Available: http://mathworld.wolfram.com/EulerAngles.html

[49] Online, "Euler angles," http://en.wikipedia.org/wiki/Euler_angles, accessed 2013.02.07. [Online]. Available: http://en.wikipedia.org/wiki/Euler_angles

[50] Festo, "Proportional directional control valves mpye," Festo data sheet, May 2012.

[51] B. McDonell and J. Bobrow, "Modeling, identification, and control of a pneumatically actuated robot," in *Proceedings of the 1997 IEEE International Conference on Robotics and Automation*, vol. 1, April 1997, pp. 124–129.

[52] A. M. Al-Ibrahim and P. D. R. Otis, "Transient air temperature and pressure measurements during the charging and discharging processes of an actuating pneumatic cylinder," in *Proceedings of the 45th National Conference on Fluid Power*. National Fluid Power Association, March 1992.

[53] Ž. Šitum, D. Kosić, and M. Essert, "Nonlinear mathematical model of a servo pneumatic system," in *9th International Research/Expert Conference" Trends in the Development of Machinery and Associated Technology"*. Antalya, Turkey: TMT 2005, Antalya, Turkey, Sept. 2005.

[54] T. Raparelli, A. M. Bertetto, and L. Mazza, "Experimental and numerical study of friction in an elastomeric seal for pneumatic cylinders," *Tribology International*, vol. 30, no. 7, pp. 547–552, 1997. [Online]. Available: http://www.sciencedirect.com/science/article/pii/S0301679X97000157

[55] NIST, "NIST Thermocouple EMF tables," accessed 03/02/2014. [Online]. Available: http://srdata.nist.gov/its90/download/type_k.tab

[56] W. Martinez and A. Martinez, *Computational Statistics Handbook with MATLAB*, ser. Chapman & Hall/CRC Computer Science & Data Analysis. Taylor & Francis, 2001, p.55.

[57] J. Wang, J. Wang, N. Daw, and Q. Wu, "Identification of pneumatic cylinder friction parameters using genetic algorithms," *IEEE/ASME Transactions on Mechatronics*, vol. 9, no. 1, pp. 100–107, March 2004.

[58] Wikipedia, "Adiabatic process," [Online; accessed 31.01.2013]. [Online]. Available: http://en.wikipedia.org/wiki/Adiabatic_process

[59] ——, "Isentropic process," accessed 31.01.2013. [Online]. Available: http://en.wikipedia.org/wiki/Isentropic_process

[60] ——, "First law of thermodynamics," accessed 31.01.2013. [Online]. Available: http://en.wikipedia.org/wiki/First_law_of_thermodynamics

[61] ——, "Second law of thermodynamics," accessed 31.01.2013. [Online]. Available: http://en.wikipedia.org/wiki/Second_law_of_thermodynamics

APPENDIX A

DEFINITIONS

Adiabatic process An adiabatic process is any process occurring without gain or loss of heat within a system (*i.e.* during the process the system is thermodynamically isolated; there is no heat transfer to/from the surroundings). This is usually associated with a fast increase in pressure, during which time no thermal exchange can happen [58].

Continuity Equation - Ideal Duct If a duct is assumed to be of a rigid nature and does not deform during the process and a steady flow of particles is present, the mass flow rate at any cross section of the duct, irrespective of the cross sectional area at any particular section, will be the same. For a compressible fluid, the continuity equation will reduce to $\rho_2 A_2 V_2 = \rho_1 A_1 V_1$ [8].

Kinematics The branch of mechanics that studies the motion of a body or a system of bodies without consideration given to its mass or the forces acting on it. It is also referred to as the geometry of motion.

Forward Kinematics Definition applied to parallel manipulators. The forward kinematics of a Gough-Stewart parallel manipulator is finding the position and orientation of the mobile platform when the strut lengths are known.

Inverse Kinematics Definition applied to parallel manipulators. The problem of inverse kinematics for Gough-Stewart parallel manipulators can be defined as finding the strut lengths needed to position the mobile platform in a certain position with the desired orientation.

Isentropic process An Isentropic process is one that takes place from initiation to completion without an increase or decrease in the entropy of the system, *i.e.*, the entropy of the system

remains constant. An isentropic flow is a flow that is both adiabatic and reversible [59].

First Law of Thermodynamics The first law of thermodynamics states that the change in the internal energy of a closed system is equal to the amount of heat supplied to the system, minus the amount of work done by the system on its surroundings. The law of conservation of energy states that the energy of an isolated system is constant [60].

Multibody Dynamic System A MBD system is one that consists of solid bodies or links that are connected to each other by joints that restrict their relative motion. The study of MBD is the analysis of how mechanical systems move under the influence of forces, also known as forward dynamics. A study of the inverse problem, *i.e.* what forces are necessary to make the mechanical system move in a specific manner is known as inverse dynamics.

Physical Standard Condition The Physical Standard Conditions for air (defined by Deutsches Institut für Normung (DIN) 1343) is a standard temperature of $T_N = 273.15\ K$ ($0°C$), a standard pressure of $p_N = 101.325\ kPa$, a gas constant of $R_N = 286.9\ N\ m\ kg^{-1}\ K^{-1}$ and a relative humidity of 0%.

Standard Temperature and Pressure (STP) The standard conditions for temperature and pressure are standard sets of conditions for experimental measurements established to allow comparisons to be made between different sets of data. According to International Organisation for Standardisation (ISO) 5011 it is defined as $T_{STP} = 293.15\ K$ ($20°C$), $p_{STP} = 101.325\ kPa$ (1 atm) and 50% relative humidity.

Second Law of Thermodynamics The second law of thermodynamics states that the entropy of an isolated system never decreases, because isolated systems spontaneously evolve towards thermodynamic equilibrium, the state of maximum entropy. The final entropy of an irreversible process is always greater than the initial entropy. For a reversible process, the entropy does not change, and the final entropy equals the initial entropy of the system. Such a process is called an isentropic process (See Isentropic Process) [61].

Technical Standard Condition The technical Standard Condition is defined by ISO 6358 as an alternative standard to DIN 1343, as it is more practical to measure and easier to achieve. According to ISO 6358 the standard temperature is $T_0 = 293.15\ K$, the standard pressure is $p_0 = 100\ kPa$, the gas constant is $R_0 = 288\ N.m.kg^{-1}.K^{-1}$ and the relative humidity is 65%.

This standard is mostly used in the conversion between volumetric flow rate ($\dot{V}$) and mass flow rate ($\dot{m}$) in gasses.

APPENDIX B

MATLAB® RTW EMBEDDED CODER INTEGRATION WITH CODE COMPOSER STUDIO V5.5

B.1 OVERVIEW

Goal: To integrate the C code generated by Matlab®'s embedded coder into CCS V5.5 and to make it available in a CCS project for later modification, compilation and debugging.

Setup/Equipment:

- TMS320F28335 Control Card with 20MHz crystal (`http://www.ti.com/tool/tmdscncd28335`)
- Texas Instruments Docking station (`http://www.ti.com/tool/tmdsdock28346-168`)
- Spectrum Digital XDS510USB programmer/debugger
- Matlab R2012b V8.0.0.783
- Matlab Embedded Coder V6.3
- MATLAB Coder V2.3
- Simulink Coder V8.3
- Simulink V8.0

- CCS V5.5.0.00077

B.1.1 Guide

This is a step-by-step guide to get a Simulink® model coded and programmed into the processor:

B.1.1.1 Environment

1) Install Matlab®, Simulink® and the Embedded Coder Support packages. Ensure that a Simulink® model can be generated and saved. 2) Install CCS (`http://www.ti.com/tool/ccstudio`), the header files (`http://www.ti.com/tool/sprc530`) for the processor, the Flash APIs (`http://www.ti.com/tool/sprc539`) and RTOS/Bios tools (`http://www.ti.com/tool/sysbios`). Header files and processor support can also be found in the control suite installation (`http://www.ti.com/tool/controlsuite`). 3) Open Matlab® and type *ver* in the command window to check for the embedded and RTW tools. 4) Type *checkEnvSetup('ccsv5','f28335','check')*. This will display the current environmental variables set to integrate CCS with Matlab®. It should look something like this:

» checkEnvSetup('ccsv5','f28335','check')

1. CCSv5 (Code Composer Studio) Your version : 5.5.0 Required version: 5.0 or later Required for : Code Generation TI_DIR="`D:\TI\ccsv5`"

2. CGT (Texas Instruments C2000 Code Generation Tools) Your version : 6.2.3 Required version: 5.2.1 to 6.0.2 Required for : Code generation C2000_CGT_INSTALLDIR="`D:\TI\ccsv5\tools\compiler\c2000_6.2.3`"

3. DSP/BIOS (Real Time Operating System) Your version : 5.42.01.09 Required version: 5.33.05 to 5.41.11.38 Required for : Code generation CCSV5_DSPBIOS_INSTALLDIR="`D:\TI\bios_5_42_01_09`"

4. XDC Tools (eXpress DSP Components) Your version : Required version: 3.16.02.32 or later Required for : Code generation

5. Flash Tools (TMS320C28335 Flash APIs) Your version : 2.10 Required version: 2.10 Required for : Flash Programming FLASH_28335_API_INSTALLDIR="`D:\TI\Flash28_API\Flash28335_API_V210`"

If they are incorrect or missing, do step 5. The XDC Tools are not important for C2000 processors.

5) Type *checkEnvSetup('ccsv5','f28335','setup')* to set up the environmental variables inside Matlab®. Follow the prompts to identify the directories. After setting the variables, check them for correctness using step 4. To get the variable loaded every time you start Matlab®, generate Windows System Variables by opening

```
Control Panel\System and Security\System
```

(Win Button-Pause) and selecting Advanced system settings. Select Environmental Variables and add the following System variables:

- `TI_DIR="D:\TI\ccsv5"`
- `C2000_CGT_INSTALLDIR="D:\TI\ccsv5\tools\compiler\c2000_6.2.3"`
- `CCSV5_DSPBIOS_INSTALLDIR="D:\TI\bios_5_42_01_09"`
- `FLASH_28335_API_INSTALLDIR="D:\TI\Flash28_API\Flash28335_API_V210"`

to match the Matlab® variables. Restart the PC.

6) Type *xmakefilesetup* in the Matlab® command window. Untick *Display operational configurations only* and select *ticcs_c2000_ccsv5* from the Configuration dropdown. *Appl* and check the paths under Tool Directories are the same as defined in the Environment setup. Clone the setup by selecting *New...* at *Configuration*. Give the Config a new name, *e.g. ticcs_c2000_ccsv5_OSS*. Select this config.

7) Open a new Simulik Model and save it as *e.g.* "Sample.slx". Select the Library Browser and drag the Target Preferences (ISA Card Icon) from Embedded Coder/Embedded Targets. It will open a window titled "sample/Target Preferences: Initialize Model Configuration Parameters". Select Texas Instruments Code Composer Studio v5 (makefile generation only), the F28335 of choice and select

"yes".

8) Open the model configuration parameters and set the solver to "Fixed-step", Stop time to "inf" and Tasking mode to "SingleTasking" and "Apply". The Fixed-step time can be set to a defined sample interval. Under Code Generation select idelink_ert.tlc. Select "Build" under Code Generation/IDE Link. In the same window select "Debug"under the Vendor Tool Chain and increase the stack size to 1024.

9) Generate a Simulink® model *e.g.* a flashing LED on GPIO34.

10) Press ctrl-B or the build button to generate code.

B.1.2 CCS

1) Open *CCS* V5.5, select "View/Target Configurations" from the menu bar. If there is not a target configuration that matches the setup you are using, generate a new configuration by right-clicking on the User Defined folder. Select "New Target Configuration" and in "File name:" enter a descriptive name, *e.g.* "TMS320F28335 CC XDS510 USB". Select "Spectrum Digital XDS510USB Emulator" from the "Connection" drop-down and "TMS320F28335" from the "Board or Device" window. Save.

2) Select "File", "New", "CCS Project", enter a Project Name and generate an empty project.

3) Expand the new project in the Project Explorer and exclude the 28335_RAM_lnk.cmd file from the build. If the "Derived" directory is included in the structure, exclude that from the build as well.

4) Right click on the active project and select "Import" and "File System" from the "General" folder. Find the generated code from Matlab® in a directory called "Sample_ticcs" (for model called "Sample") one level down from the Matlab® current directory with the Browse button. Select all the .asm, .c, .cmd, .h files as well as the .mk and defines.txt files. Click on the "Advanced" button and and select "Create links in workspace" and "Finish". Changes in the files will now be transferred to the debugger.

5) Open the defines.txt file. Right click on the project name and select "properties" or "Alt-Enter". Select "CCS Build/C2000 Compiler/Advanced Options/Predefined Symbols" and add "_DEBUG",

"__TICCSC__", "RT" and all the defines in the .txt file to the Pre-define NAME "-D" window *e.g.* "MODEL=sample".

6) Set the CCS Build parameters to the following:

- C2000 Compiler:

  Processor Options: -v 28, -ml, -mt, –float_support fpu32

  Include Options: Add all the "COMPILER_CODEGEN_ARGS" and "COMPILER_TCCFG_ARGS" include files indicated by the -I directive from the .mk file to the Compiler Include Options window *e.g.* `-I"D:/ProgramFiles/MATLAB/R2012b/toolbox/idelink/extensions/ticcs/inc"-I"D:/MEng/RTW/CCS5/sample_ticcs"-I"D:/MEng/RTW/CCS5"-I"D:/MEng/RTW"-I"D:/ProgramFiles/MATLAB/R2012b/extern/include"-I"D:/ProgramFiles/MATLAB/R2012b/simulink/include"-I"D:/ProgramFiles/MATLAB/R2012b/rtw/c/src"-I"D:/ProgramFiles/MATLAB/R2012b/rtw/c/src/ext_mode/common"-I"D:/ProgramFiles/MATLAB/R2012b/rtw/c/ert"-I"D:/TI/ccsv5/tools/compiler/c2000_6.2.3/include"`

- Advanced Options:

  Advanced Debug Options: `-g`

  Predefined Symbols:

  `-D"_DEBUG"-D"__TICCSC__"-D"RT"-D"USE_RTMODEL"-D"MODEL=sample"-D"NUMST=1"-D"NCSTATES=0"-D"HAVESTDIO="-D"ONESTEPFCN=1"-D"TERMFCN=1"-D"MAT_FILE=0"-D"MULTI_INSTANCE_CODE=0"-D"INTEGER_CODE=0"-D"MT=0"-D"CLASSIC_INTERFACE=0"-D"TID01EQ=0"`

- C2000 Linker:

  Basic Options: `-stack0x400-w`

  File Search Path:

  `-l"rts2800_fpu32.lib"and-l"..\MATLAB\R2012b\toolbox\idelink\extensions\ticcs\rtlib\IQmath_fpu32.lib"-x`

  Runtime Environment: `-c`

Once this Project setting has been populated for a model, it can be exported as an .xml file for future

use. Right click on the project and select “Export", C/C++ Project Settings, “Next", Export file name and “Finish". Using the import function, these settings can be imported into new projects.

7) Build and debug as usual. Changes in the Simulink® model will also be transferred to the files in the build.

APPENDIX C

NIST THERMOCOUPLE COEFFICIENTS

Table C.1: NIST Coefficients of Approximate Inverse Function for Type K Thermocouple

Coefficient	Value
c0	0.000000E+00
c1	2.508355E+01
c2	7.860106E-02
c3	-2.503131E-01
c4	8.315270E-02
c5	-1.228034E-02
c6	9.804036E-04
c7	-4.413030E-05
c8	1.057734E-06
c9	-1.052755E-08

APPENDIX D

SIMPLIFIED MODEL PARAMETERS

Table D.1: Values of Simplified System Parameters

Adjustment Gain	$k_m = 1.0$
Ambient Pressure	$p_A = 86\ kPa$
Average Upper Chamber Pressure	$p_U = 281\ kPa$
Average Lower Chamber Pressure	$p_L = 386\ kPa$
Mean Chamber Pressure	$\bar{p} = 667\ kPa$
Load mass	$m = 106\ kg$
Specific Heat Ratio	$\kappa = 1.4$
Viscous Friction Coefficient	$b = 530\ N.s.m^{-1}$
Equivalent Spring Constant	$c = 73.341\ N.m^{-1}$
Piston Area	$A = 7.854x10^{-3}\ m^2$
Piston Diameter	$d = 0.1\ m$
Stroke Length	$L = 0.4\ m$
Total Volume	$V = 3.142x10^{-3}\ m^3$
Damping Ratio	$\zeta = 0.095$
Natural Frequency	$\omega_s = 26.221\ rad.s^{-1}$

APPENDIX E

SIMPLIFIED MODEL CONTROLLER DESIGN PARAMETERS

Table E.1: Model and Gain Values Used and Calculated for the State Feedback Controller Design

	Šitum	SBD	Matlab®/ADAMS®
Bandwidth	1.2513	1.0001	-
ζ	0.1641	0.1641	-
ω_c	39.3322	21.3891	-
α	1.5	1.4129	-
ω_s	15.139	15.139	-
ζ_s	0.1641	0.1641	-
K_p	15.8031	3.9128	40.0
K_v	1.3393	-0.4780	1.0
K_a	0.1123	0.0666	-0.005